The University of Cape Town

Department of Mechanical Engineering

Centre for Materials Engineering

Investigation of Strain Rate Sensitivity of Polymer Matrix Composites

A Thesis in

Composite Materials and Mechanics

By

Robert O. Ochola

Submitted in Fulfilment
of the Requirements
for the Degree of

Doctor of Philosophy

October 2004

Est autem fides credere quod nondum vides;
cuius fidei merces est videre quod credis –

Faith is to believe what you do not see;
the reward of this faith is to see what you believe.

(St. Augustine)

ABSTRACT

An investigation into high strain rate behaviour of polymer composites was performed by developing a finite element model for a fibre reinforced polymer (FRP) plates impacted at varying strain rates. The work was divided into three facets, firstly to characterize the FRP material at varying strain rates, to develop a constitutive model to elucidate the relationship between strain rate and ultimate stress and lastly to use the experimental data to develop a finite element model.

Experimental work performed in support of this model includes material characterization of unidirectional carbon and glass fibre reinforced epoxy at varying impact strain rates. The data is then used to develop a suite of constitutive equations that relate the strain rate, ultimate stress and material loading type.

The model is of a linear and non-linear viscoelastic type, depending on the type of loading and is applicable to a FRP plate undergoing out-of-plane stresses. This model incorporates techniques for approximating the quasi-static and dynamic response to general time-varying loads. The model also accounts for the effects of damage, the linear and non-linear viscoelastic constitutive laws reporting failure by instantaneously reducing the relevant elastic modulus to zero. An explicit solver is therefore utilised in order to ensure stability of the numerical procedure.

Glass fibre reinforced plastics (GFRP) was found to be more strain rate sensitive in all directions when compared to carbon fibre reinforced plastics (CFRP). The validation process therefore involves plate impact experimental testing on GFRP plates. The data from these experiments compare to within 8 % of the finite element model that incorporates both damage and the developed strain rate sensitivity constitutive equations.

For the first time a model that includes progressive damage with built-in strain rate sensitivity is developed for these particular FRP systems. Furthermore, the ultimate stress has been related to strain rate using an empirical technique. This technique allows for the prediction of dynamic ultimate stresses given the quasi-static ultimate stresses, again for this particular material systems.

ACKNOWLEDGEMENTS

I am deeply indebted to the many individuals who have spent a great deal of their time to assist me in putting this thesis together. I would like to thank:

Dr. K. Marcus and Prof. G.N. Nurick, my supervisors for the duration of this PhD project, for their endless support and encouragement, many fruitful scientific discussions and for being friends and mentors over the years.

Dr. T. Franz of the Cardiovascular Unit at the University of Cape Town Medical Department for the endless work he put in throughout the duration of this work.

The Centre for Materials Engineering, Prof. R. D. Knutsen and Assoc. Prof. C. I. Lang for their constant advice and motivation, to strive for the best. The atmosphere at the Centre was completely conducive for research.

Dr. N. Petrinic of Oxford University Solid Mechanics Group for organising the use of the High Strain Laboratory. His technical advice on high strain rate testing as well as numerical modelling set in motion major aspects of this work.

Prof. N. Marais for your assistance with the numerical modelling aspect of this work.

The National Research Foundation for their financial assistance.

Aerodyne Technologies South Africa for supplying material for this work.

Dr. Mira Topic the encouragement and mentorship.

Glen Newins designing and machining the numerous samples and grips for this project, for keeping me company during those long nights, for the laughs, chats and encouragement.

Peter Jacobs for his assistance in the workshop.

Trevor Cloete high strain rate was a new area and you introduced the compression high strain rate technique to me.

Julie Henry and Norma Africa for your assistance and friendship.

My fellow students at the Centre and Department over the years for all the great times, support, understanding, this time was made enjoyable

My very special thanks to friends, Ciru, Chris, Pudding, Pumpkin, S. Mahoi, Ivandra, Sheilla, Tina and Dr. K. Jackson, my cousin Hazel, for their understanding, endless advice and support.

My family in Cape Town from the day I arrived Janet and Deon Basson, making me feel so at home, and for the words of wisdom and abundant assistance.

Finally, my Dad, Dr. S. A. Ochola, my Mum, T. A. Ochola, my brother John, my sisters Judy, Isabella, Lucy and Rachel, my niece Sarabi, for making this possible, the love, kind words, support, I believe for all of us the journey has just began.

Dedicated to my Mum and Dad, you taught me how to learn and respect

LIST OF ABBREVIATIONS

ALLAE	**Artificial Strain Energy**
ALLKE	**Kinetic Energy**
ALLIE	**Total Strain Energy**
ALLWK	**External Work**
ASTM	**American Society for Testing and Materials**
BS	**British Standards**
BVID	**Barely Visible Impact Damage**
CCHS01	**Carbon Compression High Strain Rate Specimen No 1**
CCLS01	**Carbon Compression Low Strain Rate Specimen No 1**
CFRP	**Carbon Fibre Reinforced Polymer**
CHS	**Cross Head Speed**
CI	**Confidence Interval**
CLT	**Classical Lamination Theory**
CSHS01	**Carbon Shear High Strain Rate Specimen No 1**
CSLS01	**Carbon Shear Low Strain Rate Specimen No 1**
CTHS01	**Carbon Tension High Strain Rate Specimen No 1**
CTLS01	**Carbon Tension Low Strain Rate Specimen No 1**
FEA	**Finite Element Analysis**
FEM	**Finite Element Method**
FRPs	**Fibre Reinforced Polymers**
GCHS01	**Glass Compression High Strain Rate Specimen No 1**
GCLS01	**Glass Compression Low Strain Rate Specimen No 1**
GFRP	**Glass Fibre Reinforced Polymer**
GSHS01	**Glass Shear High Strain Rate Specimen No 1**
GSLS01	**Glass Shear Low Strain Rate Specimen No 1**
GTHS01	**Glass Tension High Strain Rate Specimen No 1**
GTLS01	**Glass Tension Low Strain Rate Specimen No 1**
IITRI	**Illinois Institute of Technology Research Institute**
LVDT	**Linear Voltage Displacement Transducer**
PAN	**Polyacrylonitrile**
PMCs	**Polymer Matrix Composites**
SHPB	**Split Hopkinson Pressure Bar**
SPH	**Smoothed Particle Hydrodynamics**
UMAT	**User Material**
VUMAT	**Vectorised User Material**

NOMENCLATURE

A	**Damage zone predicted by fibre failure criterion**
A_0	**Fibre failure interaction zone**
c	**Wave speed**
C_0	**Fundamental wave velocity**
D	**Cowper Symonds factor**
D_f	**Degradation factor**
E	**Young's modulus**
E_1	**Young's modulus in the 1-plane**
E_2	**Young's modulus in the 2-plane**
E_3	**Young's modulus in the 3-plane**
E_f	**Young's modulus in the fibre direction**
E_m	**Young's modulus in the matrix direction**
F	**Function of an equation**
G_{12}	**Shear modulus in 12-plane**
i	**Index**
L	**Length**
m	**Mass**
M	**Mass matrix**
N_i	**Trial Function**
p	**Moment**
S_c	**Compressive shearing strength causing fibre failure**
S_f	**Tensile shearing strength causing fibre failure**
S_m	**Cross sectional shear strength causing matrix cracking**
S_{m23}	**Cross sectional (2-3 plane) shear strength causing matrix cracking**
S_i	**In situ shear strength of lamina**
S_{12}	**Shearing strength (1-2 plane)**
t	**Time**
u	**Displacement**
v	**Velocity**
w	**Work**
x	**Distance/position**
X	**Strength of lamina in longitudinal direction**
X_T	**Tensile strength in fibre direction**
Y_c	**Compressive strength in matrix direction**
Y_T	**Tensile strength in matrix direction**

ζ	**Isoparametric co-ordinate**
ξ	**Forward travelling waves, isoparametric co-ordinate**
η	**Backward travelling waves, isoparametric co-ordinate, viscosity**
β	**Backward travelling waves**
β_w	**Shape Function Weibull**
α	**Forward travelling waves**
γ	**Poisson's ratio**
Δ	**Change in**
e_c	**Chang-Chang constant for compressive failure**
e_D	**Chang-Chang constant for delamination failure**
e_f	**Chang-Chang constant for fibre failure**
e_M	**Chang-Chang constant for matrix failure**
δ	**Measured tensile ply strength**
ε	**Strain**
$\dot{\varepsilon}$	**Strain rate**
$\dot{u}$	**Velocity**
f	**Stiffness force**
ρ	**Density**
θ	**Orientation angle**
ν	**Poisson's ratio**
σ	**Stress**
σ_d	**Dynamic stress**
σ_s	**Quasi-static stress**
τ	**Average interlaminar stress**
[B]	**Function of the isoparametric axes**
$[C]$	**Compliance coefficient**
[*d*]	**Displacement vectors**
$[D]$	**Stiffness modulus**
[*F*]	**Force Vector**
|J|	**Jacobian Determinant**
[*K*]	**Stiffness matrix**
$[s]$	**Stiffness coefficient**

LIST OF FIGURES

LIST OF TABLES

TABLE OF CONTENTS

CHAPTER 1

INTRODUCTION

1.1. OVERVIEW

The need for performance-orientated material and structural systems has resulted in the introduction and development of advanced composite materials. These materials represent a synergy of diverse individual constituents, which in combination possess the potential for performance far exceeding that of the individual elements. More specifically, fibre reinforced polymers (FRPs) are designed so that the mechanical loads to which the structure is subjected in service are supported by the reinforcement. The function of the matrix is to support the fibres and to transfer loads between them. The main advantages of FRPs include their low density coupled with high stiffness and strength along the direction of the reinforcement. This combination forms the basis for their potential in the aircraft, automobile and the sporting industry as shown in Figure 1.1. For example the superior corrosion resistance and fatigue resistance compared to metals, make FRPs more desirable for use in automobile parts such as leaf springs and drive shafts.

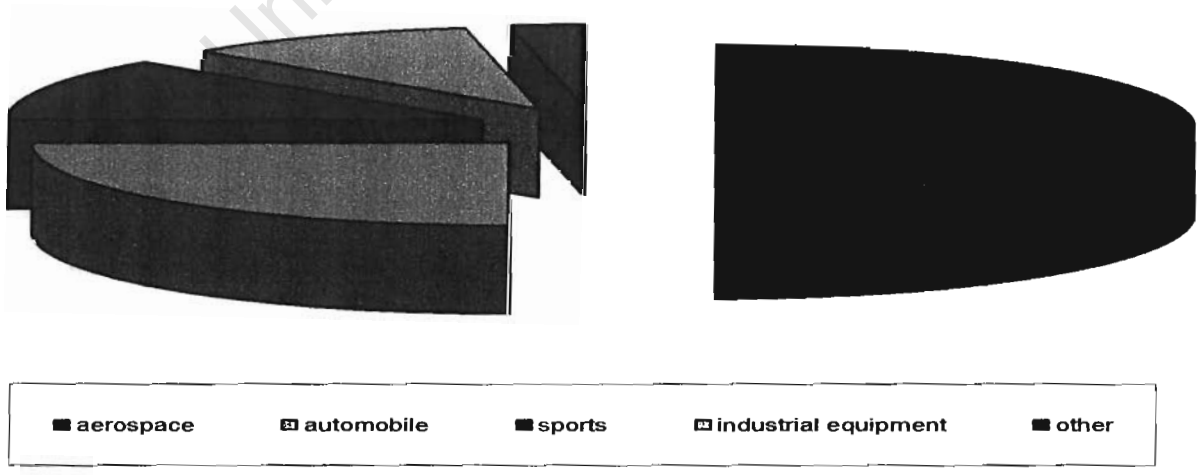

Figure 1.1: Percentage market application for FRPs in 2000 [1].

Carbon fibres are manufactured by many companies and the world production capacity exceeds 12 000 tonnes/year reported in 2001 [2]. In spite of this large production capacity carbon fibres are still relatively expensive. Nevertheless, the usage of carbon fibre increased from 1000 tonnes/year in 1981 to 8000 tonnes/year in the decade ending 1991. This is shown by the annual consumption increase in polyacrylonitrile (PAN) based fibres Figure 1.2 [2]. It was forecast that by the year 2005 polymer matrix composites (PMCs) could make up 65 percent of the structural weight of commercial transport aircraft [3]. Assuming a starting material value of $132 per kilogram, the market for the year 2005 was projected to be worth $1.5 billion for polymer matrix composite materials alone [3].

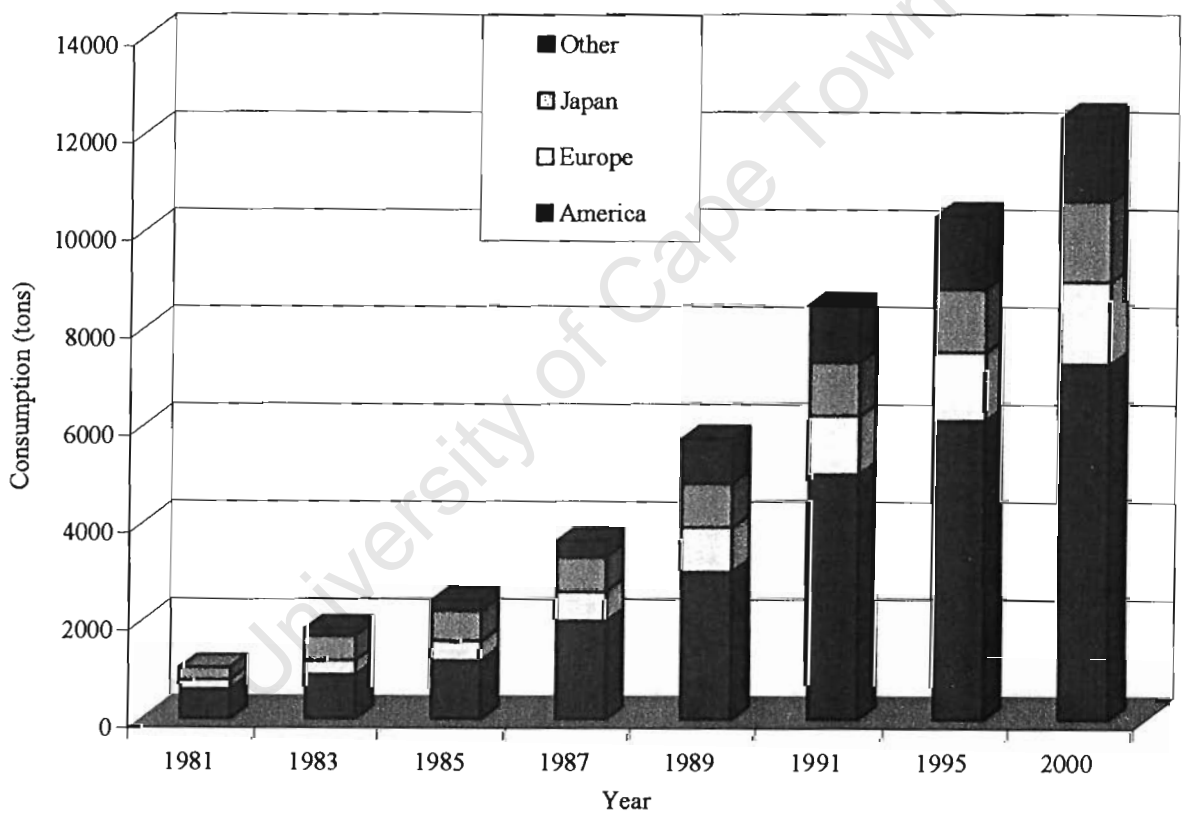

Figure 1.2: Annual consumption of carbon fibres produced from PAN, from 1981 to 2000 [2].

A major aircraft market opportunity for advanced composites is in the commercial transport sector. For example, Airbus Industry of Blagnac, France estimated that 40 % of the structure and

components of A380's the first true double-decker plane will be manufactured from the latest generation of carbon composites and advanced metallic materials (Figure 1.3). This is because they are less dense and additionally offers improved reliability, maintainability and ease of repair compared to traditional materials [4]. The A380 aircraft is one of the first to have a carbon-fibre central wing box, saving some 1.5 tonnes/aircraft compared to the most advanced aluminium alloys [5]. A monolithic carbon fibre reinforced polymer (CFRP) design has been adopted for the fin box and rudder together with the horizontal stabilizer and elevators. The upper deck floor beams, pressure bulkhead, fixed-wing leading edge and secondary brackets in the fuselage (e.g., for fixing interior trim) are likely to be made from thermoplastics [5].

Figure 1.3: An Airbus A380 showing various components made from CFRP composites [5].

The FRP materials are also considered for the ribs in the fixed leading edges of the vertical and horizontal stabilizers. The upper fuselage shell will use GLARE, a laminate with alternate layers of aluminium and glass fibre reinforced adhesive. Weight savings using this material is about 800 kg per aircraft and has the added promised bonus of enhanced fatigue and damage resistance [5].

1.2. RESEARCH MOTIVATION

The operating conditions of lightweight structures may vary significantly with regards to the loading rates imposed during service. The loading rate varies from very low rates in creep, to high rates associated with ballistic impact. The CFRP wing box shown in Figure 1.3 is prone to damage from varying impact velocities. The impact velocities vary significantly from barely visible impact damage (BVID) from a dropped tool at low strain rates, to high velocity impact from runway debris or bird impact during aircraft takeoff, leading to complete material failure. The overall strength of anisotropic materials with various failure modes such as laminate composites will be affected by varying strain rates [6]. The CFRP used to make the wing box requires full characterization over the complete range of strain rates for success in service operation. This would require comprehensive reliable testing before the release of an aircraft into action.

The cost of extensive testing precludes the establishment of a pure experimental base for the prediction of impact damage in composite structures. Due to the magnitude of varying FRP orientations and laminate properties, the results from one FRP material lay-up cannot be transferred to the next FRP system. Secondly, the operating conditions for FRP materials have been shown to vary in terms of the rates of loading. Therefore, from a cost point of view, the development of finite element (FE) codes that predict the mechanical behaviour of FRP materials of varying orientations becomes imperative. The development of FE codes that account for the change in the material property behaviour with different strain rate should be established.

Notwithstanding the extensive research that has been undertaken in the last decade on fibre reinforced polymer composites, very few attempts have been made to develop progressive damage models that include the effects of strain rate sensitivity of FRP. Progressive damage models predict the onset of various damage modes such as fibre failure, matrix cracking and delamination that are inherent in FRPs. These models give a good prediction of the onset of damage at quasi-static strain rates. The extent of failure such as delamination, interfacial splitting, disintegration and debonding perhaps do increase as the rate of loading moves from quasi-static

to dynamic. These mechanisms play active roles in the absorption of energy and have a significant impact on the overall strengthening mechanism as the rate of loading is increased.

Progressive damage models that are presently used for dynamic loading conditions use quasi-static properties, which often underestimate the onset of failure. These models presently do not account for the features that dominate high loading failure. The contribution which this research would like to make from the previous ones, is to develop models that would attempt to include the dynamic behaviour of FRPs at high strain rates.

1.3. RESEARCH OBJECTIVES

The broad objective of the current research is to develop a numerical progressive damage model to predict the onset of failure in the FRP laminates which are subjected to varying loading conditions. The main objective however was to investigate the strain rate behaviour of FRP subjected to varying loading conditions. To achieve this objective, the research will:

- Observe and quantify the behaviour of FRP under varying loading conditions. In order to achieve this, material characterization tests were designed to isolate the various damage modes and thus provide material information on the various FRP failure modes at varying strain rates. The data from the material characterization allows for the development of suites of constitutive equations that give the relationship between ultimate stresses of FRP materials at varying loading rates.
- Develop and implement numerical models that simulate the behaviour of the material characterization tests. Each model will simulate the material behaviour in uniaxial compression, shear and tension. The focus is on incorporating strain rate sensitivity parameters with a progressive damage model for FRP loaded under varying strain rates.
- Validate the experimental-numerical dual approach by undertaking a comparative study between the experimental plate impact and numerical plate impact model using the

material data derived from the experimental work and the combined constitutive equation that includes strain rate sensitivity parameters and progressive damage.

1.4. THESIS OUTLINE

Chapter 2 is a review of the material characterization testing procedures, impact damage prediction and development of strain rate sensitive constitutive equations. Chapter 3 introduces the theories used in the research for evaluating experimental results through to developing the mathematical model. This is followed by material characterization tests in chapter 4. These tests provided data about material properties, the observed failure mechanisms associated with the proposed test regimes and the varying degree of strain rate sensitivity associated with the adopted specimen geometries. Chapter 5 includes experimental results and the development of constitutive equations incorporating strain rate sensitivity parameters.

In chapter 6 the material data gained from the undertaken tests are used to develop a mathematical relationship that relates the ultimate stress to the rate of loading. This chapter includes the development of an algorithm that is incorporated in a finite element (FE) code. The algorithm provides for the progressive failure through material property degradation. The numerical algorithm is validated by the sets of experimental tests in chapter 5 that investigate the response of FRP laminates to varying impact loading, viz. quasi-static to dynamic impact. Chapter 7 gives a detailed discussion and interpretation of both the experimental and numerical results. The conclusion and basis for future work is presented in chapter 8.

CHAPTER 2

LITERATURE REVIEW

2.1. BACKGROUND

Polymer matrix composites (PMCs) constitute the most widely developed material, with a broad range of fabricated shapes and accepted commercial properties, from the family of composite materials presently in use [7]. PMCs are characterized by their low density, high strength and stiffness, corrosion resistance and fatigue resistant properties. These properties make PMCs extremely attractive for numerous engineering applications in the aerospace, civil engineering, marine and automobile industries. Many of the applications require service under varying loading conditions that may fluctuate from quasi-static to dynamic. Clearly then, a study of the behaviour of these materials under varying strain rates is imperative.

In addition, the optimum utilization of materials requires an extensive understanding of their requisite mechanical and physical properties. The timescale of the deformation process, for most materials undergoing inelastic deformation has been found to have some significant influence on the relationship between the applied force and deformation [8]. The study of creep is an important area for mechanical property determination with respect to materials or structures loaded over long time durations. High strain rate testing on the other hand is relevant to short time, transient loading. The ultimate goal is to provide design engineers with reliable data that can be used with a high degree of confidence in the design of composite structures [9].

The influence of strain rate on FRPs, specifically CFRP and (glass fibre reinforced plastics) GFRP has been the subject of research since the early 1970s, but due to experimental difficulties and the existence of limited reliable data, no significant breakthrough has been achieved [10,11]. Much of the work at the time employed the use of instrumented Charpy tests where notched beam specimens were subjected to impact bending [12]. The load-time records obtained from the

device were used to estimate the energy absorbed in the various stages of the fracturing process. At increasing loading conditions the effects of stress wave reflections coupled with the complex geometry of the specimen inhibited any fundamental analysis of the material response and its dependence on the loading rate [13]. The need for the development of tests covering a wide range of loading rates up to impact rates, in uniaxial compression, in pure shear and uniaxial tension was reported in 1977 by Adams [14].

It is understood that many materials when deformed at high rates of strain respond appreciably differently, than when loaded under static conditions, thus justifying the need for dynamic characterization [15]. At high loading rates, inertia and consequently wave propagation effects become important and the method for investigation must in some form involve the propagation of stress waves [13]. Traditionally, the split Hopkinson pressure bar (SHPB) technique was used to determine the material behaviour of isotropic materials at high loading rates. This technique was therefore adapted to the testing of FRPs in compression, shear and tension [11,15,16].

A further fundamental element in the prediction of the behaviour of composite materials involves the elucidation of the relationship between the stresses, strains and their time derivatives [17]. These relationships are referred to as the constitutive equations of the material and the determination of this relationship is a key element in the analysis and design of structural elements or systems [17]. One of the important components in the constitutive equations is the variation in material strength with the applied rate of loading and how stress and strain are related throughout a structure subjected to varying loading conditions [14]. An initially intact material develops micro-voids, micro-cracks and fibre/matrix debonding which can lead to a loss of stiffness [14]. Eventually the coalescence of these defects leads to the complete failure of the material subjected to the applied load. The interaction between these defects at varying loading conditions is not well documented. However, phenomenologically, it has been observed that the ultimate stress of most composite materials as well as metals increase as the rate of loading increases [13].

A typical plot of ultimate stress versus log strain rate is depicted for a heterogeneous material, concrete, in Figure 2.1. Although this thesis deals with PMCs, the objective of this analogy is to simply show the fundamental differences in the materials ultimate stress under compression from three distinctly different strain rates, quasi-static, medium and dynamic. Concrete falls under the composite materials family, therefore this example is deemed appropriate. The observed variation in ultimate stress with strain rate is complicated by the existence of the different constituent materials in concrete. Two principal points seem to emerge from this research on concrete; the first is the requirement of knowledge of the governing equations. Secondly, corresponding material properties, for the various loading conditions, viz. compression, shear and tension are essential, especially when characterizing materials comprising of more than one principal material such as laminate composite materials [14].

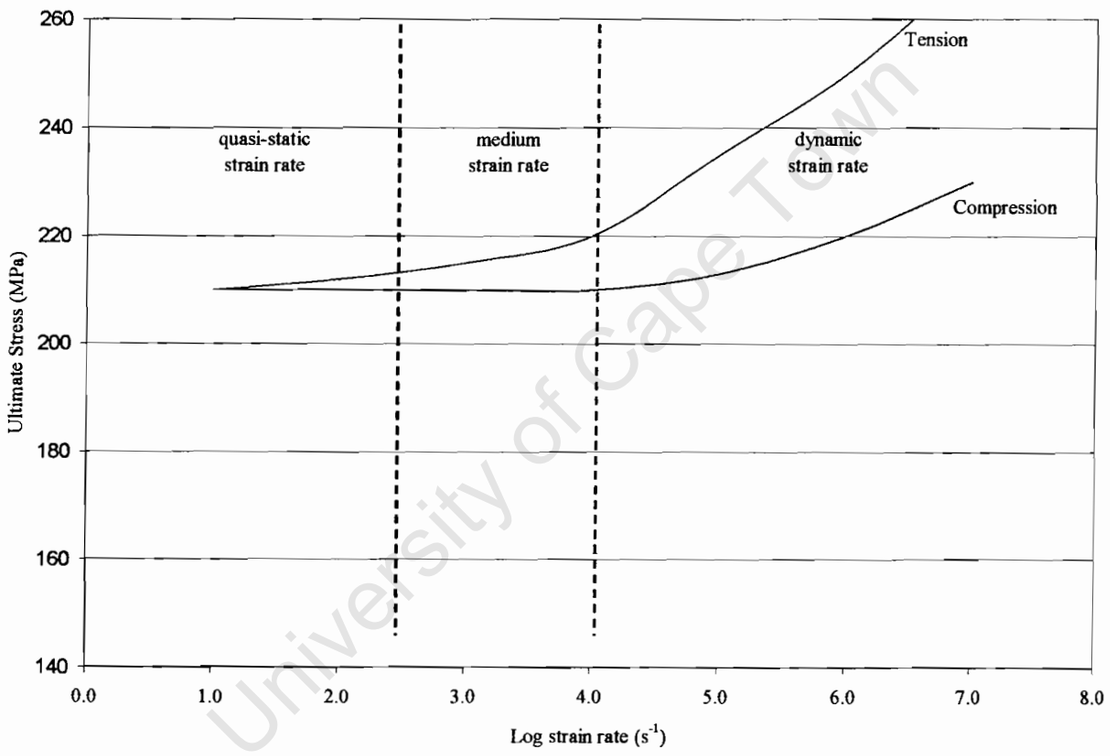

Figure 2.1: Ultimate stress versus log strain rate graph for concrete under tensile and compression loading at varying strain rates [14].

A typical fibre volume fraction for unidirectional CFRP or GFRP in an epoxy matrix often varies from 0.6 to 0.68 depending on the lay-up process [18]. Therefore, the matrix would constitute approximately 40 % of the material, resulting in various matrix dominated failure modes [18]. A study investigating the effects of strain rate on an epoxy resin showed high levels of strain rate sensitivity and considerable recovery indicative of a viscoelastic material, as Figure 2.2 shows [19]. It is thought that the need to individually characterize the various FRPs failure modes such as fibre failure, matrix cracking and delamination under varying loading conditions could result in a better understanding of the various failure mechanisms of CFRP and GFRP laminates at varying strain rates [19].

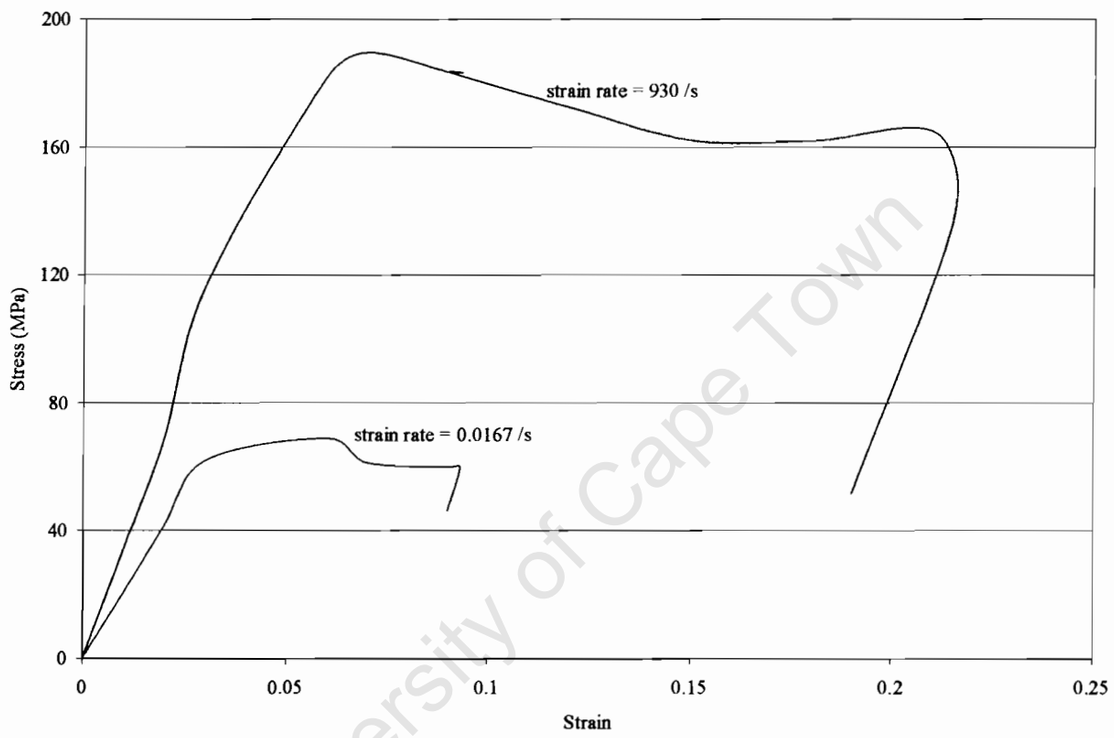

Figure 2.2: Static and dynamic stress-strain curves for epoxy under tensile loading, showing the degrees of recovery [19].

In the next section, existing literature on the various experimental methods that have been previously used to characterize laminate composites under varying strain rates is reviewed. This forms the basis for the experimental procedures used in chapter 4 for collating of material property data that are of interest in this research.

2.2. EXPERIMENTAL TESTING

2.2.1. COMPRESSION TESTS

2.2.1.1. QUASI-STATIC STRAIN RATES

The ultimate compressive stress of FRP composites is generally lower than the tensile ultimate stress. This relative weakness in compression is often seen as the limiting factor in the applications that use composite materials. However, the mechanisms of composite failure in compression are not well understood [20]. Compressive failure in laminate materials continues to constitute an area of great interest for both experimentalists and analysts alike. The main reason for this is the geometrical and material non-linearity that exists even in the simplest of configurations under compression loading.

Composite material structures are generally constructed as two-dimensional laminates, so on a structural level, laminated components such as beams, plates and shells are analysed for global stability in compression loading by extending classical beam/plate and shell theories for isotropic materials to laminated structures via classical lamination theory (CLT) [21]. Buckling prediction results for thin laminates (usually less than 36-48 plies) generated using CLT are generally good [21]. Since the theory treats the laminate as an equivalent anisotropic medium, it cannot therefore predict any material failure. Numerous experimental results reveal that material failure such as fibre buckling or kinking in plies, where the fibres are aligned with the loading axis and coupled with delamination, are the initiating mechanisms of compressive failure that lead to the eventual global instability [21]. Any numerical predictions will therefore be limited to a maximum thickness of laminate due to the assumption of CLT.

Several compressive testing methods have been standardized by the American Society for Testing and Materials (ASTM) [22]. Nevertheless a large part of the literature on compressive failure of composites is still devoted to the problem of determining what type of test configuration is best suited to measure the compressive ultimate stress of FRPs. However, a consensus seems to suggest that side loaded specimens provide the best measure of composite compressive ultimate stress. In this type of fixture, the compressive stress is transmitted to the test section through shear in the grip section, often through adhesively bonded end tabs. Examples are given in ASTM D 3410 of the Celanese and IITRI (Illinois Institute of Technology Research Institute) fixtures, shown in Figure 2.3 [22].

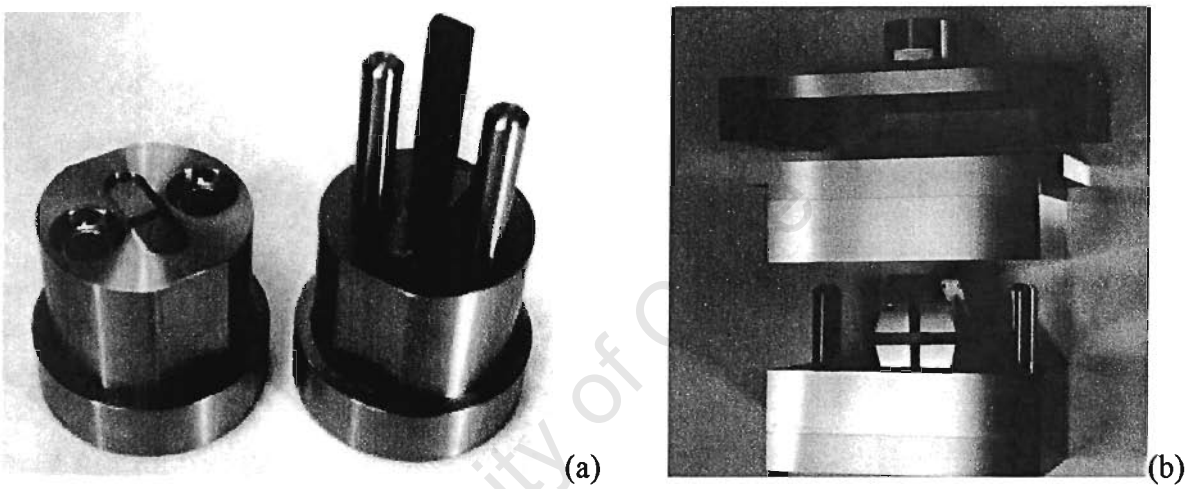
(a) (b)

Figure 2.3: Test fixtures used in compression testing (a) Celanese and (b) Illinois Institute of Technology Research Institute (IITRI) [22].

Other methods that have been explored include the direct end loading of compression specimens. However, this test may lead to unwanted failure by splitting and brooming of fibres at the point of application of the load [23]. Due to its simplicity, direct end loading is often chosen for specimens that are not suitable for testing following a standard test method. An example would be the pultruded cylinders tested at different temperatures by Dutta [24]. At low strain rates of between 10^{-5} s^{-1} to 10^{-1} s^{-1}, constant load, screw driven or hydraulic testing machines are predominantly used to obtain information that describe material behaviour. The stress-strain

behaviour generated from the quasi-static test is considered to be an inherent property of the material. However, this is only valid for the strain rate at which the test has been conducted [25].

2.2.1.2. DYNAMIC STRAIN RATES

Early research on high strain rate response of laminate composites dates back three decades. Sierakowski *et al.* in 1971 investigated the compressive ultimate stress and failure of steel reinforced epoxy composites [15]. The investigation involved mechanical testing at strain rates ranging from 10^{-5} s^{-1} to 10^{4} s^{-1}. For the composites tested, strain rates effects depend on various composite constituent properties, geometric arrangement, volume fraction of reinforcement as well as the size of the reinforcing fibres. Sierakowski *et al.* found a simple energy criterion for composite systems with a brittle matrix for predicting delamination [15]. Sierakowski *et al.* showed that high strain rate or impact failure characteristics are often distinctly different from failure observed at low strain rate testing [15].

Griffiths and Nevill investigated the dynamic behaviour of unidirectional carbon fibre composites at high strain rates to determine how the material behaviour is dependent on fibre volume fraction and fibre orientation [26]. The dynamic stress-strain characteristics of carbon-fibre composites in compression differ considerably from those under static loading. However no strain rate effects are noted for limited changes in strain rates between 320 s^{-1} and 550 s^{-1}. The reductions in the elastic modulus at high strains rates is reported to be due to the specimen geometry and are therefore not an intrinsic property of the composite [26].

The dynamic compressive behaviour of unidirectional and transverse isotropic glass-epoxy composite were determined by Kumar *et al.*, using the Kolsky pressure bar technique, for six fibre orientations, viz. 0°, 10°, 30°, 45°, 60° and 90° at a strain rate, $\dot{\varepsilon}$, of 265 (±50) s^{-1} [27]. Studies were carried out on cylindrical specimens of lengths ranging from 12 mm to 35 mm and diameters ranging 16 mm to 17 mm. Stress-strain curves for GFRP loaded at quasi-static strain rates of 2 x 10^{-4} s^{-1} were compared to stress-strain curves for GFRP loaded at dynamic strain rates of 265 s^{-1}. For all orientations of glass epoxy there was a change in the failure modes, as well as

an increase in ultimate stress at higher strain rates. The stress strain curves shown in Figure 2.4, for 0° and 10° fibre orientations show increases in the ultimate stress with increasing strain rate.

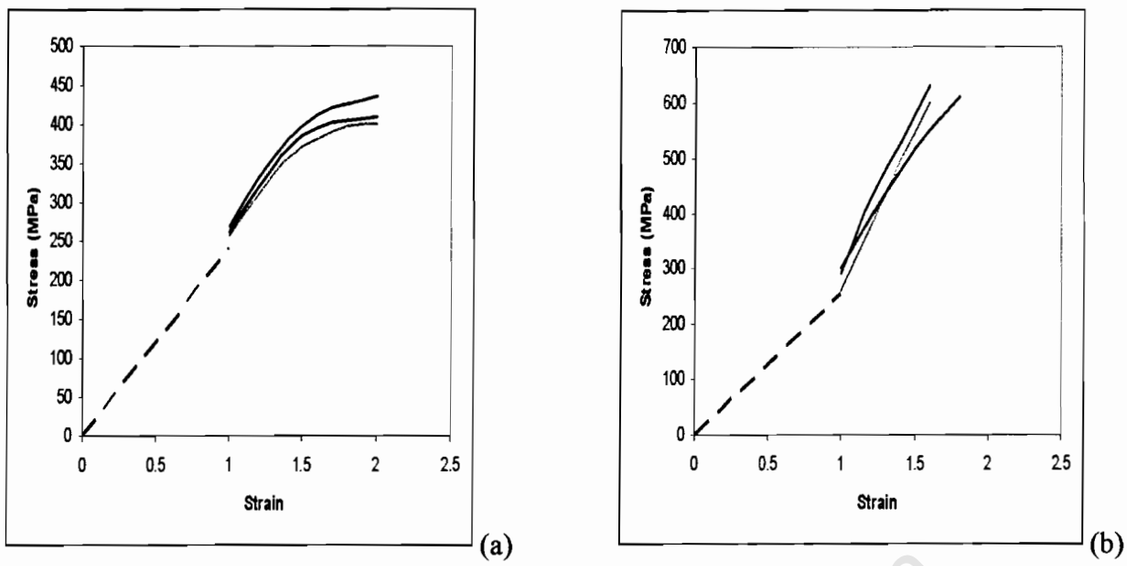

Figure 2.4: Stress-strain curves for orientations (a) $\theta = 0°$ and (b) $10°$ at $\dot{\varepsilon} = 265(\pm 50)\ s^{-1}$. Dashed curves represent quasi-static behaviour at $\dot{\varepsilon} = 2 \times 10^{-4}\ s^{-1}$ [27].

This is because the fibres at 10° will "delay" failure due to fibre buckling, this mode of failure is more prominent with a 0° structure. The quasi-static region is depicted by the dashed curves. The maximum ultimate stress in the quasi-static region is approximately 250 MPa. The dynamic ultimate stress on the other hand increases to 450 MPa and 600 MPa for the 0° and 10° orientations, respectively. Specimens of 0° orientation, fracture along the fibres by tensile splitting, due to the compressive loads causing transverse tensile strains because of the Poisson's effect. Therefore, as the transverse tensile strain exceeds the transverse strain to failure, failure occurs by tensile splitting. Specimens of 10°, 30° and 45° orientation fracture along the fibre predominantly by interlaminar shear, although cracks caused by a degree of tensile splitting are also seen on the surface of some of the specimens. Kumar *et al.* deduced that the dynamic stress-strain curves are linear up to fracture for angles of 0° and 10° and non-linear for orientations greater than 10° [27].

Daniel and LaBedz proposed a novel way of examining the high strain rate behaviour of composites [28]. They obtained dynamic stress-strain curves by radially compressing ring specimens for a short duration using an external pressure pulse. While no mention of the mechanisms of failure was stated, dynamic ultimate stresses of hoop wound ring type specimens are given with measured strain rates of 230 s^{-1}. The dynamic ultimate stress was found to be lower than the static value by 23 %. The transverse properties showed that the dynamic ultimate stress was about 1.5 times the static ultimate stress and the dynamic compressive strain to failure was 66 % of the static strain to failure [28].

El-Habak investigated the behaviour of woven glass fibre reinforced composites subjected to compressive impact loading [29]. The compression split Hopkinson bar was used to produce failure at strain rates ranging from 10 s^{-1} to 10^3 s^{-1}. A slight increase in the compressive ultimate stress for all composite variables such as fibre orientation and fibre volume fraction was noted [29]. The research concentrated on the comparison of selected matrix systems viz. vinyl ester, polyester and epoxy. The highest ultimate stress is obtained from the composite based on the vinyl ester matrix. Harding investigated the effect of strain rate and specimen geometry of woven glass reinforced epoxy laminates on two different specimen designs; (1) a solid cylinder, as commonly used with the compression version of the Hopkinson bar and (2) a thin strip, waisted in the thickness direction, as generally recommended for composite laminate compression testing [30]. The mean stress-strain curves for both specimen geometries indicated a significant increase in the initial modulus, ultimate stress and the strain to failure with increasing strain rate. Generally, under compression loading the shear resistance of the epoxy resin matrix is likely to contribute considerably to both the elastic properties of the laminate and to the resistance to shear band formation. The mechanical properties of the epoxy resin are known to be strongly rate dependent, therefore the effect of strain rate on the initial Young's modulus and the ultimate compressive stress is detected [19].

El-Habak also studied the high strain rate effects of various composite properties such as fibre volume fraction and specimen size, of glass fibre, in a polyester and epoxy resin, respectively [31]. The ultimate stress increases and the point at which complete separation takes place are delayed. El-Habak shows a change (or delay) in the mode of failure at increasing strain rates, the

specimens at low strain rates do not fail in the same sequence (with respect to the mode of failures) as specimens impacted at high strain rates [29]. For example, in the bulk of the compression specimen under low strain rates, matrix cracking occurs first, followed by delamination and finally fibre failure. However, at high strain rates matrix cracking and fibre failure in the bulk of the specimen occurred simultaneously [30]. The ultimate compressive stress is not influenced by the strain rate for values of $\dot{\varepsilon} < 100\, s^{-1}$ but varies linearly with the strain rate for values of $100\, s^{-1} < \dot{\varepsilon} < 1000\, s^{-1}$. Inherently the strain rate sensitivity was found to be dependent on the matrix type and the fibre volume fraction [29].

Tay *et al.* studied cross-woven glass fibre reinforced epoxy and pure epoxy resin subjected to dynamic compressive loading [32]. Quasi-static ($\dot{\varepsilon} \approx 10^{-3}\, s^{-1}$) and low strain rate ($\dot{\varepsilon} \approx 10\, s^{-1}$) tests were conducted on a hydraulic tester, while a split Hopkinson pressure bar was used for tests at dynamic strain rates ($\dot{\varepsilon} \approx 10^{3} s^{-1}$). They proposed a simple empirical equation based on experimental results that showed the behaviour of GFRP and pure epoxy to be strain rate sensitive [32]. The non-linear stress-strain behaviour is inherently a matrix-dominated property; therefore the same form of equation developed is applicable to both pure epoxy and GFRP.

Unidirectional glass fibre reinforced polymer composites were investigated by Takeda *et al.* using the improved SHPB apparatus that eliminates multiple loading of the compression specimen, prevalent in the conventional SHPB [33]. Scanning electron microscopic analysis of the specimens revealed that the compressive failure of the unidirectional GFRP is caused by micro buckling of the fibres under both static and impact loading conditions. The compressive ultimate stress is related to the non-linear in-plane shear modulus of unidirectional composites and the theoretical prediction agreed with the experimental results. These results indicate an increase in compressive ultimate stress with increasing strain rates [33].

The compressive behaviour of unidirectional carbon/epoxy composites was investigated at varying strain rates by Hsiao and Daniel [34]. The transverse compressive ultimate stress increases at dynamic strain rates, to approximately twice the quasi-static value. The strain to failure shows no strain rate effect, implying that a stress dominated failure criterion is needed for

analysis under dynamic loadings [34]. Longitudinal and cross-ply compressive properties were obtained for varying strain rates [35]. Increases in ultimate stress and strain to failure were obtained but only moderate increases in initial elastic modulus are reported. Studies have also been carried out on off-axis thermoplastic composite laminate specimens, which were tested at a wide range of strain rates that vary from quasi-static to dynamic. It was found that the composite behaviour is elastic up to failure in the fibre direction. Significant non-linear and strain rate dependent behaviour is exhibited by off-axis and angle-ply laminates. A comparison of the dynamic and quasi-static stress-strain curve shows the effects of strain rate [35].

There is no standardized test specimen geometry for tests on composites with the SHPB [36]. Woldesenbet and Vinson investigated the effects of varying the length to diameter (L/D) ratio and/or geometry of the specimen with respect to the material properties at varying strain rates of 4×10^2 s^{-1} to 1.3×10^3 s^{-1}. The results show no statistically significant effect of either L/D or geometry for carbon/epoxy laminates tested at three varying strain rates. Both specimen shapes result in similar high-strain rate properties, therefore comparison can be made between the ultimate stress results from tests done using varying specimen shapes, viz. cylindrical and cube shaped specimens [36].

Gary *et al.* used a nylon incident and transmitter bars, to test the strain rate behaviour of glass epoxy composite plates [37]. The failure strength of the glass epoxy plate is reported to be strain rate sensitive. Fibre orientation effects on high strain rate properties were considered for a carbon epoxy system [38]. Vinson's experimental data was used in formulating equation (2.1) that accounts for the strain rate sensitivity of the composite at different off-axis fibre orientation [38]. An exponential increase in the ultimate stress with increasing strain rates is reported.

$$\sigma_d = \sigma_s . F_1(\dot{\varepsilon}, \theta) \tag{2.1}$$

The dynamic stress (σ_d) and quasi-static stress (σ_s) are related by $F_1(\dot{\varepsilon}, \theta)$ a function that accounts for the orientation dependence on strain rate sensitivity. It is important to note that the

units of the sums of the various orders of θ are seconds, s, the overall function $F_1(\dot{\varepsilon},\theta)$ is unit less, expressed in equation (2.2) as

$$F_1(\dot{\varepsilon},\theta) = 1 + (0.03695 + 0.17927\theta - 1.82512\theta^2 + 5.65882\theta^3 - 7.85101\theta^4 + 4.95005\theta^5 - 1.14892\theta^6)\ln(\dot{\varepsilon}) \quad (2.2)$$

Attempts to characterize the high strain rate behaviour of fibre composites using off-axis laminates and the split Hopkinson bar were carried out by Ninan *et al.* [39]. Increases in the stress values of the off-axis glass epoxy composites are noted when the strain rate of the compressive loads is increased from static to dynamic for the varying fibre orientations [39]. Hosur *et al.* investigated the response of carbon/epoxy laminated composites under high strain rate compression loading [40]. This study indicates that the dynamic strength and Young's modulus increases considerably as compared to the static values. Dynamic tests results of carbon/epoxy laminate specimens in each of the principal directions invariably failed showing brittle behaviour [41]. Figure 2.5 (a) shows the static as well as two stress-strain curves at higher rates. The Young's modulus increases (from 69 GPa to 400 GPa) with increasing strain rate. The dynamic stress-strain curve for the through thickness direction in Figure 2.5 (b), is seen to have a linear portion. Thereafter the curve turns into a relatively flat plateau and then climbs up till failure.

Li and Lambros reports that the time for stress homogenisation in the through thickness direction is substantially larger than that in the fibre direction although it takes the same number of wave reflections within the specimen [41]. As a result only the failure properties can be considered valid. The strain to failure in the system is invalid due to the wave reflections. Inspection of the stress-strain curve in Figure 2.5 (a) and (b) shows an increase in ultimate stress with increasing strain rates. The results show an increase in ultimate stress at about 1800 s^{-1}, an increase in ultimate stress with increasing strain rates was also reported by Lankford [42]. Experimental results for graphite/epoxy composite materials presented by Li and Lambros confirm the existence of strain rate sensitivity for loading in all material directions in both the elastic and

damage regimes [41]. Other studies however report no strain rate sensitivity in the graphite/epoxy material [43].

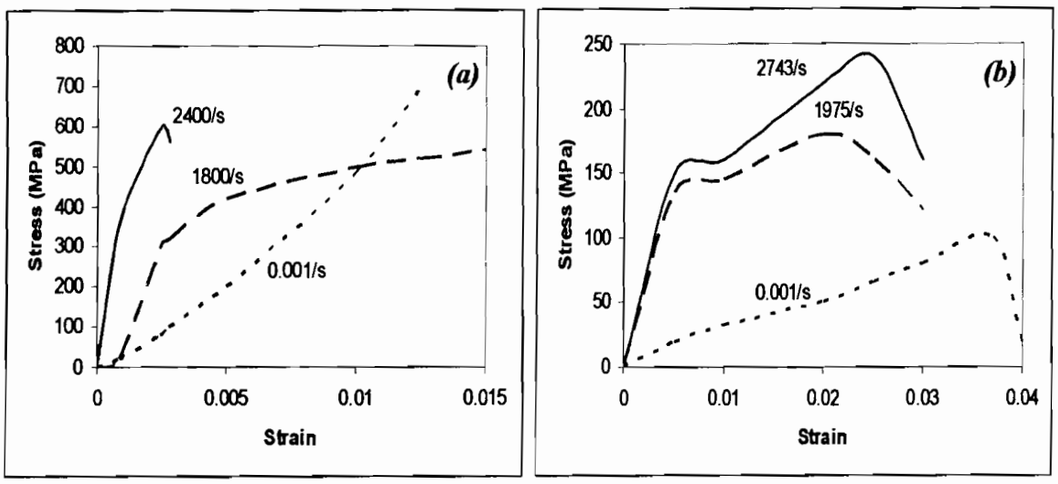

Figure 2.5: Stress-strain curves of a range of strain rates for a unidirectional graphite/epoxy composite showing (a) loading along fibres (b) loading through thickness [41].

The ultimate compressive stress value is usually dependant on the controlling failure process. A unidirectional-reinforced composite loaded parallel to the fibres is likely to fail by longitudinal splitting, whereas woven-reinforced composites loaded parallel to a direction of weave will show well developed shear bands of a width corresponding to the wavelength of the weave. The ultimate compressive stress is determined by the material properties as well as the geometry and boundary conditions of the test piece. However, for glass epoxy composites the ultimate compressive stress values is also dependant on the strain rate. This is deduced from the increase in ultimate stress with increasing strain rate observed with glass epoxy laminates [44].

2.2.2. SHEAR TESTS

2.2.2.1. QUASI-STATIC STRAIN RATES

The interlaminar shear strength is one of the most important parameters in determining the ability of a composite material to resist delamination damage [45]. The Iosipescu test set-up has been widely used to determine in-plane shear properties for composite materials since it has a uniform

shear stress distribution across the central failure plane [46]. The modified Wyoming fixture, shown in Figure 2.6 was adopted as an American standard (ASTM D5379/M-93) for testing shear [47].

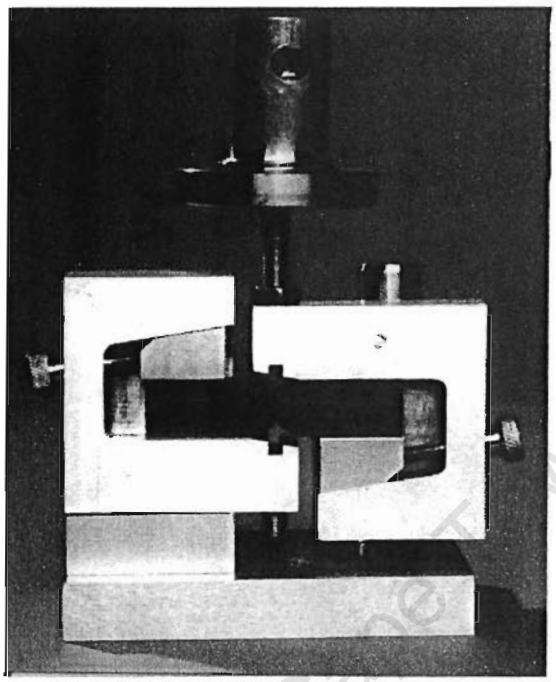

Figure 2.6: Iosipescu shear test showing a modified Wyoming fixture [48].

The Iosipescu test claims to impose a state of pure shear on a beam specimen in the region between two opposing v-notches [46]. It has however been noted that this method can give conflicting results. Xing *et al.* used Moiré interferometry and finite element analysis to determine the effect of imperfect loading conditions on experimental errors [49]. The tests were susceptible to variations in the loading points causing bending moments, resulting in tensile stresses at the notch tip. Twist as a result of imperfect loading across the width of the specimen, causes high shear stress concentrations in the test section [49]. Morton et al. using the Wyoming test fixture note similar results. The experimental errors reported are more pronounced for strength measurements than for modulus measurements [50].

Accurate characterization of the shear properties requires that a state of pure shear, independent of tensile or other failure modes, is prevalent in the specimen under evaluation [51]. The

Iosipescu test has been extensively used to investigate the shear properties of laminate composites at quasi-static strain rates [50]. However due to the various limitations of this test method under impact loadings conditions and the need to maintain uniform specimen geometry throughout the various loading regimes, a single-lap shear specimen is used at quasi-static strain rates for determining the effects of varying loading rates on the interlaminar shear strength of laminated composites [51]. The Iosipescu shear test method was utilized at low strain rates, however the problem of failure mode was encountered as the test specimens did not fail in pure shear. The specimen failed with mixed mode shear and tension, as a result an alternative method using transitional strain and obtaining the corresponding "yield" stress was reconstructed [6].

2.2.2.2. DYNAMIC STRAIN RATES

At high loading rates delamination damage frequently occurs as a result of transverse impact loading [44]. A major requirement for shear testing is to attain a uniform shear stress on the interlaminar plane and even under quasi-static loading conditions this is not easily achieved [51]. The limitation of the Iosipescu shear tests is that difficulties exist under impact loading. The requirement at quasi-static loading is that equilibrium within the specimen is achieved before the onset of failure, i.e. within 10-20 μs of the starting load. This is unattainable at dynamic strain rates [45]. In addition to experimental errors noted from the modified Wyoming test fixture at low strain rates, further complications exists when high strain rates are used. As a results the complex loading fixtures give rise to a number of stress wave interactions, a state of pure shear is therefore not obtained at the failure surface [50].

Dong and Harding developed a special single-lap specimen for use in a Hopkinson bar rig in order to examine the shear behaviour of FRPs at high strain rates [51]. Finite element analysis was used to determine the stress distribution on the failure plane of a number of different shear specimens. For double lap shear specimens, stresses are not uniform, resulting in large concentrations at the ends of the shear plane [52]. This creates problems when trying to determine the interlaminar shear strength for the shear plane as a whole. The single lap specimen was shown to give improved results when determining the average interlaminar shear strength for the shear plane. This is due to the reduction of the stress concentrations arising from the specimen design [51].

Bouette *et al.* designed a similar specimen for use in the Hopkinson bar apparatus for testing laminates at high strain rates [54]. Two different geometries were used to first measure the shear modulus and then the fracture strength. Finite element analysis was again used to determine the stress state in the central region. It was found that decreasing the overlap length affected the shear and normal stress concentrations at the ends of the failure plane [53]. The main advantage of the single lap shear specimen, with respect to high strain rate testing of FRPs, is that when the geometry is optimized, the shear stress on the central interlaminar plane is close to uniform and the normal (peeling) stress is very small. This specimen was first used by Bouette *et al.* to determine the shear modulus at high strain and then in a modified form to determine the interlaminar shear strength [53,54].

Werner and Dharan used the double-notched Hopkinson bar arrangement for testing plain-weave carbon/epoxy short beam shear specimens [55]. No effect was reported in the interlaminar shear test, however, the transverse shear strengths decreased with increasing strain rate for strain rates up to 1.8×10^4 s^{-1}. It was argued that the decrease in strengths was due to the initiation of delamination of the laminae [55]. Plain weave glass epoxy laminates exhibit high sensitivity to loading rate; both the initial shear modulus and failure strain are highly affected by the loading rate [56]. Lifshitz *et al.* tested E-glass epoxy and unidirectional carbon-fibre epoxy. The interlaminar tensile strength and modulus of two material systems were investigated experimentally at high strain rates [57]. The dynamic ultimate stress values are higher than the quasi-static values by a factor of 1.3. Experimental results of the combined interlaminar tension and shear, for E-glass epoxy were fitted to a quadratic failure criterion. The dynamic failure envelope is similar in shape, to the quasi-static envelope, but larger in size [57].

Hallett *et al.* reports on a small increase in both interlaminar shear strength and failure strain, with strain rate and a small decrease in the through-thickness shear modulus. The yield stress and strength of shear loading at strain rates that range from 500 s^{-1} to 5000 s^{-1} are investigated for woven carbon/epoxy [45]. In a similar study Chiem and Liu reported that the viscosity of the matrix material affects the ultimate stress, which is a function of the strain rate sensitivity [58].

2.2.3. TENSILE TESTS

2.2.3.1. QUASI-STATIC STRAIN RATES

Properties such as tensile strength and modulus are determined by quasi-static tension tests. The requirements for tensile tests are that the machine should be axial therefore the force acting along the longitudinal axis of the coupon. The specimen should be long and slender and the strain should be measured on a gauge section appropriately remote from the clamps. This had previously been achieved by implementing the ASTM D3039-76 procedure [59]. However, in order to avoid uncertainties related to size effects it has been suggested that the specimens should have the same geometry for all strain rates [43]. Therefore the standard ASTM D3039-76 specification for tensile testing of laminate materials is rarely employed when undertaking comparative studies at varying strain rates [43]. Various authors used a hydraulic Instron machine when testing CFRP dog-bone specimens at strain rates of 5×10^{-5} s^{-1} to 1 s^{-1}. The load cell of the machine measures the force and the strain is measured with strain gauges cemented to the specimen, in each case the specimens fracture desirably within the gauge length [10,43,60].

2.2.3.2. DYNAMIC STRAIN RATES

Harding and Welsh are amongst the earliest researchers to focus on developing a "new" method for the tensile testing of fibre-reinforced composites at impact strain rates [11]. The research focused on achieving stress equilibrium across the specimen where tensile failure occurs within 30 μs. The research also focuses on improving the underestimation of the elastic strain through the redesign of tensile specimen, using Ewin's proposal for quasi-static testing of unidirectional CFRP [11]. The modulus, fracture strength and failure mode of unidirectional CFRP are independent of strain rate. In contrast, for both the transverse and fibre direction, GFRP showed increases in failure strength at impact rates of strain. In the fibre direction, increases in failure strain and initial modulus are reported [11].

The change in mechanical response with increasing strain rate was associated with a change in the fracture appearance. For 0° specimens impacted at low rates, limited matrix cracking is reported close to the fracture surface. At impact strain rates of 10^3 s^{-1} the matrix cracks extend to cover the entire gauge section where extensive debonding between the fibre and matrix is observed. The tensile behaviour of fibre reinforced plastics under dynamic loading conditions is

an important factor for determining the impact properties of composite structures. However, because of the variety of existing testing methods, difficulty exists in the direct comparison of the obtained data [11].

Much of the uncertainty results from the difficulties of ensuring that tensile failure occurs within the gauge length, as well as achieving non-oscillant signals under high loading velocities [61]. These difficulties are more pronounced in the case of dynamic unidirectional (UD)-composites, since the material is very stiff in the longitudinal direction (0-degree loading) and very susceptible to bending forces in the transverse (90-degree-loading). Under increasing loading conditions the CFRP, 0-degree ultimate stress, remains essentially unchanged as the strain rates vary from 1 s^{-1} to 70 s^{-1}. When loaded perpendicular to the fibres, however, the UD-composite shows an increase in strength, which is due to hardening of the viscoelastic epoxy matrix [61]. The tensile strain to failure increases with increasing strain rates, due to local adiabatic heating of the deformed polymer under dynamic loading conditions [61]. In another study Kawata *et al.* show GFRP to be strain rate sensitive at strain rates that range from 0.87 x 10^{-3} s^{-1} to 2.07 x 10^{3} s^{-1}, the strain to failure is seen to vary from 4 % to 15 %, respectively [10].

Strain rate strengthening, ductility and toughening are synonymous with a brittle to ductile transition region observed in GFRP [10]. A one-dimensional constitutive equation, equation (2.3) established from experimental data described the macroscopic mechanical behaviour of unidirectional glass fibre reinforced epoxy under a tensile impact [62].

$$\sigma = 1.534 + 0.7372 \log \frac{\dot{\varepsilon}}{300} \tag{2.3}$$

where σ is the ultimate stress (Pa) and $\dot{\varepsilon}$ is the strain rate (s^{-1}).

The tension SHPB was used to study the dynamic thermo-mechanical behaviour of carbon-epoxy composites [63]. The tensile specimen is loaded along the fibre direction at strain rates that range from 1 s^{-1} to 2500 s^{-1}. A tensile stress-strain curve depicted in Figure 2.7 shows a trilinear behaviour similar to that observed during quasi-static uniaxial tension of unidirectional

composites [63]. In another study, Walter and Ravichandran investigating damage evolution in a unidirectional ceramic matrix composite under quasi-static tensile loading, also observed a similar trilinear stress-strain curve was reported [64]. Using acoustic emission techniques and post-mortem microscopy, five dominant mechanisms associated with the response of the composites at various stress levels were identified.

These mechanisms are described as follows:

1) Elastic deformation mechanism. At this stage both the fibre and the matrix carry the loads. Isolated regions of matrix cracking initiation occur but no crack growth and no other form of damage growth is noted.
2) Significant matrix cracking and localized matrix-fibre debonding becomes predominant.
3) Global matrix-fibre debonding and load transfer to the fibres.
4) Load completely transferred to the fibre and isolated fibre failure.
5) Global failure, including fibre pull-out, frictional sliding and fibre bundle failure.

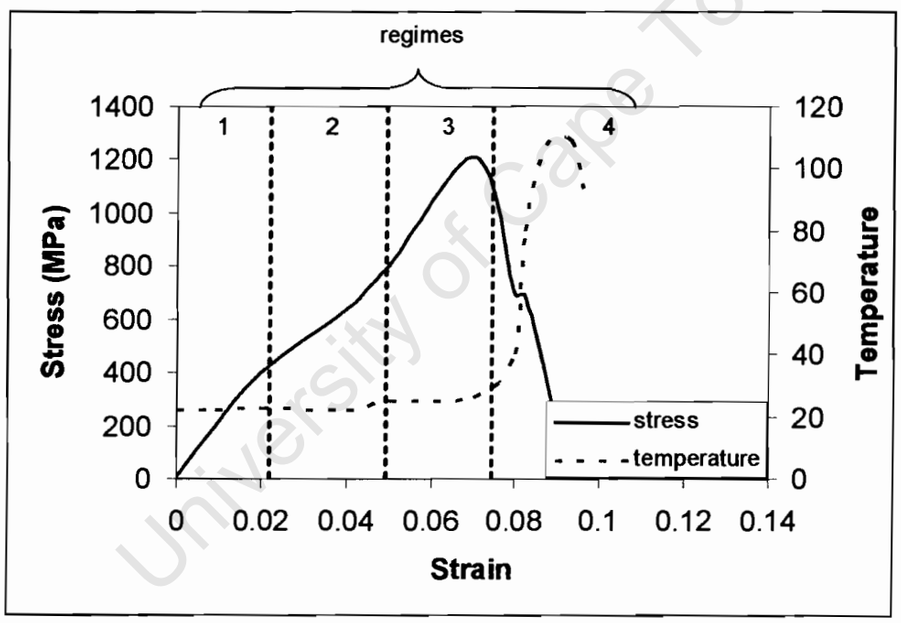

Figure 2.7: Stress that corresponds to different temperature-strain curve at 1500 s^{-1} for tension in the fibre direction showing various regimes that correspond to laminate failure modes [63].

These mechanisms are well correlated with the dynamic tension test results depicted in Figure 2.7. The first regime in Figure 2.7 is the first linear proportion of the stress-strain curve, which corresponds to elastic deformation. In the second regime of the stress-strain curve the gradient is lower than that of the regime 1, indicating a lower Young's modulus. This is due to progressive matrix cracking and initiation of matrix-fibre debonding, which subsequently causes a decrease in the stress-carrying capability. In the third regime massive matrix cracking and matrix-fibre debonding cause all loads to be carried by the fibres. The graph has a larger gradient than that of the second regime. The fourth and final regime shows a sudden decrease in stress. At this stage, fibre fracture followed by extensive fibre pull-out and friction causes the stress-carrying capability to drop drastically [63].

The temperature in the composite is seen to increase in the third regime of deformation, therefore the regime dominated by fibre/matrix debonding. An increase of 10° was observed during this regime, up to the point at which the maximum stress occurs. Coincident with the point of maximum stress is a sudden increase in the rate of heat generation. The heat generated then continues increasing in what corresponds to the fibre pull-out regime [63].

Fibre/matrix debonding generates heat in regime 3 in Figure 2.7 but the largest amount of heat generation occurs during the frictional fibre pull-out process. A temperature increase of approximately 100° C is observed during the fibre pull-out phase [63]. The dependence of these results on strain rate indicates the existence of the concept "damage rate sensitivity". Woven glass/epoxy composites at strain rates of 10^3 s^{-1} showed an increase in ultimate stress and strain to failure compared to the static values. In addition, glass/epoxy exhibited marked changes in the fracture surface appearance and extent of damage as a function of strain rate [65]. The fibres are deemed to influence the laminate strain rate sensitivity more than the matrix [65].

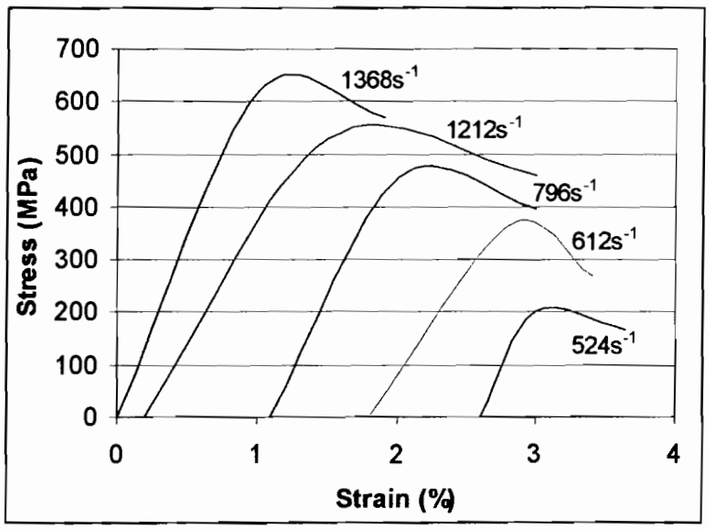

Figure 2.8: Stress-strain curves of the woven carbon/epoxy composite subjected to dynamic loading staggered along the x-axis to enhance the variation in stresses with varying strain rates [66].

Woven carbon/epoxy at strain rates that vary in the range 500 s^{-1} to 1400 s^{-1} are seen to have a significant increase in ultimate stress from 200 MPa to 630 MPa, respectively; as the strain rate increases (see Figure 2.8) [6]. Additional studies on the behaviour of glass/epoxy, graphite/epoxy and carbon/glass hybrids by Saka and Harding showed an increase in the ultimate stress with increasing strain rate [67].

A number of tensile tests were performed measuring material properties of glass/epoxy at different levels of strain rates. The results showed that the effect of the logarithm of the rate of strain on the material properties could be regarded as linear and extrapolated to provide the data at high strain rates. Microscopic analysis shows a change in failure modes from brittle fibre failure with fibre pull-out at quasi-static strain rates (1.7×10^{-2} ms^{-1}) to brittle failure with considerable matrix damage at higher loading rates. The Eyring theory of viscosity that describes the strain rate effects of most polymers was introduced. This theory assumes that the deformation of a polymer involves the motion of a chain molecule over a potential energy barrier. The Eyring

model suggests that yield stress varies linearly with the logarithm of strain rate, at higher strain rates. This is more pronounced since the FRP has less time to distribute the load "evenly" [6].

Limited data on the tensile behaviour of graphite/epoxy at high strain rates were obtained by Daniel *et al.* using the expanding ring technique and by Weeks and Sun using a split Hopkinson pressure bar [35,68]. These tests at strain rates of 500 s^{-1}, show an increase in the transverse and in-plane shear moduli as compared to the static values. Recent studies by Gilat *et al.* investigated the strain rate dependent behaviour of carbon/epoxy in tension, by examining the resin and various laminate configurations at different strain rates [60]. However, the rate of deformation does significantly affect the response of the carbon/epoxy system. In all of the configurations tested, higher stiffness is observed with increasing strain rate. The ultimate stress for the $[\pm 45°]_s$ specimens is significantly affected by strain rate. It is therefore being averred that the resin is the main driver behind the strain rate sensitivity observed in the composite. Furthermore, the need for a rate-dependent constitutive relation that adequately models FRPs is being proposed [60].

The lack of testing standards for measuring composite materials properties at varying strain rate is conspicuous and often precludes the comparison of results from different researchers. It is clear then, as seen from the reviewed literature, that there are no standards specifying specimen sizes or types, stress and temperature ranges, mechanical conditioning and test durations, all of which could affect the test results. It therefore appears that any additional experimental data on laminate composites will enhance the present knowledge of these materials. This data coupled with the appropriate failure criteria, discussed in the subsequent section, should enhance the prediction capabilities of finite element models.

2.3. FAILURE CRITERIA IN COMPOSITES

2.3.1. INTRODUCTION

Several reports have surveyed numerous theories on the failure of fibre reinforced composites [69,70,71]. A more recent survey carried out a comprehensive description of the foremost failure theories for fibre-reinforced polymer laminates. A direct comparison between theories with

predictive capabilities (viz. theories that determine the onset of failure in a laminate; as compared to Tsai Wu non interactive criteria, for example that simply introduces the failure envelope) against experimental data was undertaken [72,73]. In modelling of post-failure behaviour, assumptions are made regarding the properties of the degraded lamina. Table 2.1 summaries the different post-initial failure models adopted.

Table 2.1: Summary of the post initial failure degradation models used in the theories [73].

Name	**Failure mode**	**Parameters degraded**
Eckold		No post failure
Zinoviev	Closed cracks	$\Delta\varepsilon_2 < 0$: when $\lvert\gamma_{12}\rvert < \lvert\gamma_{12}^{*}\rvert : G_{12} = \psi G_{12}^{0}$
Rotem	After final matrix failure	$E_2 = G_{12} = 0, E_1 = E_1^{0}\exp(-k\varepsilon_1), k$
McCartney	Lamina cracking	Detailed mathematical analysis for reducing stiffness
Puck	Cracking under tension mode (A)	$E_2 = \eta E_2^{0}, G_{12} = \eta G_{12}^{0}, \nu_{12} = \eta \nu_{12}^{0},$ η parameter that varies with stress
	Cracking under compression modes (B) and (C)	$G_{12} = \eta G_{12}^{0}, \nu_{12} = \eta \nu_{12}^{0}$, where $\eta < 1$
Chamis	Matrix failure	$E_2, G_{12}, \nu_{12}, E_1$ computed from micro mechanics
Edge	Matrix failure	$E_2 = \beta_1 E_2^{0}, G_{12} = \beta_2 G_{12}^{0}, \nu_{12} = \beta_3 \nu_{12}^{0}$ $\beta_{1,2,3}$ parameters decrease with strain
Wolfe	Matrix failure	$E_2 = 0.0, G_{12} = 0.0, \nu_{12} = 0.0$
*Sun (linear)	Shear matrix failure	$E_2 = 0.0, G_{12} = 0.0, \nu_{12} = 0.0$
	Transverse matrix failure	$E_2 = 0.0$

Sun (Non-linear)	Matrix shear failure	$E_2 = E_2^0 \exp(-\alpha_E \lambda), G_{12} = G_{12}^0 \exp(-\alpha_G \lambda), \nu_{12} = 0.0$
	Transverse matrix failure	$E_2 = E_2^0 \exp(-\alpha_E \lambda)$
Tsai	Matrix failure $\varepsilon_2 > 0$	$E_m = 0.15E_m^0, \nu_{12} = 0.15\nu_{12}^0$ where E_2, G_{12} computed from micro mechanics
	Matrix failure $\varepsilon_2 > 0$	$E_2 = 0.01E_2^0, G_{12} = G_{12}^0, \nu_{12} = 0.01\nu_{12}, E_1 = 0.01E_1^0$
Chang	Matrix, fibre failures	$E_1 = 0.0, E_2 = 0.0, G_{12} = 0.0$

**Note: linear in the case of Sun refers to the singular or immediate reduction in modulus when failure is deemed to have occurred, whereas non-linear refers to the exponential or gradual decrease in modulus once failure has occurred.*

In general all the models presented in Table 2.1 share the following common features:

- All rely on ply-by-ply analysis
- All assume that fibre failure, be it in tension or in compression, constitutes final failure
- Almost all models distinguish between failures under transverse tension and failures under transverse compression. The term "transverse" is used to refer to the direction perpendicular to the fibres in a lamina.

2.3.2. CHARACTERISTICS OF FAILURE THEORIES

Each of the theories given in Table 2.1 can be characterized by a number of key features. These features are summarized as follows:

- Method of analysis: whether Classical laminate theory (CLT) or a FE program was used. All the contributors relied on CLT. Sun, Chamis and Chang used finite element codes [73].
- Modes of failure: whether the theory is able to identify the modes of failure encountered during loading. All the theories, except for Sun were able to discriminate between two or more modes of failure. Various modes of failure and failure criteria were postulated in the theories, these modes of failure range from fibre failure to matrix failure. The properties used to predict the modes of failure are lamina properties rather than constituent (fibre or matrix) properties [73].

Table 2.2: Summary of different failure theories used by researchers [73].

Authors	Failure Theory Used
Chamis	Micromechanics based failure theory
Eckold	BS4994
Edge	Grant Sanders Theory
Hart-Smith	Maximum strain theory and generalized Tresca criteria
McCartney	Fracture mechanics
Puck	Puck theory
Rotem	Rotem theory
Sun (linear)	Rotem-Hashin theory
Sun (non-linear)	Plasticity model based on Hill's yield
Tsai	Tsai-Wu quadratic theory
Wolfe	Sandhu's strain energy model;
Zinoviev	Maximum stress theory
Chang	Chang-Chang failure criteria

However, the post-failure methods employed differ in terms of the method of reducing the material properties. They can be generally classified into two main groups:

a) Models employing sudden reduction in the properties of the failed lamina. These were presented by Chang, Tsai, Wolfe and Sun (linear) [72].

b) Models employing a gradual drop in the properties of the failed lamina. These are represented by Puck, Edge, Rotem, Zinoviev, Chamis and Sun (non-linear) [72].

2.4. IMPACT DAMAGE PREDICTION

2.4.1. OVERVIEW OF IMPACT DAMAGE PREDICTION

Foreign object impact on composite laminates has received considerable attention over the past three decades. Abrate conducted an extensive review of the work on impact of laminates [74]. Cantwell and Morton have summarized those characteristics of composite materials, which govern the behaviour under impact loading conditions. Post impact compressive strength has been identified as one of the better tests for determining a materials ability to withstand impact. They concluded that some of the more important material parameters for impact resistance are: the strain energy absorption capacity of the fibres, the mode II properties of the matrix, the strength of the fibre-matrix interface and the stacking sequence. Other factors which influence test results are the target geometry and the impact velocity [75].

In another study, Davies and Zhang conclude that a finite element plate model for predicting force histories works well for in-plane degradation of carbon composites. However the model does not work well for other materials such as Kevlar, which failed by compression and delamination due to bending. Glass reinforced plastic are reported to behave like carbon but the

toughness depends on the strain rate. The damage maps for small and large plates are often different [76].

2.4.2. LOW VELOCITY IMPACT

Generally, a low velocity impact is said to occur when the impact velocity is less than 100 ms^{-1} and hypervelocity impacts speeds larger than 1 kms^{-1}. However, other definition sometimes refers to situations where complete penetration of the target is achieved at high velocity. Another definition considers high velocity impact to occur when the deformation of the structure is localized in a small zone surrounding the contact area during the duration of contact. A low velocity impact would in this instance refer to situations where, the entire structure deforms as waves propagate the boundary and are reflected back several times. Low velocity impact occurs when tools are dropped on a structure during maintenance operations for example or when debris on the runway impacts an aeroplanes structure during take-off or landing. Different behaviour is observed during ballistic impacts, which are a concern with military applications and for hypervelocity impact of spacecraft by space debris [74].

The study of impact on a laminate structure by an object travelling with a given initial velocity requires the determination of the time history and spatial distribution of the forces developed at the target-impactor contact zone. For low velocity impacts, the contact duration is such that the structure responds quasi-statically. It is well known that fibre reinforced laminated composites are very susceptible to transverse impact. Under low impact velocities, significant damage in terms of matrix cracks and delamination occur within the laminate [77].

Several analytical models were developed to study the transient dynamic response of composites due to impact. Most of these studies primarily focused on either the contact force of an impactor or on the response of the plates without consideration of the impact damage. A line-nose impactor design was chosen to simplify the impact damage mechanism from three-dimensional to two-dimensional [78]. In order to correctly predict delamination in all cases, stresses have to be re-calculated once matrix cracking has occurred. A dynamic finite element analysis was used along with a Hashin failure criterion to predict matrix cracking in impacted thin beams [74]. The analysis was also used to recalculate stresses in the vicinity of the matrix cracks and it was found

that the presence of the cracks created a large out-of-plane stress, or peel stress, which could initiate the delamination. Delamination zones are often observed near the matrix cracks [74].

Tan and Sun used a finite element approach for studying the impact of a laminated plate by a rod [78]. The plate was modelled using shear flexible plate elements, while the rod was represented using higher order rod elements. Robust experimental results were reported for both contact force and strains at several locations on the surface of the plate [74]. A three dimensional analysis was performed in order to determine out-of-plane stresses through the laminate thickness in order to predict damage. In the solution procedure, the finite element model was used once per time increment and the solution obtained was then used in the iterations required to determine the contact force [74]. Jih and Sun studied experimental predictions of delamination in composite laminates, which was subjected to low-velocity impact. The drop weight test indicated that low-velocity impact-induced delamination could be predicted by using the static interlaminar fracture toughness in conjunction with the static linear beam model [77].

A model was thus developed for predicting the initiation of the damage and the extent of the delaminations in graphite/epoxy laminated composites resulting from an impact using a stress-based failure criteria [79]. For a low velocity impact (in this case a low velocity is suggested when velocity is less than 20 ms^{-1}) the through thickness stress waves were ignored. Davies assumes that the plate will have time to respond using simple engineering theory for plates and shells and hence the application of finite element plate and shell models. It is also postulated that damage is proportional to either the force, or the bending strains. Experimental and theoretical histories showed good correlation for linear analysis without damage. With increasing incident energy the experimental composite plate specimen underwent large deflections with damage occurring in the plate. Therefore, numerically the laminae stiffness were degraded only in-plane, using the combined tension-shear criteria of Chang-Chang incorporated into the in-house finite element package FE77, to degrade any ply level and update the element stiffness accordingly, using shell elements. This showed remarkable agreement with the experimental test histories. However, without degradation the peak force of the non-linear analysis has a 50% discrepancy as compared to the experimental test histories. The results of the embedding strategy are thus misrepresented [76].

The finite element (FE) approach discussed in the previous section by Davies and Zhang employed a 2-D approach [76]. The major advantage of this type of approach is the efficiency in terms of computational cost due to its "simplicity". However, this numerical method for modelling plane-strain problems fails to provide sufficient detail and comprehensive information, such as the delamination shape in laminate plates. To perform more detailed stress analyses in laminates a 3-D finite element model (FEM) was used [80]. However, some apparent difficulties such as the exorbitant computational cost and the automatic mesh generation with the extension of delamination have been noted by Li *et al.* [81]. Furthermore, most research focused on several aspects such as: (1) mechanism of damage formation, especially the onset of damage; (2) dynamic fracture toughness for delamination extension; (3) threshold of impact energy or velocity; and (4) relationship between damage sizes and the various impact parameters. Limited work reported on the full and direct numerical simulation of the whole damage process [81]. Most of the numerical approaches roughly evaluated the delamination sizes using some simple empirical formulae, for example [82].

Progressive failure of a laminate system is simulated in a user material (UMAT) subroutine programmed into the commercial package ABAQUS standard [83]. The UMAT allows for progressive failure by successively applying a degradation factor, D_f, to the material constitutive law (see equation (2.4)) [83]. The degradation factor D_f is obtained from uniaxial tensile tests of a representative "sub-laminate" or a "local" model, which includes the damage modes and sequences. Whenever an intermediate failure occurs, the material tangential stiffness is reduced by a factor of D_f. The maximum strain criterion is used as the basis for ply failure.

$$E_{i+1} = D_f E_1 \tag{2.4}$$

In equation (2.4) the structural tangent stiffness E is degraded by a factor D_f, where i is the index of the non-linear part of the stress-strain curve. Therefore after ultimate stress has been achieved the structural tangent stiffness is degraded and the slope of this post failure curve is determined by the degradation factor D_f.

In addition, the stress increment $\Delta\sigma_i$ is

$$\Delta\sigma_i = \Delta\varepsilon_i E_{i+1} \tag{2.5}$$

where $\Delta\varepsilon_i$ is the strain increment. Predicting the ultimate failure of laminates with complicated damage modes and loadings is possible. This is deduced from the successful development of the model [83]. Recently, the stress-based failure criteria for fibre, matrix cracking and matrix crushing were summarized as shown in Table 2.3.

Table 2.3: Failure criteria of fibre and matrix with the strategy of updating stresses where X_T :fibre directional (1-axis) tensile strength; Y_T :transversal (2-axis) tensile strength; Y_C :transversal (2-axis) compressive strength; S_{12} :laminates' plane (1-2 plane) shearing strength; S_f :shearing strength causing fibre failure; S_{m23} :cross sectional (2-3 plane) shearing strength causing matrix cracking [81].

Failure stress state	Failure criteria	Updating strategy of stresses
Fibre failure	$\left(\frac{\sigma_{11}}{X_T}\right)^2 + \left(\frac{\sigma_{12}+\sigma_{13}}{S_f}\right)^2 \geq 1$	$\sigma_{11} = \sigma_{22} = \sigma_{33} = 0,$ $\sigma_{12} = \sigma_{23} = \sigma_{31} = 0$
Matrix cracking if $\sigma_{22} \geq 0$	$\left(\frac{\sigma_{22}}{Y_T}\right)^2 + \left(\frac{\sigma_{12}}{S_{12}}\right)^2 + \left(\frac{\sigma_{23}}{S_{m23}}\right)^2 \geq 1$	$\sigma_{22} = 0, \sigma_{12} = 0$
Matrix crushing if $\sigma_{22} < 0$	$\frac{1}{4}\left(\frac{-\sigma_{22}}{S_{12}}\right)^2 + \frac{Y_c^2\sigma_{22}}{4S_{12}^2 Y_c} - \frac{\sigma_{22}}{Y_c} + \left(\frac{\sigma_{12}}{S_f}\right)^2 \geq 1$	$\sigma_{22} = 0$

The failure criteria in Table 2.3 are used to check the failure state of each layer in every element for laminates [81]. At first, five stress components within a specific layer of an element are obtained by averaging the corresponding components from the Gaussian points within the

element. The averaged stress component is then submitted into the failure criteria. If the stress state satisfies the failure criteria, the material constants in this layer of the element should be modified according to the strategy in Table 2.4. Parameters d and e in Table 2.4 are determined by a pilot calculation, describing the damage-resisting capability of laminates.

Table 2.4: Strategy of updating stress and the subsequent elastic constants [81].

Updating strategy of stress	$\sigma_{11}=\sigma_{22}=\sigma_{33}=0$ $\sigma_{12}=\sigma_{23}=\sigma_{31}=0$ (*fibre failure*)	$\sigma_{22}=0, \sigma_{12}=0$ (*matrix cracking*)	$\sigma_{22}=0$ (*matrix crushing*)
Updating strategy of elastic constant $d \geq 0, e/\min(E_i, v_j, G_k) > 0,$ $e/\min(E_i, v_j, G_k) \leq 1$	$E_i = \max(E_i/d, e)$ $v_{ij} = \max(v_{ij}/d, e)$ $G_{ij} = \max(G_{ij}/d, e)$	$E_2 = \max(E_2/d, e)$ $v_{12} = \max(v_{12}/d, e)$ $G_{12} = \max(G_{12}/d, e)$	$E_2 = \max(E_2/d, e)$ $v_{12} = \max(v_{12}/d, e)$

Note: $i, j, k = 1, 2, 3$, if not specified.

The low-velocity impact of E-glass/epoxy laminated composite plates was studied experimentally and numerically [84]. It was found that the shape of the force history changes as the mass varies. The mechanical behaviour of composite structures under low-velocity impact is dependent on in-plane dimensions. The smaller the width of the rectangular composite laminates the higher the contact duration [84].

2.4.3. HIGH VELOCITY IMPACT

In the case of high velocity impacts, the response of the structure for the duration of the contact time is localized. At high velocities the dynamics of the structure is important. Finite element analysis with direct time integration procedures can be employed successfully [74]. Theoretical investigations for detailed dynamic damage in composite structures due to high velocity impact are limited. One of the main reasons is the lack of reliable rate-dependent failure criterion [85]. In a study by Chen *et al.* a modified maximum stress failure criterion is employed for dynamic

failure analysis [85]. One of the assumptions made in this analysis is that due to the ductile behaviour of the epoxy resins, the dynamic transverse strength and shear strengths of the composite were assumed to be five times their static strengths. A physics-based "first principle" smoothed particle hydrodynamics (SPH) technique that simulates the detailed perforation process, together with a macro mechanics model for fibre composites, was developed for simulating composite laminate penetrations. The study points out the need for further developments, for accurate prediction of structural composite penetrations through enhancing the high strain rate anisotropic and failure criteria [85].

The modelling of low and high kinetic energy plate impact tests was done using LS-DYNA3D [86]. The Chang-Chang model is built into the commercial FEM package and used in conjunction with Belytschko-Tsay shell elements with one integration point for each lamina and one element through the plate thickness. The reduced moduli of the damaged material are introduced at the specific integration point at the point of failure. For each energy case three simulations were performed with increasing mesh densities in order to assess the convergence of the numerical solution [85]. It is also reported that the low energy model resulted in no significant failure. This concurred with the experimental results, although no investigation of delamination failure is undertaken. For the high energy case, the damage prediction was seen to increase with mesh refinement. A comparison of the matrix cracking area in the LS-DYNA model with delamination seen in the test shows that the model over predicts damage [86]. The model under estimates the failure threshold and over estimates the amount of damage. This large discrepancy in damage prediction is due to the unsuitability of this model when solving impact problems. The model was initially developed for quasi-static tensile tests and the post failure degradation being too severe, causing too great a loss in stiffness. In a related study Kuhl *et al.* shows that the brittleness of a specimen increases with increased mesh refinement. The reason for this observation is that the strains tend to localize in a narrow zone, which is governed by the choice of discretization [87].

Okoli and Latif on the other hand conducted a study to ascertain the relationship between predicted and experimental data for the impact response of a reinforced composite laminate [88]. The analysis at lower impact velocities typically 2 ms^{-1} or below, yielded accurate predictions of the "observed" event [88]. However, with increasing impact velocities ($\geq$ 4 ms^{-1}) the analysis

becomes inaccurate. Okoli and Latif nevertheless suggests that extrapolation of quasi-static data is indeed a valid method for obtaining FE analysis results at high strain rates [88]. Figure 2.9 shows a force-time graph. The discrepancy between the experimental and numerical results at higher impact velocities of 4 ms^{-1} is depicted [88]. Modification of the failure model for better prediction is also suggested by Majeed [86].

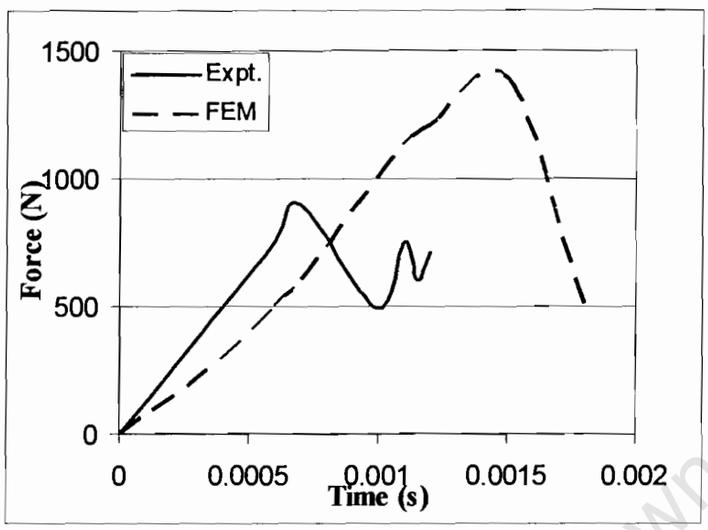

Figure 2.9: Comparison of FEM predictions and test data of a 4ms^{-1} beam impact event (filtered data 2500 Hz) [88].

2.5. CONCLUDING REMARKS

This chapter has provided some background of the effects of varying strain on FRP materials. Uniaxial compression, shear and tensile tests on the FRP specimens have shown increases in ultimate stress with strain rate increasing from quasi-static to dynamic, viz. 10^{-3} s^{-1} to 10^{3} s^{-1}, respectively. Various authors have proposed constitutive equations that are based on experimental data that give the relationship between ultimate stress and strain rate for FRP under varying strain rates. With respect to impact damage prediction using numerical techniques, a large amount of work has been done on predicting the behaviour of FRP at low velocity impact loads. The review of the literature has highlighted the fact that when developing numerical models for high impact velocities of FRP, quasi-static material data is used.

FEM has the potential to model impact damage of FRP accurately. It requires knowledge of the mechanical properties of the FRP that can be gained from simple tests in which specimens representative of the actual laminate are subjected to pure compression, shear and tension in the appropriate directions. These properties form the basis of data used in developing failure criteria implemented in numerical codes [89].

This thesis therefore attempts to establish material property data at dynamic strain rates. This material data for high strain rate impact tests should add to the knowledge of the behaviour of FRP at dynamic strain rates. From the literature review the absence of a high strain rate constitutive material model that accounts for damage based on the existing failure criteria introduced in section 2.3.2, is noted. This research provides material data as well as a constitutive relation that can implemented in various numerical models to predict the behaviour of FRP at high strain rates. Numerous failures have been introduced in section 2.3.2. These theories account for damage in FRP using different failure criteria that range from a quadratic theory proposed by Tsai, a strain energy model proposed by Wolfe and the Chang-Chang failure criteria as presented by Chang [73].

CHAPTER 3

THEORY USED IN THESIS

3.1. CHAPTER OVERVIEW

The main experimental technique used for measuring FRPs at high strain rates in this thesis is the Split Hopkinson pressure bar (SHPB). An analysis of the SHPB data requires an understanding of the one-dimensional elastic wave theory which is presented in the next section of this chapter. The results from the experimental work are then used in an empirical approach used for isotropic materials. To manipulate this information an understanding of the mechanics of unidirectional composites is imperative when developing a user material that describes the constitutive behaviour of unidirectional FRP as applied to the finite element model. This methodology is discussed later in the chapter. The development of the Chang-Chang model is introduced together with the subsequent property degradation procedure employed in the Chang-Chang criteria. The choice of the Chang-Chang criteria is mainly based on the wider use of this criterion in the literature, especially with respect to dynamic analysis. Also, this criteria was modified by Hou to include out-of-plane stresses presented in section 2.4.2 [82]. This modified criteria forms the basis for the damage model developed in this thesis. Finally, the fundamentals of finite element analysis as applied to FRPs are considered.

3.2. SPLIT HOPKINSON BAR THEORY

3.2.1. OVERVIEW

The split Hopkinson bar is one of the most popular techniques to measure material properties at high strain rates. In this section a brief description of the background and the layout of the system are presented. Next, the general test theory is discussed with the relevant one-dimensional wave propagation theory necessary for generating the stress-strain curves. Bertran Hopkinson in 1914

studied the shape and evolution of stress pulse propagation in a long elastic metallic bar [90]. Davies and Kolsky, later used two Hopkinson bars in series with the specimen sandwiched in between, to measure the dynamic stress-strain response. This device was thus named the split Hopkinson pressure bar (SHPB) [90].

In the standard Hopkinson bar analysis it is required to determine separately the incident and the reflected waves in the input bar and the transmitted wave in the output bar. However, to allow for a separation of the incident and reflected waves without using an inconveniently long input bar it is necessary to limit the duration of the loading wave and hence the maximum strain which may be applied to the specimen. To avoid this limitation, strain gauges may be sited at two different positions along the input bar. Using one-dimensional longitudinal elastic wave theory it is possible to distinguish between the two waves since, the two sets of strain gauges will record the incident wave and its subsequent modification by the reflected wave at different stages in the wave propagation process. This technique allows the velocity at the input end of the specimen to be determined with reasonable accuracy. However, in the case of polymer matrix composites the force transmitted through the specimen is much less than the that sustained by the input bar in compression. Therefore, the accuracy with which the stress on the input end of the specimen can be calculated is generally poor. As a result the specimen stress is calculated from the transmitted wave recorded on the output bar strain gauges.

The optimum specimen design for the SHPB is therefore a short specimen that would attain equilibrium and failure at an early stage of the test. This is before the first reflected wave from the free end of the output bar arrives back at the strain gauge on the output bar. Therefore, unlike the case of a ductile material where the strains to failure are often high, the effect of reflected waves on the output bar strain gauge signal, as well as multiple reflections in the input bar, may have to be taken into account when testing FRPs.

3.2.2. ONE-DIMENSIONAL ELASTIC WAVE THEORY

Wave propagation behaviour for elastic bars is well understood and mathematically predictable [91]. An axially loaded rod of length L, illustrated in Figure 3.1, will result in the displacement of particles in the rod that may be expressed by the scalar function:

$$u = u(x,t) \tag{3.1}$$

where x is the position of the cross-section under consideration and t is the time. The A, E and ρ in Figure 3.1 refer to the cross-sectional area, the elastic modulus and the density of the rod, respectively.

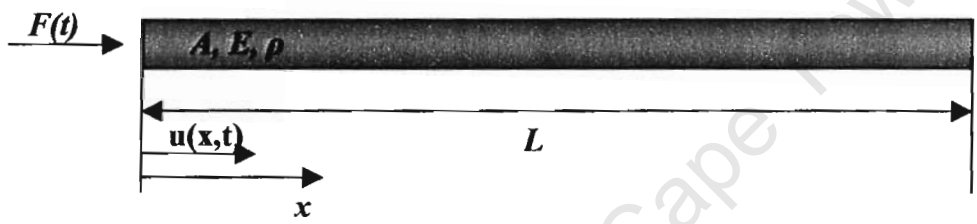

Figure 3.1: An axially loaded rod showing the direction in which the particles travel, x, resulting from the load F (t).

When the load is applied slowly the inertial forces on particles in the rod follows the relation: force = mass x acceleration:

$$f_I = m\frac{\partial^2 u}{\partial t^2} \tag{3.2}$$

The inertial forces are insignificant compared to the stiffness forces:

$$f_s = EA\frac{\partial u}{\partial x} \tag{3.3}$$

On the other hand, if the load is applied rapidly, the acceleration of particles will result in significant velocities of particles and inertial forces. Thus induced vibrations will continue until

dissipated by forces of internal friction. The equilibrium equation for a 1 dimensional (D) rod (Figure 3.2) with no body forces is given by:

$$\frac{\partial \sigma}{\partial x} = \rho \frac{\partial^2 u}{\partial t^2} \tag{3.4}$$

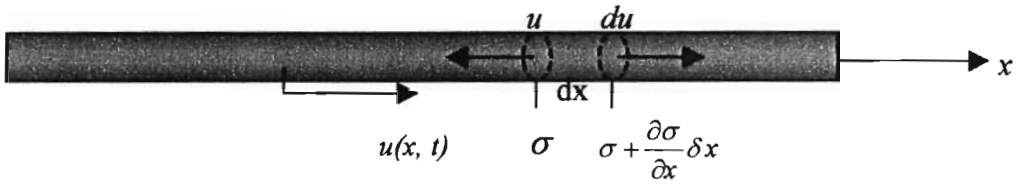

Figure 3.2: Movement of stress in an elastic thin rod subjected to forces in the x direction.

If the material is elastic, the strain is (compatibility equation):

$$\varepsilon = \frac{\partial u}{\partial x} \tag{3.5}$$

while the stress is given by the constitutive equation:

$$\sigma = E\varepsilon \tag{3.6}$$

thus transforming the 1 D wave equation for $u(x,t)$ to:

$$c^2 \frac{\partial^2 u}{\partial x^2} = \frac{\partial^2 u}{\partial t^2} \tag{3.7}$$

where the wave speed (c) is given by:

$$c = \sqrt{\frac{E}{\rho}} \tag{3.8}$$

It is noted that equation (3.7) is an approximation because an assumption is made that the plane transverse section of the rod remains plane during the passage of the stress waves. The stress is therefore said to act uniformly over the cross-section. However, in reality a longitudinal stress causes lateral contraction, given by the Poisson's ratio. This leads to a non-uniform distribution of stress across the section of the rod, which is completely neglected in this assumption. Further, the non-ideal shape of the hemispherical tip of the impactor bar and shape of support tube are also neglected.

The following substitution differentiates between the forward and backward travelling waves. For forward travelling waves:

$$\xi = x - ct \tag{3.9}$$

with a wave speed:

$$c = \frac{dx}{dt} = \sqrt{\frac{E}{\rho}} \tag{3.10}$$

and for backward travelling waves:

$$\eta = x + ct \tag{3.11}$$

where the wave speed is:

$$c = -\frac{dx}{dt} = \sqrt{\frac{E}{\rho}} \tag{3.12}$$

and using:

$$u = u(\xi, \eta) \tag{3.13}$$

results in:

$$\left.\begin{aligned} \frac{\partial^2 u}{\partial x^2} &= \frac{\partial^2 u}{\partial \xi^2} + 2\frac{\partial^2 u}{\partial \xi \partial \eta} + \frac{\partial^2 u}{\partial \eta^2} \\ \frac{\partial^2 u}{\partial t^2} &= c^2\left(\frac{\partial^2 u}{\partial \xi^2} - 2\frac{\partial^2 u}{\partial \xi \partial \eta} + \frac{\partial^2 u}{\partial \eta^2}\right) \end{aligned}\right\} \tag{3.14}$$

and after substitution in the dynamic equilibrium equation:

$$\frac{\partial^2 u}{\partial \xi \partial \eta} = 0 \tag{3.15}$$

Thus

$$u = f(\xi) + g(\eta) \tag{3.16}$$

hence the D'Alambert solution of the 1D wave equation is:

$$u(x,t) = f(x-ct) + g(x+ct) \tag{3.17}$$

Functions $f(x)$ and $g(x)$ are obtained from the initial conditions as follows:

$$f(x-0) = \frac{1}{2}u_0(x) - \frac{1}{2c}\int_0^l u_0 dx \tag{3.18}$$

$$g(x+0) = \frac{1}{2}u_0(x) + \frac{1}{2c}\int_0^l u_0 dx \tag{3.19}$$

For a forward travelling wave the value of stress is:

$$\sigma = E\varepsilon = E\frac{\partial u}{\partial x} = E\left[f'(x-ct) + g'(x+ct)\right] \tag{3.20}$$

while the particle velocity is:

$$v = \frac{\partial u}{\partial t} = -c\left[f'(x-ct) - g'(x+ct)\right] \tag{3.21}$$

where

$$f'(x-ct) = \frac{\partial f(x-ct)}{\partial(x-ct)} \tag{3.22}$$

$$g'(x+ct) = \frac{\partial g(x+ct)}{\partial(x+ct)} \tag{3.23}$$

For forward travelling waves it can be found that:

$$g(x+ct) = 0 \tag{3.24}$$

By eliminating $f'(x-ct)$ from the above expressions for stress and velocity, it follows that:

$$\frac{\sigma}{E} + \frac{v}{c} = 0 \text{ for } \frac{dx}{dt} = c \tag{3.25}$$

Similarly, for backward travelling waves

$$\frac{\sigma}{E}-\frac{v}{c}=0 \text{ for } \frac{dx}{dt}=-c \tag{3.26}$$

Recalling that equation (3.8) it follows that:

$$\sigma=\pm\rho c v \qquad \text{for} \qquad \frac{dx}{dt}=\pm c \tag{3.27}$$

where ρc are constants known as the acoustic impedance or characteristic impedance of the material. Thus it follows that there is a linear correlation between stress and velocity at any point. In this case a forward and backward travelling wave can be found,

$$\frac{\sigma}{E}-\frac{v}{c}=2f'(x-ct) \tag{3.28}$$

and

$$\frac{\sigma}{E}+\frac{v}{c}=2g'(x+ct) \tag{3.29}.$$

By integrating

$$\frac{dx}{dt}=\pm c \tag{3.30}$$

it follows that

$$x-ct=constant=A \tag{3.31}$$

and

$$x+ct=constant=B \tag{3.32}$$

The following differentiation and substitution is proposed

$$f'(x-ct)=f'(A)=constant=\frac{\alpha}{E} \tag{3.33}$$

$$g'(x+ct)=g'(B)=constant=\frac{\beta}{E} \tag{3.34}$$

The two constants α and β denote the magnitude of stress along the same characteristic lines $\frac{dx}{dt} = \pm c$, respectively (see Figure 3.3).

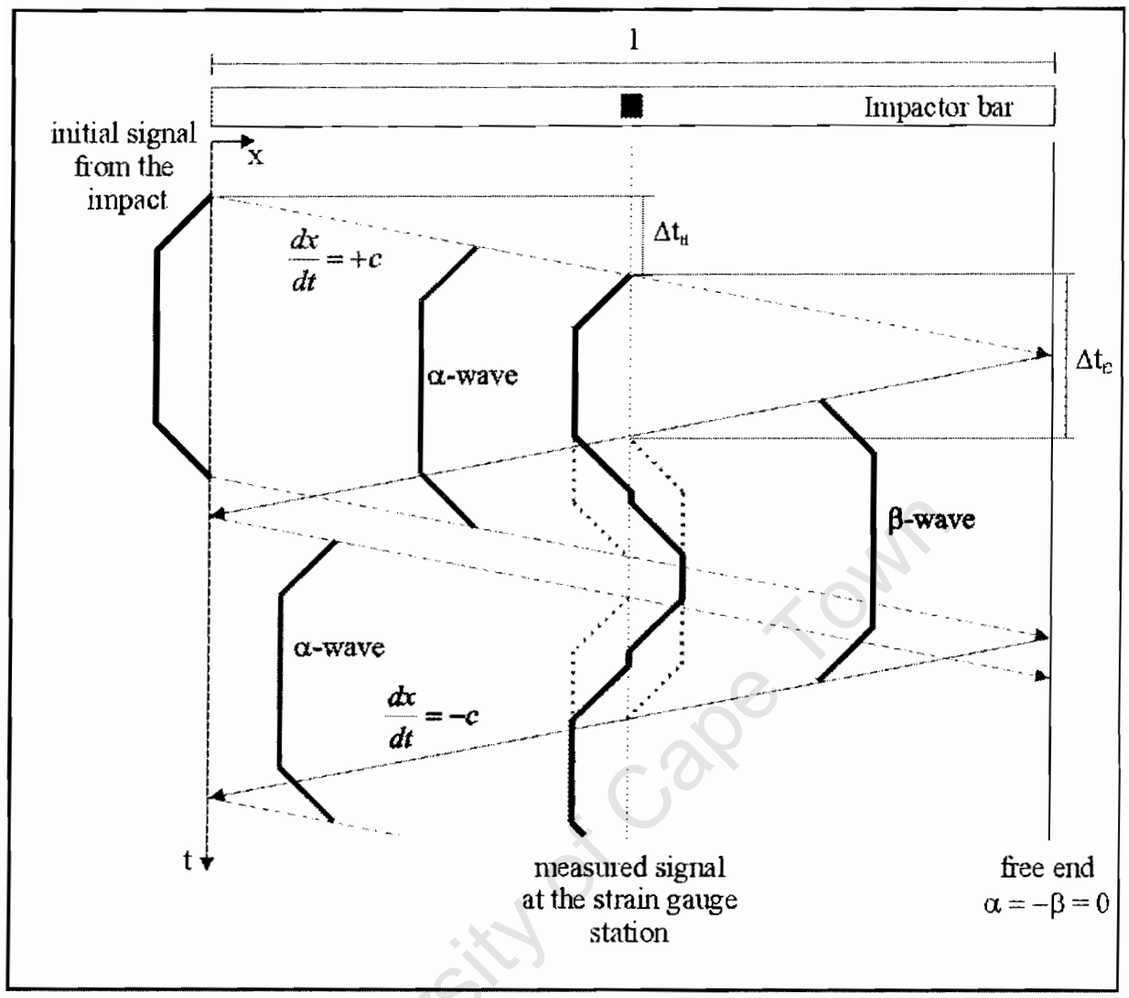

Figure 3.3: Schematic of travelling waves in the impactor bar after impact showing displacement time relationship of the α and β waves.

At $t \leq \Delta t$ only the α-wave is travelling through the structure, therefore:

$$\alpha_t^C = \sigma_{t+\Delta t}^V \tag{3.35}$$

where C and V represent the values measured at the impacted end and the strain gauge station. At time $t \geq \Delta t_1 + \Delta t_2$ the first back travelling α-wave reaches the strain gauge station. Therefore:

$$\alpha_t^C = \sigma_{t+\Delta t}^V + \alpha_{t-\Delta t}^C \tag{3.36}$$

In the case of the β-wave, at time $t \leq 2\Delta t_2$ the reflected β-wave has not reached the impacted end, therefore:

$$\beta_t^C = 0 \tag{3.37}$$

At time $t \geq 2\Delta t_2$ the first reflected β-wave reaches the impacted end, so:

$$\beta_t^C = -\alpha_{t-2\Delta t_2}^C \tag{3.38}$$

The α and β values for any x position can thus be found. By substituting equations (3.33) and (3.34) into equations (3.28) and (3.29) the following equations are derived:

$$\frac{\sigma}{E} - \frac{v}{c} = \frac{2\alpha}{E} \tag{3.39}$$

$$\frac{\sigma}{E} + \frac{v}{c} = \frac{2\beta}{E} \tag{3.40}$$

A simple rearrangement that makes $\frac{v}{c}$ the subject of the formula of equation (3.39) followed by a substitution of equation (3.39) into equation (3.40) will result in:

$$\frac{\sigma}{E} + \frac{\sigma}{E} - \frac{2\alpha}{E} = \frac{2\beta}{E} \tag{3.41}$$

This simplifies into:

$$\sigma = \beta + \alpha \tag{3.42}$$

and by substituting equation (3.42) into equation (3.27) for forward travelling waves gives:

$$\rho c v = \beta - \alpha \tag{3.43}$$

where α characterizes the forward travelling wave and β the backward travelling wave. When impact occurs a stress wave is initiated (α-wave, $\beta = 0$). This wave travels through the structure. The condition at the free end requires that:

$$\sigma = \beta + \alpha = 0 \tag{3.44}$$

Therefore

$$\beta = -\alpha \tag{3.45}$$

This means that the backward travelling wave has the same amount of stress but in the opposite direction as the forward travelling wave (see Figure 3.3). A knowledge of the value of the stress (σ^C) at the impacted end of the structure allows for the calculation of the contact force:

$$F^C = \sigma^C A \tag{3.46}$$

with A = cross-sectional area. The displacement can be obtained from the velocity by:

$$u = \int v dt \tag{3.47}$$

In addition, the longitudinal elastic strain in the thin rod can be expressed as follows:

$$\varepsilon = \frac{\sigma}{E} = \pm\frac{v}{c} \quad \text{for} \quad \frac{dx}{dt} = \pm c \tag{3.48}$$

3.3. COWPER-SYMONDS CONSTITUTIVE EQUATION

Numerical models representing the overall behaviour of materials have been extensively used in finite element simulations, especially with regards to metallic materials. For any of these models the desirable feature would be to be able to characterize the material at varying strain rates, i.e. quasi-static to dynamic, with a limited number of laboratory tests so that the simulations could be used with more confidence. A numerical method that has been well established in the literature and has been used extensively in many of the commercial finite-element computer programmes, when modelling metallic materials, is the Cowper-Symonds model [92]. In the absence of a similar hypothesis for FRP, it is proposed that the concept used by Cowper and Symonds to predict the material properties of metallic materials under high strain rates, be extended to FRP

under dynamic loading conditions. This section will look into the general principals of the constitutive equations as introduced by Cowper and Symonds.

Cowper and Symonds in 1957 introduced their constitutive equation (equation (3.49)) to characterize the effect of strain rate on the mechanical properties of various metallic materials [93]. The model was formulated by gathering experimental test data of the dynamic lower yield stress of various materials at varying strain rates. From the experimental data a best-fit curve was generated and constitutive constants for equation (3.49) were produced. From the material coefficients (D (s^{-1}) and q) the stress-strain curve of a material at a known strain rate could be scaled to determine the material properties at an unknown strain rate.

$$\dot{\varepsilon} = D\left(\frac{\sigma_0'}{\sigma_0} - 1\right)^q \tag{3.49}$$

where

- σ_0' is the dynamic flow stress at a uniaxial plastic strain rate $\dot{\varepsilon}$.
- σ_0 is the associated static stress.
- D and q were constants for a particular material

3.4. CHANG-CHANG CRITERIA

3.4.1. INITIAL DEVELOPMENT OF CHANG-CHANG

One of the earliest failure criteria developed, was based on two mechanisms, the failure of the fibre and the failure of the matrix. The first mechanism was governed by the longitudinal stress, with reference to the fibre orientation and the second mechanism was governed by the transversal

and tangential stresses to the fibre [94]. Yamada and Sun later proposed a failure criterion of a lamina:

$$\left(\frac{\sigma_{11}}{X}\right)^2+\left(\frac{\sigma_{12}}{S_{is}}\right)^2=1 \tag{3.50}$$

where σ_{11} and σ_{12} are the longitudinal and tangential stresses, X is the strength of the lamina in the fibre direction and S_{is} is the in situ shear strength of the lamina [95]. A finite element approach that accounted for the:

- type of damage
- extent of damage
- material degradation in the damaged area
- residual strength
- ultimate load (failure load)

of composite laminates with arbitrary symmetrical lay-ups was thus developed [96].

3.4.2. FAILURE CRITERIA PROCEDURE

In-plane failure is generally considered the dominant mechanism in tensile failure of fibre-dominated laminated composites. Three different in-plane failure modes seem to emerge in these materials: matrix cracking, fibre-matrix shearing and fibre breakage. In-plane failure and the corresponding failure modes are therefore predicted by the Chang-Chang failure criteria [96]. For predicting matrix cracking failure, a matrix failure criterion was proposed which has the form:

$$\left(\frac{\sigma_y}{Y_T}\right)^2 + \frac{\frac{\sigma_{xy}^2}{2G_{xy}} + \frac{3}{4}\alpha\sigma_{xy}^4}{\frac{S_c^2}{2G_{xy}} + \frac{3}{4}\alpha S_c^4} = e_M^2 \tag{3.51}$$

where σ_y and σ_{xy} are the transverse tensile stress and shear stress in each layer, respectively. e_M^2 = constant that determines whether or not matrix failure if $e_M^2 \leq 1$ the matrix remains intact, whereas if $e_M^2 \geq 1$ the matrix is deemed to have failed. Y_t is the transverse tensile strength and G_{xy} is the shear strength. S_c is the in-situ ply shear strength measured from a cross-ply laminate, $[0/90]_s$, with the same thickness as the laminate [96]. For laminates with linear elastic behaviour ($\alpha = 0$), the equation is therefore reduced to

$$\left(\frac{\sigma_y}{Y_T}\right)^2 + \left(\frac{\sigma_{xy}}{S_c}\right)^2 = e_M^2 \tag{3.52}$$

The matrix failure criterion states that when, in any of the plies in a laminate, the stresses σ_y and σ_{xy} satisfy one of the above equations ($e_M^2 \geq 1$), matrix cracking will occurs in that layer. Matrix crushing will occur from compression loading conditions. The following equation is used to determine when matrix crushing occurs in the FEM:

$$e_c^2 = \frac{1}{4}\left(\frac{-\sigma_y}{G_{xy}}\right)^2 + \frac{Y_C^2\sigma_y}{4G_{xy}^2 Y_C} - \frac{\sigma_y}{Y_C} + \left(\frac{\sigma_{xy}}{G_{xy}}\right)^2 \geq 1 \tag{3.53}$$

where Y_C is the compressive strength in the transverse direction, e_c^2 = constant that determines the compressive strength in the transverse direction, therefore if $e_c \geq 1$ matrix crushing has taken place.

Both fibre-matrix shearing and fibre breakage are predicted by the modified Yamada-Sun criterion [96]. The criterion can be expressed as

$$\left(\frac{\sigma_x}{X_T}\right)^2 + \frac{\frac{\sigma_{xy}^2}{2G_{xy}} + \frac{3}{4}\alpha\sigma_{xy}^4}{\frac{S_c^2}{2G_{xy}} + \frac{3}{4}\alpha S_c^4} = e_f^2 \tag{3.54}$$

where e_f^2 = constant that determines tensile failure, σ_x and X_t are the longitudinal tensile stress and strength in each ply, respectively. For linear elastic laminates, the following equation is used

$$\left(\frac{\sigma_x}{X_T}\right)^2 + \left(\frac{\sigma_{xy}}{S_T}\right)^2 = e_f^2 \tag{3.55}$$

The fibre failure criterion states that fibre failure occurs when the ratio of the stress in the longitudinal direction (σ_x) over the strength in the longitudinal direction (X_T) squared; plus the shear stress in the longitudinal and transverse direction (σ_{xy}) over the shear strength (S_T) squared in the longitudinal direction of the plies in a laminate, is greater than one ($e_f^2 \geq 1$), that layer fails by either fibre breakage or fibre-matrix shearing.

If matrix cracking is predicted in a layer of the laminate, a delamination can be initiated from the crack. Chang *et al.* proposed an impact-induced delamination growth criterion for low-velocity impact [97]. The criterion can be expressed as:

$$D_a\left[\left(\frac{{}^n\bar{\sigma}_{yz}}{{}^nS_i}\right)^2 + \left(\frac{{}^n\bar{\sigma}_{xz}}{{}^{n+1}S_i}\right)^2 + \left(\frac{{}^n\bar{\sigma}_{zz}}{{}^{n+1}S_3}\right)^2\right] = e_D^2 \tag{3.56}$$

$e_D^2 \geq 1$ Failure

$e_D^2 \leq 1$ No Failure

where D_a is a constant, S_3 the strength in the transverse direction and S_i is the in situ interlaminar shear strength within the laminate under consideration. The subscripts 1, 2 and 3 are local material coordinates of an individual ply within the laminate and the superscripts *n* and *n+1* correspond to the upper and lower plies of the *n*-th interface, respectively. $\bar{\sigma}_{yz}$ and $\bar{\sigma}_{zz}$ represent the average interlaminar and in-plane transverse stresses within the n-th and *(n+1)* th ply, respectively. $\bar{\sigma}_{xz}$ is the average interlaminar longitudinal stress within the *(n+1)* th ply.

3.4.3. PROPERTY DEGRADATION MODEL

Once failure has occurred the materials undergo some degree of property loss in the damaged area. The degree of property loss is strongly dependent upon the failure mechanisms resulting from damage [96]. Hence, the property degradation model is developed on the basis of the failure mode predicted by the previous failure criteria (section 2.5.1.1). For matrix cracking in a layer therefore, the transverse modulus, E_y and Poisson's ratio, v_y, are reduced to zero when the condition $e_M \geq 1$ has been met, i.e. the matrix is said to have undergone damage. However, the longitudinal modulus and the shear stress-strain relation of the layer are unchanged. Therefore in the failed layer, the in-plane properties are reduced as follows:

$$\begin{bmatrix} \frac{E_x}{1-v_{xy}v_{yx}} & \frac{v_{xy}E_y}{1-v_{xy}v_{yx}} \\ \frac{v_{xy}E_y}{1-v_{xy}v_{yx}} & \frac{E_y}{1-v_{xy}v_{yx}} \end{bmatrix} \rightarrow \begin{bmatrix} E_x & 0 \\ 0 & 0 \end{bmatrix} \tag{3.57}$$

When fibre breakage and/or fibre-matrix shearing are predicted, the degree of property degradation within the damaged area depends on the size of damage predicted by the fibre failure criterion. The property reduction model postulates that for fibre failure both E_y and v_y are reduced to zero, but the longitudinal modulus, E_x and the shear modulus, G_{xy}, degenerate according to the Weibull distribution as follows:

$$\frac{E_x^d}{E_x} = \exp\left[-\left(\frac{A}{A_0}\right)^{\beta}\right]$$
$$\frac{G_{xy}^d}{G_{xy}} = \exp\left[-\left(\frac{A}{A_0}\right)^{\beta}\right] \quad (3.58)$$

where E_x^d and G_{xy}^d are the reduced tensile and shear moduli, respectively. A is the damage zone predicted by the fibre failure criterion and $A_0\left(=\delta^2\right)$ is the fibre failure interaction zone associated with the measured ply tensile strength X_t. β_w is the shape parameter of the Weibull distribution for the property degradation. Verification of the progressive damage model with corresponding experimental data showed a good correlation [96].

3.5. MECHANICS OF UNIDIRECTIONAL COMPOSITES

The FRP materials tested in this thesis consists of individual layers of laminates which are made of unidirectional plies with the same orientation $[0]_{ns}$, where n = number of plies and s = symmetry.

3.5.1. UNIDIRECTIONAL ORTHOTROPIC LAYER

A composite layer with the simplest structure consists of unidirectional plies whose material global coordinates, 1, 2, 3, coincide with the local coordinates of the layer, *x*, *y*, *z*, as in Figure 3.4.

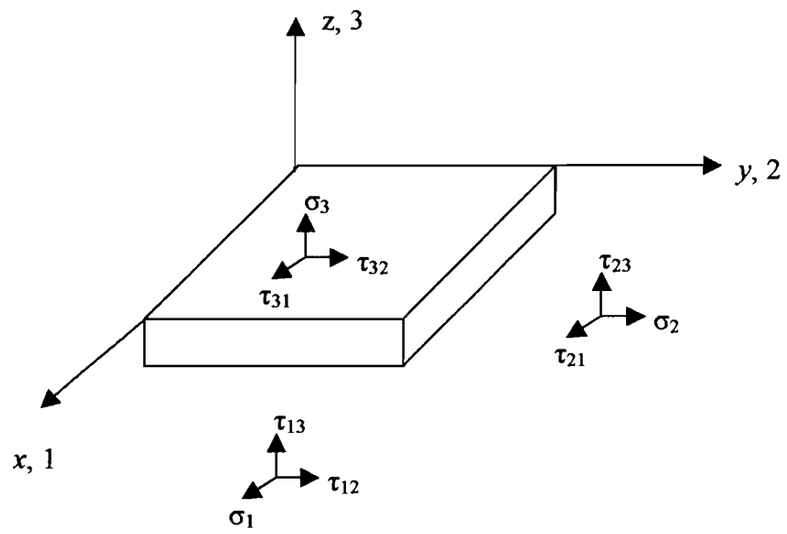

Figure 3.4: A typical orthotropic layer showing the global and local coordinates.

3.5.1.1. LINEAR ELASTIC MODEL

In order to deduce the constitutive equations for the linear elastic model the consideration of an elastic solid loaded with body and surface forces is required. These forces induce some stresses and strains that compose the field of actual static and kinematic variables [98]. This results in infinitesimal additional strains du_x, du_y, du_z that belong to a kinematically admissible field. The equation (3.59) specifies additional strains.

$$d\varepsilon_x = \frac{\partial}{\partial x}(du_x),\ d\gamma_{xy} = \frac{\partial}{\partial y}(du_x) + \frac{\partial}{\partial x}(du_y) \quad (x, y, z) \tag{3.59}$$

Because additional strains are infinitely small, we can assume that external forces do not change under such variation of the displacements. The work done can thus be calculated using the simple relationship

$$w = \underset{\sim}{f}.\underline{d} \tag{3.60}$$

The total work performed is deduced by multiplying the forces by the corresponding increments of the displacements

$$dW = \iiint_V \left(q_x du_x + q_y du_y + q_z du_z\right) dV + \iint_S \left(p_x du_x + p_y du_y + p_z du_z\right) dS \tag{3.61}$$

Here V and S are the body volume and external surface of the body. The x-components of forces and displacements in equation (3.61) are considered.

$$dW = \iiint_V \left(q_x du_x\right) + \iint_S \left(p_x du_x\right) ds \tag{3.62}$$

Equation (3.62) can be transformed by expressing p_x, p_y and p_z in terms of stress and by transforming the surface integral into a volume integral to obtain:

$$dW = \iiint_V \left[\sigma_x d\varepsilon_x + \sigma_{xy} \frac{\partial}{\partial y}\left(du_x\right) + \sigma_{xz} \frac{\partial}{\partial z}\left(du_x\right)\right] dV \tag{3.63}$$

where equation (3.63) can be written as:

$$dW = \iiint_V dU\, dV \tag{3.64}$$

where

$$dU = \sigma_{ij} d\varepsilon_{ij} \tag{3.65}$$

The function $U\left(\varepsilon_{ij}\right)$ can be referred to as specific strain energy (the energy accumulated in the unit of body volume) or elastic potential. Potential U can be expanded into the Taylor series with respect to strains therefore

$$U(\varepsilon_{ij}) = D_0 + D_{ij}\varepsilon_{ij} + \tfrac{1}{2} D_{ijkl}\varepsilon_{ij} + \ldots\ldots \tag{3.66}$$

where

$$D_{ijkl} = U\left(\varepsilon_{ij} = 0\right), = \left.\frac{\partial U}{\partial \varepsilon_{ij}}\right|_{ij}, = \left.\frac{\partial^2 U}{\partial \varepsilon_{ij}\partial \varepsilon_{kl}}\right|_{\varepsilon_{ij}=0, \varepsilon_{kl}=0} \tag{3.67}$$

Assume that in the initial state of the body corresponding to zero external forces we have $\varepsilon_{ij} = 0$, $\sigma_{ij} = 0$, $U = 0$. For small strains in the body, we can neglect high-order terms in equation (3.66) and restrict the derivation to the first systems of non-zero terms taking

$$U = \tfrac{1}{2} D_{ijkl}\varepsilon_{ij}\varepsilon_{kl} \tag{3.68}$$

Equation (3.65) will thus yield:

$$\sigma_{ij} = D_{ijkl}\varepsilon_{kl} \tag{3.69}$$

Equation (3.69) can be written in explicit form:

$$\{\sigma\} = [D]\{\varepsilon\} \tag{3.70}$$

This is referred to as a constitutive equation. This equation links stress and strains through the stiffness coefficients that specify the material mechanical properties within the framework of a linear elastic model. The inverse form of equation (3.70) is:

$$\{\varepsilon\} = [C]\{\sigma\} \tag{3.71}$$

where

$$[C] = [D]^{-1} \tag{3.72}$$

Strains are expressed in terms of stresses via the matrix of compliance coefficients that can be written in the form of a matrix. For the case of an orthotropic material the compliance matrix is

$$[D]=\begin{bmatrix} \frac{1}{E_x} & -\frac{\nu_{xy}}{E_y} & -\frac{\nu_{xz}}{E_z} & 0 & 0 & 0 \\ -\frac{\nu_{yx}}{E_x} & \frac{1}{E_y} & -\frac{\nu_{yz}}{E_z} & 0 & 0 & 0 \\ -\frac{\nu_{zx}}{E_x} & -\frac{\nu_{xy}}{E_y} & \frac{1}{E_z} & 0 & 0 & 0 \\ 0 & 0 & 0 & \frac{1}{G_{xy}} & 0 & 0 \\ 0 & 0 & 0 & 0 & \frac{1}{G_{xz}} & 0 \\ 0 & 0 & 0 & 0 & 0 & \frac{1}{G_{yz}} \end{bmatrix} \tag{3.73}$$

For a unidirectional composite layer, constitutive equations (3.70) and (3.73) yield

$$\begin{aligned} \varepsilon_1 &= \frac{\sigma_1}{E_1} - \nu_{12}\frac{\sigma_2}{E_2} - \nu_{13}\frac{\sigma_3}{E_3}, \\ \varepsilon_2 &= \frac{\sigma_2}{E_2} - \nu_{21}\frac{\sigma_1}{E_1} - \nu_{23}\frac{\sigma_3}{E_3}, \\ \varepsilon_3 &= \frac{\sigma_3}{E_3} - \nu_{31}\frac{\sigma_1}{E_1} - \nu_{32}\frac{\sigma_2}{E_2}, \\ \gamma_{12} &= \frac{\tau_{12}}{G_{12}}, \quad \gamma_{13} = \frac{\tau_{13}}{G_{13}}, \quad \gamma_{23} = \frac{\tau_{23}}{G_{23}}, \end{aligned} \tag{3.74}$$

Recalling equation (3.70) and noting that for an orthotropic material the engineering constants define the $\boldsymbol{D}$ matrix, then

$$\{\boldsymbol{\sigma}\} = \left[\boldsymbol{D}^{\boldsymbol{el}}\right]\{\boldsymbol{\varepsilon}\} \tag{3.75}$$

with the $\boldsymbol{D}^{\boldsymbol{el}}$ matrix expands to

$$
\begin{aligned}
D_{1111} &= E_1\left(1-\nu_{23}\nu_{32}\right)\Upsilon, \\
D_{2222} &= E_2\left(1-\nu_{13}\nu_{31}\right)\Upsilon, \\
D_{3333} &= E_3\left(1-\nu_{12}\nu_{21}\right)\Upsilon, \\
D_{1122} &= E_1\left(\nu_{21}+\nu_{31}\nu_{23}\right)\Upsilon = E_2\left(\nu_{12}+\nu_{32}\nu_{13}\right)\Upsilon, \\
D_{1133} &= E_1\left(\nu_{31}+\nu_{21}\nu_{32}\right)\Upsilon = E_3\left(\nu_{13}+\nu_{12}\nu_{23}\right)\Upsilon, \\
D_{2233} &= E_2\left(\nu_{32}+\nu_{12}\nu_{31}\right)\Upsilon = E_3\left(\nu_{23}+\nu_{21}\nu_{13}\right)\Upsilon, \\
D_{1212} &= G_{12}, \\
D_{1313} &= G_{13}, \\
D_{2323} &= G_{23},
\end{aligned}
\tag{3.76}
$$

where

$$
\Upsilon = \frac{1}{1-\nu_{12}\nu_{12}-\nu_{23}\nu_{32}-\nu_{31}\nu_{13}-2\nu_{21}\nu_{32}\nu_{13}} \tag{3.77}
$$

The constitutive equations presented above include elastic constants ($E_1, E_2, G_{12}, \nu_{12},$), which are determined experimentally. For in-plane unidirectional composites $G_{13} = G_{12}$ and $\nu_{13} = \nu_{12}$ [98].

3.6. FUNDAMENTALS OF FINITE ELEMENT ANALYSIS

3.6.1. THE FINITE ELEMENT METHOD

The Finite Element Method (FEM) can be stated as follows: "The FEM is a computer-aided mathematical technique for obtaining approximate numerical solutions to the abstract equations of calculus that predicts the response of physical systems subjected to external influences" [99]. The basic assumptions of structural analysis can be summarized by three separate (but linked) conditions, shown in Figure 3.5.

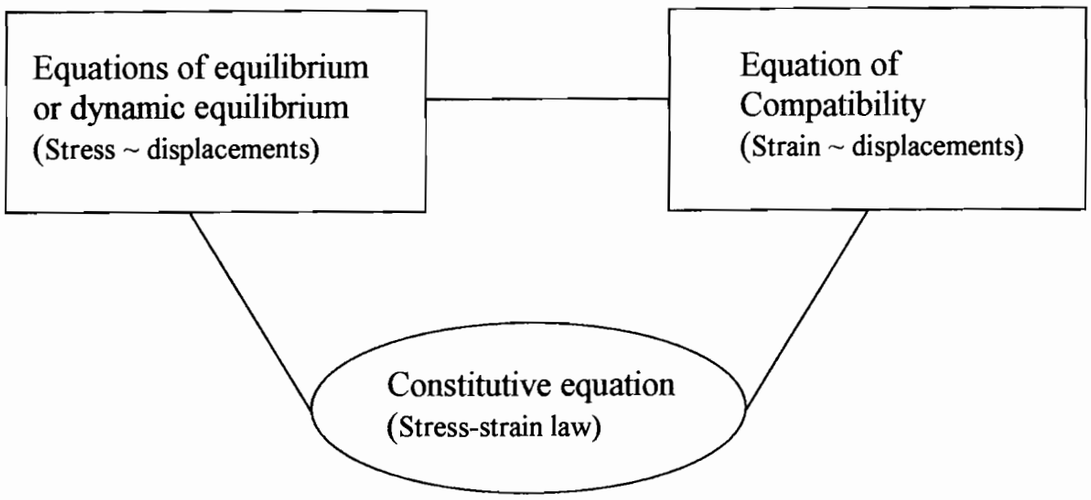

Figure 3.5: The three conditions for all structural analysis [100].

Consider that an arbitrary structure matrix notation is ideal in defining the stress fields and displacements fields. In fact in the 1950s, finite element methods were originally known as "matrix methods" [100]. Problems that can be solved using FEM include solid mechanics (e.g. elasticity, plasticity, statics and dynamics), heat transfer (e.g. conduction, convection and radiation) and fluid mechanics (e.g. flow field in the vicinity of compressor blades) and magnetic fields. A finite element is derived by assuming a form of the equation for the internal fields [101]. For example the internal strains can be listed as column matrices in terms of the three direct and shear components at time *t*:

$$\varepsilon^t = \left[\varepsilon_{xx}, \varepsilon_{yy}, \varepsilon_{zz}, \varepsilon_{xy}, \varepsilon_{yz}, \varepsilon_{zx}\right] \tag{3.78}$$

There will be one equation for each degree of freedom of each node of the element. The matrix of the coefficients becomes a "stiffness matrix" that relates forces to displacements as stated in equation (3.79).

$$[F] = [K].[d] \tag{3.79}$$

where ***[F]***, ***[K]*** and ***[d]*** are the force vectors, stiffness matrix and displacement vectors, respectively.

3.6.2. ISOPARAMETRIC ELEMENT FORMULATION

The isoparametric formulation makes it possible to generate elements that are non-rectangular and have curved sides [102]. The isoparametric formulation includes elements for solid, plate and shell problems. The features for the isoparametric elements are:

- Isoparametric elements are defined on the ξ, η, ζ axes and not on the x, y and z-axes (3D).
- Isoparametric elements are defined on the domain; $-1 < \xi, \eta, \zeta < +1$
- A mapping exists from the isoparametric domain to the problem domain. The isoparametric mapping of the isoparametric element in the in the ξ, η, ζ domain to the x, y, z domain is achieved by the mapping:

$$x = \sum N_i x_i, \; y = \sum N_i y_i, \; z = \sum N_i z_i \tag{3.80}$$

where i is the number of nodes in the element. The shape function N_i (or trial function) is a function of the isoparametric co-ordinates ξ, η and ζ. The shape function for a linear solid element (so called eight node brick element) is:

$$N_i = \frac{1}{8}(1 \pm \xi)(1 \pm \eta)(1 \pm \zeta) \tag{3.81}$$

where i = 1,2,3,.....8.

The derivation of the Jacobian, a mapping matrix, provides a numerical value to the local amount of expansion or contraction of the coordinates due to the isoparametric mapping [101]. The Jacobian is a 3 x 3 matrix for a 3D element and is given by

$$J(\xi,\eta,\zeta)=\begin{bmatrix}\frac{\partial x}{\partial \xi}\frac{\partial y}{\partial \xi}\frac{\partial z}{\partial \xi}\\ \frac{\partial x}{\partial \eta}\frac{\partial y}{\partial \eta}\frac{\partial z}{\partial \eta}\\ \frac{\partial x}{\partial \zeta}\frac{\partial y}{\partial \zeta}\frac{\partial z}{\partial \zeta}\end{bmatrix} \tag{3.82}$$

3.6.3. THREE DIMENSIONAL FEM

The linear isoparametric solid element is seen in Figure 3.6.

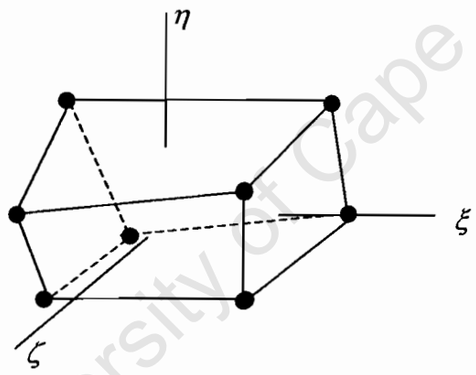

Figure 3.6: A three dimensional linear solid element [102].

The stiffness matrix for a 3 dimensional problems becomes

$$[K] = \int_{-1}^{1}\int_{-1}^{1}\int_{-1}^{1}[B]^T K[B]J d\xi J d\eta d\zeta \tag{3.83}$$

where the *Jacobian determinant*, $|J|$, expresses the ratio of volume from dx, dy, dz to $d\xi, d\eta, d\zeta$ and $[B]$ is a function of ξ, η and ζ [102].

3.6.4. NUMERICAL SOLUTION METHODS

The numerical solution methods for dynamic analysis are broadly characterized as implicit or explicit. The explicit method is especially suited to solving high-speed dynamic events. The explicit scheme used in the numerical method is based upon the implementation of an explicit integration rule together with the use of diagonal or "lumped" element mass matrices. The explicit procedure integrates through time using small time increments. The equation of motion for the body are integrated using the explicit central difference integration rule

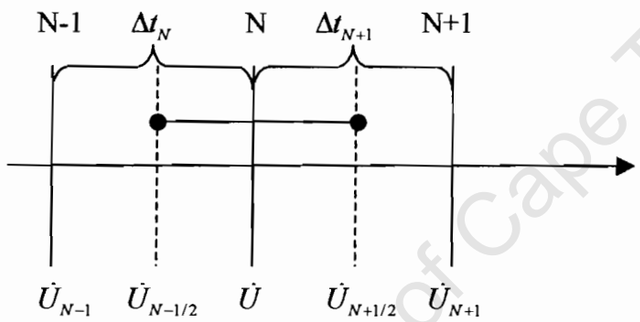

Figure 3.7: Diagrammatic representation of the central difference integration procedure

$$\dot{u}^{(i+\frac{1}{2})} = \dot{u}^{(i-\frac{1}{2})} + \frac{\Delta t^{(i+1)} + \Delta t^{(i)}}{2}\ddot{u}^{(i)} \tag{3.84}$$

where $\dot{u}$ is the velocity and $\ddot{u}$ is acceleration. The superscript (i) refers to the increment number and $(i+\frac{1}{2})$ and $(i-\frac{1}{2})$ refer to mid-increment values. The central difference integration operator is explicit in that the kinematic state can be advanced using known values of $\dot{u}^{(i-\frac{1}{2})}$ and

$\ddot{u}^{(i)}$ from the previous increment. The explicit integration rule is quite simple but by itself does not provide the computational efficiency associated with explicit dynamics procedures. The key to computational efficiency of the explicit procedure is the use of diagonal element mass matrices, because the inversion of the mass matrix that is used in the computation for the accelerations at the beginning of the increment, is triaxial:

$$\ddot{u}^{(i)} = M^{-1}.\left(F^{(i)} - I^{(i)}\right) \tag{3.85}$$

3.6.5. FINITE ELEMENTS USED FOR COMPOSITE LAMINATE ANAYLSIS

The layered nature of composite materials means that only certain types of element types can be used efficiently within the FE analysis of composites. It is considered numerically expensive to stack three dimensional brick elements with one layer of bricks representing a ply of composite materials [100]. Nevertheless, the analysis carried out in this thesis uses a three-dimensional brick element to represent one ply. This procedure does have three main advantages:

1) The model is useful in determining the through thickness stress in the material
2) When modelling very thick composite lay-ups and when the behaviour is not well represented by shell theory
3) Where there is a 3D stress field in the material

From the mechanics of UD-composites, section 3.5, it becomes clear that when modelling composite laminates, a linear elastic model that defines orthotropic material behaviour is appropriate for modelling laminates. A linear elastic model is valid for

- Small elastic strains (normally less than 5%) such as that experienced by FRPs

- Modelling problems that have properties that are dependent on other field variables such as strain rate and temperature.

The total stress is defined from the total elastic strain as

$$\boldsymbol{\sigma} = \boldsymbol{D}^{el}\boldsymbol{\varepsilon}^{el} \tag{3.86}$$

where σ is the total stress ("true" or Cauchy stress in finite strain problems), $\boldsymbol{D}^{el}$ is the fourth-order elastic tensor and $\boldsymbol{\varepsilon}^{el}$ is the total elastic strain. Linear elasticity in an orthotropic material can be defined by giving the nine independent elastic stiffness parameters, recalling equation (3.75), therefore resulting in equation (3.87):

$$\begin{Bmatrix} \sigma_{11} \\ \sigma_{22} \\ \sigma_{33} \\ \sigma_{12} \\ \sigma_{13} \\ \sigma_{23} \end{Bmatrix} = \begin{bmatrix} D_{1111} & D_{1122} & D_{1133} & 0 & 0 & 0 \\ & D_{2222} & D_{2233} & 0 & 0 & 0 \\ & & D_{3333} & 0 & 0 & 0 \\ & & & D_{1212} & 0 & 0 \\ & & & & D_{1313} & 0 \\ & & & & & D_{2323} \end{bmatrix} \begin{Bmatrix} \varepsilon_{11} \\ \varepsilon_{22} \\ \varepsilon_{33} \\ \gamma_{12} \\ \gamma_{13} \\ \gamma_{23} \end{Bmatrix} \tag{3.87}$$

where D_{ijkl} defines the materials stiffness parameters.

CHAPTER 4

EXPERIMENTAL PROCEDURES

4.1. INTRODUCTION TO TESTING PROCEDURES

A dual experimental-numerical approach to predictive modelling was adopted in this investigation. The precursors to accurate predictive modelling of the behaviour of materials and structures subjected to impact loading are:

- To conduct experiments under simple and well controlled loading conditions which allows for observations of the material's behaviour at representative scales including measurements of intrinsic materials properties.
- To devise small-scale structural experiments with well controlled loading which will enable the complete identification of non-measurable material parameters as well as the fine tuning of available/developed numerical tools at manageable scales.

4.2. MATERIALS AND SPECIMEN DESIGN

The tests were designed to examine the strain rate dependence of unidirectional CFRP (Material type: AIK-EHKF-420-UD24K-40) and unidirectional GFRP (Material type: EPO UD EST 250/600 FT 102 35% Glass), materials in compression, shear and in-plane tension at three distinct rates of strain (quasi-static strain rate of 10^{-4} s^{-1}, medium strain rate of 10^{2} s^{-1} and high strain rate of 10^{3} s^{-1}). The results from these tests provide a basic set of material properties for finite element modelling of deformation and failure of laminated composite materials. From each test the ultimate stresses were obtained. The two materials (CFRP and GFRP) were obtained from Aerodyne Technologies South Africa, in the form of 48-layered laminate prepared from prepreg in an epoxy matrix. The volume fraction for the CFRP and GFRP plates of dimension

200 x 200 x 10 mm are 60 % and 62%, respectively. The plates where cut into strips and machined into cylindrical sections of diameter 6 mm and length 9 mm for the compression specimens and into "Z shaped" sections of length 30 mm for the single lap shear specimens. In the case of the tensile specimen, 8 layered 200 x 200 x 2 mm plates where cut into strips and machined into lengths of 60 mm and widths of 10 mm. Figure 4.1 illustrates the schematic of the compression, shear and tensile specimens (see *APPENDIX I*, *APPENDIX II* and *APPENDIX III* for compression, shear and tension specimens manufacturing procedure, respectively). In order to exclude geometric and size effects and to enable a direct comparison of the results obtained at the three different rates of strain, constant specimen geometries shown in Table 4.1 were used throughout the testing regimes for compression, shear and tensile testing, respectively.

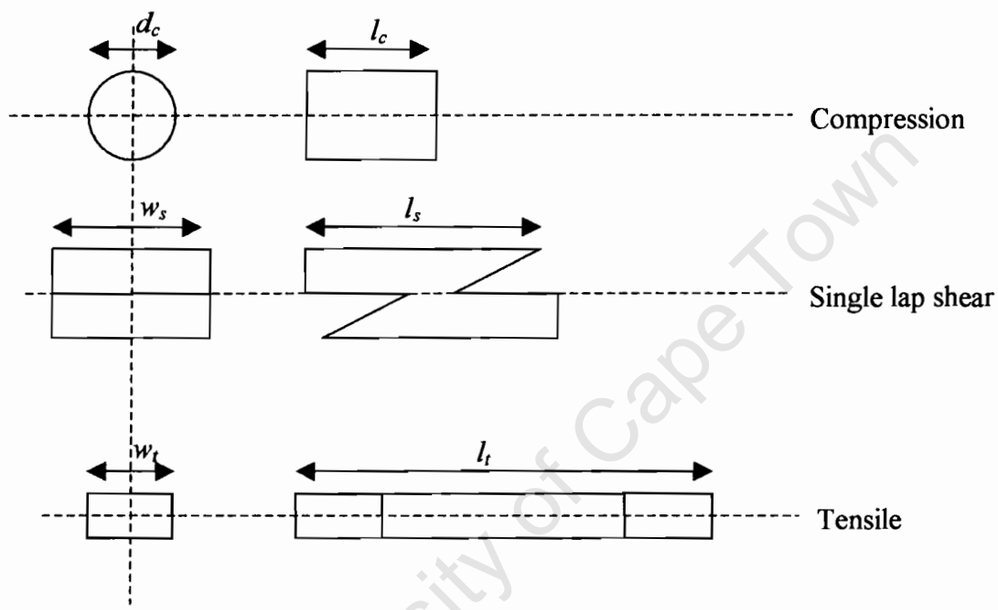

Figure 4.1: Schematic of the compression, shear and tensile specimens dimensions (Not to scale).

The specimens were carefully machined, particular care being taken with respect to applying any thermal or mechanical loading that often results in premature composite material failure. In addition, the tensile specimen design was chosen to reduce the effects of stress concentrations at

the grips that usually result in premature failure of the composite material. The design chosen is based on the design parameters earlier proposed by Welsh and Harding [11]. The compression, single lap shear and tensile specimens are all loaded in the fibre direction.

Table 4.1: Compression, single lap shear and tensile specimen geometries and tolerance.

Loading Direction	Specimen Type	Diameter (d_c) (mm)	Width (w_b, w_t) (mm)	Gauge length (l_c, l_s, l_t) (mm)	Thickness (t_s, t_t) (mm)
Compression	CFRP	6.14±0.30	N/a	8.90±0.30	N/a
Compression	GFRP	6.20±0.30	N/a	9.00±0.30	N/a
Shear	CFRP	N/a	15±0.50	30±0.70	10±0.50
Shear	GFRP	N/a	15±0.50	30±0.70	10±0.50
Tension	CFRP	N/a	10±0.50	22±0.90	8±0.50
Tension	GFRP	N/a	10±0.50	22±0.90	8±0.50

The tensile specimen dimensions given in Table 4.1 are essentially the same as those referred to in chapter 2. For a detailed sketch of tensile specimens refer to *APPENDIX III*. The emphasis of the specimen design is to ensure that failure of the tensile specimen occurs within the gauge length, and to prevent shear failure in the grips usually observed in unidirectional composites. The unidirectional specimens needed thinning in both thickness as well as the width directions. This enables the specimen failure to occur by fibre failure, within the gauge length, rather than through delamination along the ply interfaces and pull-out from the end-caps. An image of the fractured specimen in Figure 4.2 shows the fibre distribution across the thickness of the specimen, which favourably split transversely in the gauge length. This failure regions confirms the successful specimen design.

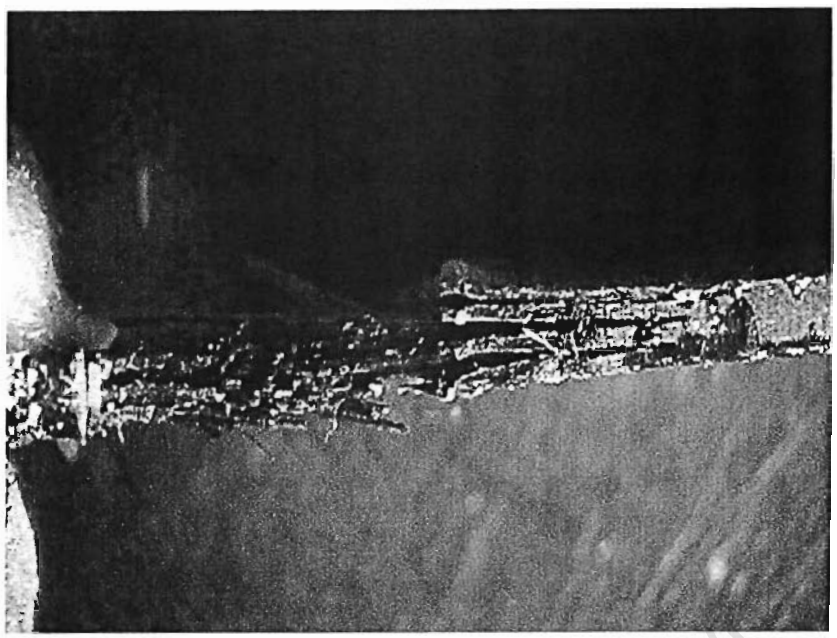

Figure 4.2: Section through a CFRP specimen that split transversely showing good fibre distribution through the specimen thickness in the central gauge region.

It is important to note that great care was taken in both the hydraulic test and the tensile Hopkinson bar to ensure that the grips were fully screwed in without pre-loading the specimen. The action of tightening the screw threads of the grips, may result in some bending or twisting load being applied on the tensile specimen. The effect of any resulting stress concentration would cause premature failure of the specimen. Great care was taken to ensure no bending loads were exerted on the specimens. Any bending strains would not be detected or recorded by the strain gauges mounted on opposite sides of the specimen. The gauges were connected in series thus electrically cancelling any differential strain gauge signals.

4.3. EXPERIMENTAL SET-UP

The experimental work carried out in this thesis was done at the Solid Mechanics Laboratory at Oxford University, UK.

4.3.1. QUASI-STATIC STRAIN RATE (10^{-3} s^{-1}) LOADING RIG

A hydraulic testing machine was used to determine the compressive, shear and tensile ultimate stresses of carbon and glass fibre specimens at quasi-static strain rates. The compressive specimens were tested between two flat metal cylinders. The shear specimens were tested between "L" shaped stages, whilst the tensile specimens are screwed at the opposite gripping ends. One end of the stage or gripping system for the various tests is attached to the movable end of the hydraulic testing machine and the second end is attached to the load cell. The typical tensile and compression set-up used is shown in Figure 4.3.

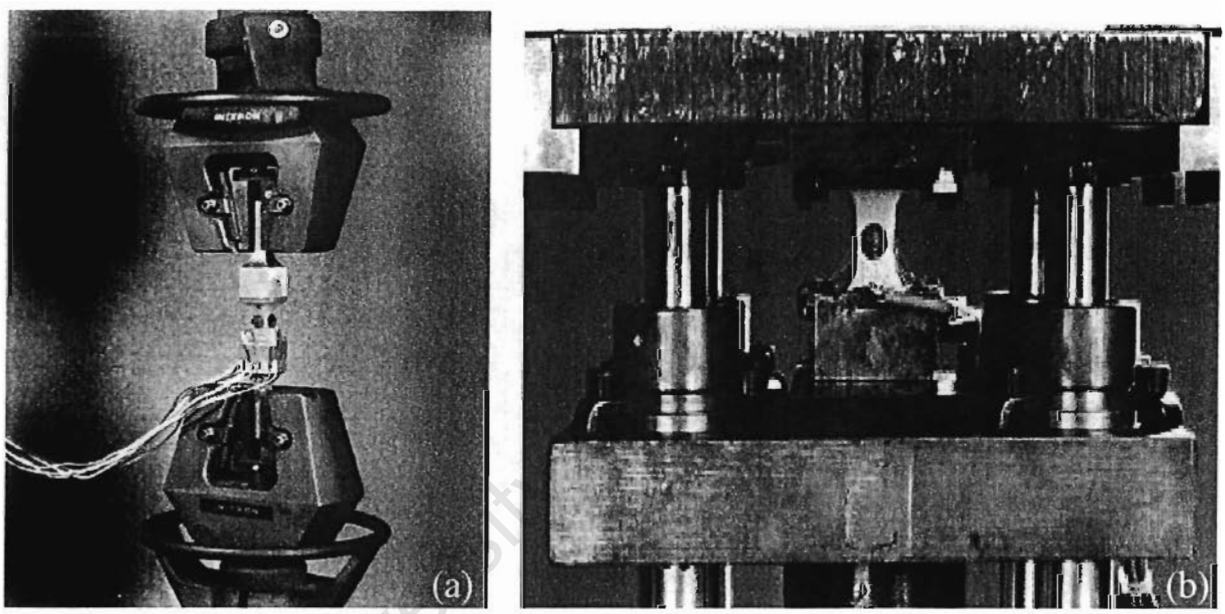

Figure 4.3: Photograph of the Instron hydraulic testing machine used for quasi-static testing of FRPs in tension (a) and compression (b), respectively.

The assembly was placed so that the various specimens were centrally located between the loading stages. The cross-head speed is set at a rate of 2.64 mm/min, which translates to a strain rate of 2 x 10^{-3} s^{-1}. The quasi-static results were recorded in the form of load displacement curves with maximum loads of 30 kN for varying displacements. This data is converted into stress-strain curves to determine the strain and ultimate stresses.

4.3.2. MEDIUM STRAIN RATE (10^2 s^{-1}) LOADING RIG

This is very similar to low strain rate testing except that the load frames require the capability to generate higher crosshead velocities and so a hydraulic ram is used. For compression the specimen is placed between two hard polished plates that maintain parallel faces during the deformation. The stroke of the ram is accurately set to ensure the desired amount of deformation at a strain rate of 114 s^{-1}. The stroke is set so that approximately the right amount of deformation occurred. For example, if a 2.9 mm spacer was used, the stroke was set to be 0.1 mm. A load cell measures the force applied and the linear voltage displacement transducer (LVDT) the strain.

4.3.3. HIGH STRAIN RATE (10^3 s^{-1}) LOADING RIG

A SHPB system typically comprises of the following:

- A gas gun and associated control valves that can launch a striker bar, to produce a controlled pulse in the incident or input bar.
- Two long bars, the input and output bars, also known as incident and transmitter bars, respectively.
- Bearing and alignment fixtures to allow the bars to move freely while retaining precise axial alignment.
- Strain gauges mounted longitudinally on both bars to measure the stress wave propagation in the bars, (labelled Gauge No. 1 and Gauge No. 2).
- Amplifiers and a data acquisition system to record the stress waves in the system.

Dynamic compression tests were conducted using the compression split Hopkinson bar. Geometric effects are discarded by maintaining the same specimen geometry. A series of dynamic compression tests are performed on cylindrical CFRP and GFRP composites to gain material property data for numerical analysis. The strain rate varied from 400 s^{-1} to 1400 s^{-1} by varying the impact velocity of the incident bar in the SHPB apparatus. The compression SHPB

analysis provides extensive amount of data such as the stress, force, nominal strain and strain rate in the composite systems undergoing impact. This information is pertinent to understanding the behaviour of the material as well as in determining the stress in the material under varying loading conditions. For the purpose of modelling however, the difference in the input and output velocities (i.e. ΔV) as well as the failure strength of the material are important (Figure 4.4).

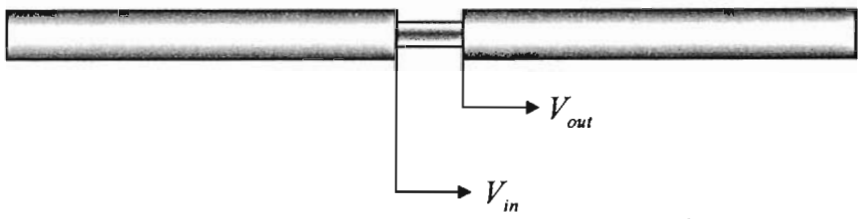

Figure 4.4: Schematic of input and output bar showing the derivation of the velocities and the displacements at the specimen bar interface.

Recall

$$\Delta V = V_{in} - V_{out} \tag{4.1}$$

$$\Delta U = (V_{in} - V_{out})\Delta t \tag{4.2}$$

The initial velocity is derived from the pressure applied to the striker bar. This pressure varies resulting in different impact velocities in the input bar (see Figure 4.4). In the case of compression testing this is referred to as the contraction velocity, for example. The compressive strengths of 150 specimens are given in the form of tables with the average compressive strength per strain rate. Additional data such as the force vs. time and nominal strain vs. time are therefore provided for in *APPENDIX IV*.

Dynamic single-lap shear tests were done using a single-lap type split Hopkinson bar where the incident pulse is loaded in compression. Geometric effects are minimized by maintaining the same specimen geometry as used in the quasi-static analysis. A series of dynamic single-lap tests are performed on CFRP and GFRP composite to gain material property data to use in the

numerical analysis. The dynamic strain rate varied from 300 s^{-1} to 800 s^{-1} by varying the impact velocity of the SHPB (see Figure 4.5: for schematic of the system).

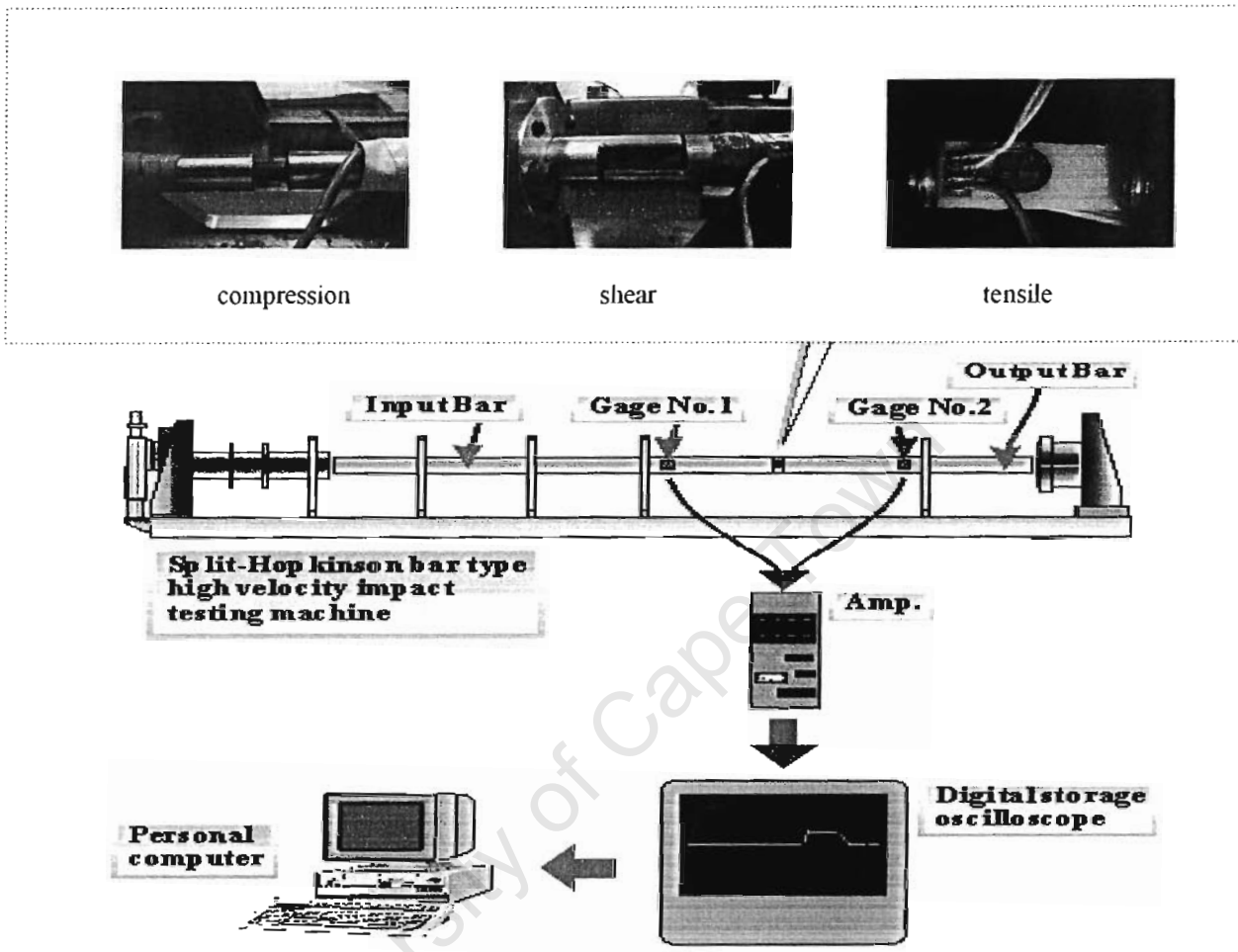

Figure 4.5: Schematic illustration of the split Hopkinson bar apparatus showing the compression, shear and tensile specimen set-up.

The relevant test specimens, compression, shear and tensile are positioned between the incident and transmitter bars (Figure 4.6, Figure 4.7, Figure 4.8 for compression, shear and tensile, respectively). A striker bar made of the same material and having the same cross-sectional area as the incident bar, is launched at the free end of the incident bar, in the case of tensile testing. This

sets up a longitudinal compressive pulse, designated σ_i, which travels down the incident bar and is recorded by the first strain gauge station. Once the pulse reach the bar/specimen interface, part of the pulse is reflected in the form of a tensile pulse, designated σ_r and is recorded by the first strain gauge station. The remainder of the pulse passes through the specimen where some of the energy of the pulse is absorbed by the specimen and then passes into the transmitter bar. The pulse travels down the transmitter bar, designated σ_t and is then recorded by the second strain gauge station.

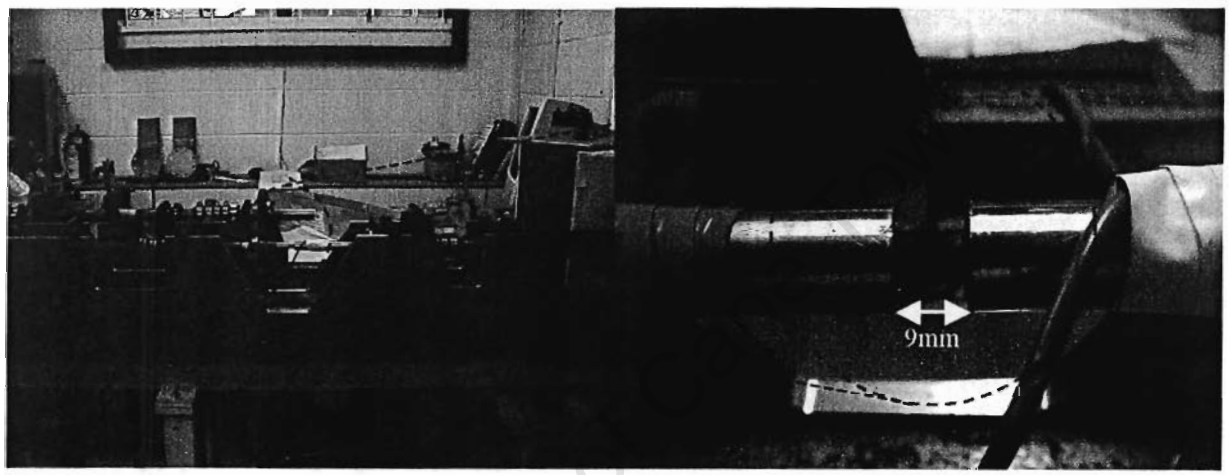

Figure 4.6: SHPB Compression set-up showing the periphery and zooming in to show the CFRP specimen between the incident and transmitter bars.

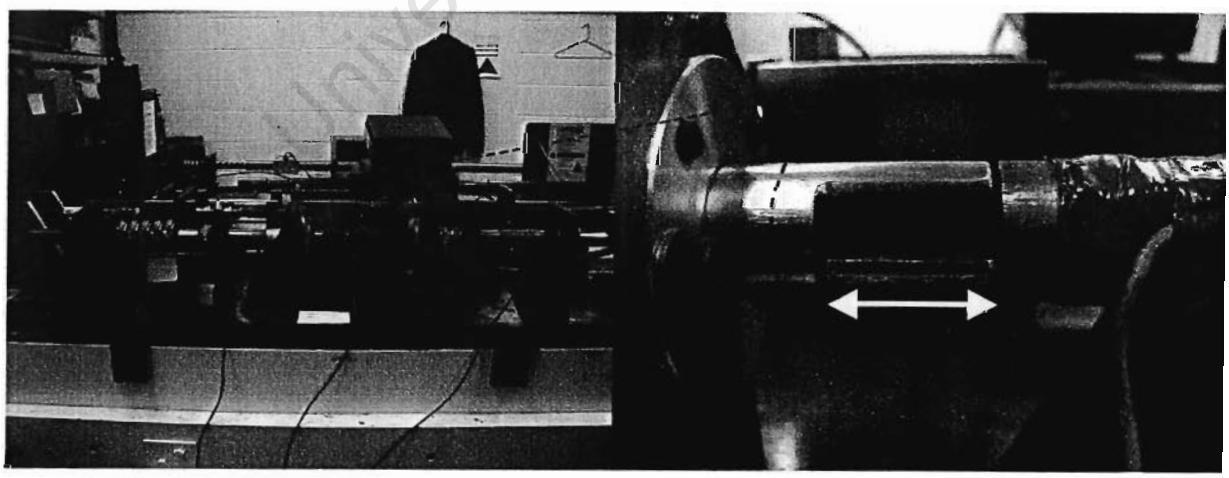

Figure 4.7: Photograph showing the periphery of the SHPB single lap shear set-up and zooming in to show the fixture of a CFRP specimen.

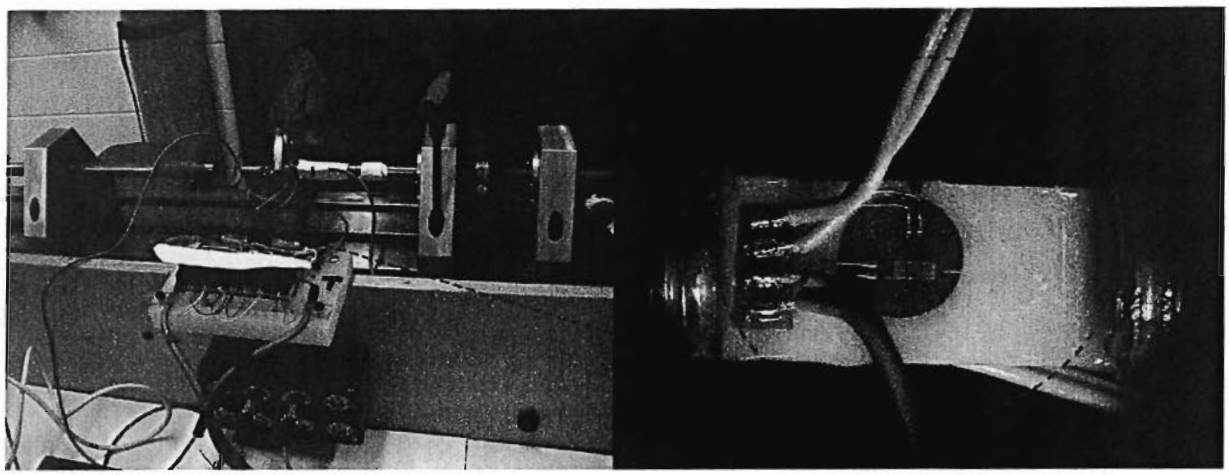

Figure 4.8: Schematic of SHPB tensile specimens showing the periphery and zooming in to the tensile specimen with a strain gauge mounted.

By varying the striker length and impact velocity, the incident pulse length and amplitude is changed. By altering the shape of the incident pulse the strain and strain rate of the specimen can be varied. The strain rate can be increased by increasing the impact velocity of the striker, for a given striker length. As the bars should remain elastic the maximum allowable impact velocity v_{max} is:

$$v_{max} = \frac{2C_0\sigma_y}{E} \tag{4.3}$$

where σ_y is the yield stress and E is the Young's modulus of the pressure bar, C_0 is the fundamental longitudinal wave velocity. The strain that the specimen undergoes is increased by increasing the length of the striker. The length of the striker must always remain less than half the length of the shorter pressure bar. This will avoid any overlap of the incident and reflected pulse at the reading station. A typical plot showing time synchronised data is presented in Figure 4.9. This data is then converted to input velocity versus time and stress versus strain graphs using the one-dimensional wave propagation theory. Graphs of the force, contraction, extension, nominal strain, nominal strain rate and nominal stress versus time are also determined and are shown in *APPENDIX IV.*

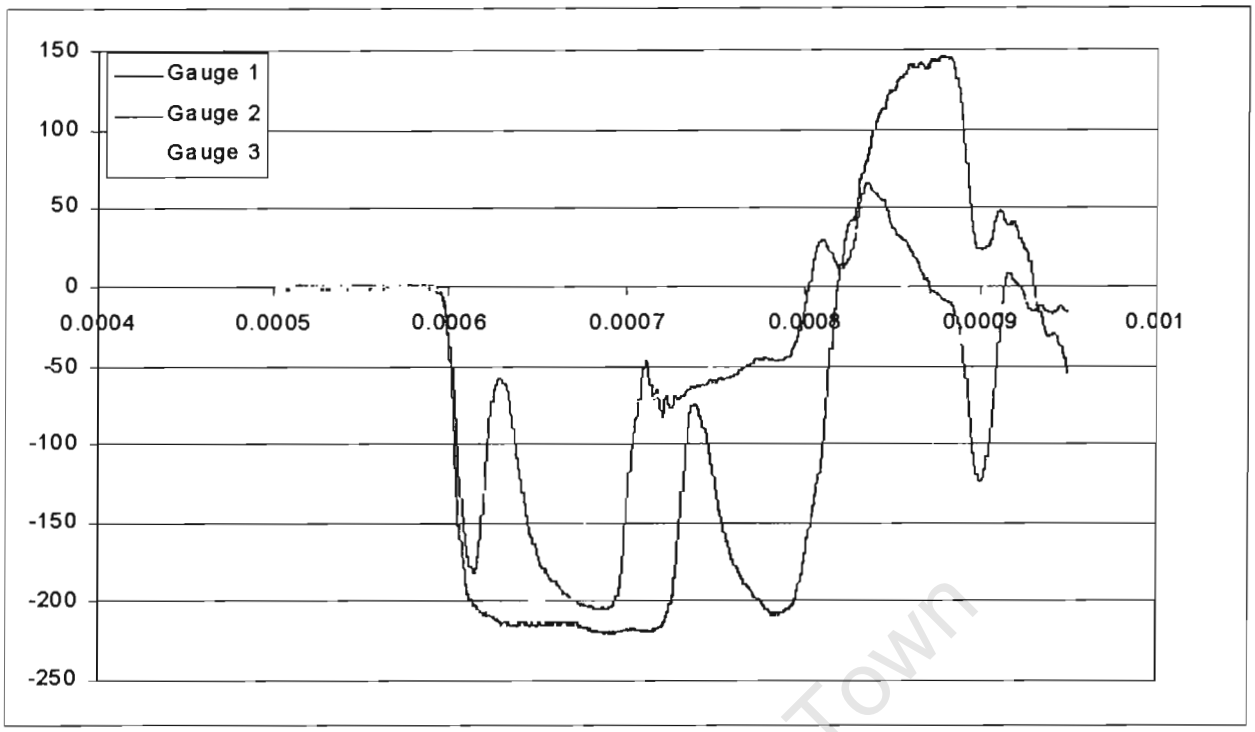

Figure 4.9: A time synchronised plot from a Hopkinson test showing readings obtained from gauge 1,2 and 3 versus time.

4.3.4. DATA ACQUISITION

The data measured during testing were recorded using PC based data acquisition equipment capable of recording data at frequencies up to 20 MS/s (Mega-Samples/second). The following data were acquired during testing

- Tests at quasi-static loading rates
    - Total resisting force as a function of time (using a 10 kN load cell),
    - Extension of a chosen parallel gauge length as a function of time (using LVDT);

- Tests at medium loading rates
    - Total resisting force as a function of time (instrumented short bar),

- Extension of a chosen parallel gauge length as a function of time (LVDT);

- Tests at high rates of loading
  - Strains in the cross section of the instrumented loading bar as function of time (instrumented loading bars).

4.3.5. DATA ANALYSIS

The data obtained from the experimental tests are in the form of analogue signals. These results need interpretation for use in analytical/numerical analyses concerned with the prediction of mechanical behaviour of the FRP materials subjected to the various loading conditions, viz. compression, shear and tension loadings.

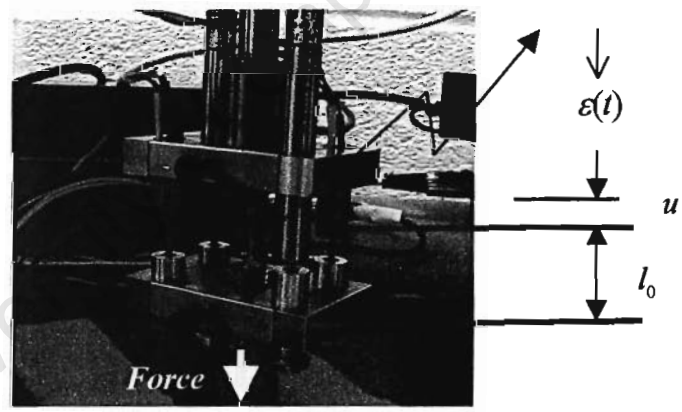

Figure 4.10: Quasi-static and medium rate uniaxial tensile test giving force-extension measurements showing the direction of the applied force, the original specimen length (l_0), the displacement (u) and the strain as a function of time.

In the experimental programme concerning compressive, shear and uniaxial tensile loading, a set of calibrated load cells and extensometers were used in tests with quasi-static and medium rate loading thus providing the relationship between the measured analogue electrical signals for the force and extension, respectively (Figure 4.10).

In the case of experiments at high strain rates by means of the SHPB apparatus the analogue electric signals obtained from calibrated strain gauge signals on the loading bars were used for obtaining both resisting force and specimen extension using the one-dimensional stress wave analysis [103]. As a result, force-extension curves were obtained directly using the calibration factors following each experiment.

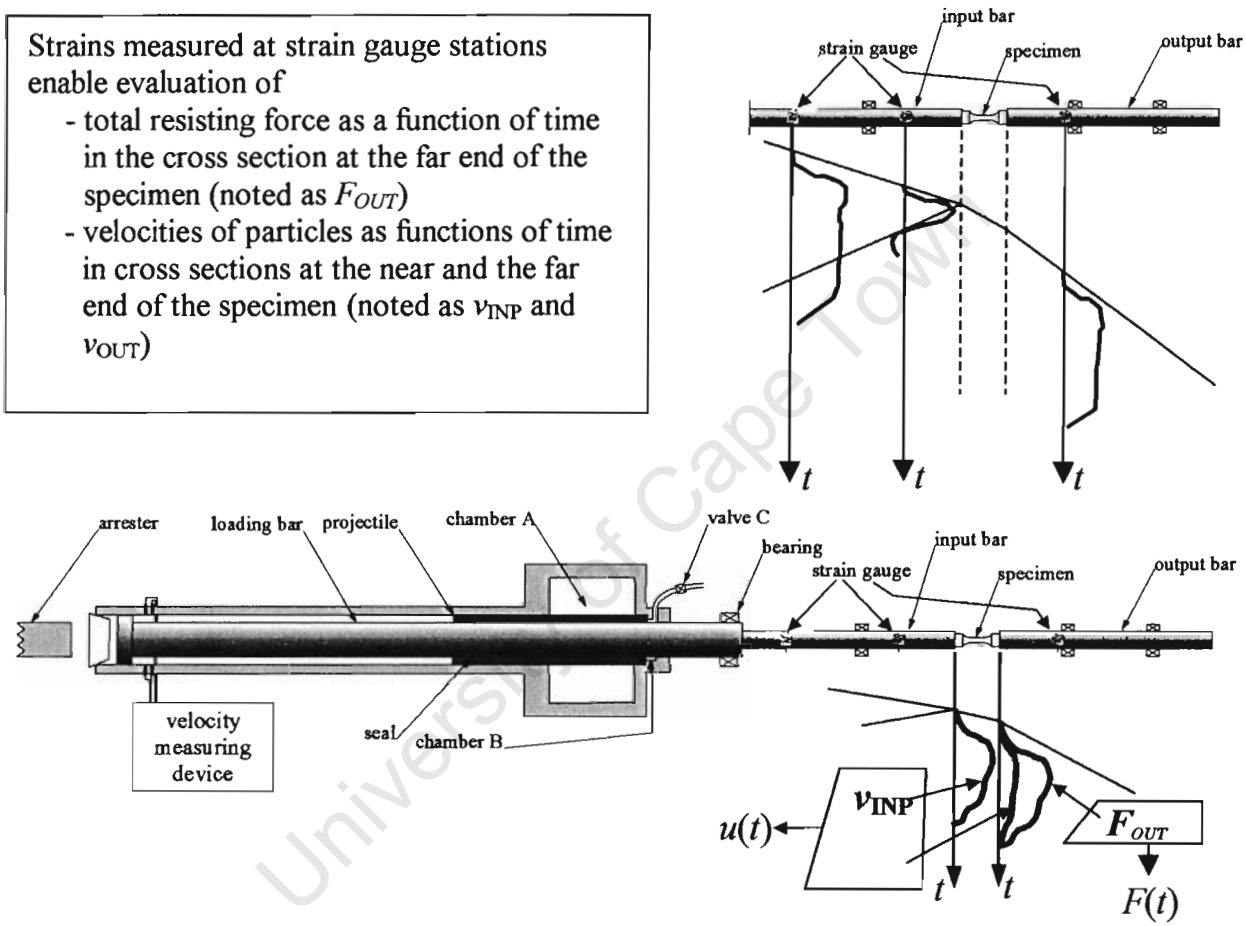

Figure 4.11: Diagrammatic representation of measurements at high rates of strain showing the incident, reflected and transmitter pulses.

Finally, the obtained force-extension data were used to provide nominal stress-strain curves by taking into account the initial cross-section area and gauge length of the specimens under consideration. In addition strain gauges on the specimen surfaces were used to measure strains directly, since neither the extensometers employed could provide the required level of accuracy of strain measurements at small strains. The use of strain gauges is essential in experiments with

materials whose strain to failure are as low as those observed in GFRP and CFRP composite materials. The extensometers were used to measure extensions beyond the limit of the surface strain gauges thus providing values of strain to failure.

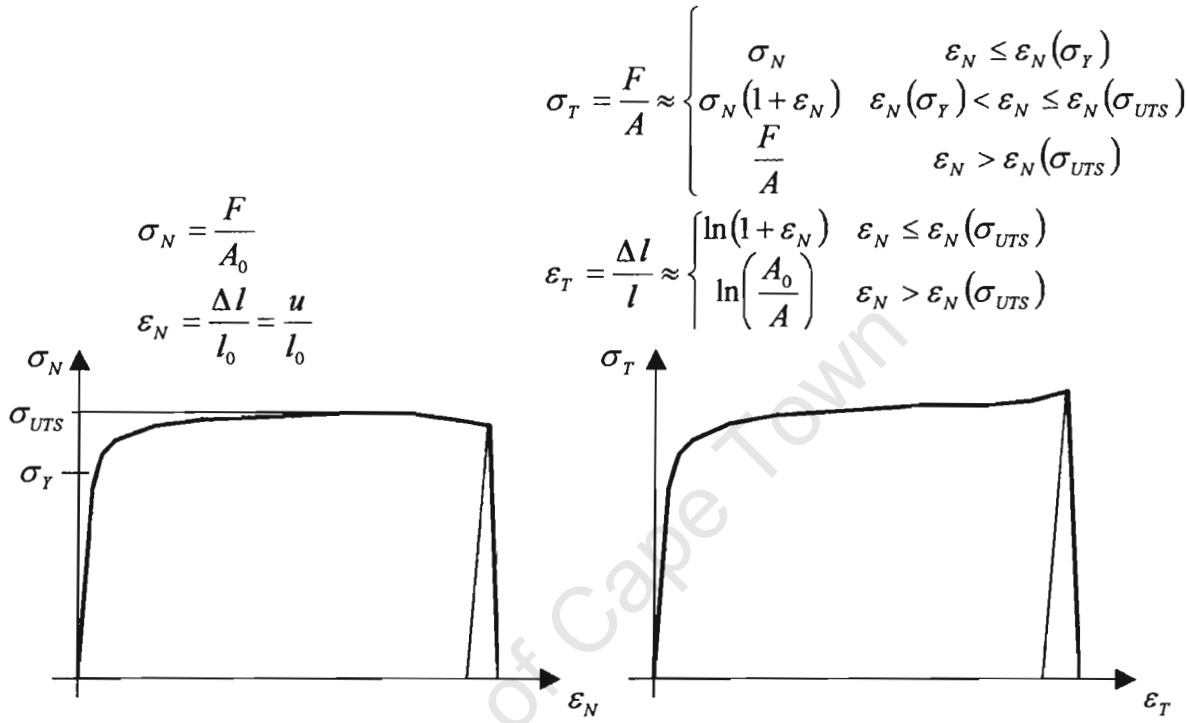

Figure 4.12: Uniaxial tensile test: evaluation of stress-strain relationship showing the yield, ultimate and nominal stresses. The conversion equations from nominal to true stress and strain are also presented.

4.3.6. STRAIN GAUGE CONSIDERATION

Due to the poor thermal dissipation normally associated with FRPs, the strain gauges heat up as soon as they are connected into the circuit. This can gravely affect the readings taken from the strain gauges. Therefore the first step in reducing these thermal effects, is to connect the gauges into the circuit prior to testing. Secondly, if the temperature changes between the time of the unstrained and strained readings, errors incurred can be seen from the strain plot. These errors are in the form of a strain offset. Therefore the method used in this case employs "dummy" gauges

mounted on the same materials, CFRP and GFRP specimens, accordingly. The "dummy" or inactive gauges are subjected to the same ambient temperatures as the active gauges. The active pair accompanied by an inactive pair connected into the circuit form a Wheatstone bridge (see Figure 4.13). The configuration used in the tests consisted of two 0° - 90° rosettes.

Resistors one (R1) and three (R3), in Figure 4.13, are located on the specimen to be tested. The reference or "dummy" resistors, two (R2) and four (R4), are located on the unstrained composite specimen. During the test, the gauges all experience the same strain due to thermal expansion, however, only the gauges on the specimen record the strain from extending the specimen. The Wheatstone bridge arrangement allows the thermal effects to be negated and only the actual strain in the specimen is recorded.

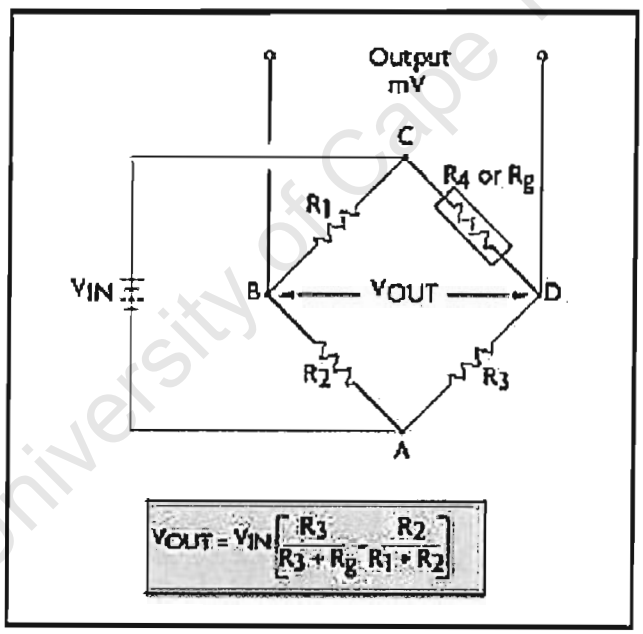

Figure 4.13: Full Wheatstone bridge used for temperature compensation effects during testing.

4.4. MEASUREMENT OF STRAIN TO FAILURE

4.4.1. COMPRESSION TESTING

The strain to failure is measured by attaching strain gauges on the specimens. The overall specimen length limits the use of strain gauges for measuring strain. It was found that any impact of the compression specimens results in premature damage of the strain gauge before the compression specimen has undergone complete loading.

4.4.2. SINGLE LAP SHEAR TESTING

The single-lap shear specimen strain values were measured using ±45° strain gauge rosettes mounted on the specimens to determine the magnitude of strain to failure under single-lap shear loading. The shear bands are expected to be extremely localized, therefore gauges with the shortest available gauge length were used. Secondly the inclusion of strain gauge rosettes confirmed that the specimens were indeed under a state of pure shear. This is due to the strain gauge output showing signals of equal magnitude in opposite directions, $\varepsilon_{+45} = -\varepsilon_{-45}$.

4.4.3. TENSILE TESTING

In order to determine various material properties such as the elastic modulus, as well as to validate the strain readings under uniaxial tensile testing conditions, various strain gauge readings and calculations were undertaken. For example, at quasi-static loading conditions the elastic modulus in the fibre direction (E_1) for unidirectional CFRP is presented in the stress-strain curve in Figure 4.14. Both the strain gauge and the elongation sensor readings depicted in the graph in Figure 4.14 gave a good correlation. The elastic modulus for CFRP was found to be 123±2 GPa.

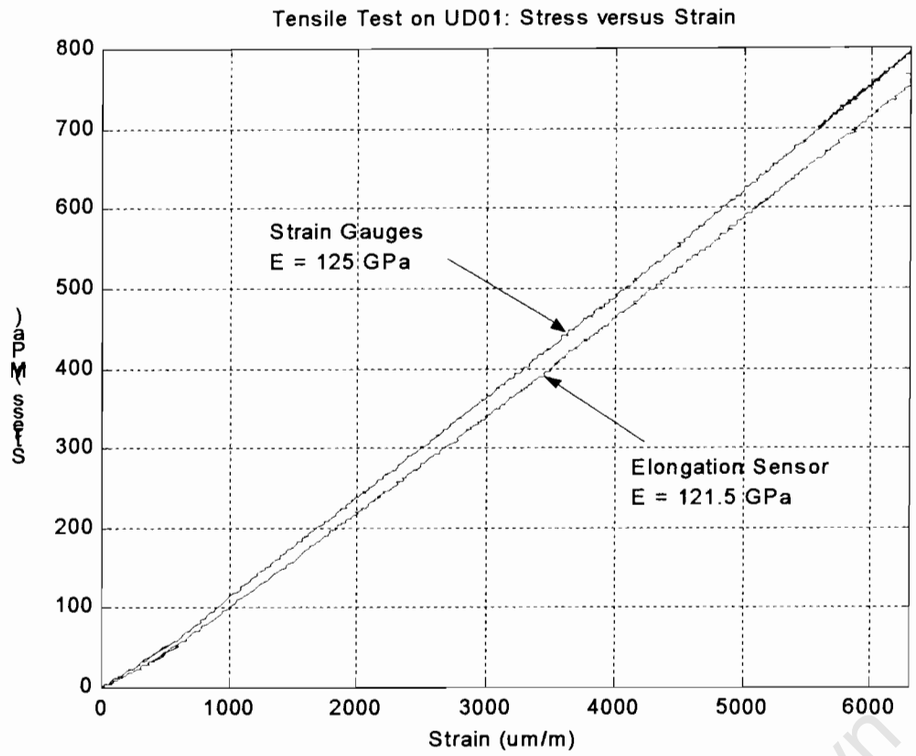

Figure 4.14: Stress-strain graph showing strain gauge and elongation sensor readings used to determine the elastic modulus in the fibre direction (E_1) for CFRP under tensile quasi-static loading.

A strain gauge rosette was also used to determine the Poisson ratio of the CFRP and GFRP specimens. In this case the Poisson ratio for CFRP is determined by plotting a graph of the strain gauge reading in the transverse direction against the strain gauge reading in the longitudinal direction in Figure 4.15. The Poisson's ratio was determined by equation (4.4):

$$\gamma_{12} = -\frac{\varepsilon_{22}}{\varepsilon_{11}} \tag{4.4}$$

γ_{12} is the Poisson's ratio in the 12-plane ε_{22} is the transverse strain gauge reading and ε_{11}, the longitudinal strain gauge reading.

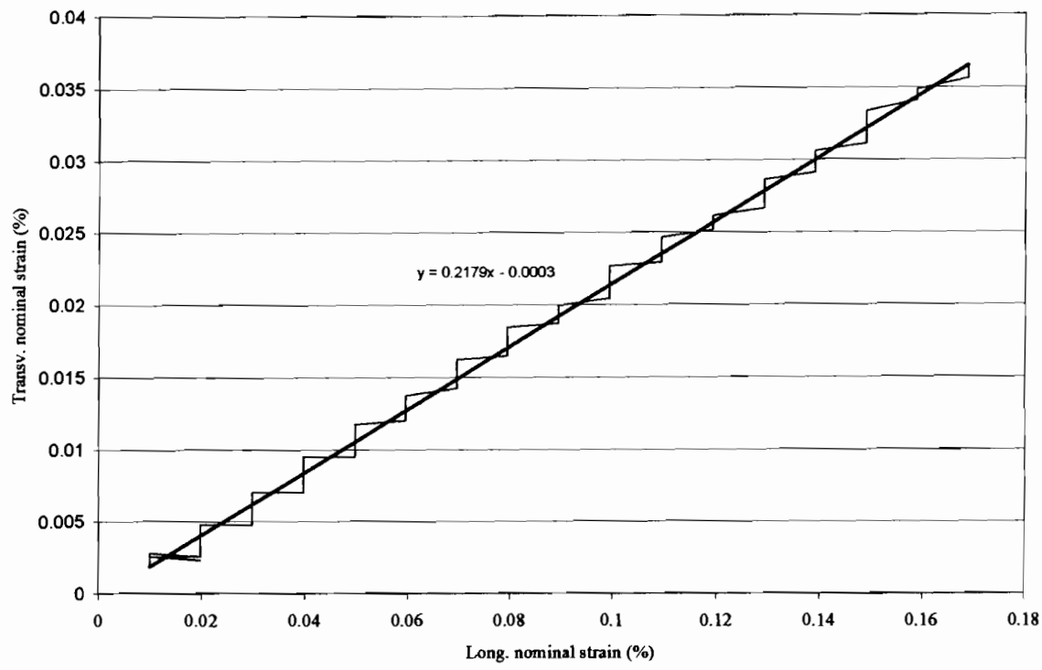

Figure 4.15: Transverse nominal vs. longitudinal nominal strain from the strain gauge at quasi-static loading, with a best fit curve to determine the gradient of the curve.

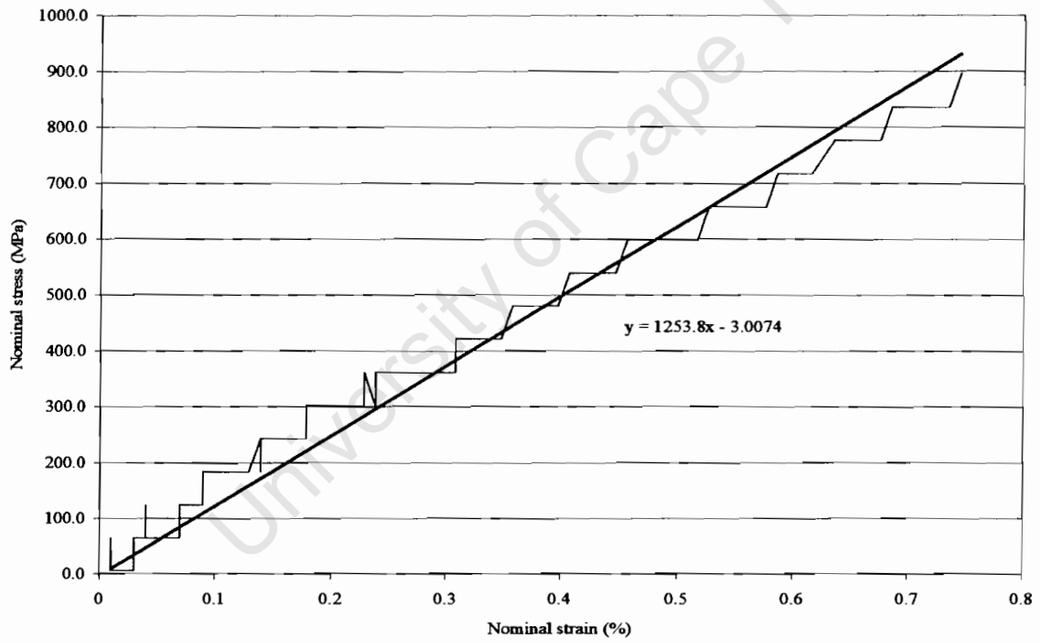

Figure 4.16: Nominal stress vs. nominal strain for CFRP at high strain rates.

Figure 4.16 depicts the nominal stress against nominal strain for CFRP derived from the strain gauges placed on the specimen. The best-fit curve drawn through the data points gave a modulus of 125.4 GPa for the CFRP specimen. This value obtained at high strain rates correlates well with the elastic modulus of 123 GPa derived earlier for quasi-static strain rates.

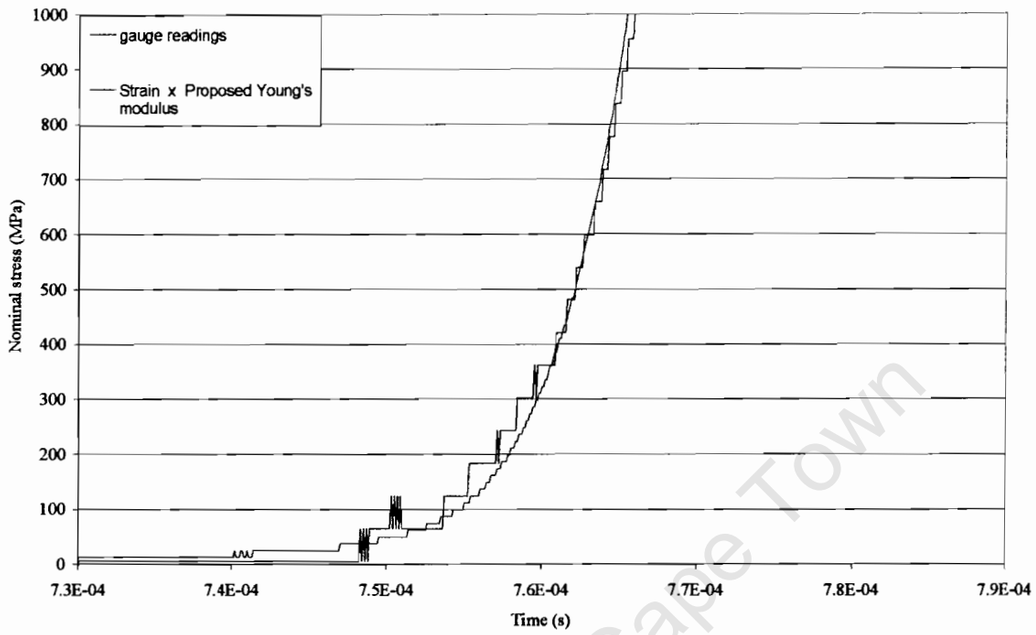

Figure 4.17: Nominal stress vs. time comparing the strain gauge reading to strain multiplied by the proposed elastic modulus.

A graph of nominal stress against time for CFRP loaded at high strain rates (10^3 s^{-1}) is shown in Figure 4.17. The SHPB strain readings are from the strain gauges attached to the bars. With this in mind the strain, as given by the strain gauges may be used to compare the nominal stress recorded by the strain gauges on the specimens. This is done by shifting the wave in the strain gauge reading from the output bar to the specimen bar interface. The strain (ε) value is then multiplied by a chosen Young's modulus ($E_{Proposed}$) shown in Figure 4.17, to determine the nominal stress value (σ_{nom}).

$$\sigma_{nom} = \varepsilon E_{proposed} \quad (4.5)$$

The strategy employed confirms that the strain gauge reading from the strain gauges attached to the output bar multiplied by the Young's modulus should give the same stress results as the nominal stress deduced from the strain gauges on the specimen. The elastic modulus that best achieves this relationship will therefore be the elastic modulus of the material. In this case the value the elastic modulus ($E_{Proposed}$) is 125 GPa, shown in Figure 4.17.

4.5. PLATE IMPACT EXPERIMENTAL SET-UP

4.5.1. THE GAS GUN

In order to realise a defined impact process on the FRP plates, the gas gun (Hopkinson device) set-up shown in Figure 4.18 was used. This device allows the impact of a titanium bar with a hemispherical tip on the FRP plates, which were vertically supported by a long brass tube that rest on bearings to ensure minimal friction during movement of the tube.

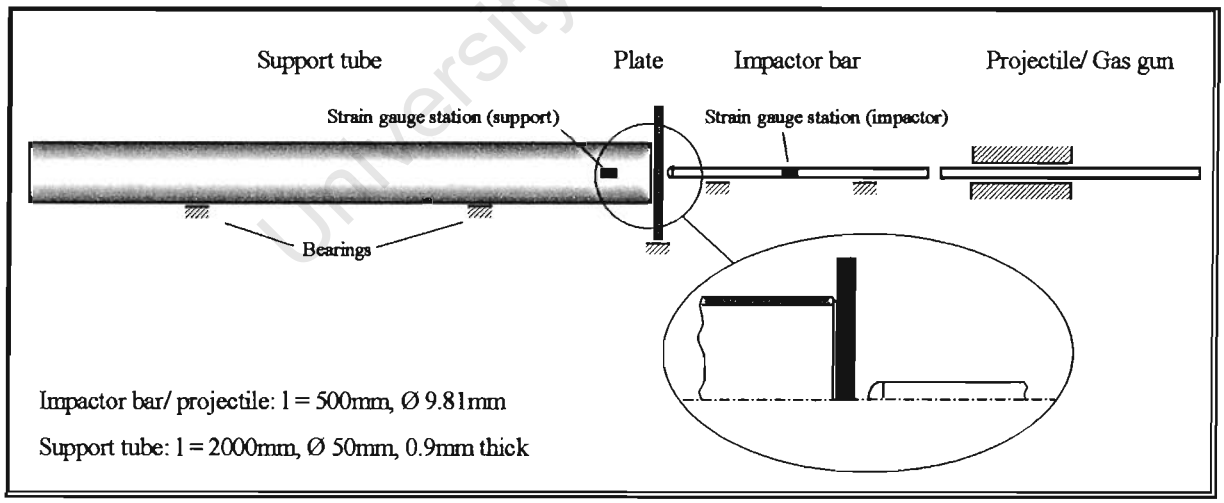

Figure 4.18: Schematic of the Hopkinson device as used to test the plate impact of the FRP materials.

A projectile of a certain mass (m) driven by high air pressure, hits the impactor bar also of mass m. The principal of using the same mass bars is to ensure the "complete" transfer of kinetic energy from the projectile to the impactor bar. The impactor bar will thus hit the FRP plate causing it to deform. This deformation of the plate results in a backward movement of the support tube (see Figure 4.18).

In this case only two strain gauge stations are in used for data acquisition compared with the characterization set-up at high strain rates where three strain gauge stations record the data. One gauge is placed at the centre of the impactor bar in the axial direction (see Figure 4.19), another set of four gauges is placed in parallel around the support tube 100 mm away from the ring in the axial direction as well. The initialised axial strain within the bar and support were recorded by the strain gauges and transferred into voltage using an uncompensated Wheatstone bridge. A trigger rate of 1 MHz was used. The re-calculation of the time dependant voltage signal *V (t)* into a force signal is done by multiplying *V (t)* with a calibration factor *f* (units of N/V).

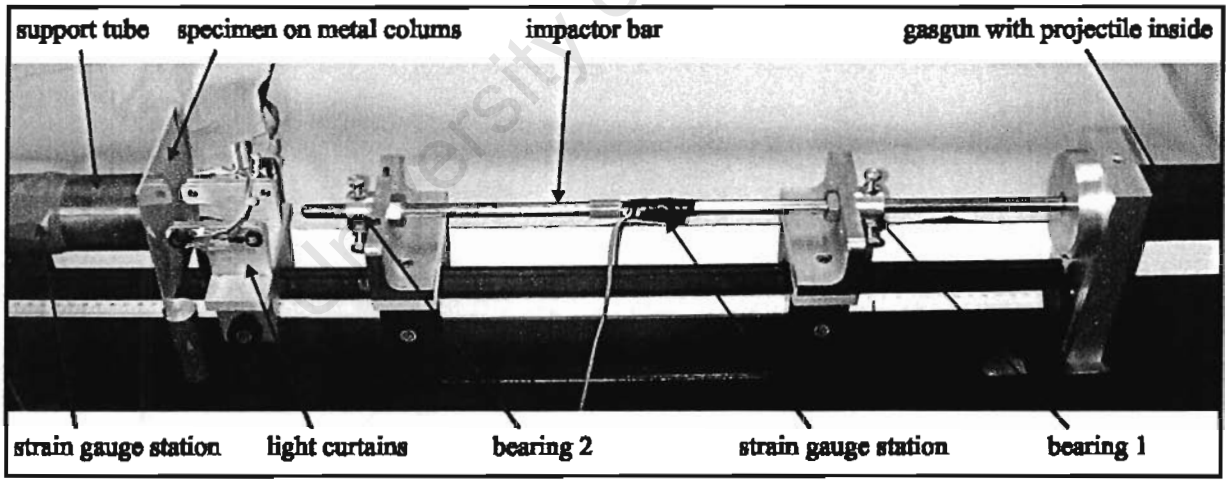

Figure 4.19: Overview of individual components that make up the Hopkinson device as used for plate impact.

4.5.2. ENERGY BALANCE CALCULATION

There are two ways of calculating the dissipated energy in the FRP plates from the Hopkinson impact set-up:

- using an energy balance calculation
- calculate the area under a force-deflection curve

By calculating the kinetic and initial energy of both impactor bar and support tube an energy balance can be drawn and the dissipated energy as a result of damage can be determined. From the recorded strain gauge signals $V_{I(t)}$ and $V_{S(t)}$, the acting forces can be obtained by:

$$F^{V}_{I/S} = f_{I/S} V_{I/S(t)} \tag{4.6}$$

where the subscripts V, I and S represent the voltage signals, the impactor bar and support tube.

The stress at the strain gauge station is given by:

$$\sigma^{V}_{I/S} = F^{V}_{I/S} A_{I/S(t)} \tag{4.7}$$

The values for $\alpha(t)$ and $\beta(t)$ for every x-position on the impactor bar and the support tube are given by the 1D wave theory described in chapter 3. The stress and velocity at any position and time can be found using equations (4.8) and (4.9) derived earlier in chapter 3:

$$\sigma = \beta + \alpha \tag{4.8}$$

$$\rho c v = \beta - \alpha \tag{4.9}$$

A description of the contemplated system is given in the following diagram:

Situation t_0=0

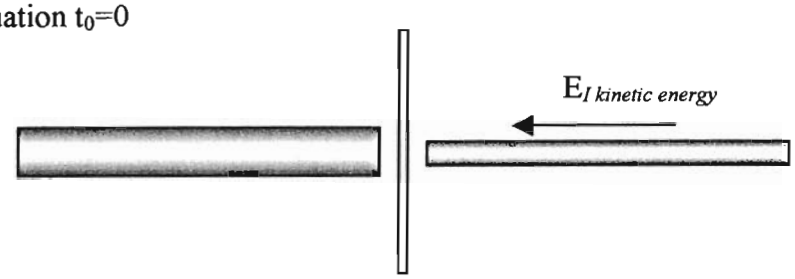

Situation t_1=0.005s

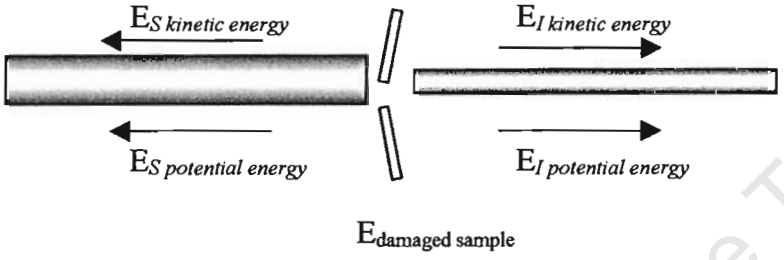

$E_{damaged\ sample}$

Figure 4.20: Schematic of the contemplated system depicting the direction of the kinetic energy before impact. The direction of the potential energy and the energy from damage to the specimen after impact are also depicted.

It is assumed that the frictional forces between the impactor bar and the rod, as well as between the support tube and rod are insignificant during the contemplated time interval of around 0.005s. If is assumed that the impact bar is free from elastic stresses before it hits the sample (recorded stress waves are separated by filtering the raw data), the kinetic energy can be easily calculated using:

$$E_{I\ kinetic\ energy} = \frac{m_I}{2} v_I^2 \tag{4.10}$$

where the velocity (v) is determined using the light curtain readings as follows:

$$v_I = \frac{\Delta x_{light\ curtains}}{\Delta t_{light\ curtains}} \tag{4.11}$$

where $\Delta x_{light\ curtains}$ is the distance between the light curtains and $\Delta t_{light\ curtains}$ is the time the impact bar takes to travel between the light curtains.

During the impact event the tip of the impactor hits the sample, the stress waves travel through the specimen, part is reflected at the impact bar specimen interface and part will travel through to the support tube. The stress waves travels at different velocities depending on its position x along the bar or support tubes at certain time intervals. Therefore, the instantaneous kinetic energy values may be calculated using:

$$E_{I/S(t)\,kinetic\,energy} = \frac{m_{I/S}}{2}\left(\frac{\int_0^l v_{I/S(x,t)}dx}{x}\right)^2 \tag{4.12}$$

In order to determine the overall kinetic energy in the system, the bar/tube is divided numerically into n numbers of partitions (see Figure 4.21). This enables the calculation of the overall kinetic energy of the bar/tube support at a certain time t. The summation is thus deduced using the equation:

$$E_{I/S(t)\,kinetic\,energy} = \frac{m_{I/S}}{2}\left(\frac{\sum_{i=0}^{n} v_{i\,I/S(t)}}{n}\right)^2 \tag{4.13}$$

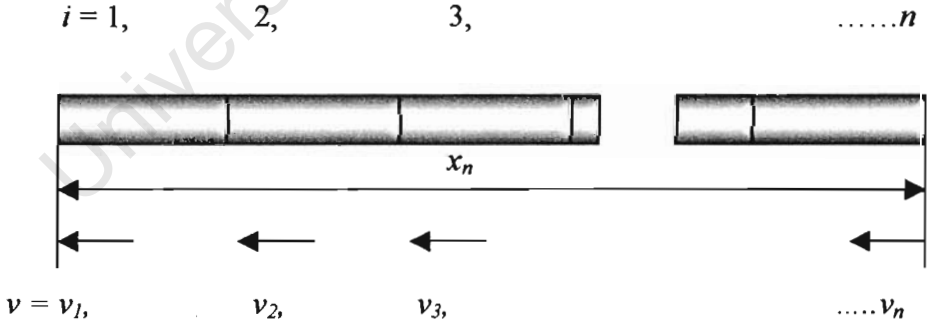

Figure 4.21: Numerically divided bar/tube in order to determine the overall velocity in the system.

The velocity for each partial mass at a particular time t can be calculated as

Impactor bar: $v_{iI(t)} = v_{0I} - (\alpha^{T}_{t-\Delta t(x)} - \beta^{T}_{t+\Delta t(x)})/\rho c$ with $\Delta t(x) = \frac{x_i^2}{c_I l_I}$ (4.14)

Support tube: $v_{iS(t)} = (\alpha^{R}_{t-\Delta t(x)} - \beta^{R}_{t+\Delta t(x)})/\rho c$ with $\Delta t(x) = \frac{x_i^2}{c_S l_S}$ (4.15)

with x_i being the position of the mass element along the bar/tube; c_I / c_S is the characteristic wave speed of the materials and l_I / l_S the length of the bar/tube. The contemplated bars are of homogeneous mass and geometry. The mean bar/tube velocity is calculated as an average value of the defined partitions as given in equations (4.14) and (4.15). The second part of the contributed energy is stored as potential energy in the bar and tube.

The stress values are therefore given by:

Impactor bar: $\sigma_{iI(t)} = \alpha^{T}_{t-\Delta t(x)} + \beta^{T}_{t+\Delta t(x)}$ with $\Delta t(x) = \frac{x_i^2}{c_I l_I}$ (4.16)

Support tube: $\sigma_{is(t)} = \alpha^{R}_{t-\Delta t(x)} + \beta^{R}_{t+\Delta t(x)}$ with $\Delta t(x) = \frac{x_i^2}{c_S l_S}$ (4.15)

An energy balance can thus be calculated by subtracting the values for energy stored in the system from the input energy $E_{I\ kinetic\ energy}$ for each time step:

$$\Delta E(t) = E_{kinetic\ energy} - E_{I\ kinetic\ energy} - E_{S(t)kinetic\ energy} - E_{I\ potential\ energy} - E_{S(t)\ potential\ energy} \quad (4.16)$$

where $\Delta E(t)$ is the released energy from the system. It is important to note when the impactor is in contact with the plate, part of the energy will be stored in the elastic bending. This energy is released when the force of the impactor tip and support tube dissipates.

4.5.3. FORCE-DEFLECTION CALCULATION

The limits for the contemplated system (presented in the last section) used for the energy balance are difficult to define. An alternative method is exists for calculating dissipated energy. A typical contact force over plate deflection for the impactor tip and support tube is presented in Figure 4.22.

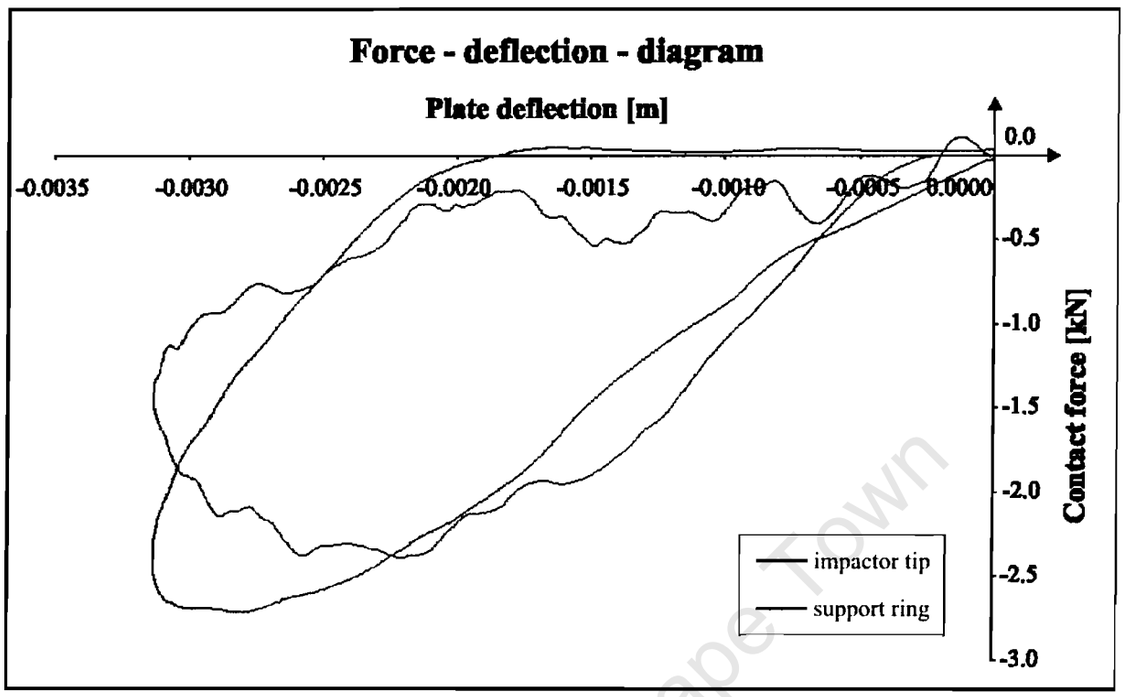

Figure 4.22: Typical force-deflection diagram from impact testing using the Hopkinson device [104].

The general equation for the work of a spring is:

$$W = \int_0^{y_1} F dy \tag{4.17}$$

where W is the emitted energy rate during this cycle of impact and separation from the plate. By neglecting the mass of the plate and assuming it acts as a spring-damper system, the energy value corresponding to the area encased by the function force over deflection is equal on both sides of the system. This may be confirmed using Newton's 2nd axiom:

$$m_1 v_1 + \int F_1 dt = m_2 v_2 + \int F_2 dt \tag{4.18}$$

or in the form

$$\sum \vec{p}_i = p_1 + \Delta p_1 = p_2 + \Delta p_2 = cons\ldots \tag{4.19}$$

where p represents momentum. The values for $W_{I(t)}$ and $W_{s(t)}$ must be equal after a full impact cycle has occurred (see Figure 4.23).

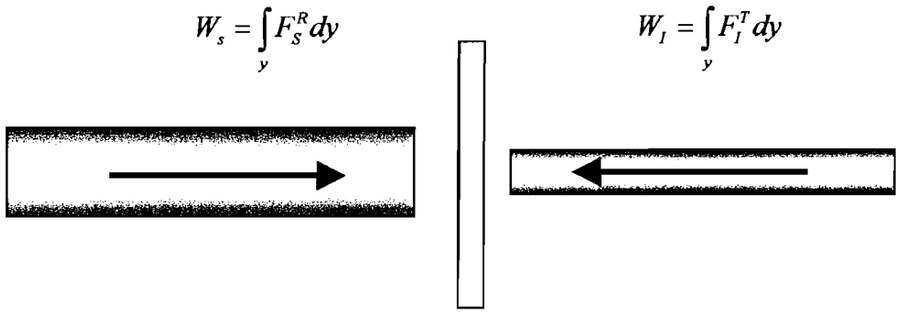

Figure 4.23: The contemplated system for the determination of the emitted energy rate W during impact.

4.6. CONCLUDING REMARKS

The main objective of the compression cylindrical specimen design is to ensure a relatively uniform stress state through the specimen mid-section in order to minimise compressive buckling of the fibres. The single-lap shear specimen design ensures that failure initiates at the notched region and then propagates through the matrix without shearing of any fibres. The material characterization test in tension uses a dog-bone specimen that is thinned in both the longitudinal and transverse directions of the gauge length. Unidirectional specimens designed in this manner fail desirably within the gauge length and not prematurely at the grips. The plate impact set-up uses the force-deflection calculation to determine the behaviour of the FRP systems under plate impact loading conditions.

CHAPTER 5

EXPERIMENTAL RESULTS

The experimental results can be broadly separated into four major groups:

- Uniaxial compression tests to determine the elastic and strength properties
- Single lap shear tests to determine the elastic and strength properties
- Uniaxial tension tests to determine the elastic and strength properties
- Impact testing of FRP plates

The results of these experimental tests are presented in the respective sections of this chapter in which the experimental measurements and observations are discussed in detail.

5.1. DATA PROCESSING PROCEDURES

The results from the quasi-static tests done using the hydraulic testing machine in compression, shear and tension are presented in the form of force-displacement data deduced from the load cell readings. Note that in the case of all the quasi-static stress graphs presented in this chapter, the strain (x-axis) are staggered so as to highlight the peak stress values that represent the ultimate stress. This data is then converted into stress-strain data. In the case of the high strain rate results from the SHPB tests the compression, shear and tensile under went the following data processing procedure. The raw data in the time-synchronized form presented in Figure 4.9 is converted into contraction (in the case of compression loading) velocity versus time using equations (3.5) to (3.27). These equations convert the raw data from the strain gauges into velocity. The strain from the gauges is converted into stress. This stress together with the speed of sound in the bars, c, is used to determine the velocity. The contraction velocity, strain rate and stress versus time for five

CFRP are presented as examples for the data processing procedure shown in Figure 5.1, Figure 5.2 and Figure 5.3, respectively.

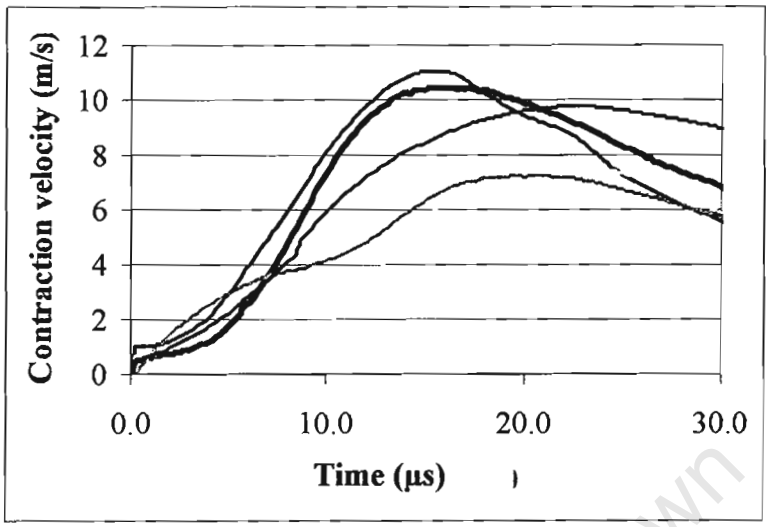

Figure 5.1: Contraction velocity versus time for CFRP under high strain rate loading conditions.

In Figure 5.1, the contraction velocity vs. time data for five compression specimens shows the maximum velocity that range from 7.3 ms^{-1} to 11 ms^{-1}. An average axial strain rate is determined from the impact velocity and the specimen length, as shown in equation (5.1):

$$\dot{\varepsilon} = \varepsilon / t = V / L \qquad (5.1).$$

Therefore, given velocities of 7.3 ms^{-1} and 11 ms^{-1} and a specimen length of 9 mm, the strain rates vary between 811 s^{-1} to 1222 s^{-1}, respectively. The strain rate-time data for the various CFRP specimens tested is presented in Figure 5.2. The stress in the specimen was calculated by multiplying the stress in the (transmitter) bar by the ratio of the area of the bar/area of the specimen. This results in data shown in graphical form in Figure 5.3. The graph shows the dynamic compressive ultimate stress for CFRP as a function of time, varying between 820 MPa to 1380 MPa. The graphs in Figure 5.1, Figure 5.2 and Figure 5.3, are mainly used as initial

loading conditions and input data in the numerical modelling of compression, at dynamic loading conditions. The full data processing procedure is presented in *APPENDIX IV*.

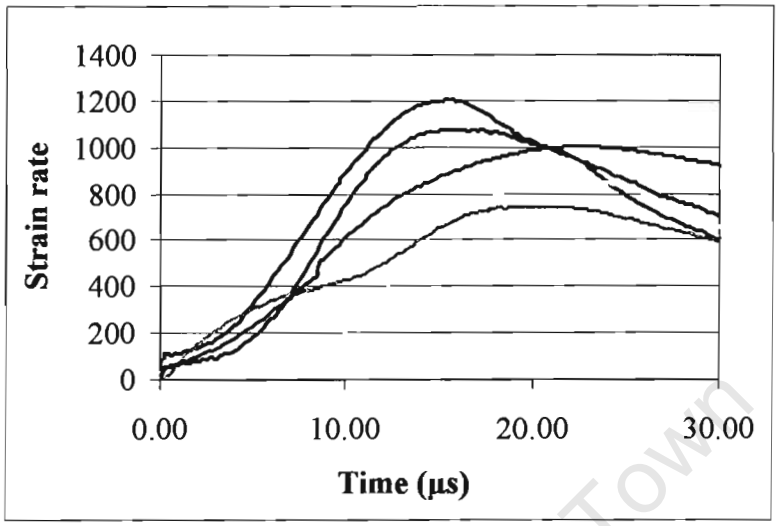

Figure 5.2: Strain rate versus time for CFRP under high strain rate loading conditions.

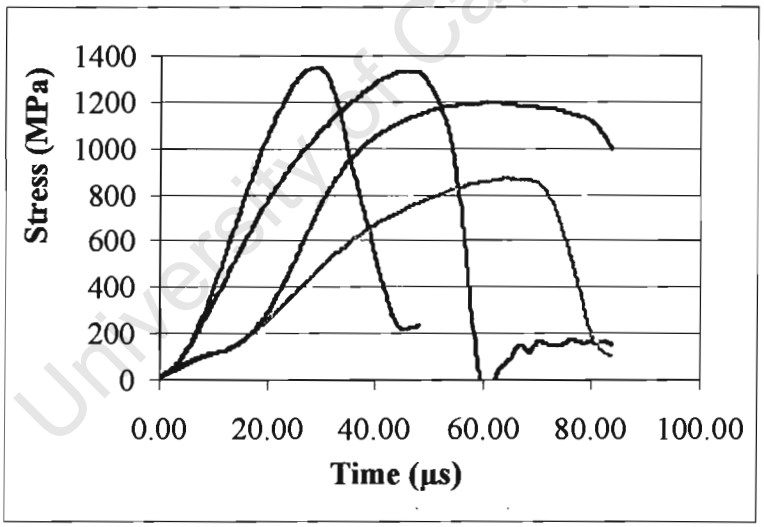

Figure 5.3: Compression stress vs. time from the SHPB apparatus under high strain rate loading conditions.

5.2. UNIAXIAL COMPRESSION TESTS

5.2.1. QUASI-STATIC STRAIN RATES

5.2.1.1. CFRP STRESS-STRAIN BEHAVIOUR

Selected results for CFRP stress-strain behaviour at quasi-static compression loading are presented in Figure 5.4. The curves show linear trends up to failure.

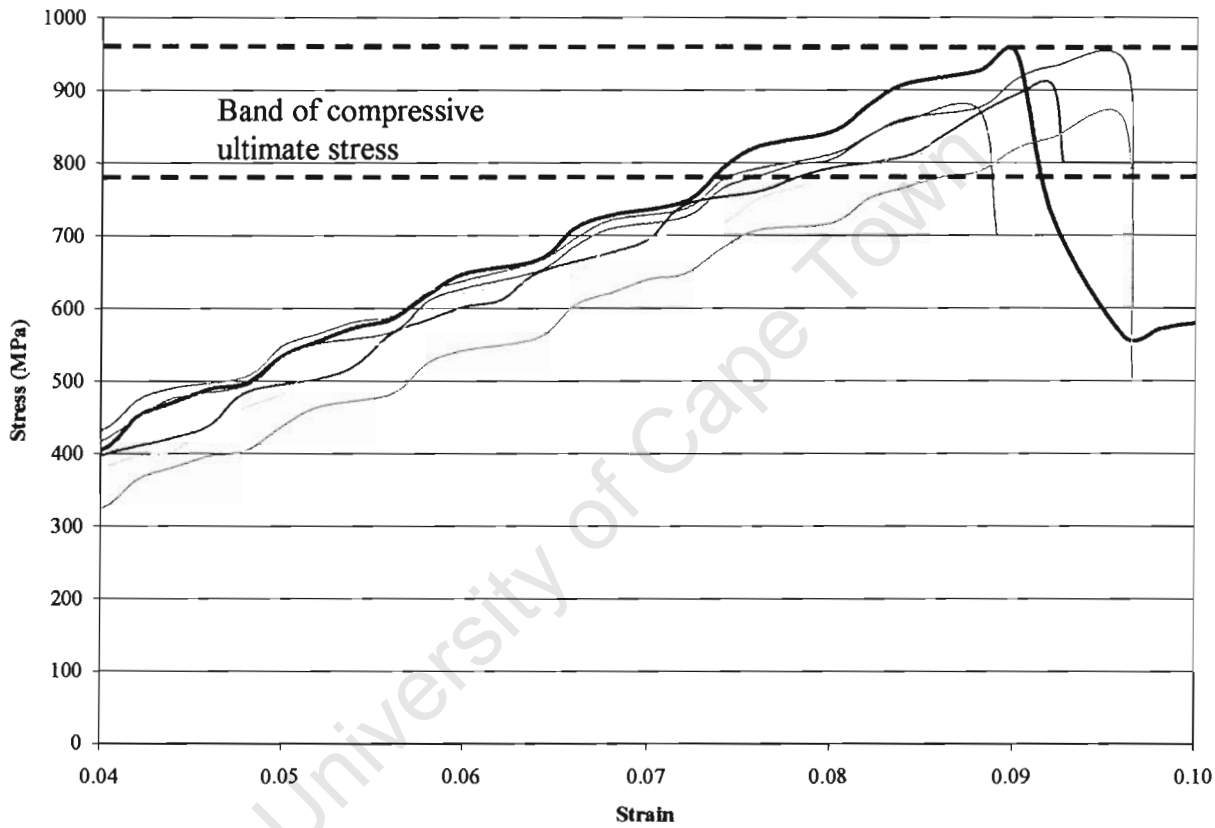

Figure 5.4: Staggered stress vs. strain graphs showing the compressive strengths of 6 CFRP specimens under quasi-static loading. The full results of the 20 specimens tested are presented in APPENDIX V.

The main purpose of the quasi-static compressive tests is to establish a detailed database for the compressive strength of these materials. The graphs in Figure 5.4 shows that a zone of the ultimate compressive strengths of 20 CFRP specimens occur between 791 MPa and 980 MPa. The measurement of the strain to failure under compression loading of the cylindrical specimens

presents difficulties in terms of the accuracy due to buckling and uneven fracture of the compression specimens. This resulted in an uneven strain distribution within the specimen and the attached strain gauge. The thesis focuses on stress based criteria and the relationship with strain rate. The strains to failure values are therefore neglected. The average compressive failure strength was found to be 903 MPa with a standard deviation of 56 MPa resulting in a percentage variation of the mean of 6 %. The compression strength data for the individual CFRP specimens at quasi-static loadings are tabulated in Table 5.1.

Table 5.1: Compressive failure strengths of 20 CFRP specimens under quasi-static loading. Where CCLS00 is the equivalent to carbon compression low strain rate specimen number.

Specimen No.	**Ultimate Stress (MPa)**	**Specimen No.**	**Ultimate Stress (MPa)**	**Specimen No.**	**Ultimate Stress (MPa)**	**Specimen No.**	**Ultimate Stress (MPa)**
CCLS01	951	CCLS06	836	CCLS11	917	CCLS16	868
CCLS02	856	CCLS07	949	CCLS12	1010	CCLS17	939
CCLS03	974	CCLS08	937	CCLS13	866	CCLS18	909
CCLS04	880	CCLS09	941	CCLS14	846	CCLS19	791
CCLS05	975	CCLS10	907	CCLS15	861	CCLS20	855
						Average Stress	903

5.2.1.2. COMPRESSION FAILURE MODES FOR CFRP

Microscopic analysis of the loaded surface (labelled A in Figure 5.5) reveals longitudinal cracks, delaminations and cracks at the matrix interface. These features are seen to extend into the specimen as indicated in Figure 5.5. The brittle nature of the material ensures that the fracture lines propagate along the full depth of the specimen (i.e. in the 3-direction in Figure 5.5). The maximum compressive strength will depend on inducing the appropriate failure process, through ensuring the appropriate material specimen design. The failure process is dependent on the

reinforcement geometry and the direction of loading of the specimen material. Thus the unidirectional CFRP system, which was loaded parallel to the fibres, is seen to fail by longitudinal splitting, matrix cracking and delamination.

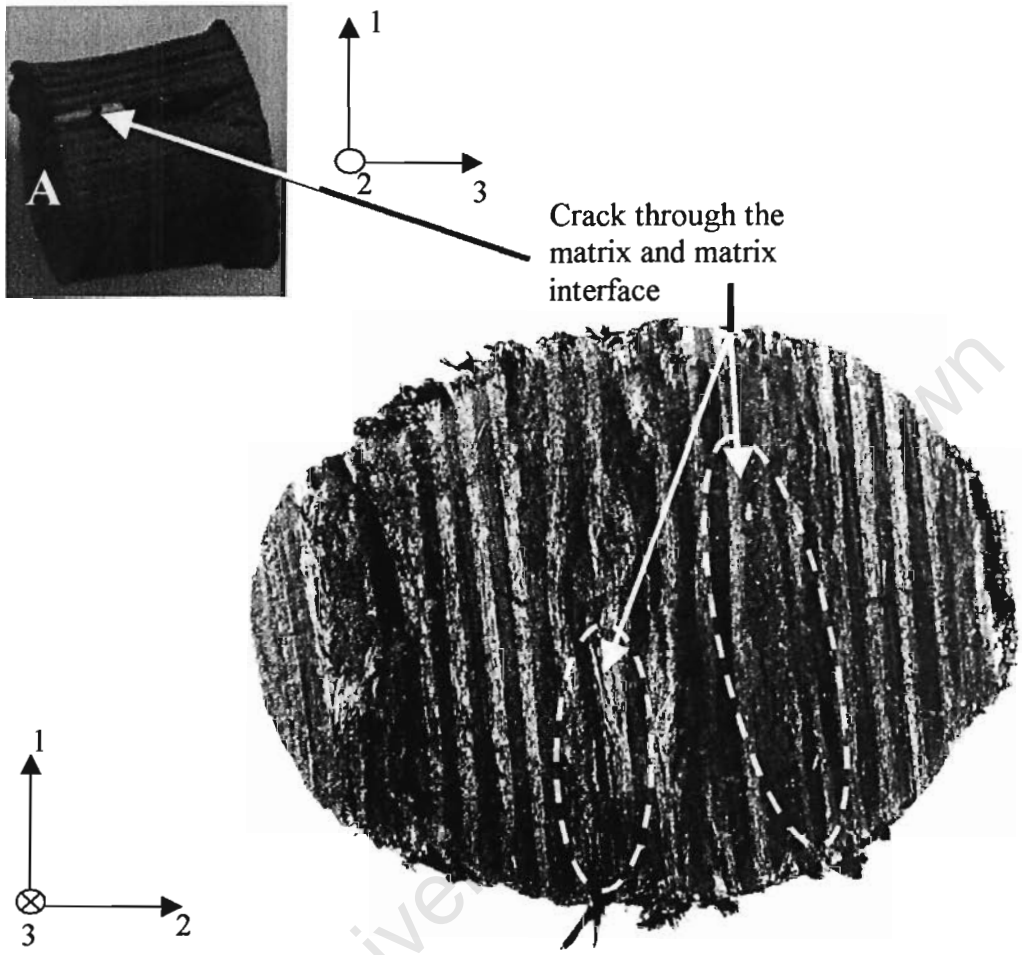

Figure 5.5: Microscopic and visual analysis of the loaded surface of the CFRP specimen showing regions of matrix cracking, delamination failure and debonding.

The longitudinal splitting in the through-thickness direction of the specimen is associated with a plane of weakness or resin rich zone between the individual laminate layers. Figure 5.5 shows irregular matrix thickness along the fibre-matrix interface. The longest crack is seen to propagate through this resin rich zone. This feature appears to be typical of all the CFRP specimens tested at quasi-static strain rates. The modes of failure depicted in Figure 5.5 are triggered by fibre micro buckling, when the individual fibres buckle inside the matrix. The bulking process is controlled

by fibre misalignment, the shear modulus and the shear strength of the CFRP. The main concern with regards to compression testing is to ensure that failure in the specimen is purely due to compression stresses with minimal shear failure.

5.2.1.3. GFRP STRESS-STRAIN BEHAVIOUR

The compressive strength of GFRP lies between 803 MPa and 1060 MPa, shown in Figure 5.6 as the band of compressive ultimate stress. As is the case with CFRP the measurements, the strain to failure under compression loading presented difficulties in terms of the accuracy due to buckling and uneven fracture of the compression specimens. The values of strain are neglected.

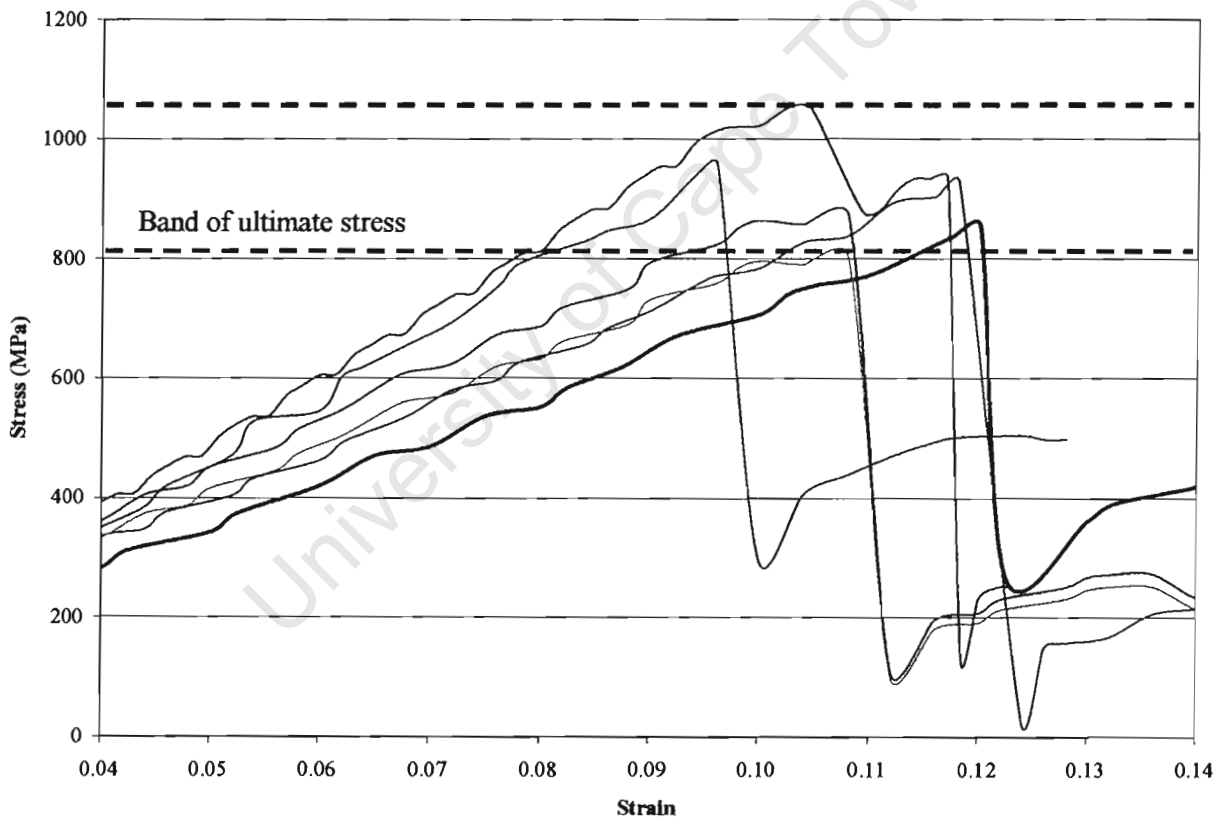

Figure 5.6: Stress vs. strain graphs showing the compressive strengths of GFRP specimens under quasi-static loading. The full results of the 20 specimens tested are presented in APPENDIX V.

The compression strength data for the individual GFRP specimens at quasi-static loading rates are shown in Table 5.2.

Table 5.2: Compressive failure strengths of 20 GFRP specimens under quasi-static loading.

Specimen No.	Ultimate Stress (MPa)	Specimen No.	Ultimate Stress (MPa)	Specimen No.	Ultimate Stress (MPa)	Specimen No.	Ultimate Stress (MPa)
GCLS01	855	GCLS06	1060	GCLS11	809	GCLS16	942
GCLS02	930	GCLS07	939	GCLS12	959	GCLS17	909
GCLS03	883	GCLS08	959	GCLS13	984	GCLS18	879
GCLS04	942	GCLS09	803	GCLS14	856	GCLS19	989
GCLS05	941	GCLS10	837	GCLS15	832	GCLS20	993
						Average Stress	915

5.2.1.4. COMPRESSION FAILURE MODES FOR GFRP

The average compressive strength of GFRP is 915 MPa with a standard deviation of 69 MPa, resulting in a percentage variation of the mean of 7.5 %. Whereas the compression failure of CFRP shows that fibre buckling is the overriding factor dictating the compressive strength of CFRP, the dominant failure in GFRP is a combination of kinking and micro buckling of the glass fibres. The major modes of failure in the GFRP are shown in Figure 5.7. The cylindrical specimen failure is dominated by interfacial splitting and delamination through the thickness of the specimen (3-direction). The non-loaded end (labelled B) appears to mushroom out resulting in multiple interfacial splits existing at the bottom circumference. The GFRP specimens remain intact after quasi-static loading, as compared to the more brittle CFRP. Further analysis of the

fracture surface reveals striations, with multiple delaminations and kinks at the non-loaded end, suggesting a certain degree of ductility as seen in Figure 5.7.

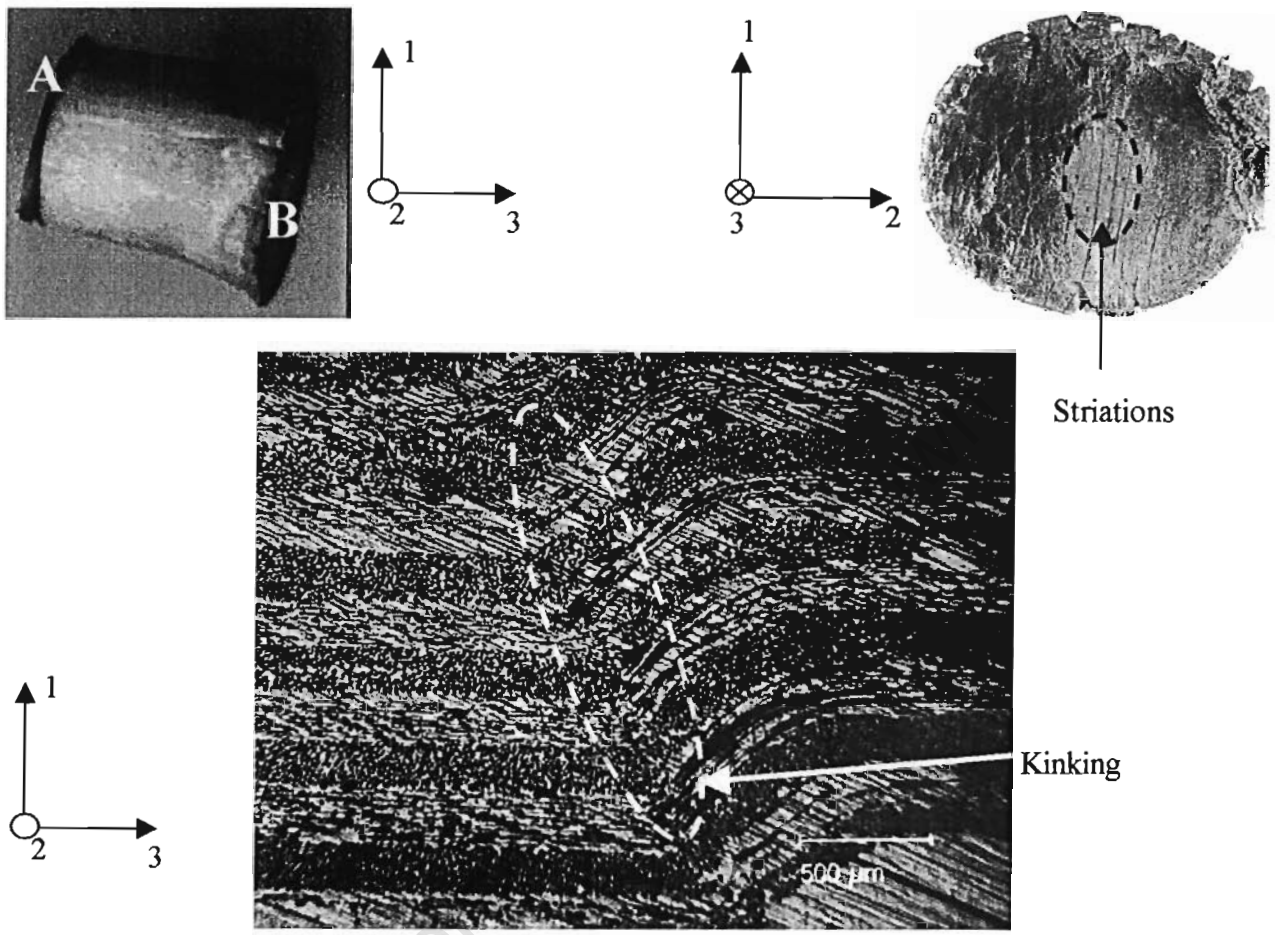

Figure 5.7: Microscopic and visual analysis of the GFRP specimen showing kinking within the specimen. The non-loaded surface of the specimen labelled B shows striations caused by the compression at quasi-static loading rates.

5.2.2. DYNAMIC STRAIN RATES

5.2.2.1. CFRP STRESS-STRAIN BEHAVIOUR

A summary of the results in *APPENDIX V* are presented as stress strain relations in Figure 5.8 for CFRP impacted at varying strain rates. Each line represents a different average strain rate. This section of the experimental procedure focuses on acquiring data on the high strain rate behaviour of CFRP under varying dynamic strain rates. The stress in the graphs are seen to gradually increase and after failure of the specimen, to reduce rapidly. The strain rate varies from 417 s^{-1} to 1359 s^{-1} resulting in increases in stress from 932 MPa to 1429 MPa, respectively.

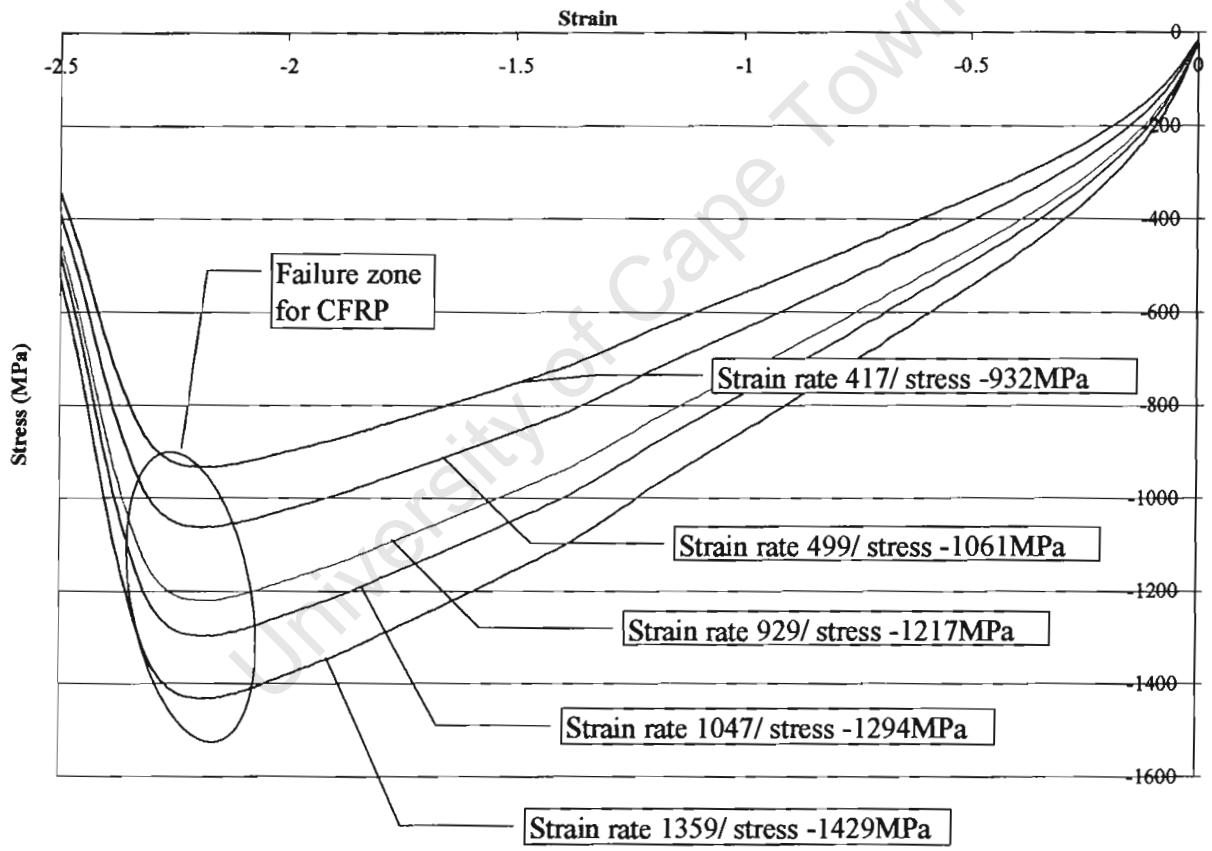

Figure 5.8: Stress vs. strain graph showing the compressive strengths of CFRP specimens under varying dynamic loading conditions.

The compression strength data for the individual CFRP specimens at 20 different high strain rates of loading are tabulated in Table 5.3.

Table 5.3: Average compressive failure strengths of 20 CFRP specimens under varying dynamic loading rates.

Specimen No.	Average Ultimate Stress (MPa)	Specimen No.	Average Ultimate Stress (MPa)	Specimen No.	Average Ultimate Stress (MPa)	Specimen No.	Average Ultimate Stress (MPa)
CCHS01	1025.6	CCHS06	961.6	CCHS11	1275.4	CCHS16	1422.8
CCHS02	1071.2	CCHS07	1133.8	CCHS12	1267.4	CCHS17	1343.2
CCHS03	1010.4	CCHS08	1174	CCHS13	1356.8	CCHS18	1141.8
CCHS04	932	CCHS09	1200.4	CCHS14	1429	CCHS19	1272.4
CCHS05	988.2	CCHS10	1232.2	CCHS15	1351	CCHS20	947.4

5.2.2.2. COMPRESSION FAILURE MODES FOR CFRP

A macroscopic and microscopic examination of the failure mode for the unidirectional CFRP specimens impacted at dynamic strain rates revealed extensive interfacial splitting, debonding and delamination. The CFRP specimen disintegrated into a powder-like form, resulting in retention of approximately 60 % of the initial specimen size. Scanning electron microscopic (SEM) analysis did not reveal any outstanding features. Therefore the light microscope, which is limited by depth of field, was employed to examine the failure modes of the compression specimens. At low magnifications examination of the non-impacted end of the specimens revealed various striations and a large extent of delamination within the specimen core. The post-impact specimen fibres-matrix bundles flaked off along interfacial splitting planes in the fibre direction on minimal contact. The remains of the post-impacted specimen are shown in Figure 5.9. Microscopic and macroscopic analysis of the various compression specimens impacted at dynamic strain rates of 417 s^{-1} to 1359 s^{-1} revealed similar modes of failure. This is despite the gradual increase in compressive failure strength noted with increasing strain rate.

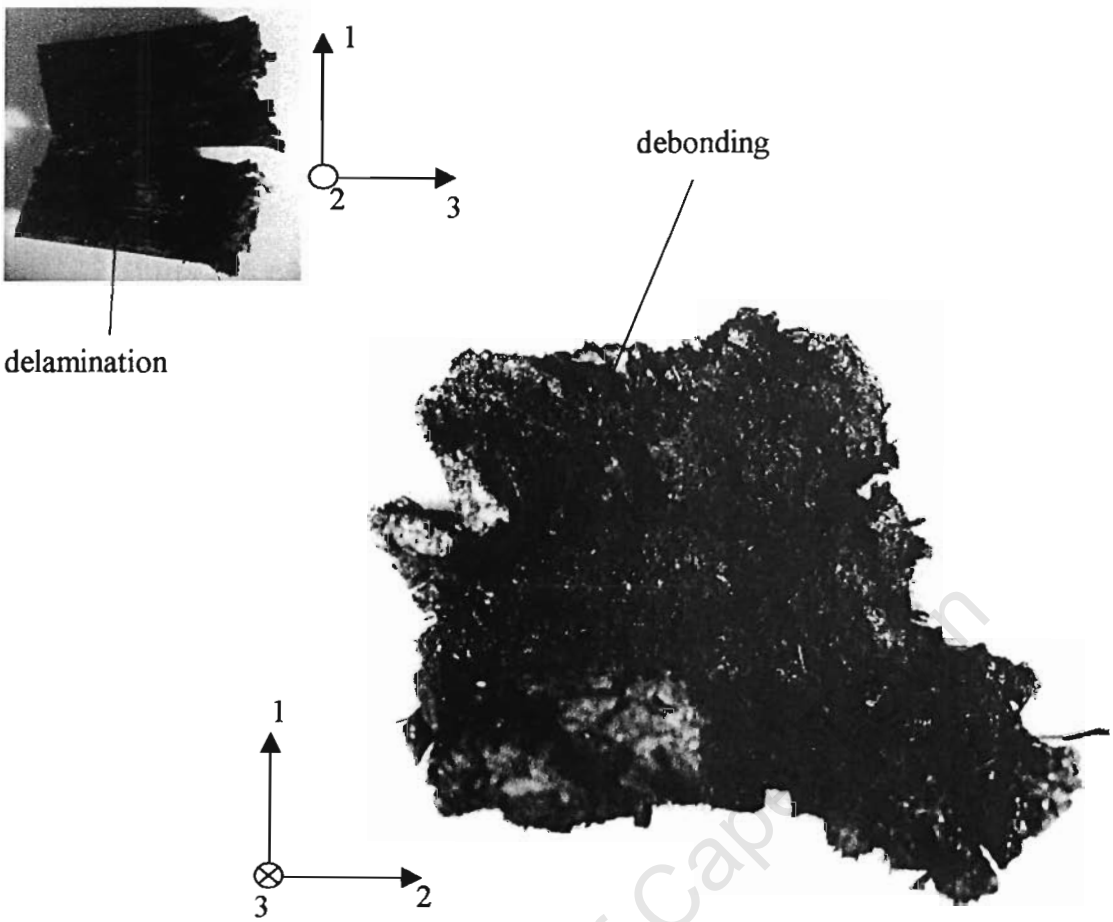

Figure 5.9: Microscopic and visual analysis of the loaded surface of a CFRP specimen showing delamination and debonding.

5.2.2.3. STATISTICAL CONSIDERATIONS OF EXPERIMENTAL RESULTS

The statistical considerations are derived in this section. Any subsequent derivation of constants will follow the procedure laid out in this section. Due to the brittle nature of the FRP materials, variations are expected in the failure strengths recorded from a batch of test data. As a result statistical analysis is performed using a confidence interval (CI) [105]. A CI of 95 % is selected, which is a measure of the degree of reliability of the interval. This means that only 5 % of all samples selected would yield an erroneous interval. An introduction to the procedure for determining the CI is presented as:

$$\overbrace{\bar{X}-1.96\sigma/\sqrt{n}}^{1.96\sigma/\sqrt{n}}\ \bar{X}\ \overbrace{\bar{X}+1.96\sigma/\sqrt{n}}^{1.96\sigma/\sqrt{n}} \tag{5.2}$$

where $\bar{X}$ is the mean value, σ the standard deviation and n the number of sample data points. The area under the standard normal curve between -1.96 and 1.96 is 0.95, a 95 % confidence interval (CI) is therefore evaluated [105]. A concise expression for the interval is given in equation (5.3):

$$\bar{X} \pm 1.96 \cdot \sigma / \sqrt{n} \tag{5.3}$$

where (–) gives the left endpoint or lower limit and (+) gives the right endpoint or upper limit. The following statistical procedures for determining the CI for the various material characterization tests are given in the subsequent individual sections.

5.2.2.4. DERIVATION OF CONSTANTS FOR CFRP IN COMPRESSION

The data given in *APPENDIX V* is developed into graphical form shown in the stress-strain rate graph in Figure 5.10. The determination of a 95 % CI for the true average of the compressive strengths for CFRP at quasi-static to dynamic loadings gives $\bar{X}$, σ and n values. The resulting relationships are developed for the upper (equation (5.4)), median (equation (5.5)) and lower (equation (5.6)) curves, respectively.

$$\sigma'_{0\,upper} = 0.0002\dot{\varepsilon}^2 + 0.2\dot{\varepsilon} + 903 \tag{5.4}$$

$$\sigma'_{0\,median} = 0.0002\dot{\varepsilon}^2 + 0.2\dot{\varepsilon} + 887 \tag{5.5}$$

$$\sigma'_{0\,lower} = 0.0002\dot{\varepsilon}^2 + 0.2\dot{\varepsilon} + 872 \tag{5.6}$$

where σ'_0 = compressive strength and $\dot{\varepsilon}$ = strain rate.

Recalling Cowper and Symonds suggested constitutive equation in chapter 3:

$$\dot{\varepsilon} = D\left(\frac{\sigma_0'}{\sigma_0} - 1\right)^q \tag{5.7}$$

This equation is written in logarithmic form to resemble the equation of a linear graph, y = mx + c, therefore:

$$\log_e \dot{\varepsilon} = q \log_e \left(\frac{\sigma_0'}{\sigma_0} - 1\right) + \log_e D \tag{5.8}$$

where $\log_e \dot{\varepsilon}$ is plotted against $\log_e \left(\frac{\sigma_0'}{\sigma_0} - 1\right)$ with the gradient and intercept given by q and $\log_e D$, respectively.

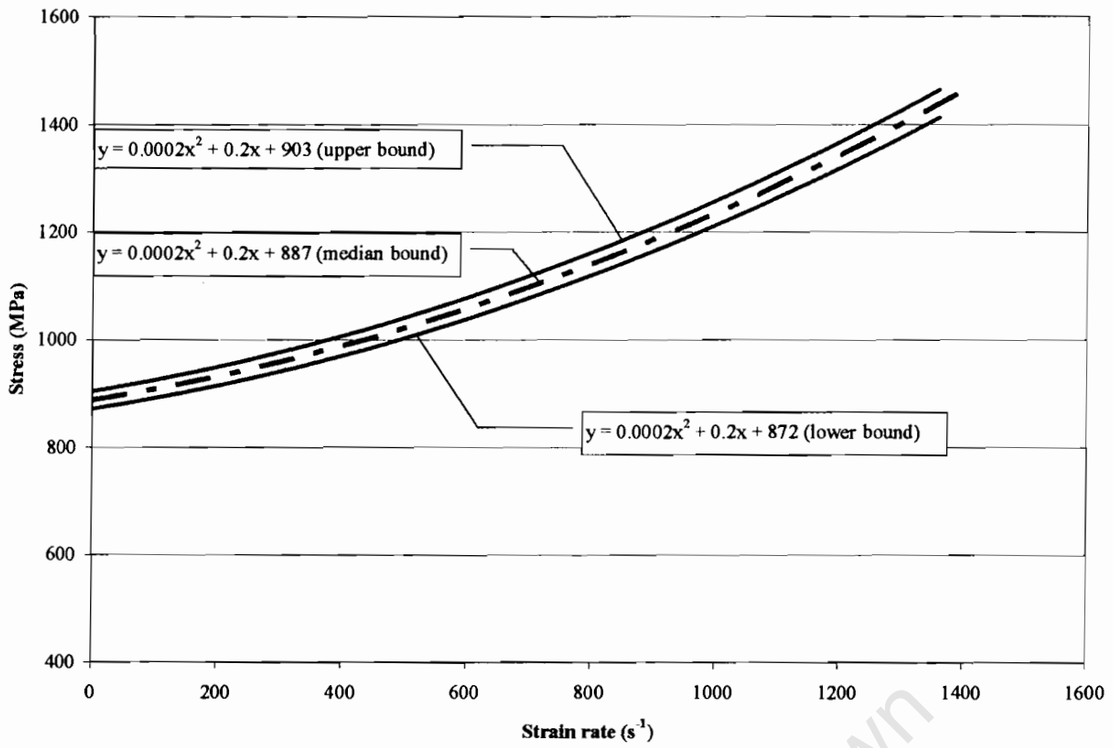

Figure 5.10: Stress versus strain rate graph for CFRP showing the relationship from quasi-static to dynamic strain rates.

The upper, median and lower curves in Figure 5.10 are converted using equation (5.8). This conversion results in three straight-line graphs, which overlap each other. They have the following relationship (which is in the form of an equation of a straight line from equation (5.8))

$$\log_e \dot{\varepsilon} = q \log_e \left(\frac{\sigma_0'}{\sigma_0} - 1 \right) + \log_e D \qquad (5.9)$$

$$\overbrace{y \quad = \quad 0.75x \quad + \quad 7.53}$$

Therefore determining the gradient and point of intercept of the curve, gives values for q and $\log_e D$ of 0.75 and 7.53, respectively.

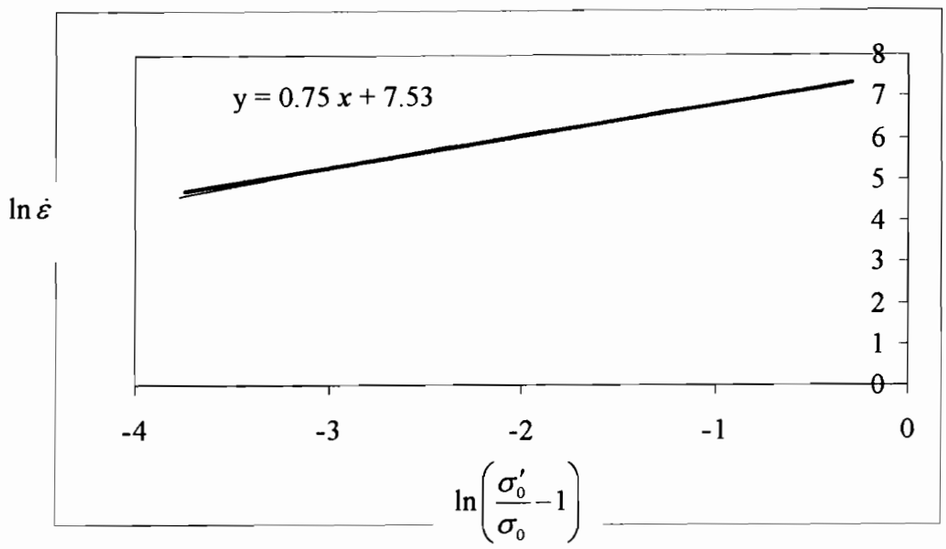

Figure 5.11: Straight-line graph plotted to deduce the q and D constants for CFRP.

The q and D values are worked out to 0.75 and 1863, respectively, for compression of CFRP. The two constants will thus be referred to as q_{comp_cfrp} and D_{comp_cfrp}.

5.2.2.5. GFRP STRESS-STRAIN BEHAVIOUR

High strain rate compression results for GFRP are also determined using a SHPB. The results are depicted in Figure 5.12. The strain rate varies from 450 s^{-1} to 1133 s^{-1}, resulting in stresses of 945 MPa to 1301 MPa, respectively. Table 5.4 gives a summary of the results in *APPENDIX V* for GFRP specimens impacted at high strain rates. The stress increases linearly with strain up to the point of failure. The failure zone labelled in the graph shows the brittle nature of failure, followed by a drop in stress beyond the ultimate stress. The ultimate stress increases with increasing strain rates. The compression strength data for the individual CFRP specimens at 20 different high strain rates of loading are tabulated in Table 5.4.

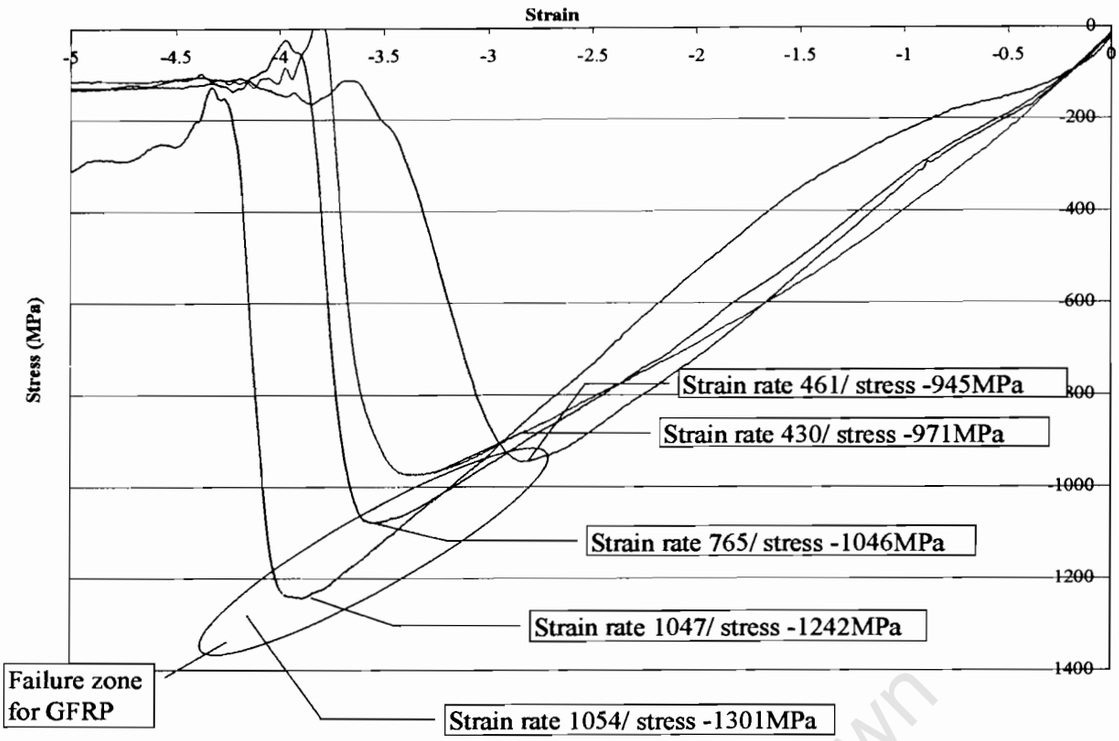

Figure 5.12: Stress vs. strain graph showing the compressive strengths of GFRP specimens under varying dynamic loading conditions.

Table 5.4: Average compressive failure strengths of 20 GFRP specimens under varying dynamic loading conditions.

Specimen No.	Average Ultimate Stress (MPa)	Specimen No.	Average Ultimate Stress (MPa)	Specimen No.	Average Ultimate Stress (MPa)	Specimen No.	Average Ultimate Stress (MPa)
GCHS01	1050	GCHS06	1254	GCHS11	971	GCHS16	1143
GCHS02	1034	GCHS07	1242	GCHS12	1260	GCHS17	1223
GCHS03	1023	GCHS08	1301	GCHS13	1138	GCHS18	1090
GCHS04	1046	GCHS09	964	GCHS14	981	GCHS19	956
GCHS05	1076	GCHS10	945	GCHS15	992	GCHS20	1026

5.2.2.6. *COMPRESSION FAILURE MODES FOR GFRP*

The GFRP system is seen to have various failure modes at dynamic strain rates compared to the CFRP system. The first distinct difference is that the GFRP is not seen to disintegrate into multiple pieces (see Figure 5.13), a feature prominent with CFRP under high loading conditions. The macroscopic analysis reveals large regions of debonding, interfacial splitting and delamination, Figure 5.13. The non-impacted ends (labelled A in Figure 5.13) of the GFRP specimen show regions of kinks along the bottom circumference of the cylindrical specimen.

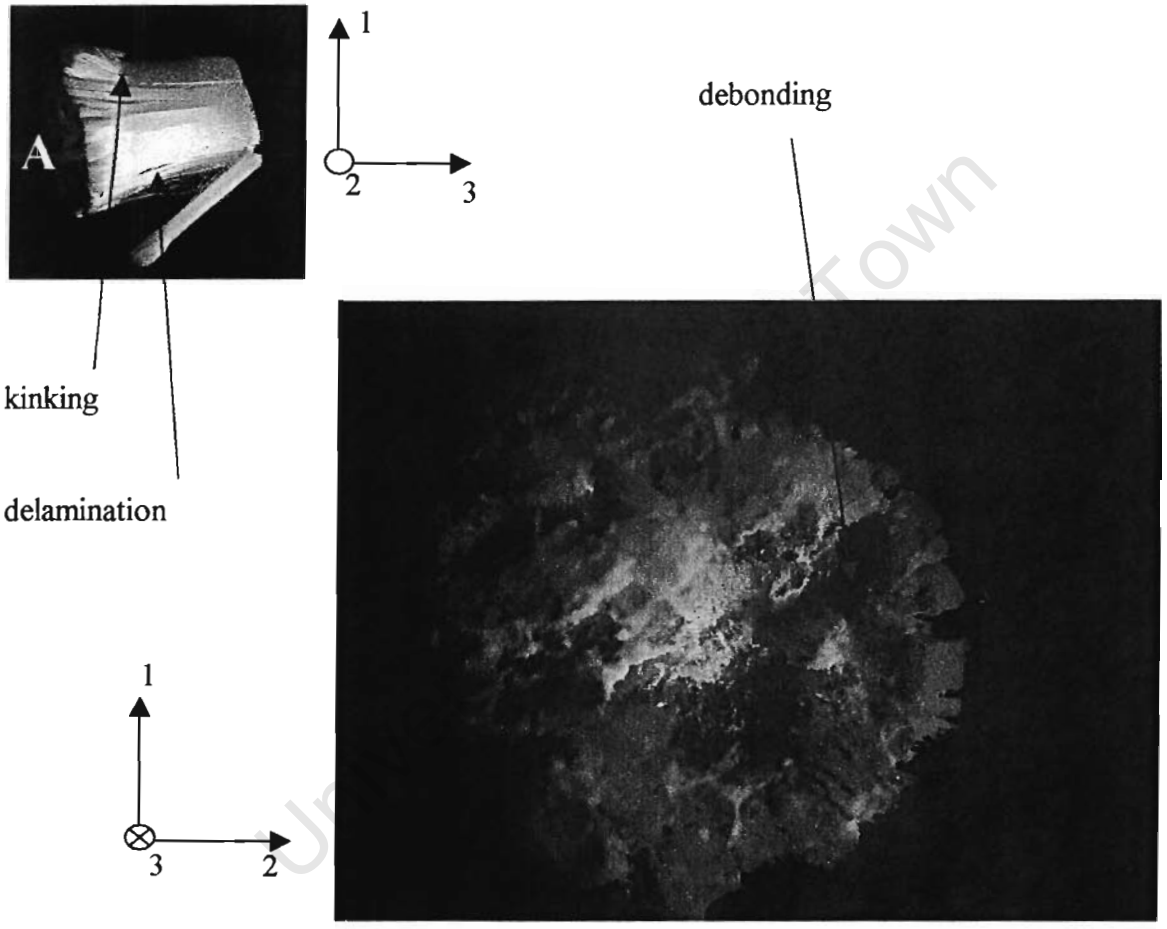

Figure 5.13: Microscopic analysis and visual analysis of the loaded surface of a GFRP specimen showing kinking, delamination and debonding.

5.2.2.7. *DERIVATION OF CONSTANTS FOR GFRP IN COMPRESSION*

The test series consisted of 150 GFRP specimens impacted at an average of 30 different strain rates with results shown in *APPENDIX V*. The dynamic strain rate values vary from 400 s^{-1} to

1180 s^{-1} with the corresponding dynamic compressive strengths varying from 945 MPa to 1301 MPa, respectively. A 95 % CI for the true average of the compressive strengths for GFRP at quasi-static to dynamic loadings gives $\bar{X}$, σ and n values that are shown in *APPENDIX V*. The values are plotted in the form of a stress-strain graph shown in Figure 5.14. The individual curves in Figure 5.14 follow the relationships:

$$\sigma'_{0\,upper} = 0.0002\dot{\varepsilon}^2 + 0.06\dot{\varepsilon} + 916 \tag{5.10}$$

$$\sigma'_{0\,median} = 0.0002\dot{\varepsilon}^2 + 0.07\dot{\varepsilon} + 894 \tag{5.11}$$

$$\sigma'_{0\,lower} = 0.0002\dot{\varepsilon}^2 + 0.09\dot{\varepsilon} + 873 \tag{5.12}$$

Equation (5.10), (5.11) and (5.12) refer to the upper, median and lower curves, respectively, shown in Figure 5.14. The upper, median and lower curves in Figure 5.15 are converted into linear curves using equation (5.8). This conversion results in three straight-line graphs, which overlap each other with the following relationship (it takes the form of an equation of a straight line).

$$\underbrace{\log_e \dot{\varepsilon}}_{y} = \underbrace{q}_{0.65}\underbrace{\log_e\left(\frac{\sigma'_0}{\sigma_0} - 1\right)}_{x} + \underbrace{\log_e D}_{7.69} \tag{5.13}$$

Therefore determining the gradient and point of intercept of the curves, gives values for q and $\log_e D$ of 0.63 and 2228 (lower), 0.65 and 2175 (median) and 0.67 and 2116 (upper), respectively. The values are similar in magnitude therefore the average values of q and D are 0.65 and 2173, respectively, for compression of GFRP is deemed sufficient. The two constants will thus be referred to as q_{comp_gfrp} and D_{comp_gfrp} for the GFRP specimens under compression.

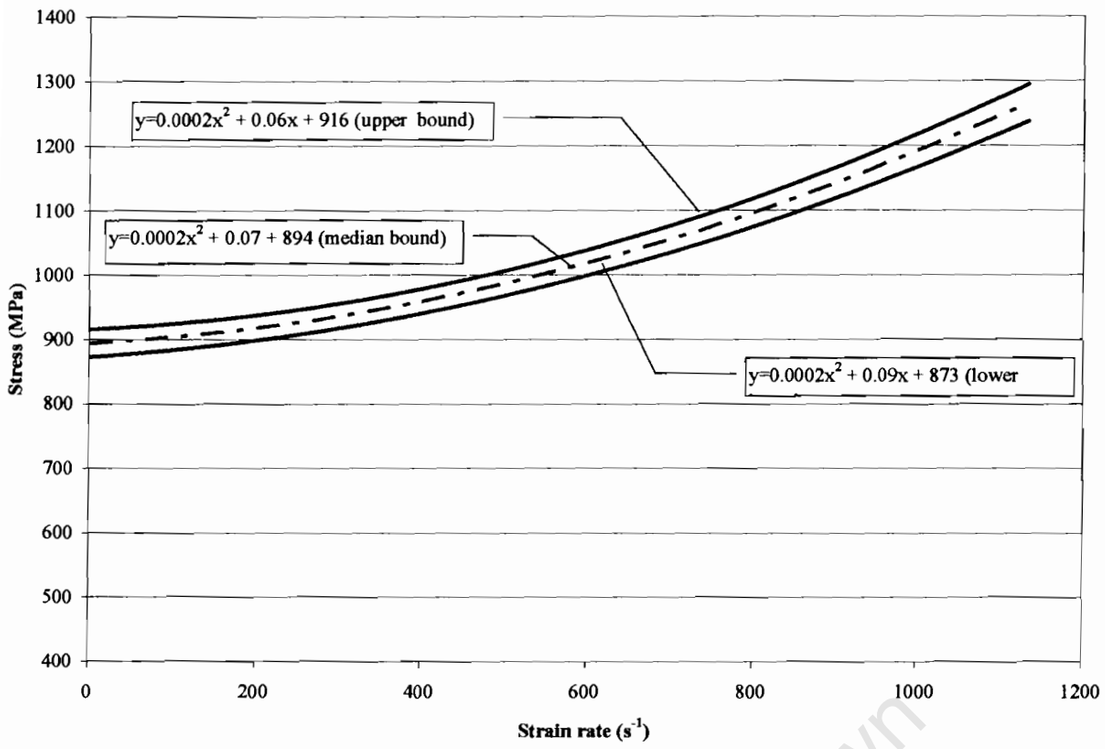

Figure 5.14: Stress versus strain rate graph for GFRP showing the relationship from quasi-static to dynamic strain rates.

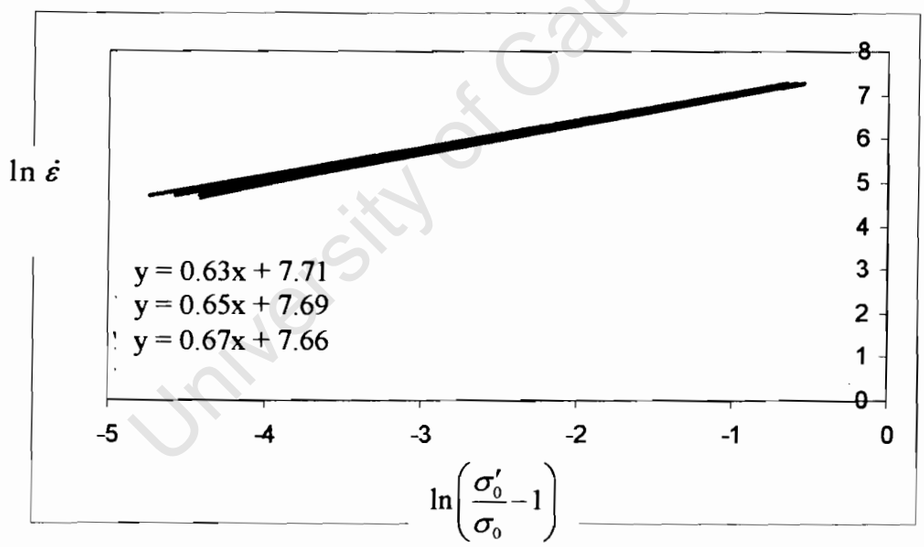

Figure 5.15: Straight-line graphs plotted to deduce q and D constants for GFRP.

5.3. SINGLE LAP SHEAR TESTS

5.3.1. QUASI-STATIC STRAIN RATES

5.3.1.1. CFRP STRESS-STRAIN BEHAVIOUR

The stress-strain graphs in Figure 5.16 show a linear relationship to failure. In each case the nature of failure is brittle. This is seen from the sudden drop in stress at the point of final fracture. The 20 tests performed give shear strength values that vary from 42.1 MPa to 60.3 MPa. The average shear strength from the data in Table 5.5 is 52.1 MPa with a standard deviation of 6.9 resulting in a percentage variation of the mean of 13.4 %.

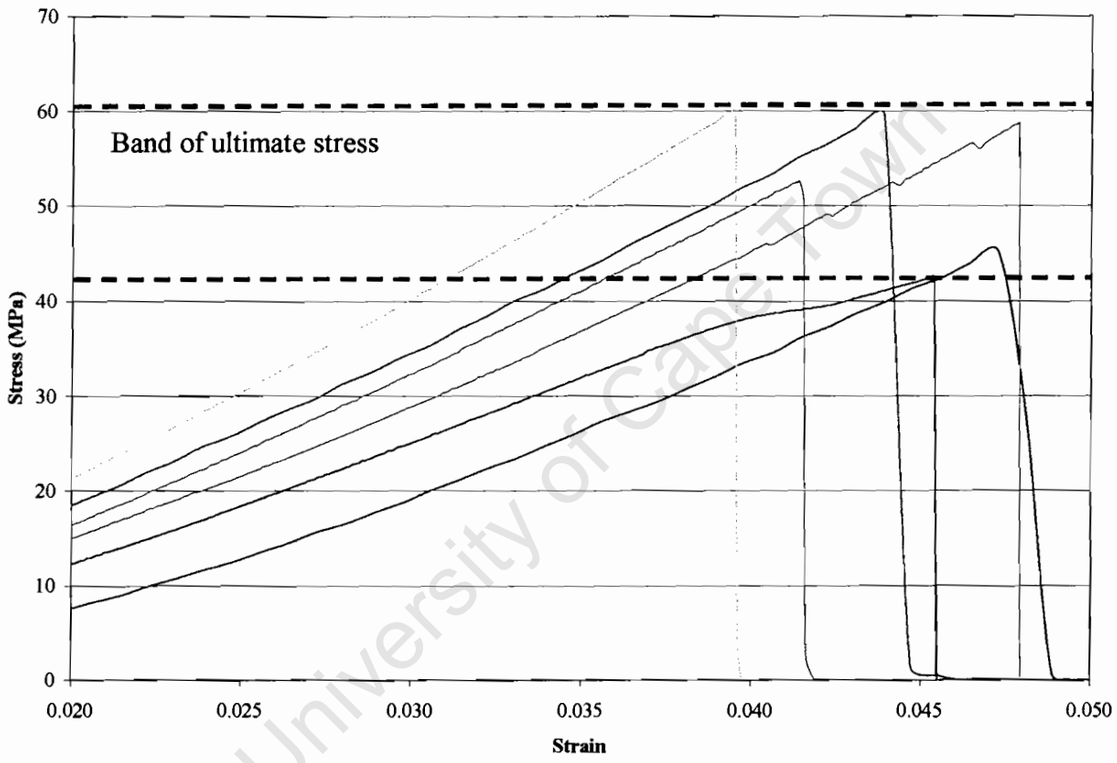

Figure 5.16: Stress vs. strain graph showing the shear strengths of CFRP specimens under quasi-static loading.

Table 5.5: Shear ultimate stresses of 20 CFRP specimens under quasi-static loading.

Specimen No.	Ultimate Stress (MPa)	Specimen No.	Ultimate Stress (MPa)	Specimen No.	Ultimate Stress (MPa)	Specimen No.	Ultimate Stress (MPa)
CSLS01	54.6	CSLS06	57	CSLS11	35.6	CSLS16	56.9
CSLS02	56.5	CSLS07	59.5	CSLS12	42.1	CSLS17	55.8
CSLS03	56	CSLS08	42.5	CSLS13	49	CSLS18	53.6
CSLS04	43.3	CSLS09	58.7	CSLS14	60.3	CSLS19	49.8
CSLS05	45.13	CSLS10	57	CSLS15	52.6	CSLS20	56.3
						Average Stress	52.1

5.3.1.2. FAILURE MODES FOR CFRP IN SHEAR

The interlaminar shear strength is a matrix dominated property because shear acts on a plane parallel to the fibre direction and propagates through the matrix without the fibre resisting the shear stress induced from the testing (see Figure 5.19). It can be seen that the shear crack propagates through the laminate interface and splits the laminate at the matrix and/or fibre-matrix interface, in the fibre direction. The shear stress applies a shear load along the fibre direction. Therefore, the interlaminar shear strength is affected by the fibre-matrix interface and matrix bonding strength.

It is important to note that due to dimensional flaws in the single lap shear material specimen manufacturing procedure a certain percentage of the materials did not fail within the required failure zone (labelled zone 1 in Figure 5.17). A tolerance was deduced from the experimental tests. Specimens that failed outside the tolerance were discarded. This tolerance varied depending on the specimen material and impact velocities.

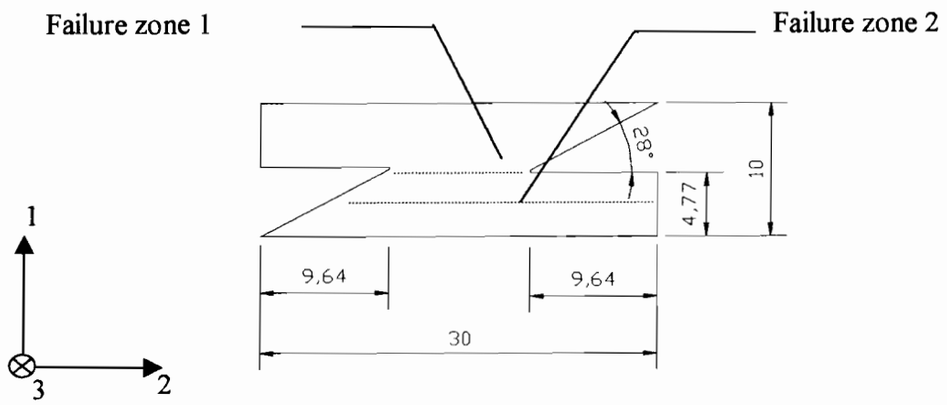

Figure 5.17: Single lap shear specimen showing zones for failure within the specimen.

The specimens outside the tolerance failed along the plane denoted as zone 2 in Figure 5.17. This would have a direct effect on the calculation of stress (force/area). Zone 2 would have a larger area, hence if this area is used to calculate the resulting shear stress would be less. As a result the assumption used in this thesis is to calculate the area using the dimension for all. The justification for this assumption is based on the background knowledge of the origins for the single lap shear tests, viz. the double-notched specimen (Figure 5.18).

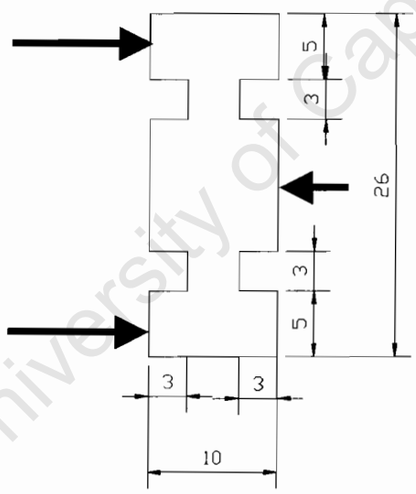

Figure 5.18: Double notched specimen used to introduce the principal of the single lap specimen, failure is expected within the stress concentration zones. The arrows show the point of loading.

Figure 5.19: Microscopic analysis of the loaded surface of the CFRP specimen showing the region of shear failure.

The single lap specimen is based on the same concepts as the double notched specimen depicted in Figure 5.18. The area of fracture and forces applied determine the magnitude of stress. The double-notched specimen is designed to fracture along the notched regions. This same principal applies to the single lap specimens. Therefore, it is imperative that the area of fracture is clearly identified in order to ensure that the accurate shear stress is determined. Figure 5.19 shows that the CFRP specimen does not fracture exactly along the notched zone. Nevertheless, the failure zone is within the calculated tolerance. This result is therefore considered valid.

5.3.1.3. GFRP STRESS-STRAIN BEHAVIOUR

The results for single-lap shear GFRP specimens at quasi-static loading are presented in Figure 5.20. The shear strengths of 20 GFRP specimens range between 33.4 MPa and 57.9 MPa. The data in Table 5.6 show the various shear failure results from the quasi-static tests performed, an average shear strength of 49.2 MPa, resulting in a standard deviation of 6.5 is calculated. The percentage variation of the mean is equal 13.2 %.

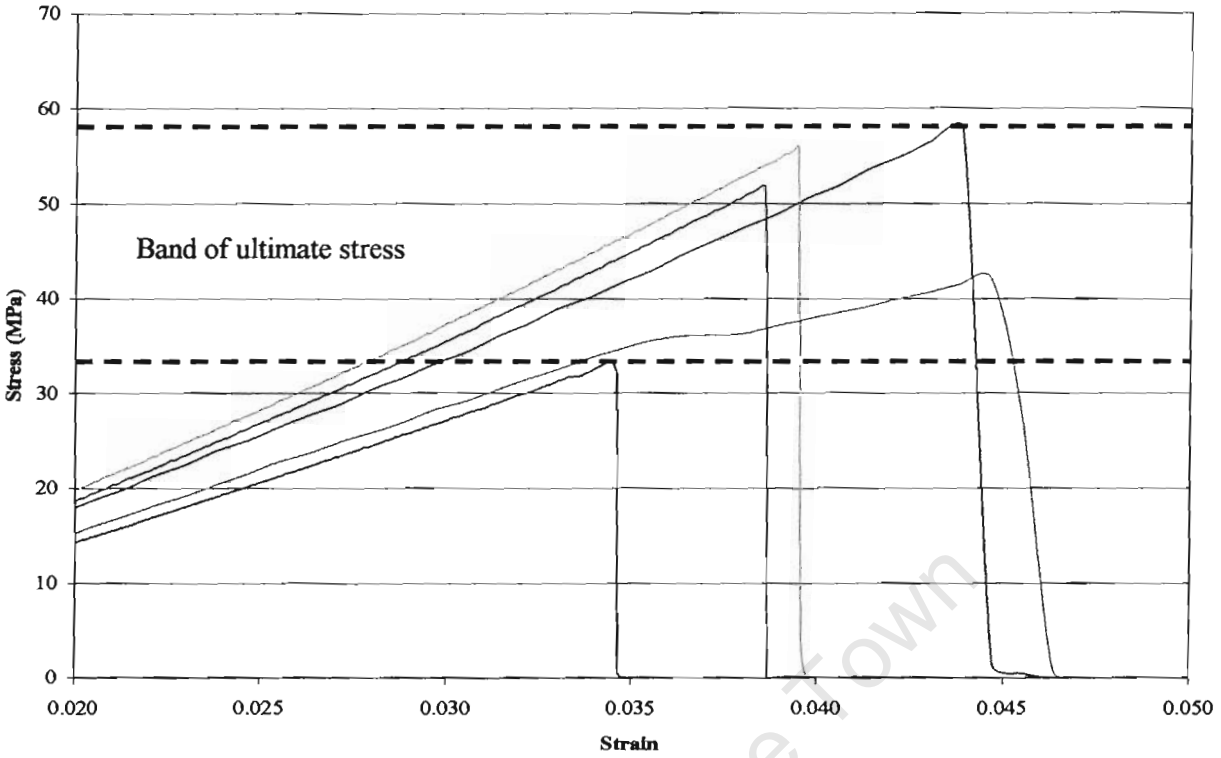

Figure 5.20: Stress vs. strain graph showing the shear strengths of GFRP specimens under quasi-static loading.

Table 5.6: Single-lap shear failure strengths of 20 GFRP specimens under quasi-static loading.

Specimen No.	**Ultimate Stress (MPa)**	**Specimen No.**	**Ultimate Stress (MPa)**	**Specimen No.**	**Ultimate Stress (MPa)**	**Specimen No.**	**Ultimate Stress (MPa)**
GSLS01	54.5	GSLS06	55.1	GSLS11	33.4	GSLS16	52.5
GSLS02	49.8	GSLS07	57.9	GSLS12	39.5	GSLS17	51.8
GSLS03	49.3	GSLS08	39.8	GSLS13	46.5	GSLS18	53.6
GSLS04	42.1	GSLS09	55.4	GSLS14	56.0	GSLS19	48.2
GSLS05	43.9	GSLS10	53.4	GSLS15	49.9	GSLS20	49.8
						Average Stress	49.2

5.3.1.4. FAILURE MODES FOR GFRP IN SHEAR

The single-lap shear is again a matrix dominated failure. This is confirmed by the analysis of the failure mode in the GFRP specimen, as well as the low shear strength values recorded. Quasi-static analysis of the GFRP specimen reveals a failure plane that runs parallel to the fibre and propagates through the matrix without any fibre failure. Secondly, the interlaminar shear strength gives values that are similar to the CFRP specimens under the same loading. Therefore average shear strength for GFRP was 49.2 MPa as compared to a shear strength value of 52.1 MPa for CFRP. The same drawbacks due to inconsistent specimen size are also noted for GFRP. The same principal used in determining the area of failure discussed for CFRP is used in the case of the GFRP shear specimens. Figure 5.21 shows shear failure that occurred outside the required tolerance. If this specimen is used then the area for failure will give a low interlaminar failure stress. This value will be inaccurate due to manufacturing flaws. The importance of ensuring failure within the notched zone is therefore emphasised.

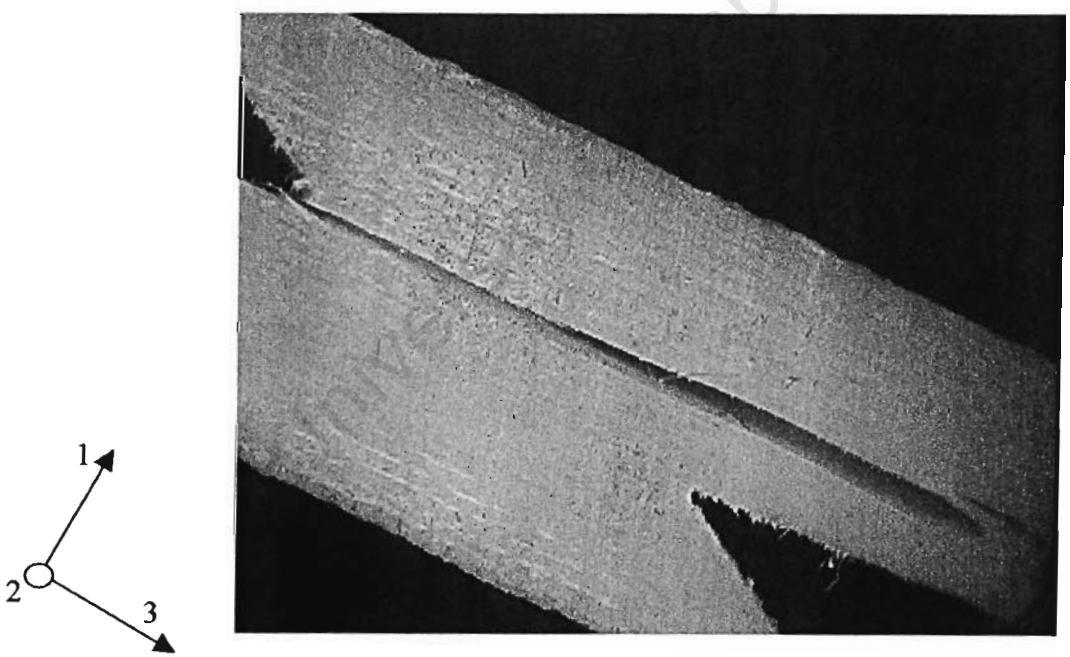

Figure 5.21: Microscopic analysis of the loaded surface of a GFRP specimen showing regions of shear failure. This specimen is an example of a shear specimen that falls outside the required tolerance. The distance from the notch of the actual failure is greater than the required tolerance.

5.3.2. DYNAMIC STRAIN RATES

5.3.2.1. CFRP STRESS-STRAIN BEHAVIOUR

The stress strain graph for CFRP specimen loaded at varying dynamic strain are presented in Figure 5.22. The graph shows increasing stress with strain rate. The data for CFRP specimen under single-lap shear impact at dynamic strain rates is presented in *APPENDIX V*. Therefore, Table 5.7 gives a summary of the single-lap shear impact results at dynamic strain rates. Each of the ultimate stress results presented in this table refers to a different strain rate value. The ultimate stress for CFRP under single lap shear specimen ranges from 61.6 MPa to 115 MPa for strain rates of 326 s^{-1} to 811 s^{-1}, respectively.

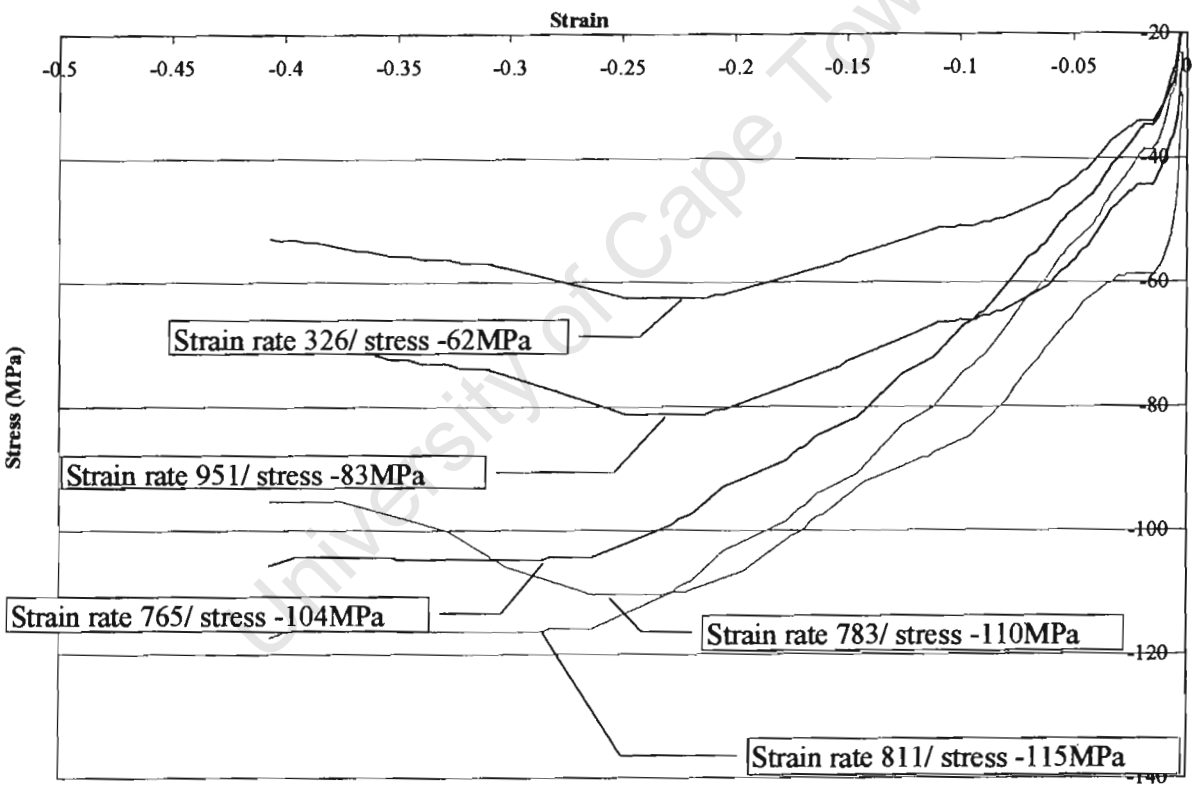

Figure 5.22: Stress vs. strain graph showing the shear strengths of CFRP specimens under varying dynamic loading.

Table 5.7: Average shear stress of 20 CFRP specimens under dynamic loading.

Specimen No.	Ultimate stress (MPa)	Specimen No.	Ultimate stress (MPa)	Specimen No.	Ultimate stress (MPa)	Specimen No.	Ultimate stress (MPa)
CSHS01	78	CSHS06	66.4	CSHS11	104	CSHS16	115
CSHS02	75	CSHS07	69.2	CSHS12	109	CSHS17	104
CSHS03	61.6	CSHS08	71	CSHS13	115	CSHS18	110
CSHS04	76.6	CSHS09	108	CSHS14	70.8	CSHS19	115
CSHS05	70.8	CSHS10	118	CSHS15	62	CSHS20	68

5.3.2.2. FAILURE MODES FOR CFRP IN SHEAR

The analysis of the SEM micrograph (Figure 5.23) reveals a cleavage plane due to shearing along the fibre-matrix interface and/or matrix plane. Further analysis shows that the fibres remain intact. There appears to be negligible effect on the fibres from the shear loading at high strain rates. The image shows the plane of failure from a plan view (labelled direction of SEM image).

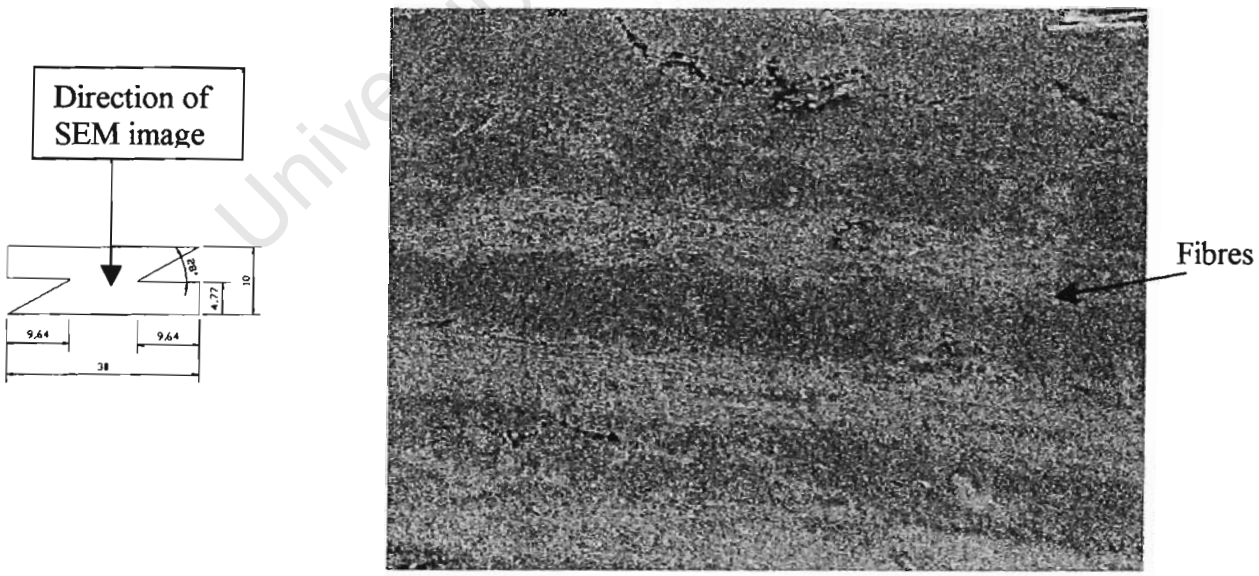

Figure 5.23: Scanning electron microscope image of the shear failure surface for CFRP under high strain rate loading.

The results form the basis for the data used in the shear failure stress versus strain rate graph shown in Figure 5.24. Considerable scatter is shown in the failure stresses measured under impact, however a distinct increase is seen from the failure stress-strain rate graph shown in Figure 5.20. Analysis of the quasi-static specimens shows no significant change in the mode of failure. At higher strain rates the material continues to fail by shearing of the matrix plane with limited fibre failure.

5.3.2.3. DERIVATION OF CONSTANTS FOR CFRP IN SHEAR

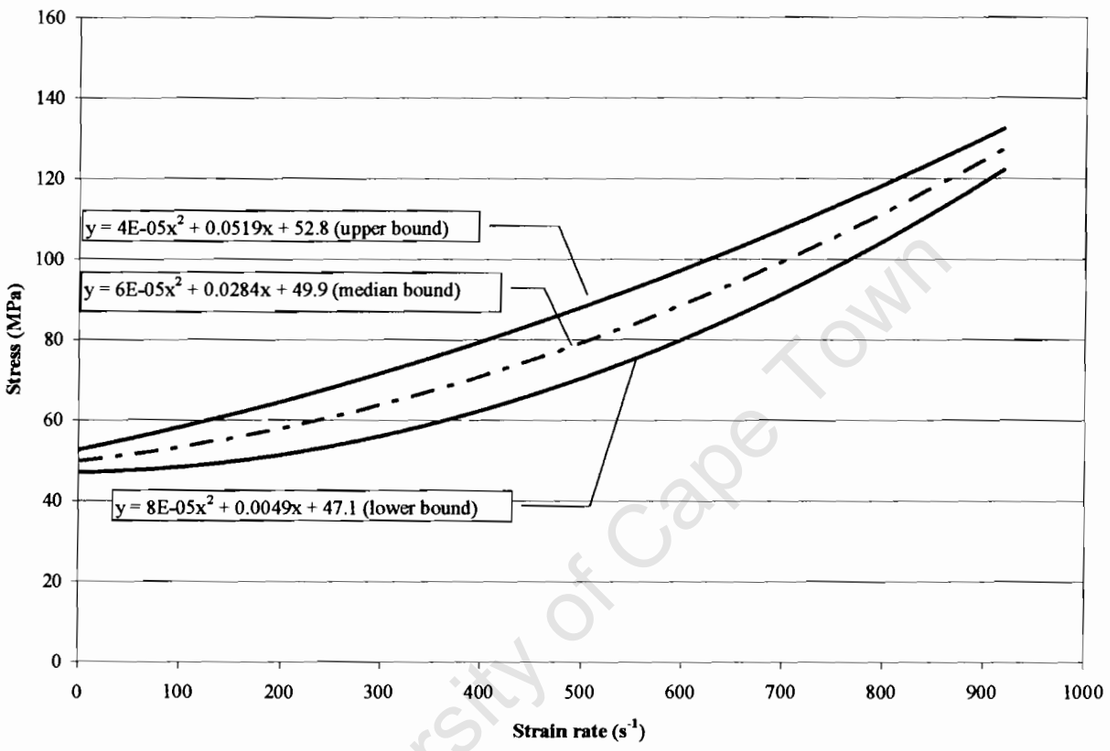

Figure 5.24: Effect of strain rate on the interlaminar shear strength of CFRP.

The upper, median and lower curves in Figure 5.24 are presented in equations (5.14), (5.15) and (5.16). Following the same procedure used for the ultimate compression stress data, the graphs in Figure 5.24 are converted into straight-line graphs shown, using equation (5.8).

$$\sigma'_{0\,upper} = 0.00004\dot{\varepsilon}^2 + 0.0529\dot{\varepsilon} + 52.8 \quad (5.14)$$

$$\sigma'_{0\,median} = 0.00006\dot{\varepsilon}^2 + 0.0284\dot{\varepsilon} + 49.9 \quad (5.15)$$

$$\sigma'_{0\,lower} = 0.00008\dot{\varepsilon}^2 + 0.0049\dot{\varepsilon} + 47.1 \quad (5.16)$$

Figure 5.25 is thus drawn to determine the gradient and point of intercept of the curve. This gives values for q and $\log_e D$, respectively. The gradient of the curves vary when comparing the upper, median and lower values. Therefore a comparative study is undertaken in order to determine the degree of discrepancy in the values with respect to determining the values of for q and $\log_e D$ for each curve.

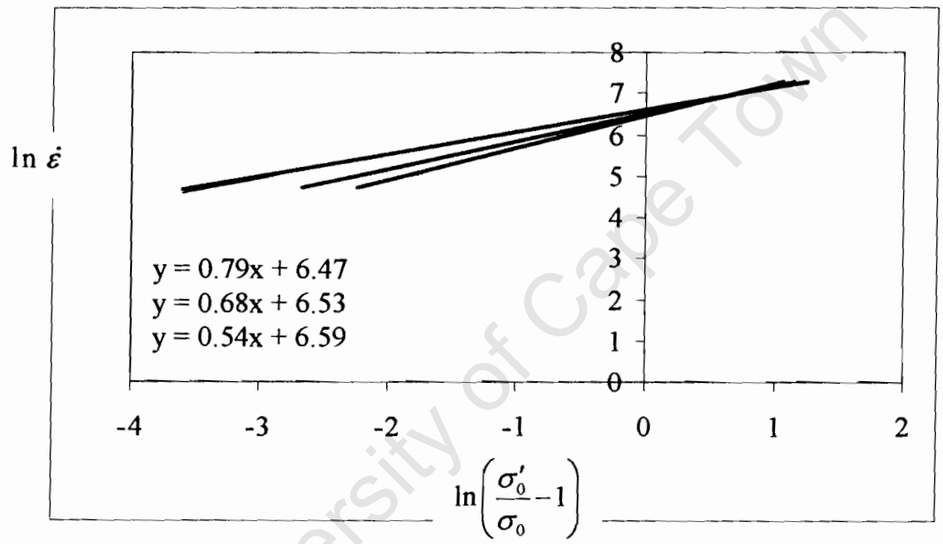

Figure 5.25: Straight-line graph plotted to deduce q and D constants for CFRP under shear loading conditions.

Equations (5.14), (5.15) and (5.16) results in the following q and D values 0.54, 727; 0.68, 685 and 0.79, 646; respectively, for single lap shear of CFRP. The two constants referred to as

q_{shear_cfrp} and D_{shear_cfrp} will therefore have values within the range 0.7 ± 0.13 and 688 ± 42, respectively.

5.3.2.4. GFRP STRESS-STRAIN BEHAVIOUR

GFRP tested under dynamic single lap shear shows increasing stress as a result of increasing strain rates. At strain rates of 370 s^{-1} to 791 s^{-1} the peak stress is seen to increase from 52.6 MPa to 108 MPa, respectively (see Figure 5.26). An increase is seen in the failure stress with increasing strain rate.

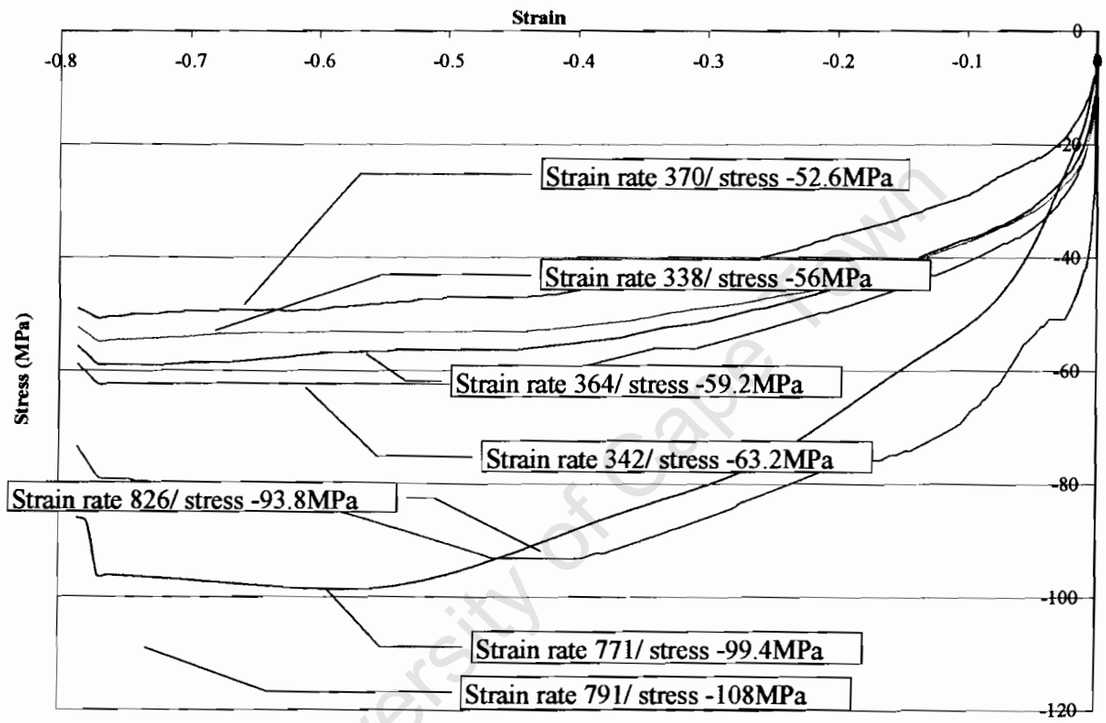

Figure 5.26: Stress vs. strain graphs showing the shear strengths of GFRP specimens under dynamic loading.

Table 5.8: Average shear stress of 20 GFRP specimens under varying dynamic loading. A summary of the single lap shear results is presented in APPENDIX V.

Specimen No.	Ultimate Stress (MPa)	Specimen No.	Ultimate Stress (MPa)	Specimen No.	Ultimate Stress (MPa)	Specimen No.	Ultimate Stress (MPa)
GSHS01	63.2	GSHS06	99.4	GSHS11	109	GSHS16	57
GSHS02	59.2	GSHS07	106	GSHS12	61.8	GSHS17	50.8
GSHS03	56	GSHS08	113	GSHS13	53.6	GSHS18	54
GSHS04	93.8	GSHS09	97	GSHS14	114.4	GSHS19	60
GSHS05	108	GSHS10	51.8	GSHS15	57	GSHS20	52.6

These results form the basis for the data used in the shear failure with the strain rate graph shown in Figure 5.27. Microscopic analysis using SEM revealed no significant features. This observation suggests that the mode of failure was dominated by matrix shearing.

5.3.2.5. DERIVATION OF CONSTANTS OF GFRP IN SHEAR

The shear stress vs. strain rate graph in Figure 5.27 depicts the variation in ultimate stress with increasing strain rate for single lap shear GFRP specimens subjected to increasing strain rates. This graph is then converted into a series of straight-line curves for deducing the various q and D constants.

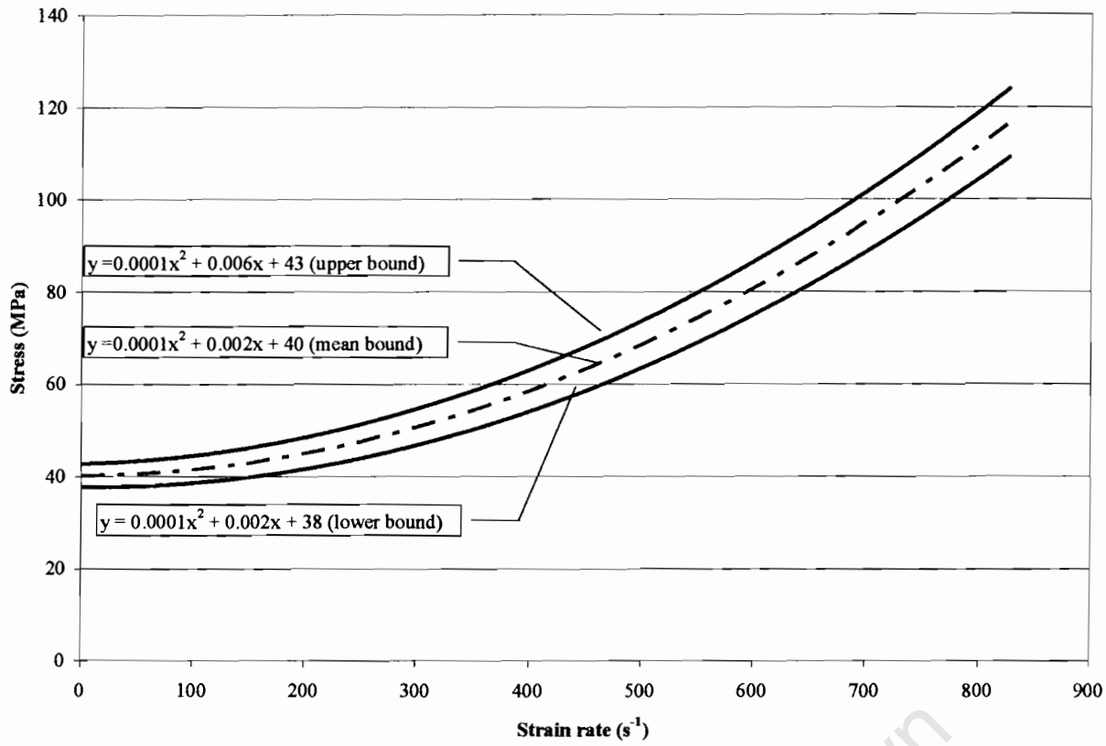

Figure 5.27: Effect of strain rate on the interlaminar shear strength of GFRP.

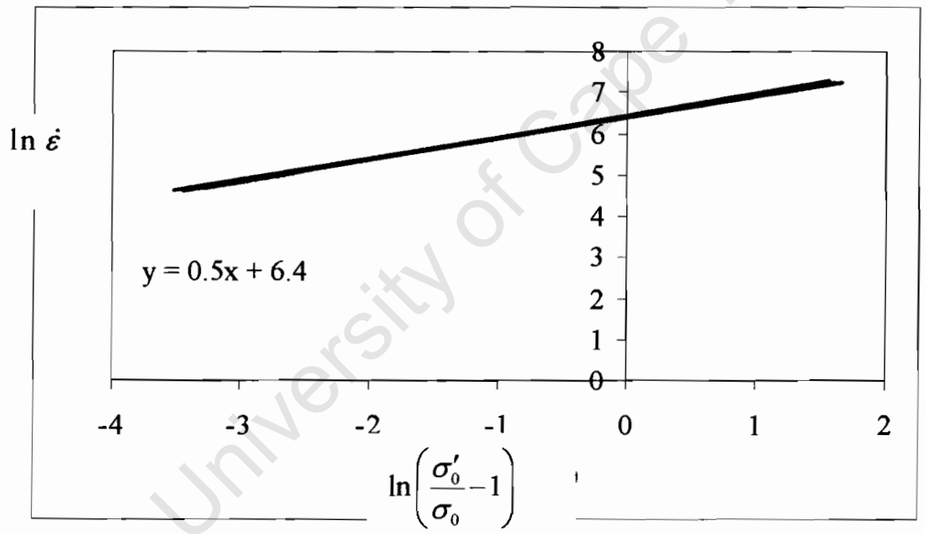

Figure 5.28: Straight-line graph plotted to deduce q and D constants for GFRP under shear loading conditions.

The gradient of the curves in Figure 5.28 are similar, therefore q and D have values of 0.5 and 622, respectively, for shear of GFRP. The two constants will thus be referred to as to as q_{shear_gfrp} and D_{shear_gfrp}.

5.4. UNIAXIAL TENSION TESTS

5.4.1. QUASI-STATIC STRAIN RATES

5.4.1.1. CFRP STRESS STRAIN BEHAVIOUR

The stress-strain curves for the CFRP specimens tested at quasi-static strain rates are presented in Figure 5.29. The ultimate stresses for 20 specimens loaded quasi-statically are presented in Table 5.9. The test condition were kept constant, the same Instron cross-head speed is used in testing the 20 specimens under quasi-static loading. At quasi-static loading rates the stress-strain curves for each material are linear up to failure. All the specimens are seen to fail in a brittle manner along the gauge length. The tensile strengths of 20 CFRP specimens range between 1080 MPa and 1448 MPa. The data in Table 5.9 show the tensile failure strength results from the quasi-static tests performed. The average tensile strength is calculated to 1292 MPa, with in a standard deviation of 88.1. The percentage variation of the mean is equal 6.8 %.

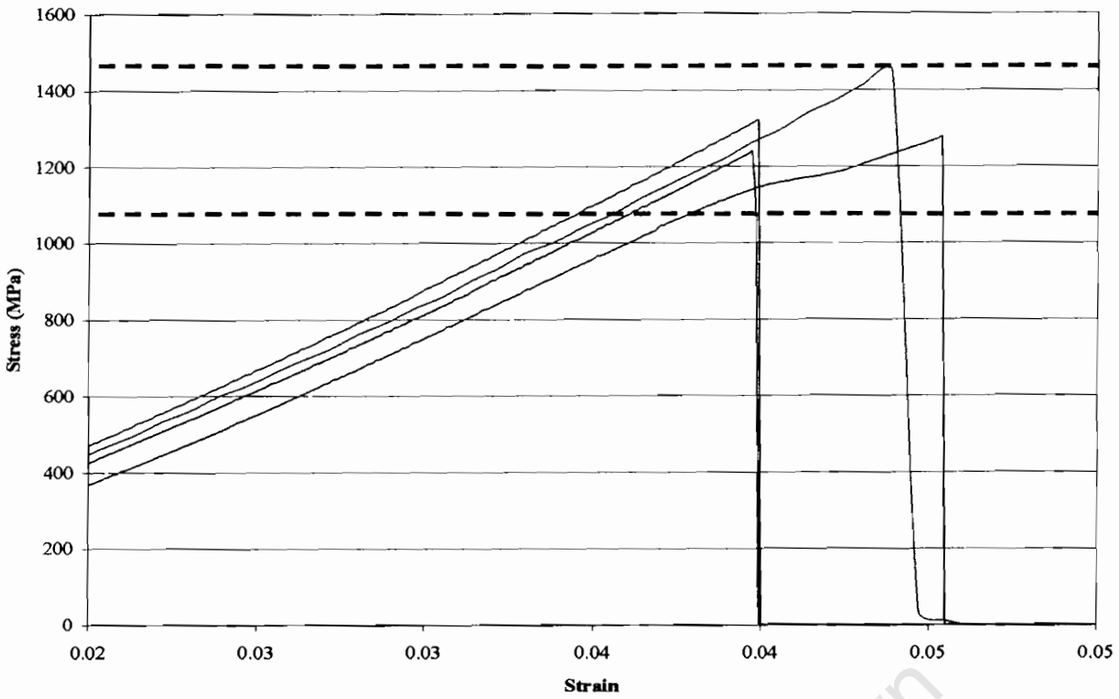

Figure 5.29: Stress-strain graphs for CFRP specimens under quasi-static tensile loading.

Table 5.9: Tensile failure strengths of 20 CFRP specimens under quasi-static loading.

Specimen No.	**Ultimate Stress (MPa)**	**Specimen No.**	**Ultimate Stress (MPa)**	**Specimen No.**	**Ultimate Stress (MPa)**	**Specimen No.**	**Ultimate Stress (MPa)**
CTLS01	1080	CTLS06	1378	CTLS11	1353	CTLS16	1360
CTLS02	1264	CTLS07	1448	CTLS12	1341	CTLS17	1250
CTLS03	1331	CTLS08	1275	CTLS13	1289	CTLS18	1334
CTLS04	1215	CTLS09	1296	CTLS14	1350	CTLS19	1265
CTLS05	1267	CTLS10	1306	CTLS15	1090	CTLS20	1341
						Average Stress	1292

5.4.1.2. FAILURE MODES FOR CFRP IN TENSION

SEM analysis of the fracture surface reveals brittle fibre failure. Figure 5.30 shows certain portion where the matrix stays attached to the fibre. This observation suggests that in certain regions the fibre-matrix interface is stronger than the fibre.

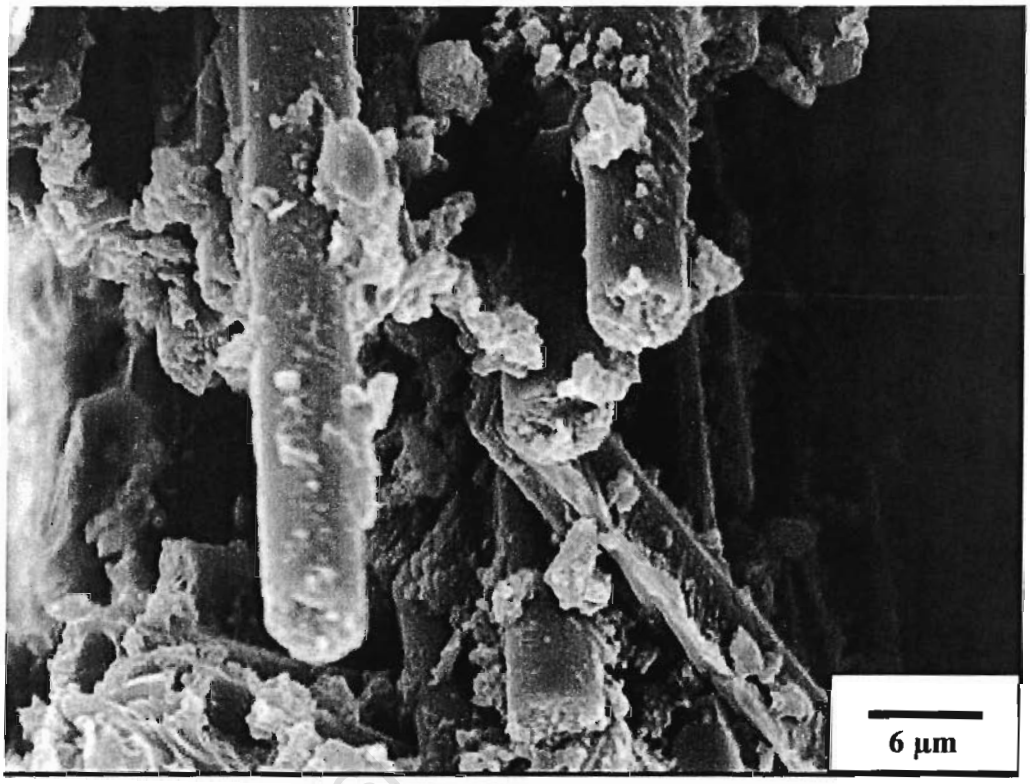

Figure 5.30: Microscopic analysis of the loaded surface of the CFRP specimen showing the brittle nature of fibre failure.

5.4.1.3. GFRP STRESS-STRAIN BEHAVIOUR

The failure strengths for the GFRP specimens are not comparable to those of CFRP. In fact the GFRP is seen to fail at an average value of 756 MPa under quasi-static loading. The tensile failure strength of GFRP laminate is about 59 % of the CFRP tensile failure value. The stress-strain curves for the CFRP specimens are presented in Figure 5.31. At quasi-static loading rates the stress-strain curves for each material are linear up to failure. All the specimens fail in a brittle manner along the gauge length. The standard deviation is 29.6 giving a percentage variation of the mean of 3.9 %.

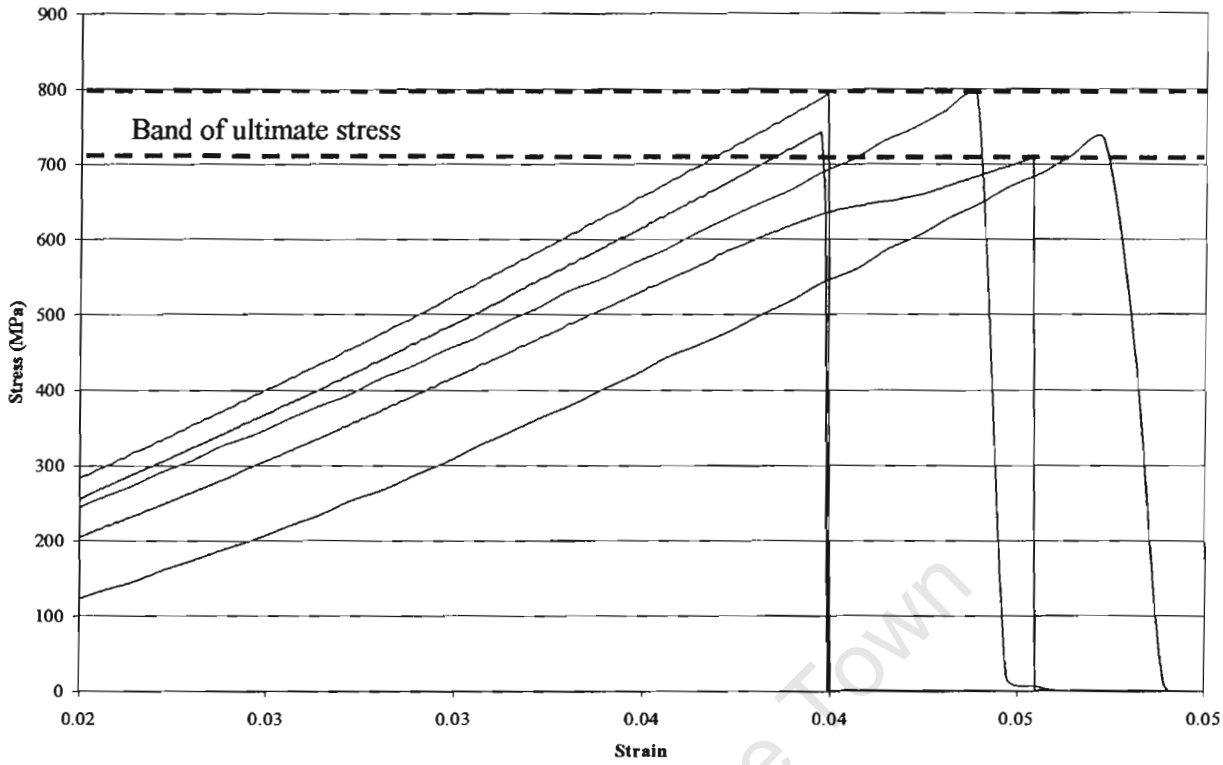

Figure 5.31: Stress vs. strain graph showing the tensile strengths of GFRP specimens under quasi-static loading.

Table 5.10: Tensile failure strengths of 20 GFRP specimens under quasi-static loading.

Specimen No.	**Ultimate Stress (MPa)**	**Specimen No.**	**Ultimate Stress (MPa)**	**Specimen No.**	**Ultimate Stress (MPa)**	**Specimen No.**	**Ultimate Stress (MPa)**
GTLS01	744	CTLS06	759.7	CTLS11	762	CTLS16	794
GTLS02	792	CTLS07	790	CTLS12	789	CTLS17	726
GTLS03	717	CTLS08	709	CTLS13	743	CTLS18	746
GTLS04	702	CTLS09	778	CTLS14	779	CTLS19	737
GTLS05	732	CTLS10	783	CTLS15	789	CTLS20	755
						Average Stress	756

5.4.1.4. FAILURE MODES FOR GFRP IN TENSION

SEM analysis of the fractured surface of GFRP is shown in Figure 5.32. The fibres are seen to fail in a brittle manner. Further examination of the micrograph reveals the cleavage planes which can be associated with brittle failure.

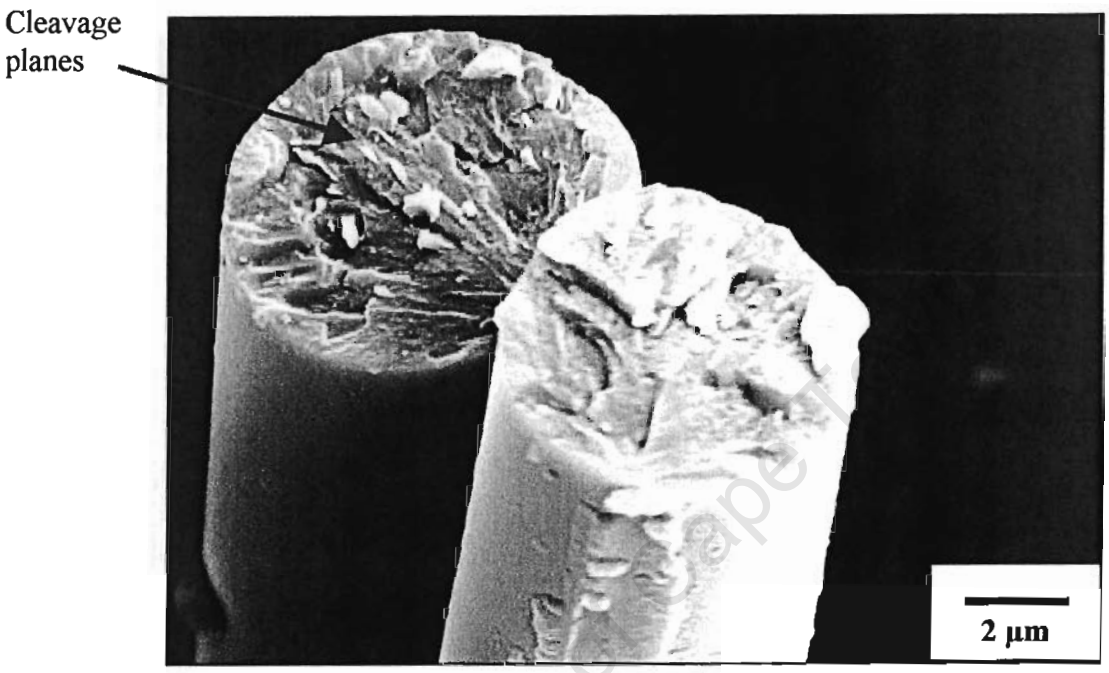

Figure 5.32: Microscopic analysis the GFRP specimen showing cleavage planes in the glass fibres.

5.4.2. DYNAMIC STRAIN RATES

Dynamic tensile tests using a tensile split Hopkinson bar as described previously in chapter 4 are performed on tensile specimens. Geometric effects are discarded by maintaining the same specimen geometry as used in the quasi-static analysis. A series of tensile tests are performed on CFRP and GFRP composite to gain material property data for numerical analysis. The dynamic strain rate varied from 500 s^{-1} to 1800 s^{-1} by varying the impact velocity of the SHPB device.

5.4.2.1. CFRP STRESS-STRAIN BEHAVIOUR

The results for the dynamic tensile tests done on CFRP are presented in the form of a nominal stress vs. nominal strain graph after processing of the SHPB data. The peak stress values in each case represent the ultimate stress of the tested material. Figure 5.33 is drawn from the stress strain curves of CFRP at high strain rates. Results from Table 5.11 forms the basis for the data used in the tensile strength versus strain rate graph shown in Figure 5.35.

The strain to failure values for tensile testing presented a major challenge with respect to recording accurate strain values. The CFRP under high strain loading fails in a brittle manner within a very short time. The nominal strain as recorded are not considered accurate therefore the focus in this research is on the stresses. This also means that the elastic modulus from the gradient of the curve will not yield meaningful results.

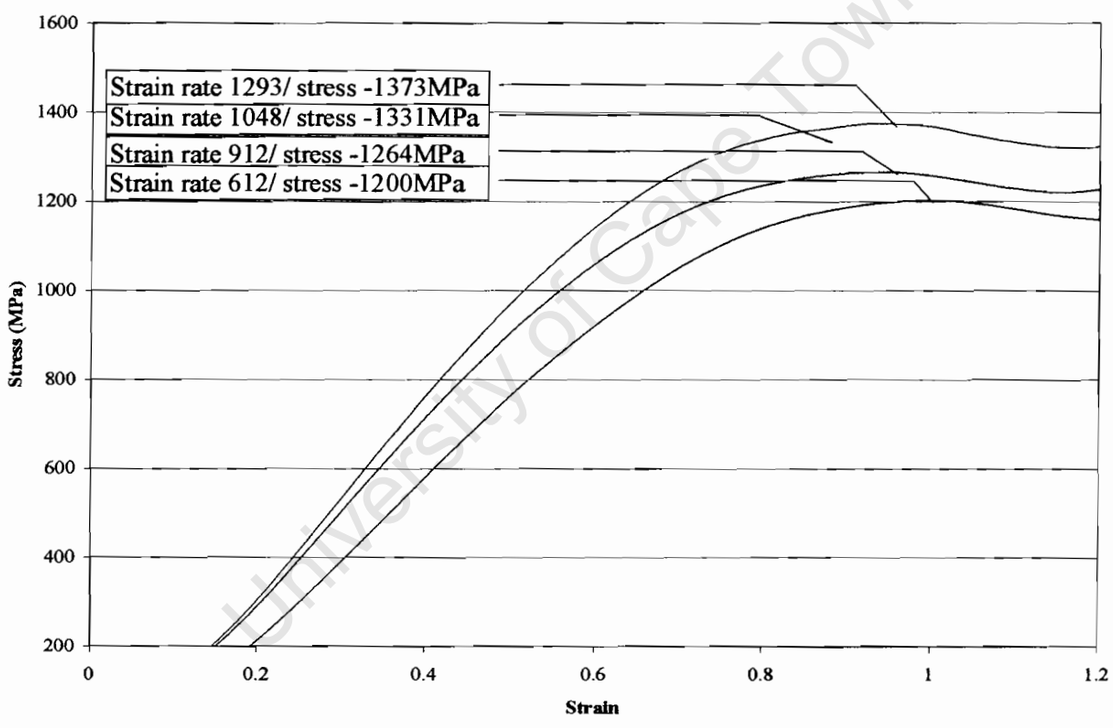

Figure 5.33: Average stress vs. strain results for CFRP specimen under high strain rate tension.

Table 5.11: High strain rate ultimate stress values for CFRP under varying tensile loading conditions.

Specimen No.	Ultimate Stress (MPa)	Specimen No.	Ultimate Stress (MPa)	Specimen No.	Ultimate Stress (MPa)	Specimen No.	Ultimate Stress (MPa)
CTHS01	1305	CTHS06	1375	CTHS11	1264	CTHS16	1368
CTHS02	1299	CTHS07	1255	CTHS12	1314	CTHS17	1378
CTHS03	1314	CTHS08	1210	CTHS13	1327	CTHS18	1345
CTHS04	1243	CTHS09	1290	CTHS14	1317	CTHS19	1342
CTHS05	1373	CTHS10	1200	CTHS15	1336	CTHS20	1331

5.4.2.2. FAILURE MODES FOR CFRP IN TENSION

Some scatter is shown in the failure stresses measured under tensile impact. However a gradual increase is seen in the failure stress-strain rate graph shown in Figure 5.35. Analysis of the post-impact specimen shows no significant change in the mode of failure. At higher strain rates the material continues to fail by brittle fibre failure. Examination of the CFRP fibre reveals granular structures, a feature that is associated with brittle failure, Figure 5.34. This feature is noted at both low and high strain rates. Therefore, a change in strain rate from quasi-static to dynamic values has no significant effect on the failure modes observed through microscopic investigations for the CFRP system.

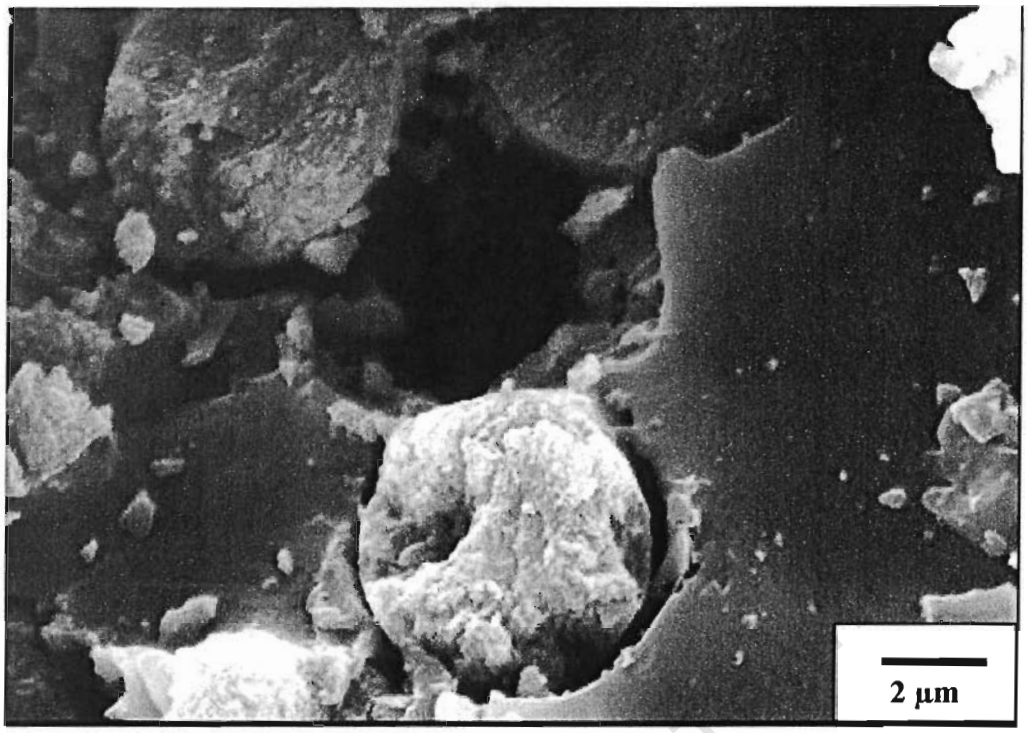

Figure 5.34: SEM micrograph showing a region of brittle failure for a CFRP specimen loaded at high strain rates.

5.4.2.3. DERIVATION OF CONSTANTS FOR CFRP IN TENSION

The three curves in Figure 5.35 follow the relationships below:

$$\sigma'_{0\,upper} = 0.02\dot{\varepsilon} + 1306 \tag{5.17}$$

$$\sigma'_{0\,median} = 0.03\dot{\varepsilon} + 1281 \tag{5.18}$$

$$\sigma'_{0\,lower} = 0.04\dot{\varepsilon} + 1256 \tag{5.19}$$

These relationships are only valid for the interval $0 \leq \dot{\varepsilon} \leq 2000\ s^{-1}$.

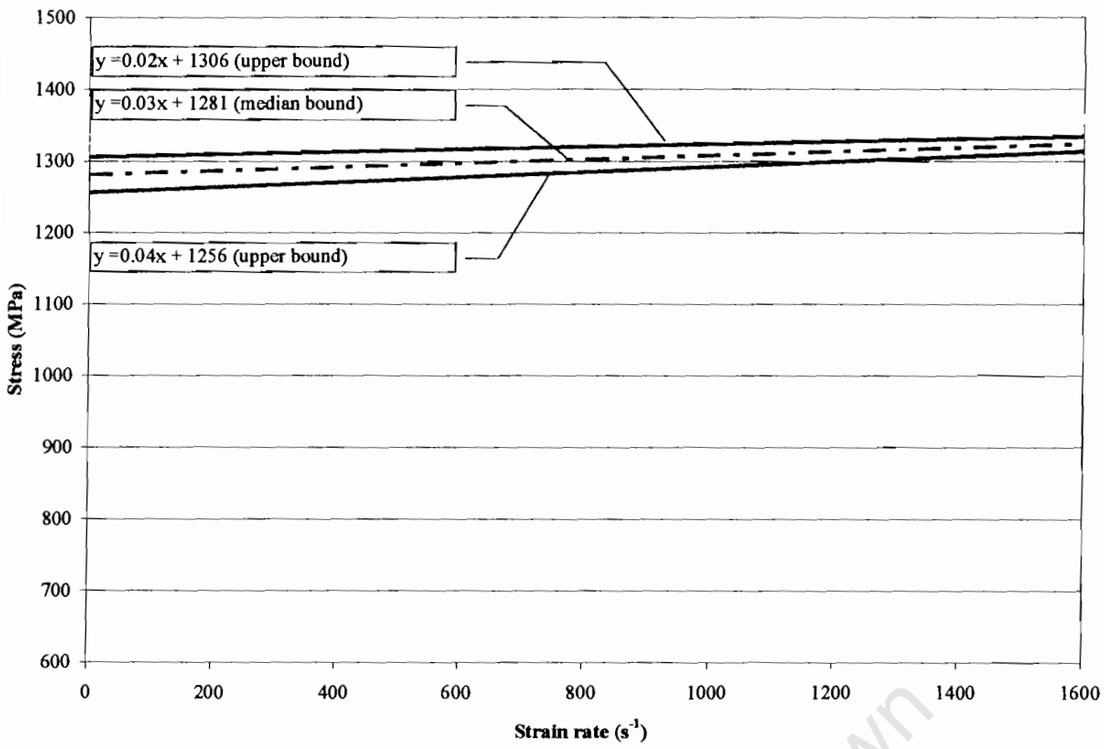

Figure 5.35: Stress vs. strain rate graphs for CFRP tensile loading at varying strain rates.

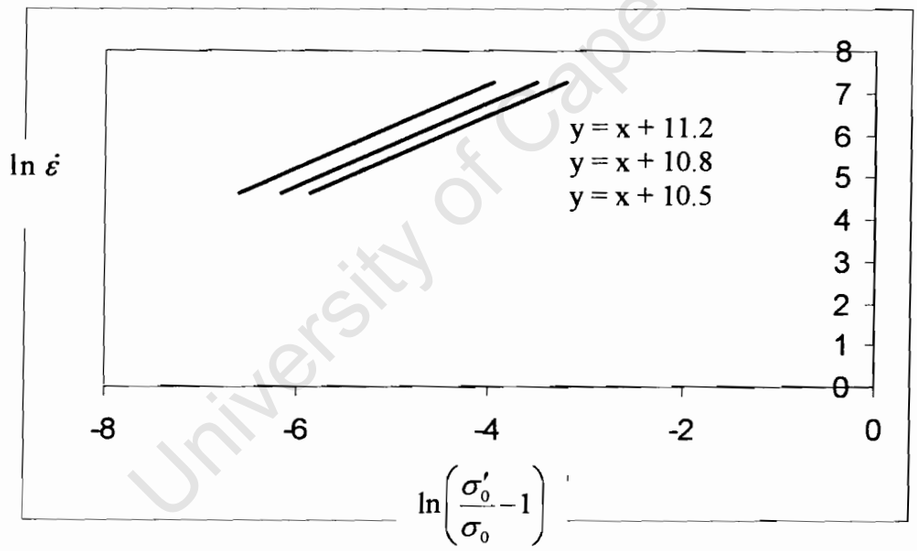

Figure 5.36: Straight-line graphs plotted to deduce q and D constants for CFRP under tensile loading conditions.

The relationships from each curve appear to be linear with negligible variation in gradient as the strain rate increases from quasi-static to dynamic. The gradient of the three curves in Figure 5.36 are equal to one. Therefore q and D have values of 1 and 54279±19072, respectively, for CFRP under tension. The two constants will thus be referred to as q_{tens_cfrp} and D_{tens_cfrp} for the CFRP specimens under tension.

5.4.2.4. GFRP STRESS-STRAIN BEHAVIOUR

The data for GFRP specimen under tensile impact at dynamic strain rates is presented in *APPENDIX VII*. These results form the basis for the data used in the tensile strength strain rate graph shown in Figure 5.39. Some scatter is shown in the failure stresses measured under tensile impact. However, a distinct increase is seen from the failure stress-strain rate graph shown in Figure 5.35.

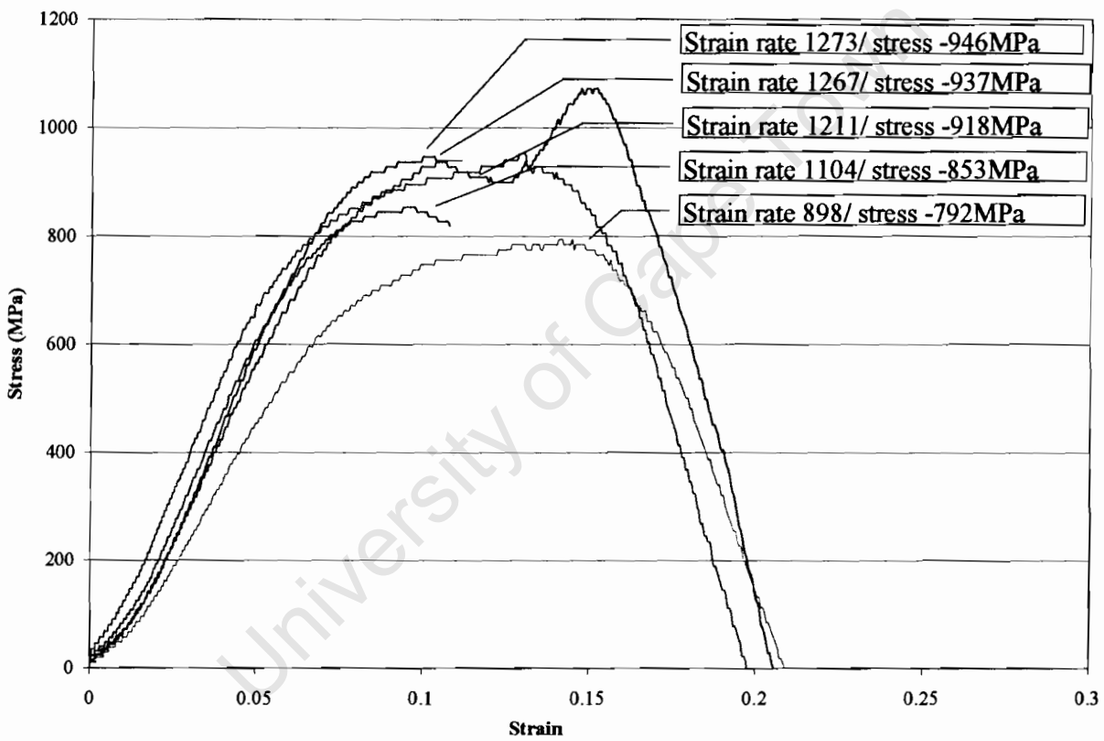

Figure 5.37: Average stress vs. strain results for GFRP specimen under high strain rate tension.

Results of GFRP tested at varying high rates of loading are presented in Table 5.12.

Table 5.12: Tensile failure strengths of 20 GFRP specimens under dynamic loading.

Specimen No.	Ultimate Stress (MPa)	Specimen No.	Ultimate Stress (MPa)	Specimen No.	Ultimate Stress (MPa)	Specimen No.	Ultimate Stress (MPa)
GTHS01	843	GTHS06	990	GTHS11	792	GTHST16	918
GTHS02	854	GTHS07	875	GTHS12	821	GTHS17	830
GTHS03	879	GTHS08	869	GTHS13	946	GTHS18	875
GTHS04	937	GTHS09	815	GTHS14	908	GTHS19	879
GTHS05	880	GTHS10	827	GTHS15	876	GTHS20	869.6

5.4.2.5. FAILURE MODES FOR GFRP IN TENSION

Analysis of the post-impact specimen shows no significant change in the mode of failure, at higher strain rates the material continues to fail by brittle fibre failure with large regions of fibre pull-out. The bundles of fibres, which have pulled out of the matrix, are seen to exist at high strain rates. Examination of the GFRP fibre reveals cleavage planes a feature that is associated with brittle failure, for both low and high strain rates (see Figure 5.38).

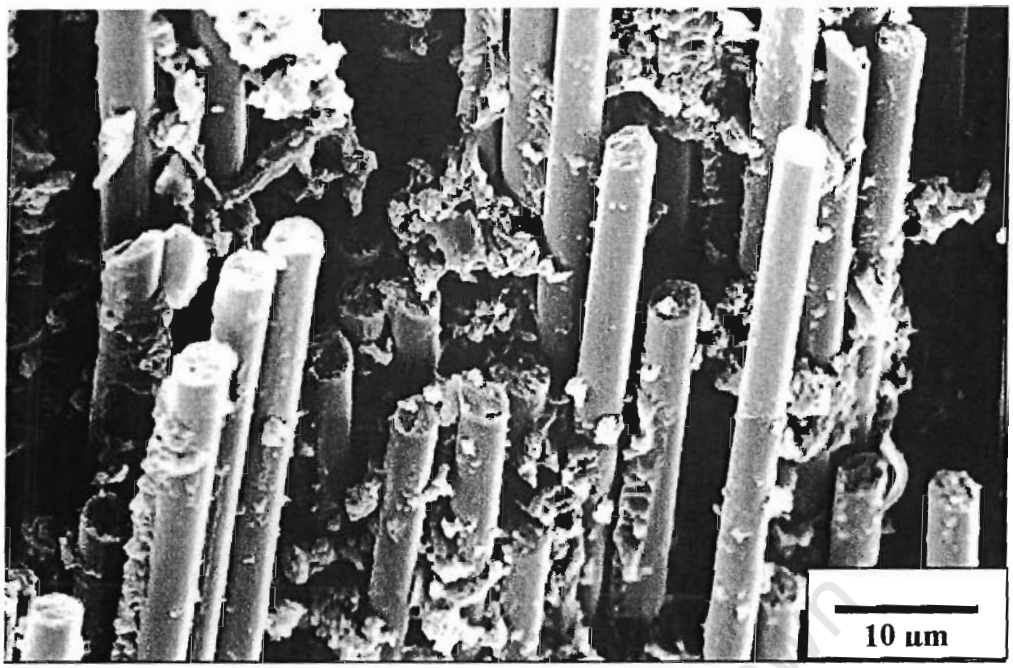

Figure 5.38: Microscopic analysis of the loaded surface of the GFRP specimen showing bundles of fibre pull-out.

5.4.2.6. DERIVATION OF CONSTANTS OF GFRP IN TENSION

The three curves in Figure 5.39 follow the relationships below:

$$\sigma'_{0\,upper} = 0.08\dot{\varepsilon} + 779 \tag{5.20}$$

$$\sigma'_{0\,median} = 0.08\dot{\varepsilon} + 770 \tag{5.21}$$

$$\sigma'_{0\,lower} = 0.08\dot{\varepsilon} + 763 \tag{5.22}$$

Equations (5.20), (5.21) and (5.22) translate in to the linear graphs shown in Figure 5.40. This graphs results in q and D values of 1 and 9228, respectively. The two constants will thus be referred to as q_{tens_gfrp} and D_{tens_gfrp} for the GFRP specimens under tension.

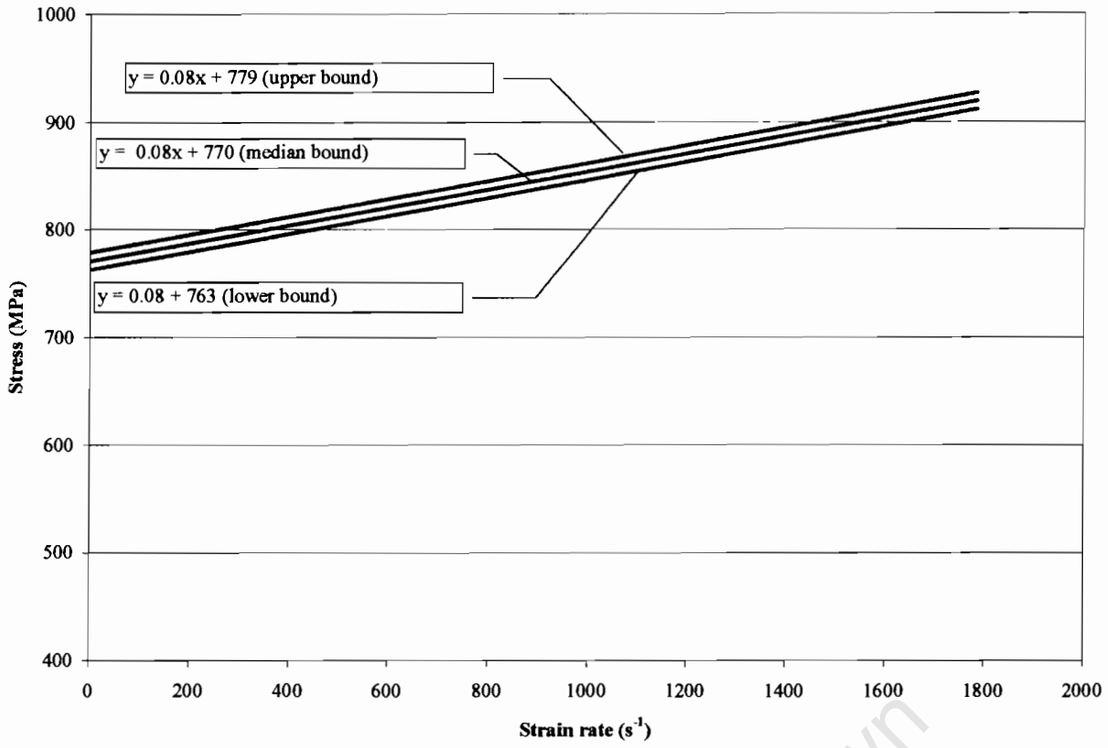

Figure 5.39: Stress vs. strain rate graph for GFRP tensile loading at varying strain rates.

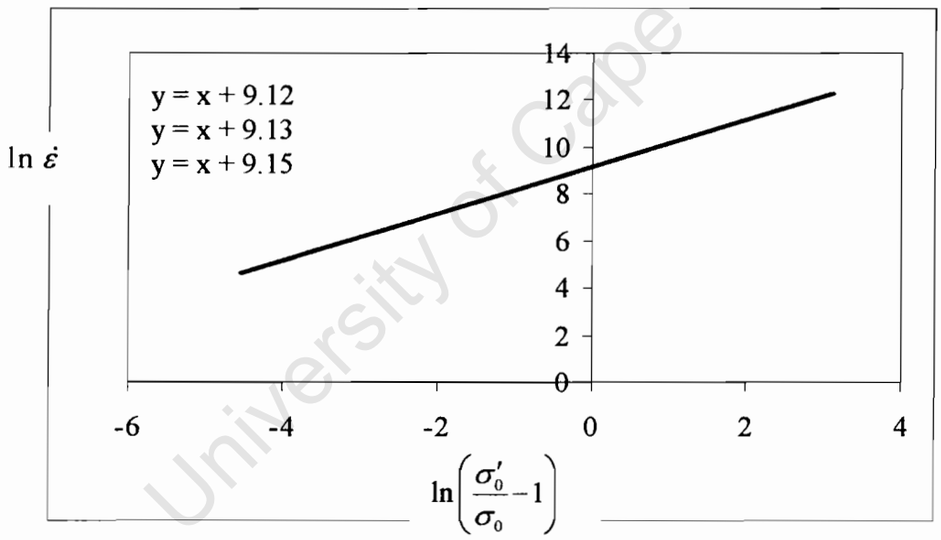

Figure 5.40: Straight-line graph plotted to deduce q and D constants for GFRP under high strain rate tensile loading conditions.

5.5. SUMMARY OF MATERIAL CHARACTERIZATION RESULTS

In total 20 tests at quasi-static strain rates (10^{-3} s^{-1}) were done on CFRP and GFRP in compression, shear and tension, respectively. At dynamic strain rates an average of 5 tests were tested were carried out for 30 different dynamic strain rates. The results show increases in strength with strain rate for CFRP in compression and shear, whilst increases in strength with strain rate are recorded for GFRP under compression, shear and tensile loading conditions. These results have been summarised in Table 5.13.

Table 5.13: Summary of material characterization results.

Loading condition	**Quasi-static strength CFRP (SD) (MPa)**	**Quasi-static strength GFRP (SD) (MPa)**	**Dynamic strength > 10^3 s^{-1} CFRP (MPa)**	**Dynamic strength > 10^3 s^{-1} GFRP (MPa)**
Compression	903 (56)	915 (69)	>1200	>1200
Shear	52 (6.9)	49.2 (6.5)	>88	>100
Tension	1292 (88)	756 (29.6)	>1300	>850

The following q and D constants were determined from the experimental work these results are presented Table 5.14. The degree of strain rate sensitivity may be determined by the q and D constants that have been determined from the experimental data. Recalling the Cowper-Symonds equation in a recast form

$$\frac{\sigma_0'}{\sigma_0} = 1 + \left(\frac{\dot{\varepsilon}}{D}\right)^{1/q} \tag{5.23}$$

Equation (5.23) shows that $\sigma_0' = 2\sigma_0$ when $\dot{\varepsilon} = D$, regardless of the value of q. For example the dynamic stress of CFRP (σ_0') in compression would double at a strain rate of 1863 s^{-1}. On the other hand the dynamic shear strength of GFRP would double at strain rates of 622 s^{-1}. The q and

D (s^{-1}) constants allow the determination of the degree of strain rate in a system. The higher the D (s^{-1}) constant the less strain rate sensitive the material as compared to a D constant of a different system, in the case laminate materials at different loading directions. It is suggested that the success of the Cowper-Symonds equation, for the particular CFRP and GFRP systems, is therefore based on the comparative nature of derived q and D constants. Secondly, the constitutive relation places a relatively small demand on the experimental test programmes. The data from the experimental tests gives reasonable agreement with available experimental data. Finally, the constitutive equation was based on examining the behaviour of FRP under various simple dynamic loads for, compression, shear and tension. The data from these experiments undergoes the same procedure followed by Cowper-Symonds. This relation has been used successfully to determine q and D constants for materials that are not strain rate sensitive as well as materials that show non-linear increases in strain rate, all based on previous experimental work undertaken by numerous researchers [93]. Table 5.14 shows that the influence of strain rate sensitivity manifests itself as a strengthening effect however, to differing extents. Both CFRP and GFRP are strain rate sensitive in shear and compression, with the GFRP showing a certain degree of strain rate sensitivity in tension. The high value of D for CFRP in tension suggests that it is not strain rate effect sensitive.

Table 5.14: Summary of q and D constants determined from the experimental work carried out in this chapter.

Constants	Compression	Shear	Tension
q_{cfrp}	0.75	0.7±0.13	1
q_{gfrp}	0.65	0.5	1
D_{cfrp}	1863	688±42	54279±19072
D_{gfrp}	2173	622	9228

In conclusion one of the principal aims of these experiments was to identify and compare the ultimate strengths with varying strain rates. Secondly, to investigate the fracture behaviour of CFRP and GFRP composites to determine how failure mechanisms such as fibre breakage and pull-out noted in Figure 5.30 and Figure 5.38, respectively, vary with strain rate.

5.6. IMPACT BENDING TEST RESULTS

In order to verify the results of the numerical calculation (to be described in the next section) impact bending tests on CFRP and GFRP specimens were performed. The specimens were tested on the Hopkinson device. The measured data was analysed by employing the 1D wave theory as described in chapter 3.

5.6.1. EXPERIMENTAL TESTING OF FRP PLATES

FRP plate specimens made from CFRP and GFRP where manufactured for impact bending tests. The average geometry and impact velocities used in this experimental set-up are depicted in Table 5.15. Preliminary tests showed that impact velocities of 12 ms^{-1} delivered sufficient energy to deform and just fracture the FRP specimens. The purpose of the plate impact tests was to verify the numerical model. Therefore this velocity was kept constant at 12 ms^{-1} resulting in sufficient initial failure of the FRP plate specimens (see *APENDIX XII*). The measured signal was filtered and the force deflection calculation is used to depict the behaviour of the FRP plate specimens. An average force of 3100 N is determined from the force deflection graph (Figure 5.41).

Table 5.15: Plate impact specimen geometry and impact velocity for CFRP and GFRP plates used in the plate impact test.

Specimen (mm)	Thickness (mm)	Width (mm)	Length (mm)	Weight (g)	Velocity (ms^{-1})
CFRP	5.99	99.18	99.36	52.74	12.1
GFRP	6.01	99.26	99.51	34.59	11.9

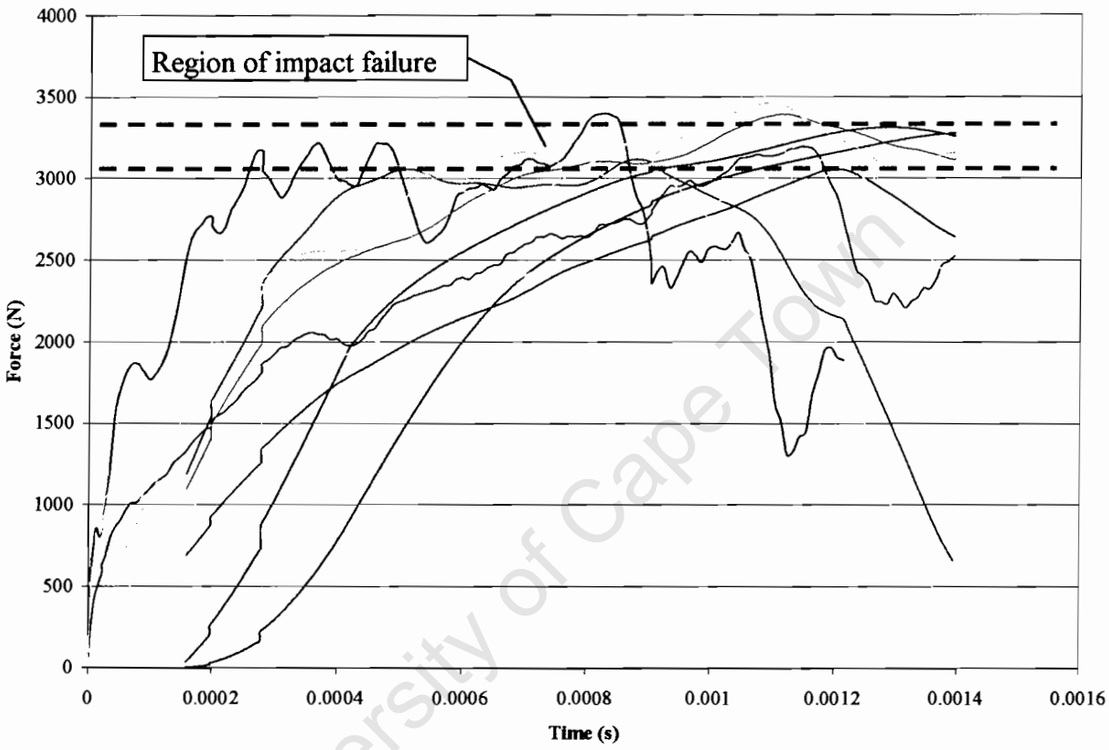

Figure 5.41: Force–deflection graph showing plate impact tests results of GFRP specimen.

CHAPTER 6

NUMERICAL ANALYSIS AND RESULTS

6.1. ABAQUS/EXPLICIT

ABAQUS/Explicit uses an explicit dynamic finite element spatial sub-discretised and central difference explicit time integration scheme formulation. This makes it suitable for analysis of short, transient dynamic events such as high strain rate impact events. These events have been described and simulated in laboratory conditions in chapters 4 and 5. Explicit methods require a small time increment size that is dependent on the highest natural frequency of the model and is independent of the type and duration of loading. The loads in chapter 4 were applied rapidly as a result the structural change are severe. Any subsequent finite element analysis requires fast tracking of stress waves within the system in order to capture the dynamic response [106].

6.1.1. STRESS WAVE PROPAGATION

The explicit method can be explained by considering a force, P, propagating through a model. The state of the force is monitored incrementally through a given time. In the first time increment the first node closest to the point of application of the load has a given acceleration, $\ddot{u}_1$. The acceleration causes the node to have a velocity, $\dot{u}_1$, which in turn causes a strain rate, $\dot{\varepsilon}_{el1}$, in the subsequent element [107]. Consequently, the strain in the element, $d\varepsilon_{el1}$, is obtained by integrating the strain rate through the time of the first increment. The total strain, ε_{el1}, is the sum of the initial strain, ε_0 and the strain increment. In the first increment the initial strain is zero. Once the strain is calculated, the element stress, σ_{el1}, is obtained by applying the relevant material constitutive model. M_1 and M_2 represent the mass of the elements. For a simple case such as linear elasticity, the stress is deduced from the elastic modulus multiplied by the total strain, equation (6.1).

$$\ddot{u}_1 = \frac{P}{M_1} \Rightarrow \dot{u}_1 = \int \ddot{u}_1 dt \Rightarrow \dot{\varepsilon}_{el1} = \frac{\dot{u}_1}{l} \Rightarrow d\varepsilon_{el1} = \int \dot{\varepsilon}_{el1}$$
$$\Rightarrow \varepsilon_{el1} = \varepsilon_0 + d\varepsilon_{el1} \Rightarrow \sigma_{el1} = E\varepsilon_{el1} \tag{6.1}$$

In the second increment, the stresses in the first element apply internal forces to the rest of the nodes ($P - F_{el1}$). Equation (6.2) is associated with the element. The element stresses are then used to calculate the dynamic equilibrium of all the nodes in this element. The process continues so that at the start of the next increment there are stresses and forces in subsequent elements and nodes, respectively. The analysis will be discontinued at the desired total time.

$$\ddot{u}_1 = \frac{P - F_{el}}{M_1} \Rightarrow \dot{u} = \dot{u}_1^{old} + \int \ddot{u}_1 dt$$
$$\ddot{u}_2 = \frac{F_{el1}}{M_2} \Rightarrow \dot{u}_2 = \int \ddot{u}_1 dt$$
$$\dot{\varepsilon}_{el1} = \frac{\dot{u}_2 - \dot{u}_1}{l} \Rightarrow d\varepsilon_{el1} = \int \dot{\varepsilon}_{el1} dt \tag{6.2}$$
$$\Rightarrow \varepsilon_{el1} = \varepsilon_1 + d\varepsilon_{el1}$$
$$\Rightarrow \sigma_{el1} = E\varepsilon_{el1}$$

6.1.2. TIME INTEGRATION

A central difference rule is used by ABAQUS/Explicit to integrate the equations of motion explicitly through time. This is by using the kinematic conditions at one increment to calculate the kinematic conditions at the next increment [106]. The term "explicit" refers to the fact that the state at the end of the increment is based solely on the displacements, velocities and accelerations of the preceding increment. This method integrates constant accelerations exactly. For the method to produce accurate results, the time increments must be sufficiently small so that the accelerations are nearly constant during an increment (see *APPENDIX VI* for a more detailed outline of the time integration procedure).

6.1.3. PRE-PROCESSOR

The ABAQUS/CAE is utilized as a pre-processor to create the geometry of the test specimen and specify material data and boundary conditions. This program has the ability to develop the required input file that is modified by introducing various vectorised user material sub routines that house the material models. These material models describe the nature of the orthotropic behaviour as well as introduce the required progressive failure criteria.

6.1.4. ABAQUS EXPLICIT LIMITATIONS

ABAQUS/Explicit does not have the option of enabling various laminate layers within one continuum element. Therefore each element is taken to be one layer thick [108]. This introduces two drawbacks, the model is computationally expensive and secondly the model has a high aspect ratio in thick laminates. A three dimensional continuum 8 node tri-linear displacement brick element (C3D8R) with reduced integration and hourglass control are employed in all the analysis.

6.1.5. POST-PROCESSING PROCEDURE

In each case the results are analysed using the ABAQUS/viewer post processor. This has the ability of viewing contour plots of the stress and strain state at various time states or time histories for the duration of the simulations. The default setting of ABAQUS/viewer is to average the values occurring at the central integration point of an element to the element nodes for continuity. The data from the time history plots is extracted by means of an ASCII file and graphed along with the experimental data using Microsoft EXCEL, as well the ABAQUS/CAE built-in graphing option.

6.2. HOURGLASSING

Linear reduced-integration elements are prone to a pattern of non-physical deformation called hourglassing under certain loading conditions. Figure 6.1 shows the physical elucidation. Consider a single first order, reduced integration element modelling a small piece of material exposed to pure bending. The dotted visualization lines are seen to pass through the single integration point in the element.

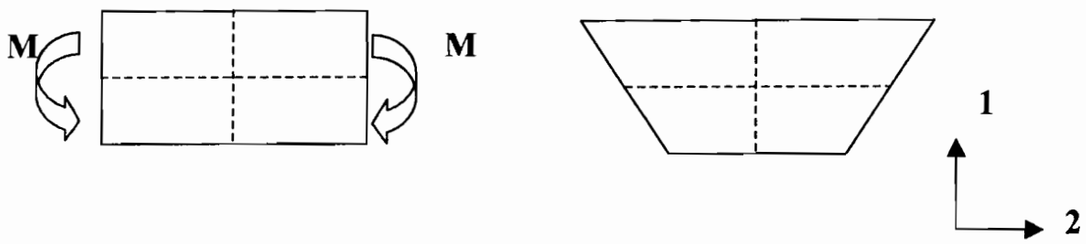

Figure 6.1: First-order element deformed with reduced integration subjected to a bending moment.

Regardless of the deformation of the element, neither of the dotted visualisation lines changes in length nor the angle between them. This form of deformation is therefore a zero energy mode, "hourglassing", because no strain energy is generated by distorting the element in this manner [109]. The element is unable to resist this type of deformation since it has no stiffness in this mode. In coarser meshes this zero-energy mode can propagate through the mesh, producing incorrect results. ABAQUS/Explicit includes sophisticated controls to prevent hourglassing from being a problem such as the first-order reduced integration quadrilateral and hexahedral elements with hourglass modes built-in. However, in some cases hourglassing can propagate through the mesh before the built-in control can correct the problem. The built-in controls work by applying corrective forces and may take few increments to control hourglassing [109]. In this case, monitoring the ratio of the artificial to elastic strain energy as well as the mesh distortion becomes imperative.

6.3. DETERMINATION OF STABILITY

When modelling complex materials under explicit loading conditions the degree of stability in the structure is monitored to ensure realistic results [106]. The kinetic energy may be used to determine the degree of stability in the system. The advantage of monitoring the kinetic energy over monitoring a particular degree of freedom is that the kinetic energy is the summation of the kinetic energy over the entire model (see *APPENDIX XIII*).

6.4. PARAMETRIC STUDY

A parametric study is undertaken in ABAQUS/Explicit and automated using the ABAQUS Scripting Interface. The ABAQUS Scripting Interface is an extension of the Python object-oriented programming language. It allows automation of repetitive tasks such as parametric studies. Parametric studies were carried out on the models to assess the effects of the mesh density on the failure stress of the material and secondly to assess the effects of the initial velocity (to simulate the change in strain rate) as a function of failure stress. Therefore only two parameters change in the parametric study carried out in these modelling sequences, the mesh density and the initial velocity. The Scripting Interface developed (see *APPENDIX IX*) incrementally modifies the mesh density and initial velocity of the part referring to the object being modelled in the FEA.

Figure 6.2 shows the relationship between increasing mesh density and the failure strength of CFRP under high loading compression. The failure strength is seen to increase with a reduction in the element size or increase in mesh density. This observation is in line with the literature, which states that when using continuum elements with reduced-integration (C3D8R), the mesh density should be increased [110]. However, the graph in Figure 6.2 shows that an optimum mesh density exists beyond which the stress appears to remain constant regardless of the reduction in the mesh density. The advantage of this optimum mesh density value is the reduction in run time.

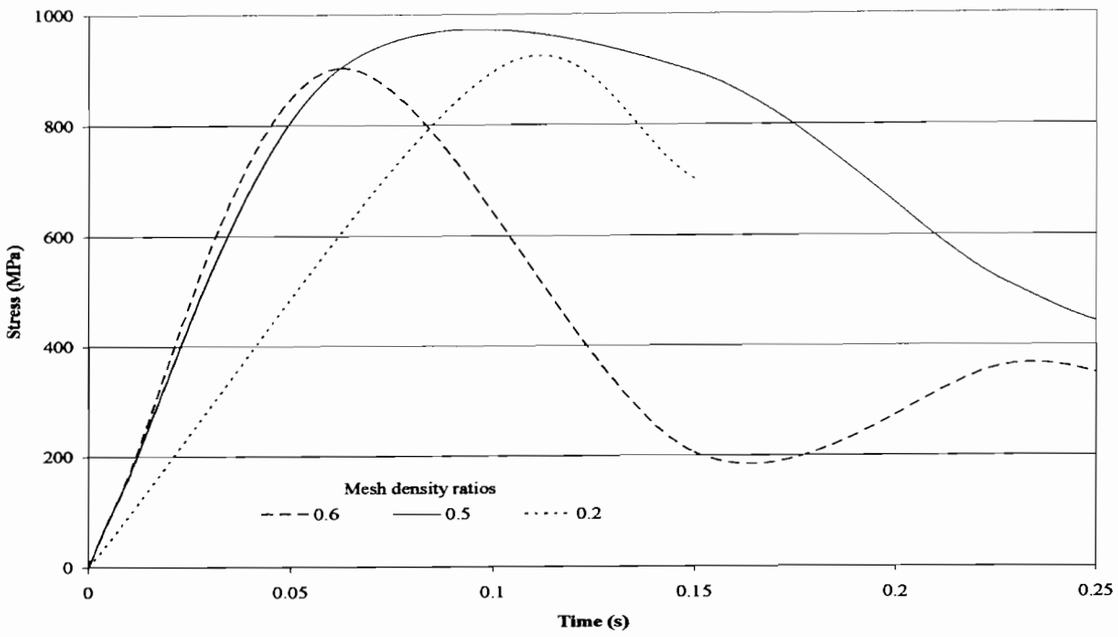

Figure 6.2: Mesh density versus failure strength for CFRP under high loading.

6.5. PATCH TEST

The patch test is applied numerically to test the final form of an element. The basic requirements for its satisfaction, by shape function, (introduced in chapter 3) that violate compatibility can be forecast accurately if certain conditions are satisfied in the choice of such functions. These conditions follow from the requirement that for constant strain states, the virtual work done by internal forces acting at the discontinuity must be zero [111]. The patch test done however considers the element from a "non-isoparametric element" state.

The patch test is performed numerically on a single C3D8R element. Consider this element in a single-patch subjected to constrained boundary conditions, in which all displacements on the external boundary of the patch are prescribed. The simplest loading case is considered for the 3-D solid continuum element. Due to the development of the user material, the patch test undertaken is a comparative study between the ABAQUS/verification patch test on three-dimensional solid elements and the C3D8R element developed in this thesis (through the user material or VUMAT)

[112]. The C3D8R element developed in this thesis follows the constitutive equation described in section 3.5 of chapter 3.

The following loading and analytical solutions are performed and compared to the ABAQUS/Verification analysis [112]. The user material developed allows for failure after a certain stress has been achieved. Therefore the patch test compares the user material without damage to the built-in ABAQUS/Explicit orthotropic element. These are both essentially linear elastic models.

The elements are seen to yield exact solutions with respect to the maximum displacement in Figure 6.3. The built-in orthotropic linear elastic element of ABAQUS/Explicit and the user material element developed in this thesis, yield the same results. This is shown in Figure 6.3 for one element loaded parallel to the fibre direction. The displacement of both elements yields a maximum displacement of -1000 mm, due to the compressive displacement applied to one end of the element. The element therefore passes this patch test.

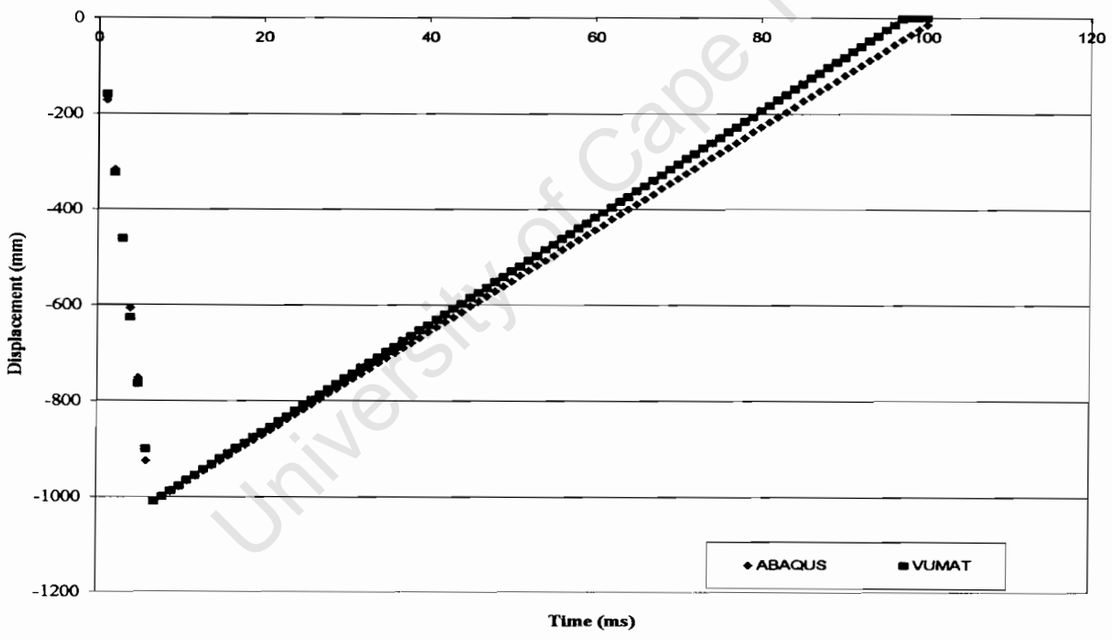

Figure 6.3: Displacement vs. Time graph for comparison of VUMAT against the linear elastic option built-in to ABAQUS used for validating the VUMAT.

A second patch test involves applying an impact load on a single element from a rigid impactor of a certain diameter. Figure 6.4 shows that the kinetic energy of both the user material and built-in ABAQUS elements are identical with an increase in time. The numerical patch test demonstrates simply that the user material element is robust as compared to the built-in ABAQUS/Explicit element. Under identical impact conditions both elements are seen to increase the kinetic energy with time up to 0.04 kilojoules as the impact time increase to 80 milliseconds. *APPENDIX X* shows the loading and analytical conditions for the patch test. Both elements show an identical kinetic energy against time relationship.

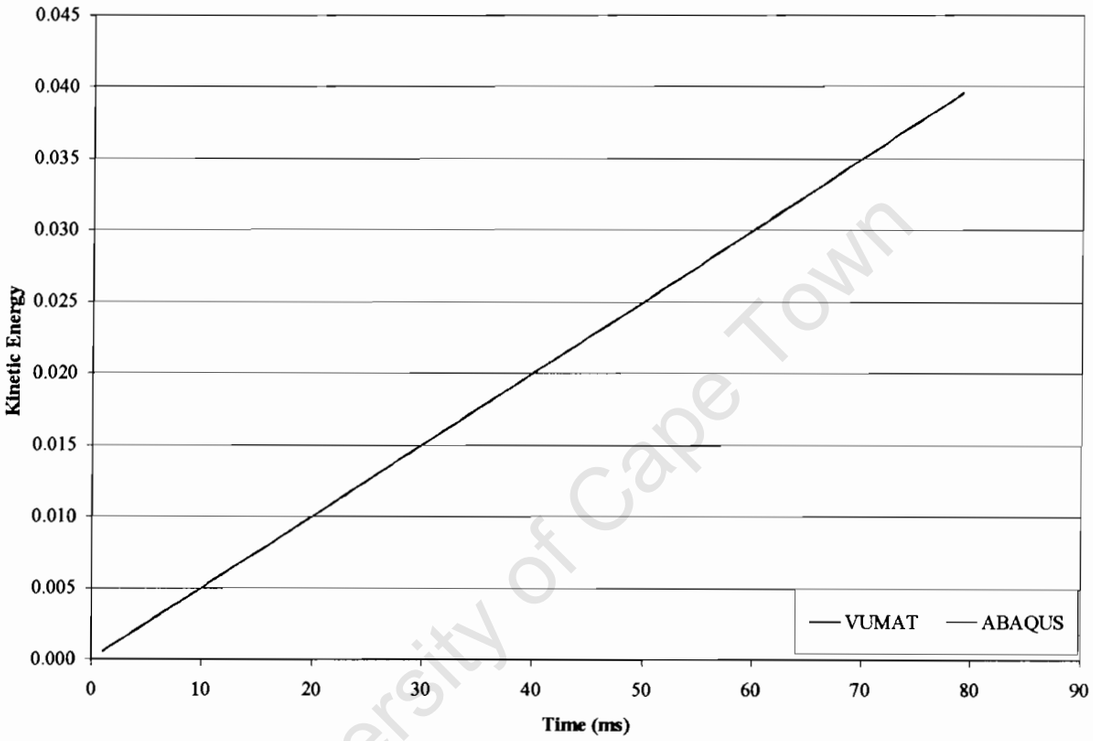

Figure 6.4: Comparison of VUMAT versus Normal ABAQUS Elastic option for rigid body impact on one element. The graph shows the kinetic energy (kJ) against time.

6.6. MATERIAL DATA

The following quasi-static material data, which was attained from the various experimental work, covered in chapter 4 is presented in Table 6.1 and Table 6.2 for CFRP and GFRP, respectively.

Table 6.1: CFRP material data used in the finite element model.

Symbols	Material Properties	Value
E_1	Elastic modulus transverse to the fibres	9.80E9 Pa
E_2	Elastic modulus normal to the fibres	9.80E9 Pa
E_3	Elastic modulus longitudinal to the fibres	125E9 Pa
ν_{12}	Poisson's ratio in the 12 direction	0.218
ν_{13}	Poisson's ratio in the 13 direction	0.020
ν_{23}	Poisson's ratio in the 23 direction	0.020
G_{12}	Shear modulus transverse to the fibres	2.64E9 Pa
G_{13}	Shear modulus normal to the fibres	3.90E9 Pa
G_{23}	Shear modulus longitudinal to the fibres	3.90E9 Pa
ρ	Density of the CFRP	1.82E3 kgm^{-3}
X_T	Longitudinal tensile strength	1289E6 Pa
X_c	Longitudinal compressive strength	902E6 Pa
Y_T	Transverse tensile strength	54.7E6 Pa
Y_C	Transverse compressive strength	231E6 Pa
Z_T	Normal tensile strength	54.7E6 Pa
Z_C	Normal compressive strength	231E6 Pa
S_{23}	Shear strength (23-direction)	51.9E6 Pa
S_{13}	Shear strength (13-direction)	51.9E6 Pa
S_{12}	Shear strength (12-direction)	51.9E6 Pa

Table 6.2: GFRP material data used in the finite element model.

Symbols	Material Properties	Value
E_1	Elastic modulus transverse to the fibres	11.3E9 Pa
E_2	Elastic modulus normal to the fibres	11.3E9 Pa
E_3	Elastic modulus longitudinal to the fibres	43.0E9 Pa
ν_{12}	Poisson's ratio in the 12 direction	0.218
ν_{13}	Poisson's ratio in the 13 direction	0.020
ν_{23}	Poisson's ratio in the 23 direction	0.020
G_{12}	Shear modulus transverse to the fibres	2.43E9 Pa
G_{13}	Shear modulus normal to the fibres	2.86E9 Pa
G_{23}	Shear modulus longitudinal to the fibres	2.86E9 Pa
ρ	Density of the GFRP	2.53E3 kgm^{-3}
X_T	Longitudinal tensile strength	750E6 Pa
X_c	Longitudinal compressive strength	905E6 Pa
Y_T	Transverse tensile strength	49.8E6 Pa
Y_C	Transverse compressive strength	219E6 Pa
Z_T	Normal tensile strength	49.8E6 Pa
Z_C	Normal compressive strength	219E6 Pa
S_{23}	Shear strength (23-direction)	41.5E6 Pa
S_{13}	Shear strength (13-direction)	41.5E6 Pa
S_{12}	Shear strength (12-direction)	41.5E6 Pa

Note: The Cartesian coordinate system is not used; in this case therefore the global direction 1 represents the Cartesian 3 direction.

It is important to note that the loading of the specimen is also applied according to the various curves recorded by the experimental devices shown in the graphs herein. The quasi-static loading for example is deduced from the cross-head speed (CHS) of the universal Instron tester, in this case for strain rates of the order 10^{-3} s^{-1}, the CHS is 0.00054 ms^{-1}. The dynamic loading

conditions follow the velocity time graphs recorded by the split Hopkinson bar velocity acquisition system.

The loading curves for a typical quasi-static and dynamic loading condition are presented in Figure 6.5. These curves are used to represent the boundary conditions of the initial velocities applied to the relevant numerical mesh nodes; this information represents the full loading regime of the quasi-static and dynamic numerical analysis.

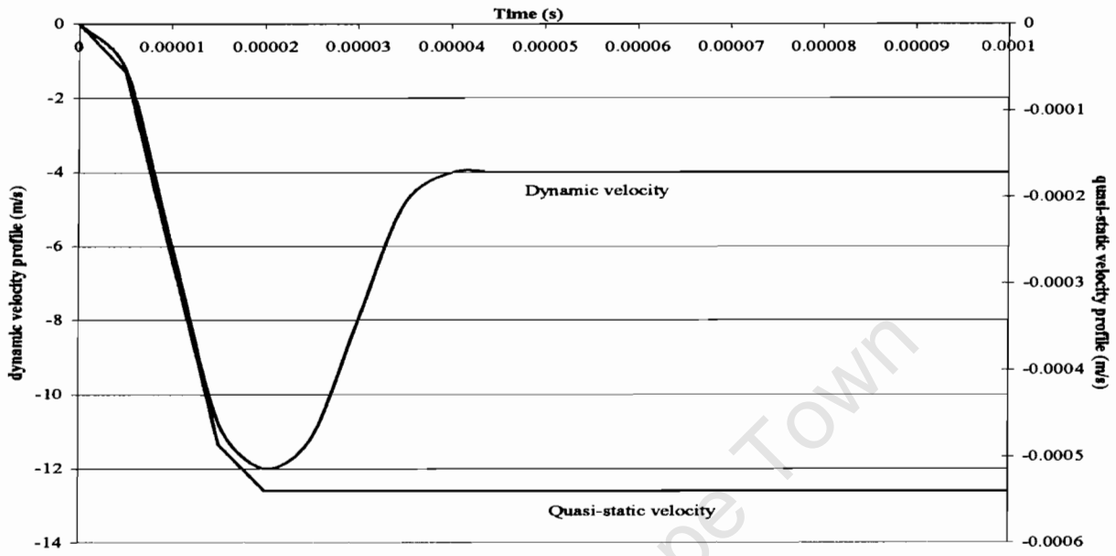

Figure 6.5: Graphs showing loading regime for both quasi-static and dynamic conditions.

6.7. DEVELOPMENT OF VECTORISED USER MATERIAL

ABAQUS/Explicit has an interface that allows for the implementation of a constitutive equation when none of the existing materials models accurately represents the behaviour of the material being modelled. In ABAQUS/Explicit the user defined material model is implemented in a user subroutine known as a vector user material or VUMAT [109]. The VUMAT is developed to model the behaviour of an orthotropic material that fails when the ultimate stress has been achieved according to the modified Chang-Chang criteria. The progressive failure introduced in chapters 2 and 3, includes out-of-plane stresses as presented by Hou [82]. However due to the

strain rate sensitivity established in the experimental results presented in chapter 5, equation (5.7), the VUMAT also incorporates the constitutive equations that account for the increases in ultimate stress as a result of the increasing in strain rate the varying loading regimes.

6.7.1. DESCRIPTION OF VUMAT PROCEDURE

The relevant ABAQUS model is set up to simulate the behaviour of the relevant material specimens as per the experimental procedures presented in chapter 4. The VUMAT is called at the appropriate stage, the part of the program that required the description of the material constitutive behaviour. The VUMAT checks that the elements used are 3D continuum elements. If this criterion is met then the program proceeds to the next stage, otherwise an error is given. The material properties are read into the VUMAT from the ABAQUS code. The strain rate of loading is determined in order to ascertain the material ultimate stress as per the experimental results and constitutive equations that describe the strain rate behaviour of the FRPs. These constitutive equations were developed in chapter 5 (see section 5.2.1.). The D matrix for the 3D element is determined from the equation (3.56) derived in chapter 3.

A check of the state variables defining the material state determines whether failure has occurred. Failure refers to the element exceeding the ultimate stress. The relevant state variable is updated accordingly to ensure that failed elements do not "heal" in the next iteration. Intrinsically due to the explicit procedure the next step involves determining the stress rate for the next step (termed k^{th} step in the flow chart) using the strain rate. An integration step in rate form deduces the stress for all the material directions. A simple check determines whether a compression or tension load has been applied at the integration point. The appropriate material data is used according to the loading condition. The next procedure introduces the rate dependant constitutive equation. This procedure involves implementing the ultimate stress values as a result of the applied strain rate. The Chang-Chang criteria are then applied to interrogate the material state and the relevant stiffness matrix is updated accordingly. The final procedures are inherent to the FEA including an update of the internal specific energy as well as an update of the dissipated inelastic specific energy. A final check and update of the state variables is undertaken. The program then returns to ABAQUS for the next iteration.

6.7.2. SCHEMATIC OF VUMAT PROCEDURE

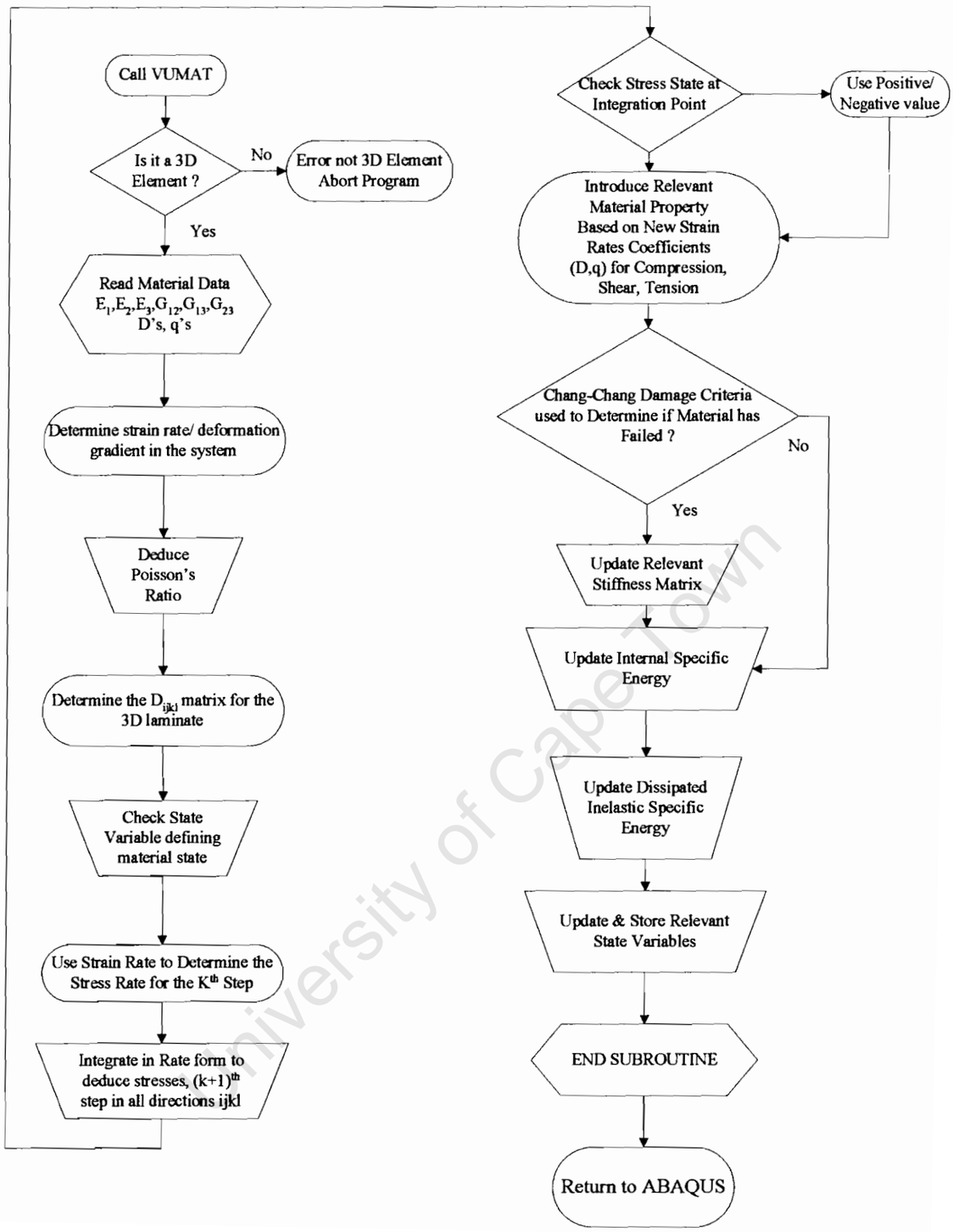

6.7.3. MATHEMATICAL DERIVATION

The VUMAT subroutine mathematical derivation (see *APPENDIX XI* for the VUMAT code) is considered for an orthotropic material with damage and strain rate sensitivity built-in. The basic assumptions and definitions of the model are as follows:

- In general the strain rate is decomposed into an elastic and plastic part using an additive decomposition:

$$\dot{\varepsilon} = \dot{\varepsilon}^{el} + \dot{\varepsilon}^{pl} \tag{6.3}$$

- The plastic part of the strain rate in this case is non-existent due to the brittle nature of the FRP, hence the plastic part of equation (6.3) is:

$$\dot{\varepsilon}^{pl} = 0 \tag{6.4}$$

- In order to determine the strain rate in the system ABAQUS/Explicit will give the various deformation gradient tensors at each material point at the beginning of the increment stored in 3-D as (F_{11}, F_{22}, F_{33}, F_{12}, F_{13}, F_{23}, F_{31}, F_{21}, F_{32}). Furthermore, the various ultimate stresses based on strain rate sensitivity equation, for example the ultimate fibre stress $\sigma_{iiultimate}$ are determined for the particular strain rate condition as follows

$$\sigma_{iiultimate} = (1 + (D/\dot{\varepsilon})^{1/q}).X_T \tag{6.5}$$

where X_T is the quasi-static tensile strength in the fibre direction, D and q are the Cowper-Symonds constants as deduced from chapter 5. The various ultimate strengths are calculated for the particular strain rate according to the inherent strain rate in the system.

- The stress rate is assumed to be purely due to the elastic part of the strain rate and is expressed in terms of:

$$\dot{\sigma}_{ii} = D_{iiii}\left(\dot{\varepsilon}_{ii}^{el}\right) + D_{iijj}\left(\dot{\varepsilon}_{ij}^{el}\right) + D_{iikk}\left(\dot{\varepsilon}_{ik}^{el}\right) \tag{6.6}$$

where D_{ijkl} are the orthotropic material stiffness parameters.

- The orthotropic constitutive model is integrated in a rate form as follows. A trial elastic stress is computed for each principal direction:

$$\sigma_{ii\,new}^{trial} = \sigma_{old} + D_{iiii}\left(\Delta\varepsilon_{ii}\right) + D_{iijj}\left(\Delta\varepsilon_{ij}\right) + D_{iikk}\left(\Delta\varepsilon_{ik}\right) \tag{6.7}$$

$$\sigma_{jj\,new}^{trial} = \sigma_{old} + D_{jjjj}\left(\Delta\varepsilon_{jj}\right) + D_{iijj}\left(\Delta\varepsilon_{ij}\right) + D_{jjkk}\left(\Delta\varepsilon_{jk}\right) \tag{6.8}$$

$$\sigma_{kk\,new}^{trial} = \sigma_{old} + D_{kkkk}\left(\Delta\varepsilon_{kk}\right) + D_{iikk}\left(\Delta\varepsilon_{ik}\right) + D_{jjkk}\left(\Delta\varepsilon_{jk}\right) \tag{6.9}$$

$$\sigma_{ij\,new}^{trial} = \sigma_{old} + D_{ijij}\left(\Delta\varepsilon_{ij}\right) \tag{6.10}$$

$$\sigma_{ik\,new}^{trial} = \sigma_{old} + D_{ikik}\left(\Delta\varepsilon_{ik}\right) \tag{6.11}$$

$$\sigma_{jk\,new}^{trial} = \sigma_{old} + D_{jkjk}\left(\Delta\varepsilon_{jk}\right) \tag{6.12}$$

where the subscripts *old* and *new* refer to the beginning and end of the increment, respectively. If the trial stress does not exceed the yield stress the new stress is set to the trial stress. If the ultimate stress is exceeded the failure criteria is introduced, therefore if:

$$\sigma_{ii\,new} > \sigma_{iiultimate} \tag{6.13}$$

then

$$D_{iiii} \Rightarrow 0 \tag{6.14}$$

$$D_{jjjj} \Rightarrow 0 \tag{6.15}$$

$$D_{kkkk} \Rightarrow 0 \tag{6.16}$$

$$D_{iijj} \Rightarrow 0 \tag{6.17}$$

$$D_{iikk} \Rightarrow 0 \tag{6.18}$$

$$D_{jjkk} \Rightarrow 0 \tag{6.19}$$

$$D_{ijij} \Rightarrow 0 \tag{6.20}$$

$$D_{ikik} \Rightarrow 0 \tag{6.21}$$

$$D_{jkjk} \Rightarrow 0 \tag{6.22}$$

These conditions are determined for all the laminate directions, viz. $i,j,k \equiv 1,2,3$ accordingly.

6.8. MODELLING OF COMPRESSION TESTS

6.8.1. MESH GENERATION

Unidirectional cylinders of CFRP and GFRP are modelled using the commercial package ABAQUS/Explicit. The dimensions of the compression specimens used in the model for both CFRP and GFRP are identical to the experimental test specimen, viz. a diameter 8 mm and a length 9 mm. Compression modelling was undertaken using the mesh shown in Figure 6.6, with 3220 nodes and 2475 continuum elements (C3D8R). One end of the specimen is loaded (see direction of the arrow in Figure 6.6), whereas the opposite end has its nodes held encastré (direction 3 represents the direction of the fibres),

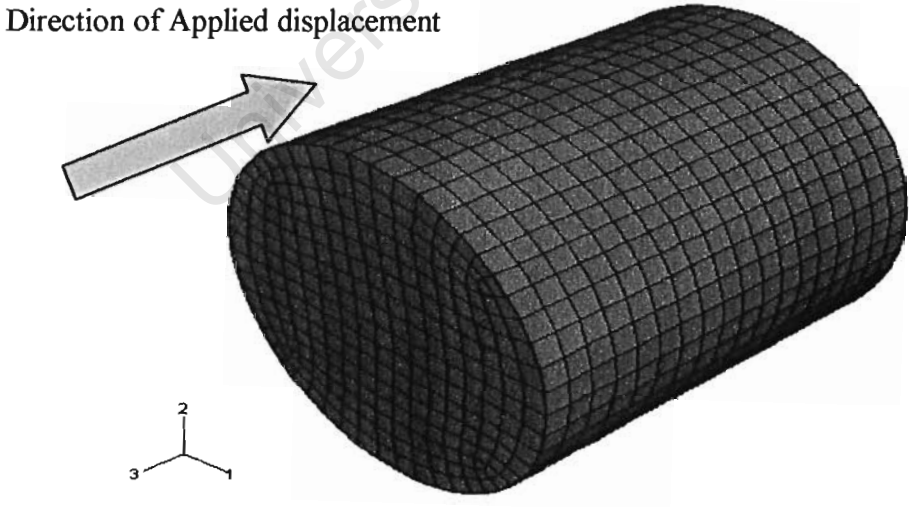

Figure 6.6: Model of the compression specimen used in ABAQUS/Explicit. Note the 3-direction is equivalent to the fibre direction (0-degrees).

6.8.2. LINEAR QUASI-STATIC MODEL

The initial loading conditions of the model were based on the quasi-static conditions (see chapter 4 Experimental Procedure), which concentrated on a simple linear analysis to elucidate the need for damage. The results of this analysis show that the onset of initial damage is undefined from the stress strain graph (Figure 6.7). The stress strain relation will continue to rise infinitely with a constant gradient equivalent to the Young's modulus given in the material property data. The stress–strain graph in Figure 6.7 depicts a typical stress analysis of a linear elastic orthotropic material (CFRP). This model does not account for the non-linearity associated with brittle fracture and is therefore of limited use. The experimental results distribution (chapter 5) is placed in Figure 6.7 to show the expected region of failure, viz. the ultimate stress.

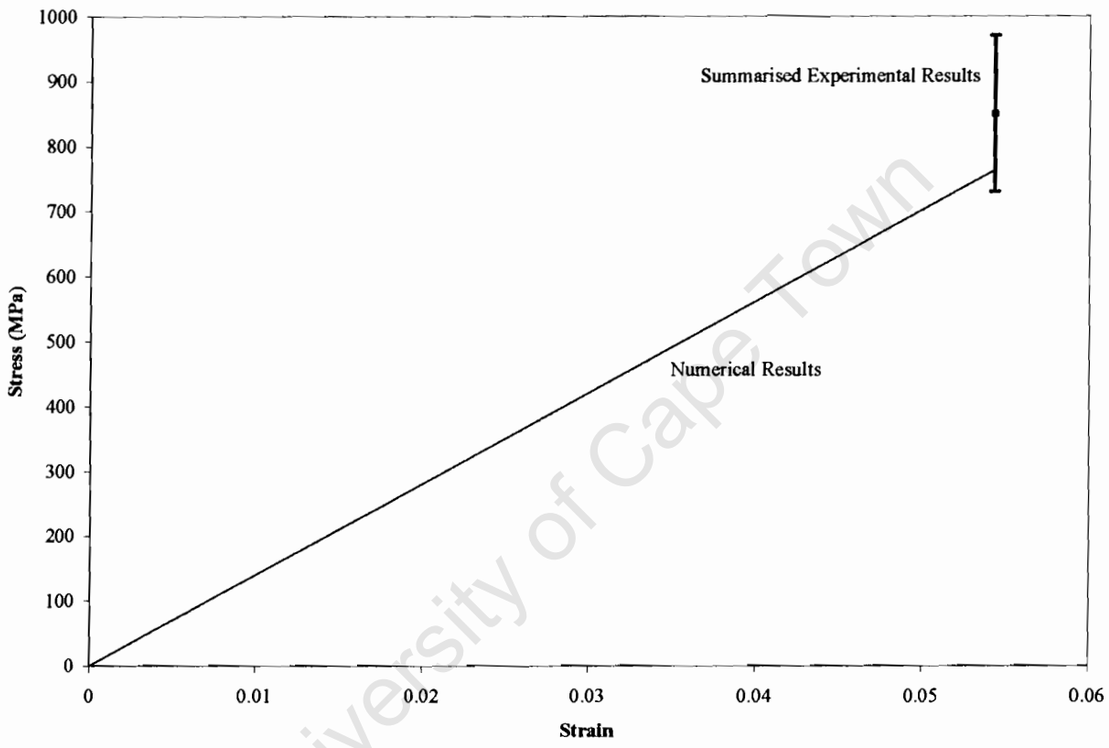

Figure 6.7: Graph showing comparison between ABAQUS/Explicit and summarised experimental results. The graph will continue to rise according to the gradient given by the Young's modulus. A drop in stress with increasing strain which is synonymous with failure is unattainable with this linear model.

6.8.3. NON-LINEAR QUASI-STATIC ANALYSIS

Most composite structures are brittle and as a result they fracture in a non-linear manner. A quasi-static compression model that includes damage through progressive damage failure criteria is therefore developed to predict the onset of failure accurately. It is important to note that the criteria uses a stress-based criteria therefore the accuracy of the strain to failure values are of limited use.

6.8.4. TIME HISTORY COMPARISONS

The time history comparison of the non-linear criteria that is included through the VUMAT subroutine results in better correlation with the experimental results as compared to the linear model. A comparison of the numerical and experimental results for a GFRP specimen is presented in Figure 6.8 for a non-linear quasi-static compression situation. The numerical stress-strain data show good correlation with the experimental data throughout the loading regime. Point A in Figure 6.8 reveals the initiation of damage at a stress value of 890 MPa. This value is synonymous with fibre buckling under compression loading.

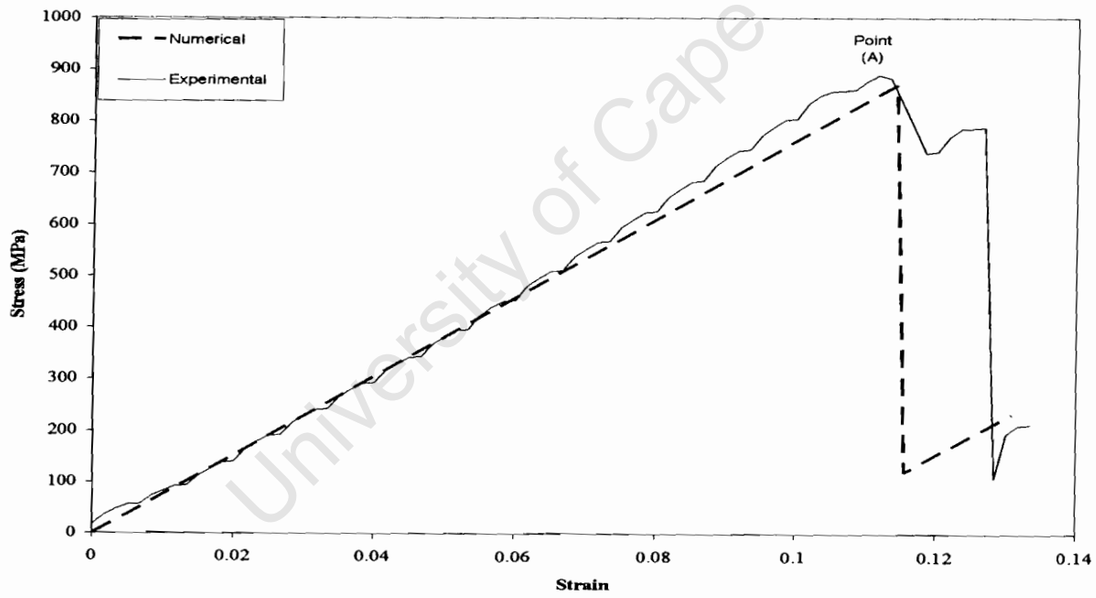

Figure 6.8: Stress-strain graph of quasi-static compression showing the comparison between experimental vs. FE model with damage.

6.8.5. DAMAGE PREDICTION

Analysis of the contour plots gives an indication of the state of damage or progression of damage through the material. The contour plot shown in Figure 6.9 gives the stress distribution in the compression specimen under dynamic loadings of 1000 s^{-1}. This model includes damage. Damage refers to the application of the progressive damage criteria, where as non-damage applies to the linear loading case. Small regions where tensile stresses occur in the system are visible from the contour plot. The maximum recorded tensile stress in the numerical model occurs at 1295 MPa. However, the dominating mode of failure in the CFRP model is due to compressive failure of the fibres. The compressive ultimate stress of the CFRP in fibre direction is 1255 MPa. The contour plot in Figure 6.9 shows regions that represent the maximum ultimate compressive stress in the system.

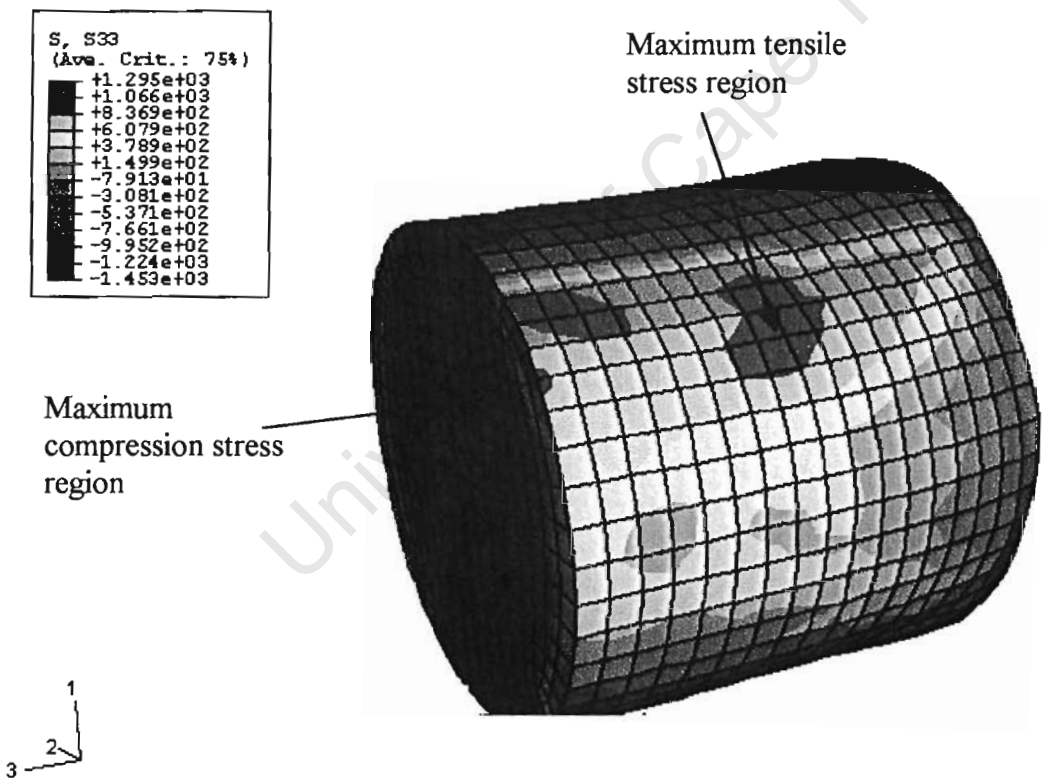

Figure 6.9: A typical contour plot of the compressive strength loaded in the 3-direction for CFRP, the fibres are aligned in the 3-direction. The contour plot represents the behaviour of at dynamic strain rates of 1000 s^{-1}.

The numerical analysis allows for the monitoring of the displacement of the nodes in the specimen. The contour plot presented in Figure 6.10 represents a time of 150 μs after the impact load is applied, through a compression velocity. The displacement contour plot reveals an equal displacement of the nodes in the 2-direction. At this time stage the node displacement of both ends, left hand side without damage (L_n) and right hand side without damage (R_n), with respect to the 2-direction, are equal to 0.009542 mm with respect to its initial position.

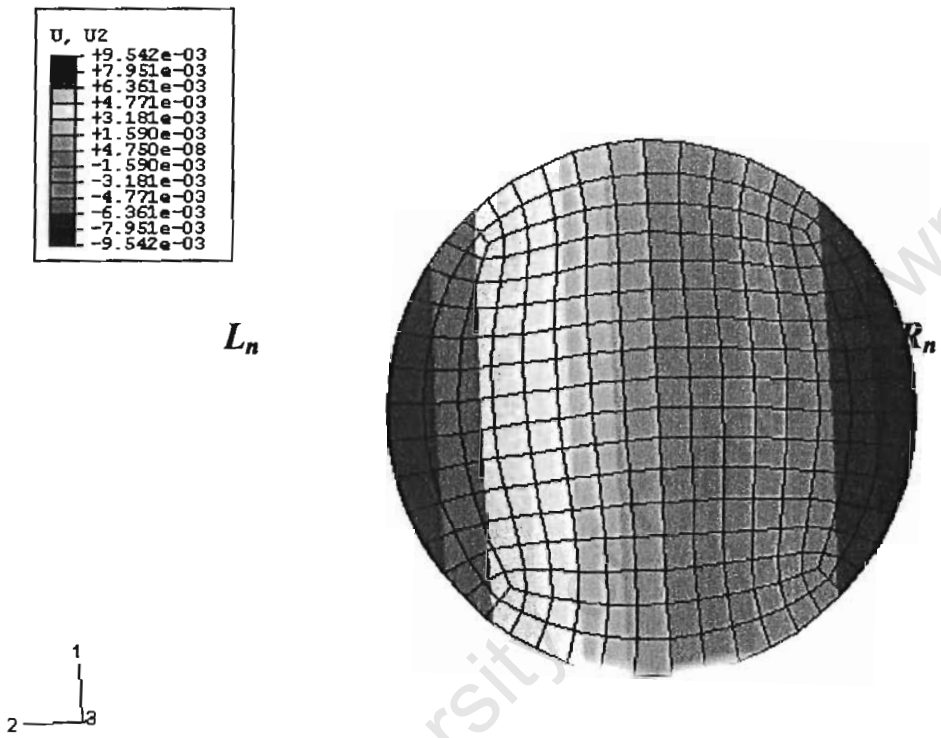

Figure 6.10: Contour plot of displacement in the 2-direction for CFRP specimen without damage.

The contour plot in Figure 6.11 shows the displacement of the nodes for a compression model with damage. The outer circumference of the compression material depicts varying displacements, with the side labelled L_d (left hand side with damage included) having its nodes displaced by 0.2 mm in Figure 6.11 more than the equivalent side labelled L_n in Figure 6.10. A comparison of the contour plot that includes damage and one without damage reveals the extent of non-linearity. The analysis reinforces the need for a damage model to account for the non-

linearity that results from the degradation of the materials stiffness parameters according to the principals of progressive damage criteria. The contour plot in Figure 6.11 is representative of all compression numerical iterations analysed at quasi-static to dynamic strain rates with damage.

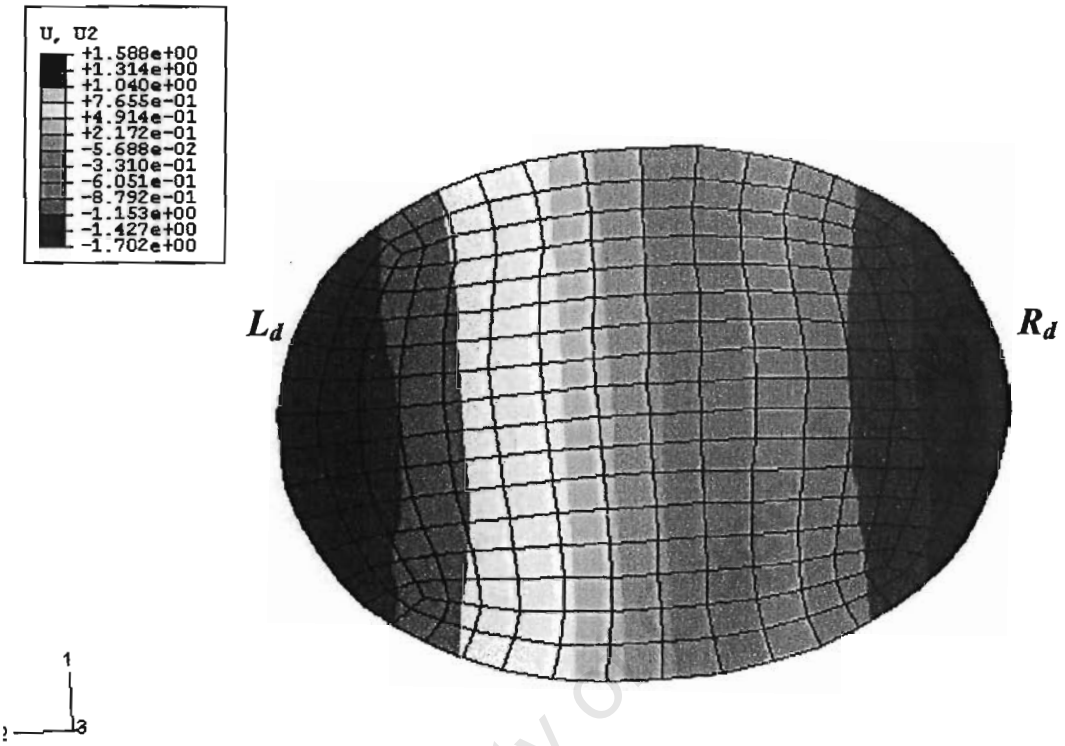

Figure 6.11: Contour plot of the displacement in the 2-direction of CFRP with damage.

The initial conditions for loading are presented in Figure 6.12. The contraction velocity versus time graph shows the loading conditions of a compression CFRP specimen as recorded by the SHPB device. Experimental results for two loading cases for specimens C_0_1_B and C_0_1_E (compression specimens labels). These specimens have maximum contraction velocities of 12 ms^{-1} and 13.5 ms^{-1}, respectively. The numerical model applies the experimental initial velocities depicted in Figure 6.12 to both the damaged and non-damaged numerical simulation. In this particular case the numerical model is based on the experimental contraction velocity history of specimen C_0_1_B. Specimen C_0_1_E undergoes the higher loading rate.

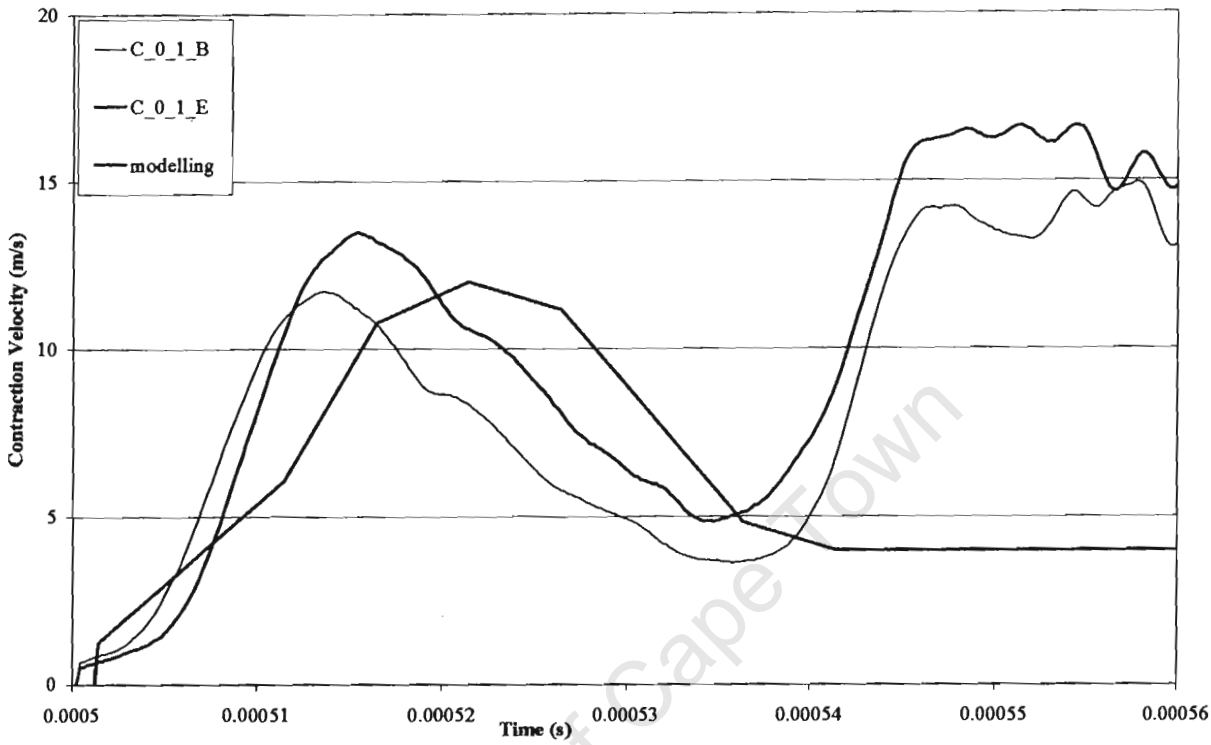

Figure 6.12: Comparative study of contraction velocity versus time, in the form of a graph giving loading conditions for numerical modelling with damage and without damage, as well as two experimental tests results.

Analysis of Figure 6.13 allows for the deduction of the contraction regime of the compression specimen. The damaged and non-damaged numerical analysis loading conditions are identical, therefore these graphs lie on top of each other. The contraction for the damaged numerical analysis follows a similar trend as that of the numerical analysis that excludes damage. Figure 6.13 is simply the integration with respect to time of the contraction velocity versus time graph shown in Figure 6.12. Numerical analysis using either damaged or non-damaged parameters results does not result in a significant discrepancy in the contraction versus time output.

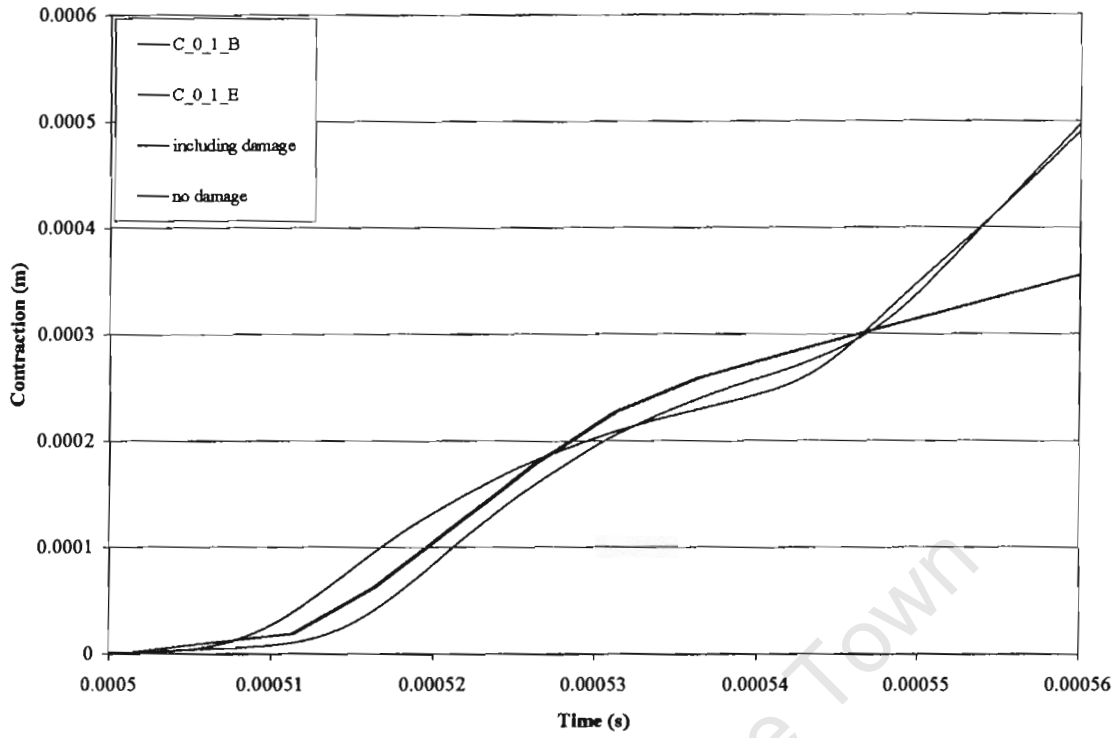

Figure 6.13: Comparative study of contraction versus time, for a compression specimen numerical modelled with damage and without damage, as well as two experimental tests results.

The nominal stress versus time data is presented in the form of a graph shown in Figure 6.14. The peak of the nominal stress time data represents the ultimate stress. The experimental specimens C_0_1_B and C_0_1_E show peaks of approximately 900 MPa and 1180 MPa, respectively. The non-damaged numerical analysis nominal stress continues to rise after 530 μs. The numerical model that includes damage however, shows a drop in nominal stress at approximately 527 μs. The numerical model results with damage shows a peak at 970 MPa, this corresponds to the ultimate stress of the FRP. Thereafter the material is deemed to have undergone brittle failure.

The ultimate stresses for the series of numerical tests data with damage are presented with the experimental data for compression determined in the experimental tests carried out in chapter 4. This data is presented in the form of a stress strain graph shown in Figure 6.15. The GFRP data lies on the primary y-axis where as the CFRP data lies on the secondary y-axis. The ultimate

stress values of all the numerical modelling results are presented in the form of points on graph in Figure 6.15.

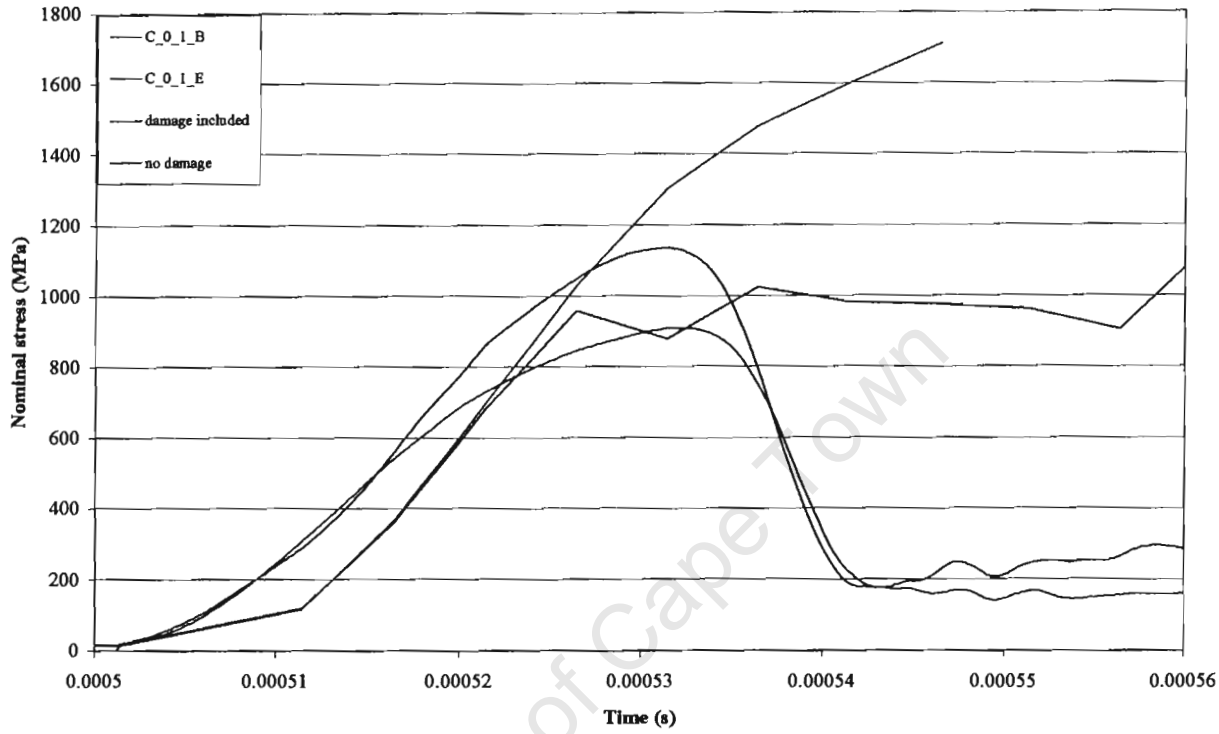

Figure 6.14: Comparative study of nominal stress versus time, for a compression specimen numerically modelled with damage and without damage, as well as two experimental tests results.

Through the parametric studies the strain rate is varied for the varying numerical analysis with damage and the ultimate stress values are thus calculated. The triangles (blue) in Figure 6.15 represent the GFRP ultimate stress as deduced from the numerical results. The ultimate stresses for GFRP under increasing strain rates range from 900 MPa to 1200 MPa at quasi-static strain rates to 1000 s^{-1}, respectively. These values lie within the trend line (blue) upper and lower boundaries. The trend lines were deduced from the experimental results of chapter 5. The squares (red) depict the ultimate stress of the CFRP numerical results. The CFRP ultimate stress values range from 900 MPa at quasi-static strain rates to 1250 MPa at 1000 s^{-1}. These values are expected because they rely on the input data of from experimental work. The VUMAT is

programmed to induce failure once the ultimate stress has been attained. This is true for all loading cases.

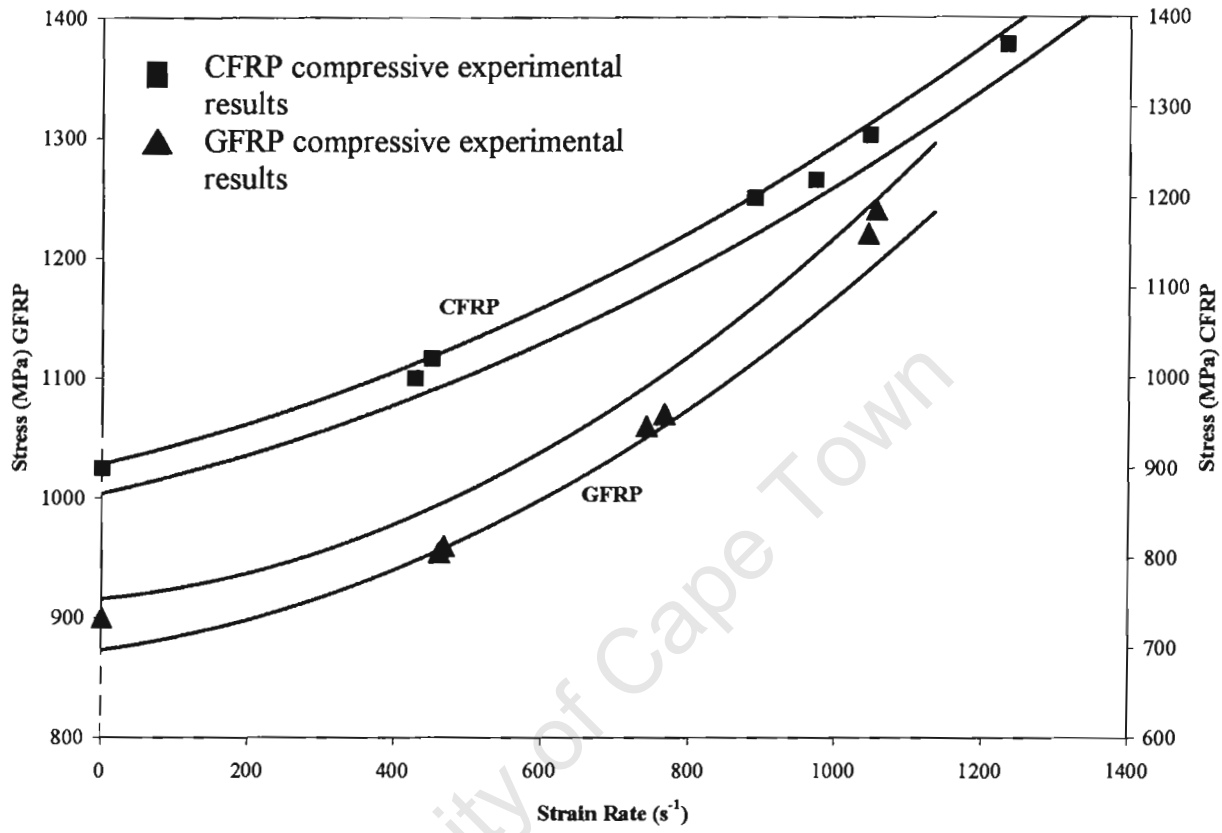

Figure 6.15: Numerical modelling results with damage presented with experimental results deduced in chapter 5. This information is given in the form of a stress versus strain rate graph.

6.9. MODELLING OF SHEAR TESTS

6.9.1. MESH GENERATION

The unidirectional single lap specimens for both CFRP and GFRP are modelled using continuum elements (C3D8R). The boundary conditions for the specimens are depicted in Figure 6.16. The nodes held encastré are labelled ***A,*** whereas the loaded nodes are labelled ***B***. The specimen is loaded in the fibre direction, i.e. 1-plane. The fibre direction corresponds to the local 1-direction, shown in Figure 6.16. An initial velocity is applied to the loaded end (***B***). In the case of single lap

shear loading condition the initial condition follows the same format as that used for compression loading. The aspect ratio of the elements in the mesh are concentrated at the point where shear will occur, labelled *C* in Figure 6.16.

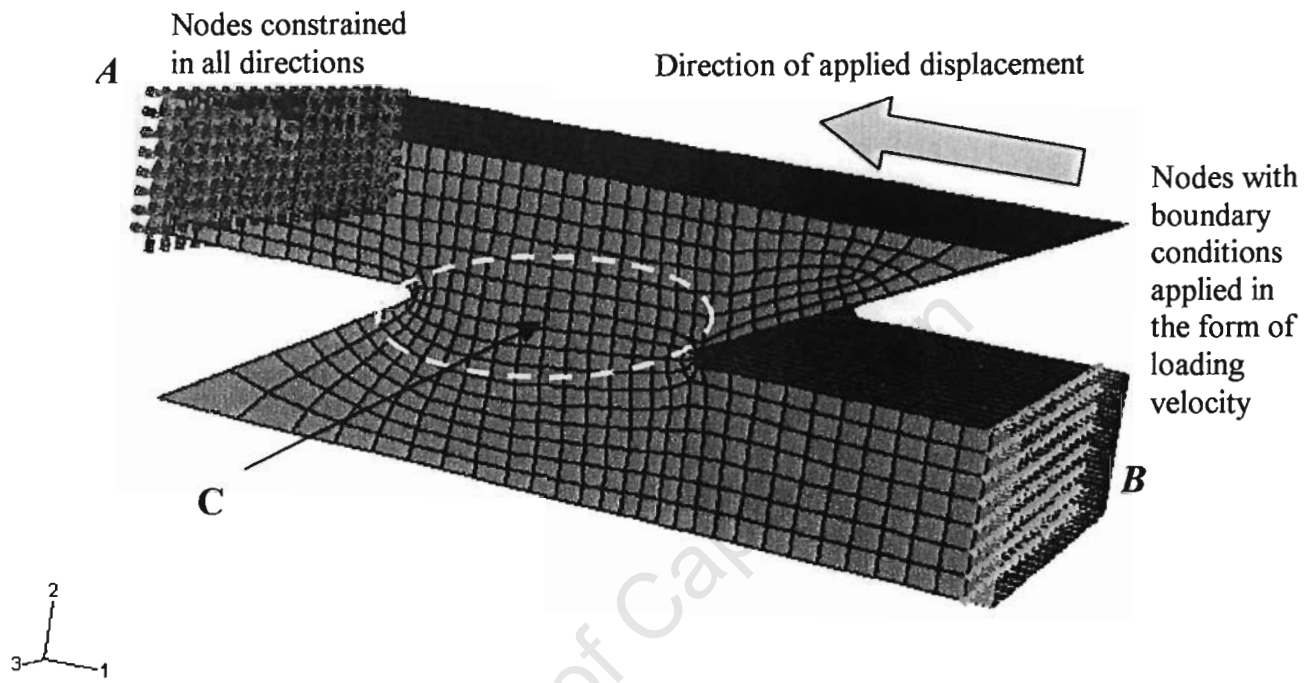

Figure 6.16: Mesh generated for the single lap shear specimen. The arrow indicates the direction of loading. In this case the 1-direction is equivalent to the fibre direction.

6.9.2. DAMAGE PREDICTION

The damage prediction is based on a single lap GFRP system impacted at 450 s^{-1}. The shear stress distribution in the single lap shear model is shown in Figure 6.17. The contour plot presents data of the shear stress in the local 1-2 direction. The initial shear failure point occurs at shear stress of 66.9 MPa (see Figure 6.17). This region of shear failure is seen as green, labelled *C*.

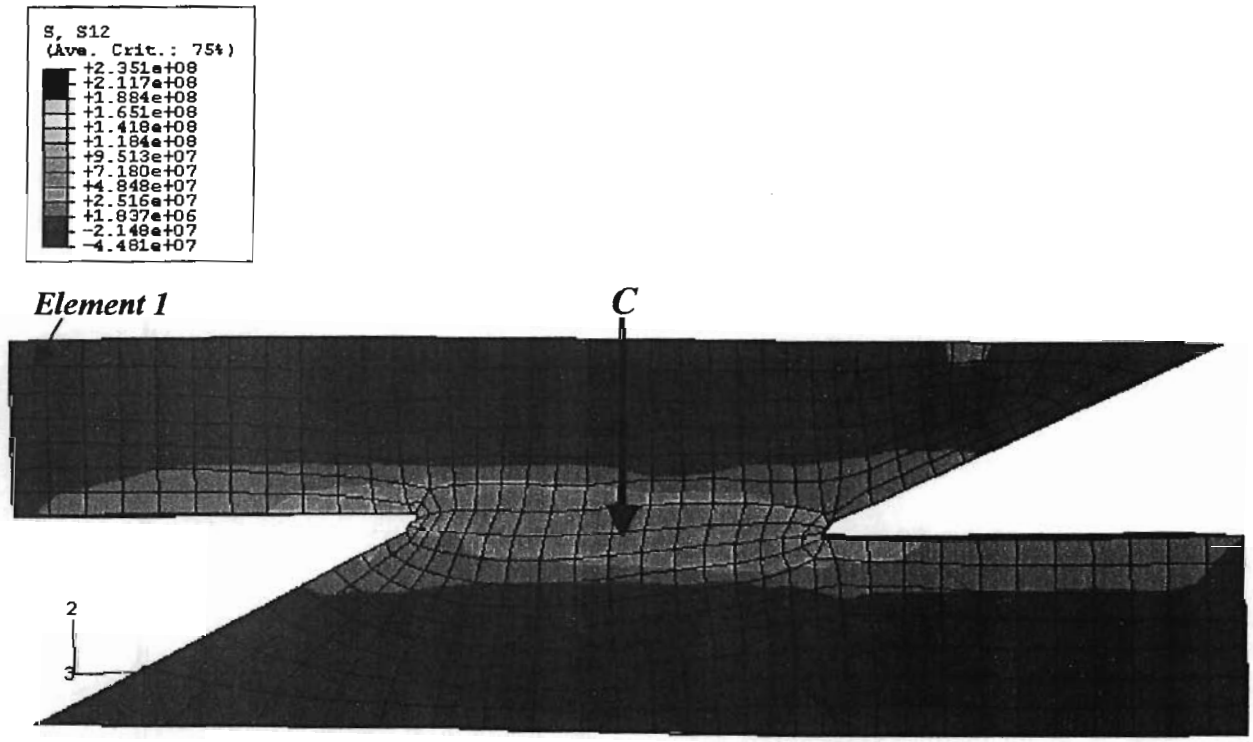

Figure 6.17: Shear stress contour plot in the local 1-2 direction for a single lap specimen.

The parametric study enables the automatic variation of strain rate when modelling the single lap shear for CFRP and GFRP specimens. The upper and lower ultimate shear stress values from the experimental results of chapter 5 are labelled for the GFRP and CFRP, respectively. The ultimate stresses for the GFRP and CFRP under shear loading varies according to the rate of loading. Each triangle and square represents the varying interlaminar shear strength values for the GFRP and CFRP under increasing loading conditions. At quasi-static strain rates the numerical interlaminar shear strength for CFRP is 40 MPa. At strain rates of 800 s^{-1} the numerical strengths increase to 110 MPa. For CFRP similar increasing trend interlaminar shear strengths are recorded numerical, see Figure 6.15.

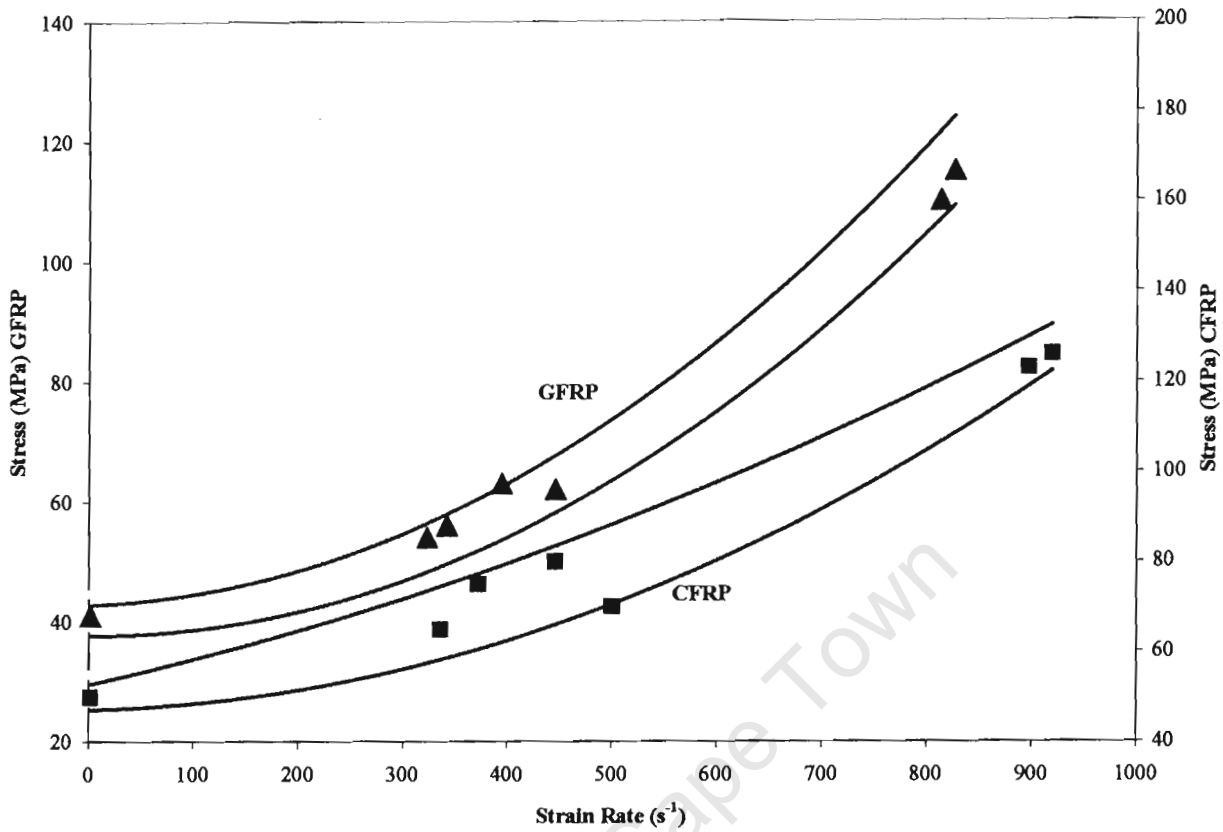

Figure 6.18: Stress versus strain rate graph of the numerical modelling results with damage presented with experimental results deduced in chapter 5.

6.10. MODELLING OF TENSILE TESTS

6.10.1. MESH GENERATION

The tensile mesh is developed on the same geometry as the unidirectional experimental tensile specimen introduced previously in chapter 4. The load, in the form of a displacement boundary condition, is applied as an initial velocity to the selected nodes. The opposite end has its nodes held encastré. As is the case with the single lap shear mesh, the mesh has a higher mesh density in the zone labelled C. The failure or stress concentration is expected in this region.

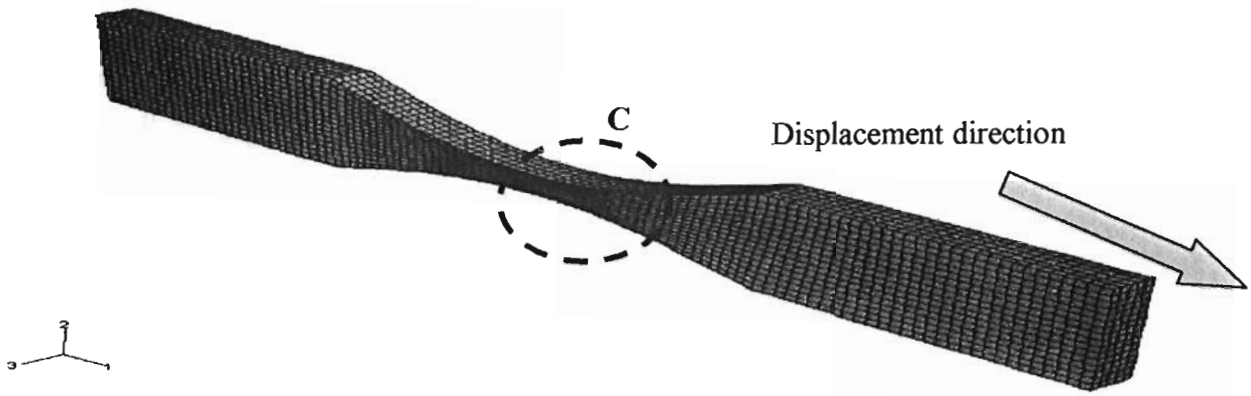

Figure 6.19: A typical finite element mesh used for modelling the tensile behaviour of GFRP and CFRP tensile specimens.

6.10.2. DAMAGE PREDICTION

The stress distribution in the finite element tensile stress CFRP specimen at quasi-static strain rates, is depicted in Figure 6.20. The contour plot is presented at the end of the loading cycle. The maximum stress in the system occurs at the stress concentration zone and is shown as red in the contour plot (labelled *C*). This corresponds to an ultimate stress of 1230 MPa (see contour plot

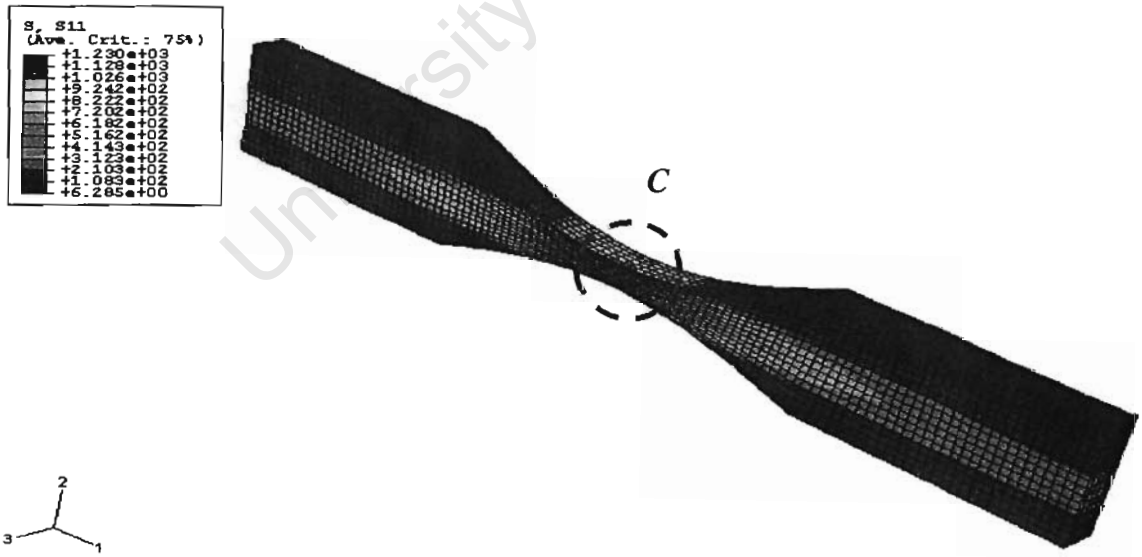

legend Figure 6.20).

Figure 6.20: Contour plot of the stress distribution in the tensile specimen.

A close examination of the contour plot in Figure 6.21 shows that failure will begin at the edge of the specimen and then ingress through the mesh. The stress contour plot in this section of Figure 6.21 is evenly distributed with respect to the progression of failure. The stress appears to progressively increase from the centre of the stress concentration zone and proceeds outwards to the specimen ends, in the 1-direction.

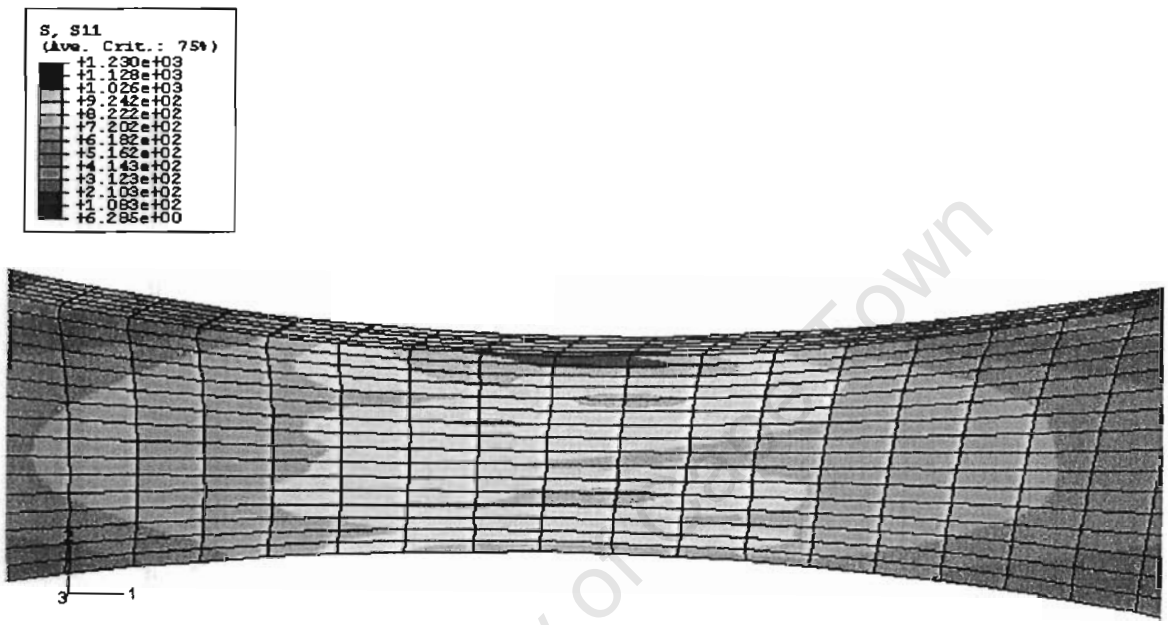

Figure 6.21: Enlarged view of zone C from Figure 6.20 to showing the stress distribution.

A stress time graph drawn from the numerical element integration point reveals a linear increase in stress up to failure. The tensile specimen is seen to break in a brittle manner which is characterized by an immediate drop in stress beyond the ultimate stress value. In the numerical model the stress versus time relationship is recorded from the integration point an individual element. Figure 6.22 gives an ultimate stress of approximately 1250 MPa at quasi-static strain rate of loading.

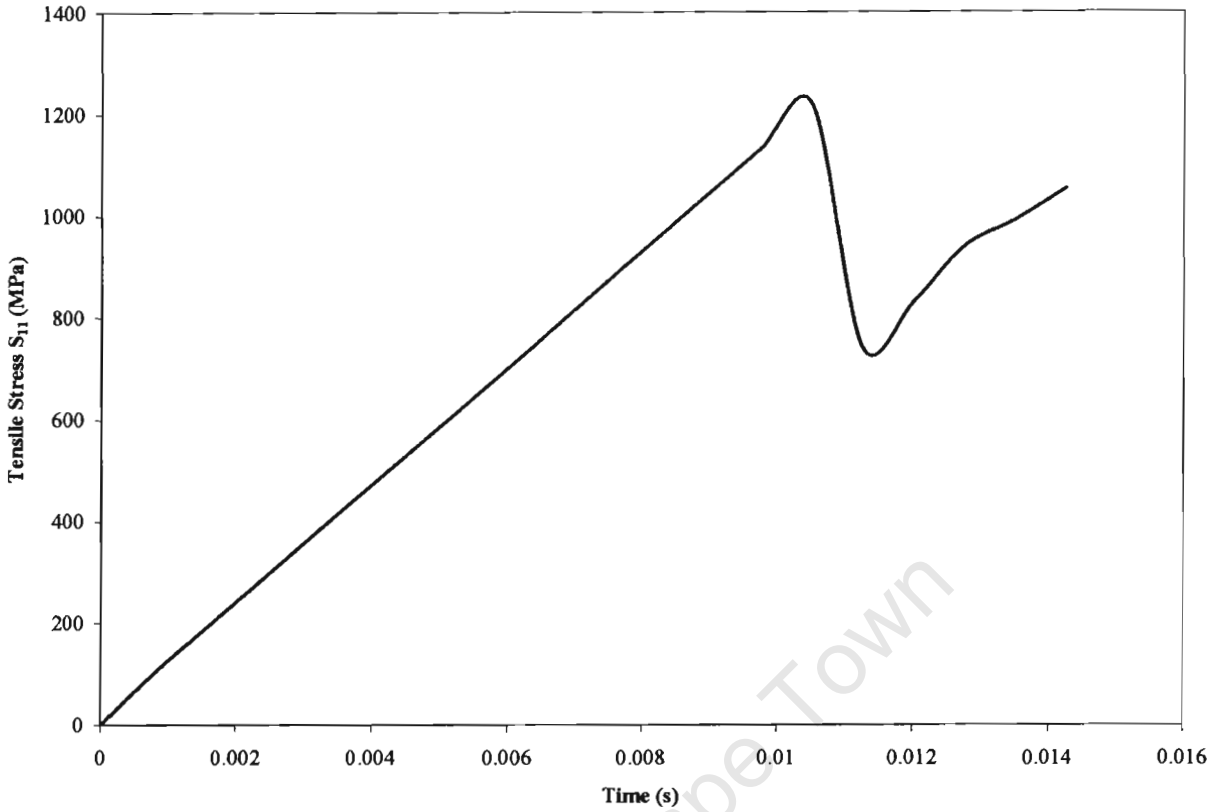

Figure 6.22: Tensile stress versus time graph of an element that lies within the stress concentration zone of Figure 6.20. The relationship shows a peak stress beyond which the stress value drops.

The numerical model is developed to simulate varying strain rates in order to investigate the relationship between strain rate and ultimate tensile stress for both CFRP and GFRP. The parametric study explained previously allows for automation of this analysis, in terms of altering the strain rate of loading after each run. The resulting ultimate tensile stress values from the numerical models are presented in Figure 6.23. The triangles represent the GFRP numerical model results whereas the squares represent the CFRP. The upper and lower ultimate tensile stress values from the experimental results of chapter 5 are given in blue and red trend lines for GFRP and CFRP, respectively. The ultimate stress for CFRP is approximately 1300 MPa for increasing strain rates. GFRP on the other hand shows increases in ultimate stress from 750 MPa at quasi-static strain rates to 940 MPa at 1600 s^{-1}.

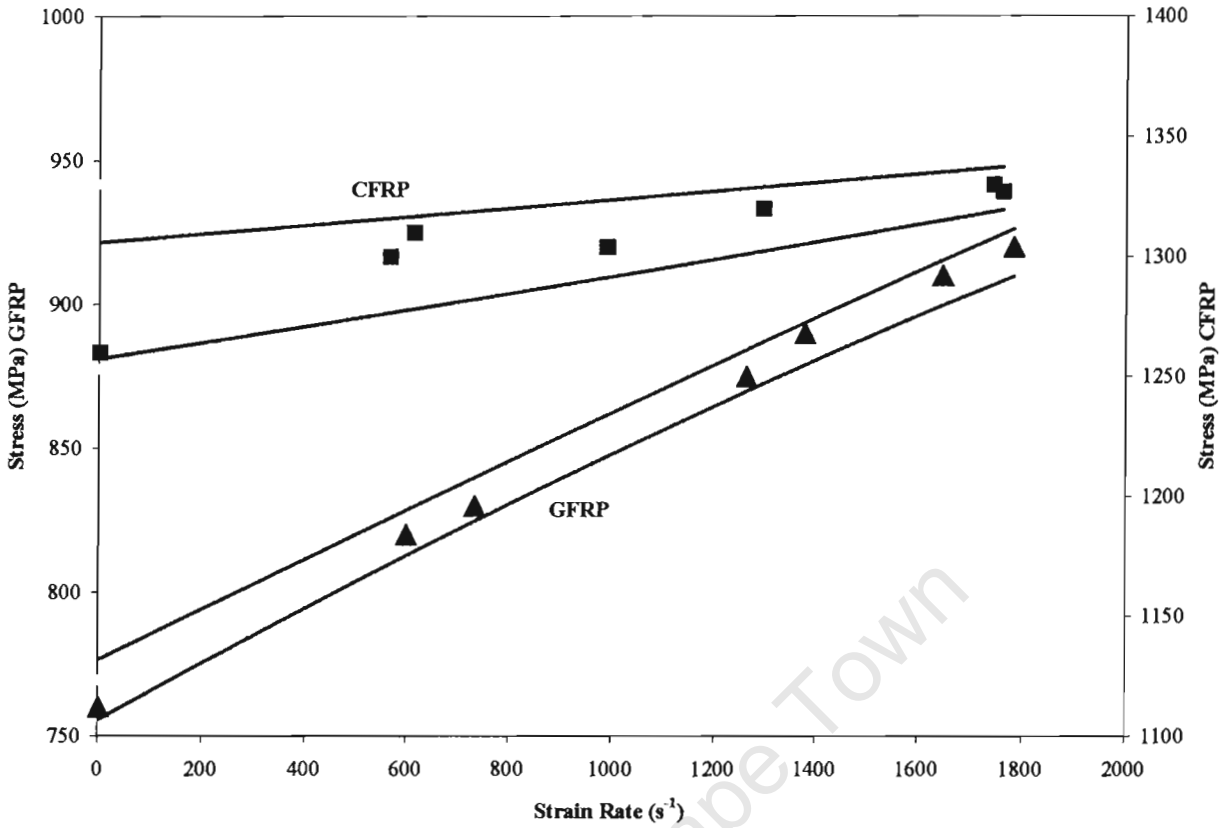

Figure 6.23: Stress versus strain rate graph of the numerical modelling results of a tensile specimen with damage, presented with experimental results deduced in chapter 5.

6.11. NUMERICAL MODELLING OF A PLATE IMPACT

6.11.1. PLATE IMPACT BEHAVIOUR

The objective of the plate impact model is to determine the overall effect of increasing ultimate stress values, recorded for increasing strain rates reported experimentally and numerical, in this thesis. In order to investigate the effects of increasing ultimate stress with strain rate GFRP plates are modelled. The GFRP has shown increasing ultimate stresses for all loading direction, from compression, shear to tension. The CFRP on the other hand only shows increasing ultimate stresses values in compression and tension. For this reason in this section the numerical modelling is based solely on GFRP plates.

The GFRP plates were modelled using a quarter-model mesh shown in Figure 6.24. The plate is modelled with 8751 C3D8R elements and 10242 nodes. The impactor is modelled as a rigid body with a diameter of 6 mm. Modelling the impactor as a rigid body reduces the computational time expense of the overall model.

The GFRP plate has its fibres running in the local 1-direction. The impact velocity is increased progressively for the various numerical models to simulate increasing strain rates that are deduced from the velocity of the hemispherical impactor. The results in the form of contour plots, force-time and stress-time graphs are developed to compare the numerical to experimental results.

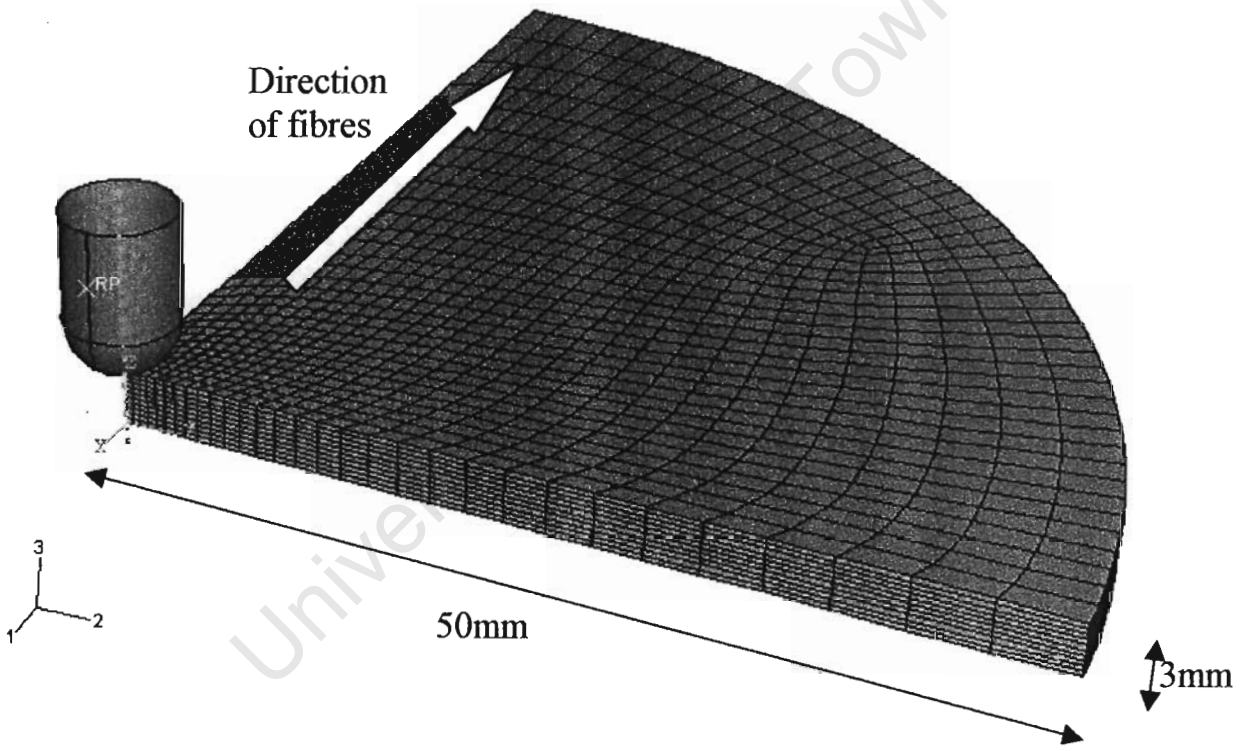

Figure 6.24: Mesh used to model the GFRP plate impact.

6.11.1.1. TIME HISTORY COMPARISON

Preliminary results given in Figure 6.25 shows the need for a damage model when modelling plate impact problems. The force versus time graph in Figure 6.25 depicts the discrepancy between the experimental results and numerical plate impact model that has no damage included.

The experimental and modelling set-up considers a 12-layered unidirectional 6 mm thick GFRP plate. The maximum force from the experimental test is 2800 N. The numerical model with damage has a maximum force of 2500 N. The numerical model without damage records a maximum force of 4400 N. A comparison of the experimental and numerical modelling that includes damage gives differences of less than 400 N as compared to the 1600 N difference seen in the numerical model without damage. This is equivalent to an improvement of 54.2 % of the experimental value, reducing the margin of error in modelling to 13.6 %.

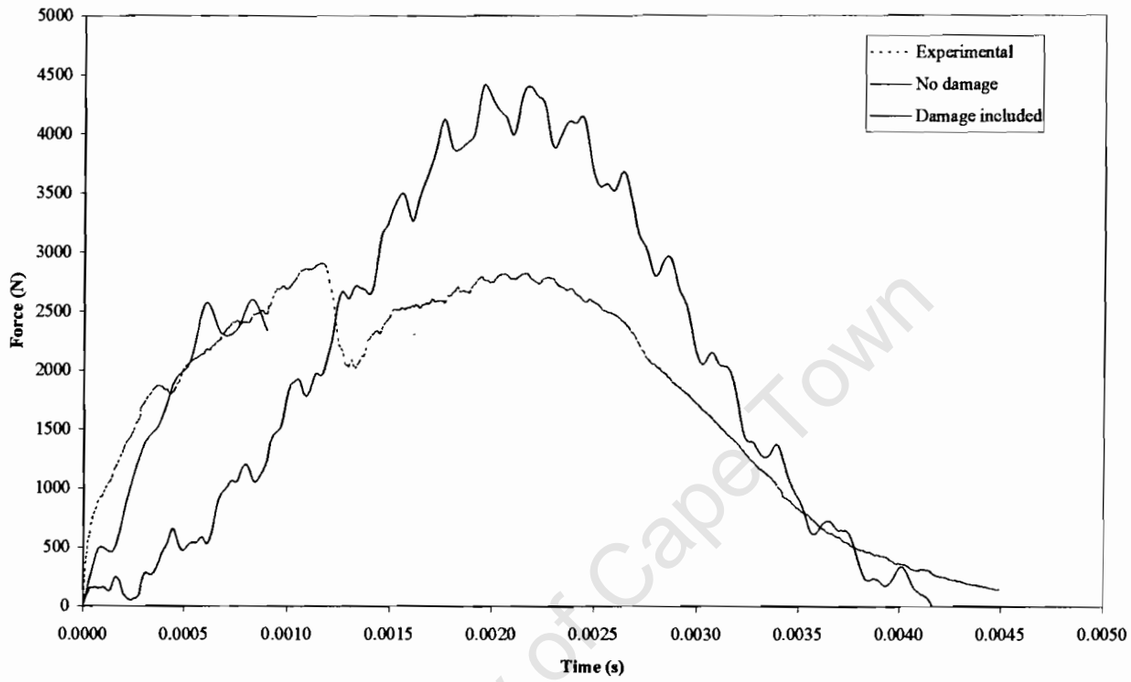

Figure 6.25: Force displacement graph for a GFRP specimen showing a large discrepancy in numerical versus experimental results for quasi-static strain rates.

The numerical results are also compared to investigate the relationship between inclusion of the strain rate sensitivity relations (derived in chapter 5) and a model without any strain rate sensitivity at strain rates of 10^3 s^{-1}, using GFRP properties determined in the experimental tests (Table 6.2). The numerical model is done on a 3 mm unidirectional GFRP plate impacted at 12 ms^{-1}. The first simulation uses the quasi-static material properties of GFRP. This analysis results

in a maximum force of 1260 N. The numerical model that includes the strain rate sensitivity on the other hand, gives a maximum stress of 1470 N. Finally the experimental test on a 6 layered 3 mm GFRP plate impacted at strain rates of 10^3 s^{-1} give maximum forces of 1600 N (Figure 6.26). The experimental results of the plate impact tests together with photographs of the damaged GFRP specimens are presented in *APPENDIX XII*.

The discrepancy between the experimental value and the numerical model without strain rate sensitivity included is 21 % (20 % discrepancy is reported previously for the 6 mm thick GFRP plate). The inclusion of strain rate sensitivity shows a reduction from 21 % to 8 % discrepancy when compared to the experimental value.

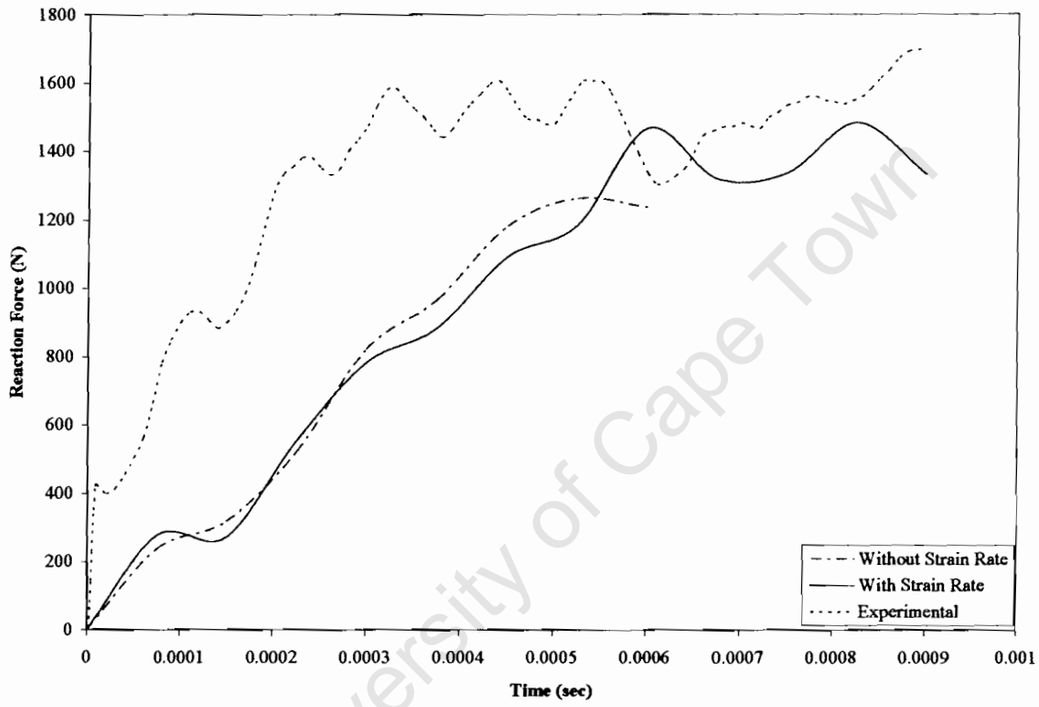

Figure 6.26: Force time history of plate impact test on GFRP modelled with and without the strain rate sensitive model included.

The following comparison focuses on the modelling results with and without the inclusion of the strain rate sensitivity relationships. A tensile stress versus time graph (Figure 6.27) shows that the

maximum tensile stress recorded with the inclusion of strain rate is 1180 MPa, whereas the maximum tensile stress without strain rate is 1060 MPa.

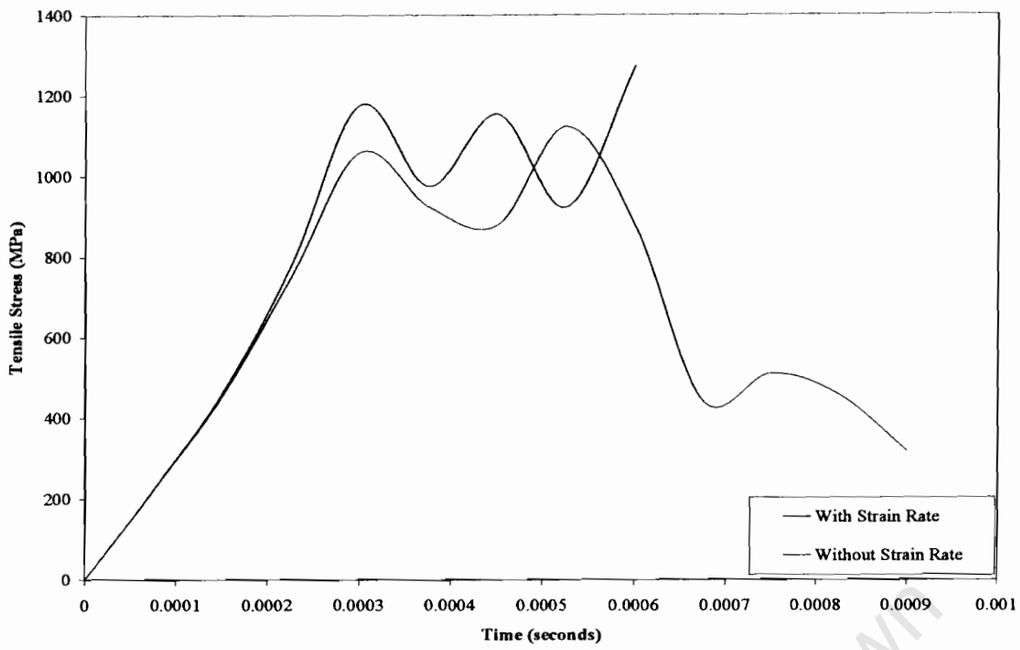

Figure 6.27: Tensile stress vs. time for plate model with and without strain rate sensitivity.

6.12. CONCLUDING REMARKS

- Numerical modelling of CFRP and GFRP under uniaxial compression, shear and tension was undertaken. The inclusion of damage based on the Chang-Chang criteria for matrix cracking, matrix crushing, delamination and fibre failure was implemented through the VUMAT subroutine in Abaqus/Explicit. Damage in the numerical model is attained when the ultimate stress is exceeded. This model successfully predicts the onset of initial damage.

- The numerical model was also developed to investigate the effects of increasing strain rate. In order to achieve this, the constitutive equations developed in chapter 5 are built-in through the VUMAT. The numerical model therefore automatically calculated the

ultimate stress based on the actual strain rate of loading. This model is seen to work well for the uniaxial tests modelled.

- Finally, the interaction of the failure mechanism in compression, shear and tension is investigated using a plate impact model. The reaction force is improved by including both damage and the strain rate constitutive model for plate impact at high strain rates of loading.

CHAPTER 7

DISCUSSION

7.1 OVERVIEW

The motivation for developing high strain rate data for CFRP and GFRP composites was to improve the prediction of numerical simulations on these materials at impact rates of strain. Few results had been previously reported on the strain rate behaviour of CFRP and GFRP under varying strain rate conditions. The current investigation has shown that at increasing strain rates, the ultimate stress values for GFRP and CFRP increase sufficiently to warrant the introduction of a strain rate sensitive constitutive model that is developed from experimental data. No attempt has been made to fully describe the underlying materials science, nor is any attention given to the practical difficulties encountered in high strain rate tests such as stress wave effects and inertia of the test rigs. In tension the GFRP shows more strain rate sensitivity than compared to CFRP. As a result the interaction of the various failure modes under increasing strain rate conditions is investigated through testing the impact behaviour of a structural component, a plate under a hemispherical impact load.

Numerical modelling serves as a useful and cost effective method for predicting damage in FRP. However, its success in terms of the accuracy of the results is gravely dependant on the input data and the ability of the constitutive equations to describe the actual material behaviour under the simulated loading conditions. The numerical loading conditions must resemble that of the experimental test. Clearly then, the inclusion of any degree of strain rate sensitivity recorded in the experimental data must be included in the constitutive equations. Subsequently, a modification of the constitutive equation was implemented to include the strain rate sensitive recorded in the data. The resultant constitutive equation used in the numerical modelling procedure included both progressive damage, which is based on the Chang-Chang criteria, and the proposed strain rate constitutive equation that is based on the Cowper-Symonds relationship.

The VUMAT in the FE model is the vehicle used to implement progressive damage and the strain rate constitutive equation.

The results from the numerical model that include both damage and strain rate sensitivity are discussed, with emphasis on the effect of strain rate sensitivity to improve the numerical modelling results of the individual modes of failure in compression, shear and tension all at higher rates of loading. In addition, the interaction of the various modes of failure at increasing strain rates is discussed with particular reference to the potential sequence of failure at high strain rates. Finally, the merits of including the strain rate sensitivity constitutive equation is discussed by considering the improved prediction of the numerical model on a structural component, viz. the plate impact numerical model.

In developing interactive failure criteria for laminated composite structures impacted at varying strain rates, the strain rate effects need to be considered. The Chang-Chang failure criteria are widely used for the prediction of impact damage in composites [82]. Recently, the delamination criterion proposed by Chang-Chang has been included in an attempt to improve the numerical predictions of a composite plate undergoing impact [97]. The approach used is the inclusion of the strain rate constitutive relations in an attempt to make the interactive progressive failure criteria proposed by Chang-Chang for matrix failure, delamination and fibre failure, applicable to static as well as dynamic conditions.

7.2 INTRODUCTION TO THE APPROACH

A generic approach is developed where an orthotropic elastic stress analysis is first performed for a given composite structure subjected to a known impact loading. The use of average elastic constants for composites, loaded in the principal directions parallel to the reinforcement is required. This allows for the estimates of the stress-strain relation for a given loading condition. It is seen from experimental results reported in this work that the values of certain material properties for FRPs vary with the loading rate. The critical stress levels below which the

composite deforms elastically and above which catastrophic failure occurs, are needed in determining the limiting impact loading the composite materials can support without failure.

However, complications are anticipated when the generic approach is followed. This is due to the initial non-catastrophic damage occurring at low stresses. Such damage is often modelled by arbitrarily modifying the effective elastic constants and hence the subsequent stress distribution in the structure [113]. Due to the orthotropic nature of composite materials and the inherent varying damage modes or failure processes, final failure is likely to result from an accumulation of damage from a range of different processes. Thus the generic approach to the problem is to characterize the "material" properties of the given composite. In particular the effect of strain rate on the materials' strength and failure mode under different loading configurations, using specially designed small specimens is investigated. Such tests would, it was hoped, allow the determination of critical stress levels at which different damage processes initiated, propagated and subsequently resulted in failure. This data may then be used in conjunction with stress analysis of the impacted structure to predict when and how failure might occur.

A combination of the two approaches is used in this thesis. This involves using the data from the generic approach, which gives a general idea of the impact response of the polymer composite, in modelling a small-scale structural numerical simulation of a laminate plate. To supplement the generic approach an empirical approach is employed. The empirical approach starts with the particular form of composite structure of interest. This approach requires the design of an impact test on a structural component, such as a composite plate used in this work. The loading configurations that are approximate to the particular composite structure of interest are applied. The applied loading and resulting deformations are closely monitored and recorded. Empirical data on the failure mode and the load at which it occurs was monitored.

7.3 THE NEED FOR A DAMAGE MODEL

The detailed development and elucidation of the damage criteria used for modelling damage in the FEA, through the Chang-Chang criteria has been explained in chapter 3. However, the full benefits of introducing damage criteria's in FEM is determined by comparing the numerical analysis of a quasi-static linear model without damage, to that of a non-linear model including the

equations proposed by Chang-Chang. These equations account for fibre failure, matrix cracking and delamination failure in laminates modelled using FE techniques [96].

The damage criteria in simple terms involve the discount of the relevant material properties within an element in the FEA. For example, an orthotropic material where the tensile loading in the local 1-direction exceeds the ultimate stress in the local 1-direction, the elastic modulus of the element in the 1-direction would be reduced to zero. This interaction would result in the stress being redistributed in the numerical model. Any adjacent element would therefore carry the redistributed load. This iteration would continue in the numerical analysis accordingly, up to final failure, or until the load is exhausted. The exclusion of a failure criteria in the numerical model would be akin to a linear model where no element will fail, i.e. have its material property degraded. Such a numerical model result does not predict failure. In the case of an orthotropic material any linear stress-strain analysis would show a constant rise in stress as a function of strain, according to the gradient set by the elastic modulus in the specific material direction. An FEA with built-in damage criteria depicts a distinct drop in the stress at the point of failure determined by the ultimate stress of the material. The numerical analysis prediction, with damage, compares well with experimental results of the actual system with respect to the prediction of ultimate stress. The drawback in the numerical model is its inability to determine the strain to failure accurately. The limitation is based on the criteria being solely stress based.

7.4 COMPRESSION BEHAVIOUR OF FRP

7.4.1 MECHANICAL BEHAVIOUR

The development of the strain rate constitutive equation was done in phases. The first phase involves determining the strain rate behaviour of CFRP and GFRP composites to compression loads. The choice of the FRP materials made from CFRP and GFRP was proposed in order to investigate the relationship between a brittle composite system such as CFRP and a quasi-brittle GFRP system. The main mechanism for absorbing energy in FRP is the strain energy to failure of the fibres. GFRP have a larger energy absorbing capacity as compared to CFRP [18]. The second motivation behind the choice of GFRP and CFRP is based on previous experimental studies that

show GFRP to be strain rate sensitive under compression loading [37]. Strain rate increases are also reported to have an effect on failure strength the CFRP [40].

In CFRP and GFRP systems, the resulting increase in the ultimate compressive stress under increasing loading conditions for the CFRP was not anticipated. Although the matrix is known to be rate dependent, the overall CFRP system is known to behave in a brittle manner [40]. The current investigation has shown that under increasing loading conditions, specifically from quasi-static to dynamic loading, a significant change or increase in the modes and sequence of failure occurs at high strain rates. The changes in failure modes and sequence of failure for increasing strain rates seem to be independent of the fibre type. At high strain rates for the designed compression specimens, the failure modes such as interfacial splitting, delamination and fibre buckling that are also present at quasi-static strain rates, becoming more pronounced at dynamic loads.

For both the CFRP and GFRP systems the ultimate compressive stress values of approximately 800 MPa at quasi-static strain rates, increase to 1200 MPa at dynamic strain rates characterize. The magnitude of the compressive ultimate stress values suggests that fibre buckling and longitudinal splitting dominate failure for both systems. Other authors however, have reported on the observed increase in ultimate stress in compressive loading is due to the strongly rate dependent matrix [19,31]. The ultimate stress in a material is determined by the capacity of the material to absorb energy. Therefore any increase in ultimate stress as a result of increasing strain rate is due to a change from low energy absorbing failure mechanisms at lower strain rates, to higher energy absorbing mechanisms at higher strain rates. The compression specimens at low strain rates remain intact after impact. The sites of delamination, matrix cracking and interfacial splitting are relatively localized. The specimens impacted at higher strain rates on the other hand have global damage sites. The specimens undergo multiply sites of delamination, matrix cracking and interfacial splitting. Harding and Ruiz proposed that the failure process under compression loading conditions has a direct impact on the ultimate stress of GFRP [44]. This theory has been reinforced by the results described in this section.

7.4.2 DEVELOPMENT OF CONSTITUTIVE EQUATION

The strain rate sensitivity recorded from the ultimate stress results for both CFRP and GFRP tested under dynamic strain rates, essentially the generic approach, justifies the development of a strain rate sensitive constitutive equation. Cowper and Symonds proposed a constitutive model to describe how the material properties of metallic materials are affected by strain rate [93]. This principle forms the basis of constitutive equations developed in this work. Experimental data in the form of ultimate stress values increase as the strain rate increases from quasi-static to dynamic. The failure mechanism under increasing compression loading is seen to change as the strain rates of loading are increased. The sites of delamination and interfacial splitting increase with increasing strain rate. This increase is non-linear and it has been shown that at increasing strain rates to 1800 s^{-1}, a non-linear rise in ultimate stress occurs [41,42]. Kumar *et al.* stated that for unidirectional laminates with fibre orientations greater than 0°, the dynamic stress-strain behaviour is non-linear [27]. The non-linear dynamic stress-strain behaviour failure mechanisms, coupled with the failure mechanisms that dominate compressive failure of the FRP at increasing strain rates, suggest a non-linear stress-strain rate constitutive equation.

From this analysis of the compressive failure modes of the FRPs, as well as the experimental data points recorded for increasing strain rates, a non-linear constitutive equation was developed. Vinson and Woldesenbet developed a non-linear constitutive equation that also accounts for orientation dependence [38]. This equation was based on fitting a curve to experimental data points. The same approach is utilised in this work. The experimental data of ultimate stress versus strain rates results in a second order polynomial constitutive equation. The constant variable in the second order polynomial is equivalent to the quasi-static ultimate stress value. The equation is manipulated in logarithmic form to give the equation of a straight-line graph. This enables the determination of D and q constants. The $q_{comp\_cfrp}, D_{comp\_cfrp}, q_{comp\_gfrp}, D_{comp\_gfrp}$ for CFRP and GFRP specimens under compression have values work of 0.75, 1863; 0.7 and 2716 respectively. These values represent material constants for the particular carbon (AIK-EHKF-420-UD24K-40) and glass fibre (Material type: EPO UD EST 250/600 FT 102 35 % Glass) system, respectively.

The following equation applies to the CFRP and GFRP systems under compression loading, respectively:

$$\dot{\varepsilon} = 1863\left(\frac{\sigma_0'}{\sigma_0} - 1\right)^{0.8} \tag{7.1}$$

and

$$\dot{\varepsilon} = 2716\left(\frac{\sigma_0'}{\sigma_0} - 1\right)^{0.7} \tag{7.2}$$

From the statistical analysis carried out in chapter 5, equations (7.1) and (7.2) can be used with a 95 % confidence limit when determining the ultimate stress values in compression for CFRP and GFRP. The derivations stipulates that given the materials quasi-static ultimate compressive stress, the dynamic ultimate stress can be determined using the equations (7.1) and (7.2).

7.4.3 NUMERICAL BEHAVIOUR

The implementation of the constitutive equation for damage at quasi-static loading conditions is undertaken. The numerical prediction gives a good correlation with the experimental results. Particular emphasis was made with relation to the ultimate failure stress point. The numerical predictions show a drop in stress at a particular strain. The inclusion of the Chang-Chang damage model also resulted in a more realistic contour plot of displacement in the front face of the compression mesh. The mesh is seen to extend outwards in the perpendicular direction to the direction of the fibre. The linear model results in a circular mesh that is identical to the original mesh before any load is applied. This illustration is given in Figure 7.1 where the contour plots of both the linear (a) and non-linear models (b) are superimposed onto the actual micrograph. Figure 7.1 (b) presents a combination of half the numerical analysis contour plot and half of the

experimental specimen micrograph. Keeping in mind the dominating failure mechanism, some discussion can be made of the good correlation of the micrograph with the contour plot. The micrograph and contour plots represented in each case refer to the non-impacted end of the compression specimen (see chapter 5).

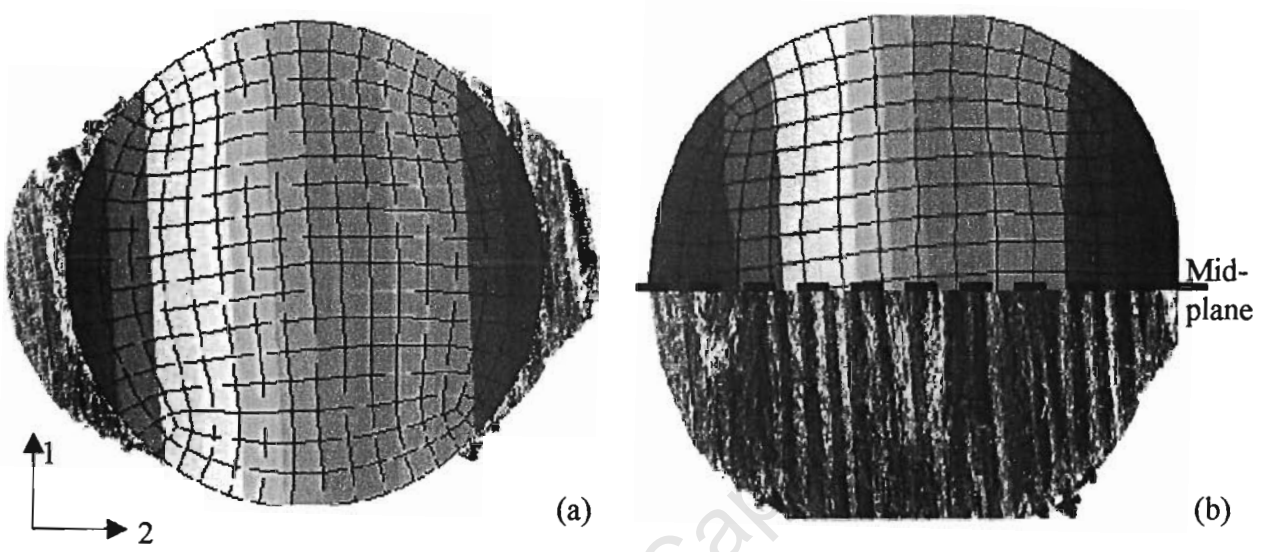

Figure 7.1: Image of superimposed to show the improvement in accuracy of a model with damage.

This observation is unexpected, as the numerical model is an ideal system with no flaws or voids. The similarity in distortion of the compression specimens to that of the numerical compression mesh suggests a sequential and repeatable progressive failure mechanism of unidirectional FRPs under compressive uniaxial loadings. The numerical models with built-in damage criteria through the VUMAT, suggest matrix failure at about 231 MPa and 219 MPa, for CFRP and GFRP, respectively. The subsequent distortion of the compression specimen, as seen from the analysis of the micrograph, results in a distortion in the 12-plane or shear plane. This implies that shear failure or delamination is triggered at this stage. The final failure, which is equivalent to the ultimate stress, will result in longitudinal compressive stress of about 902 MPa and 905 MPa, for CFRP and GFRP, respectively. The similarity in the micrographs and displacement contour plots for experimental compression specimens, would suggest that for unidirectional CFRP and GFRP material with limited manufacturing flaws, the ideal post impacted specimens displacement can

be predicted. It is postulated that the contour plot from the numerical model with damage for a compression FRP may be used to predict the shape of the post impacted experimental micrograph. This however only applies to quasi-static strain rates of loading.

At dynamic strain rates the "random" disintegration of the CFRP specimen, requires a more analytical approach. Investigating the micrographs and the displacement through contour maps of the mesh does not allow for reasonable comparisons. The numerical contour mesh does not account for disintegration of the laminate material constituents.

7.4.4 SUMMARY OF COMPRESSION BEHAVIOUR

From the various uniaxial tests carried out at varying strain rates it appears that the degree of non-linearity that is induced in the GFRP and CFRP is increased due to the interaction of the failure modes in both laminate systems. Uniaxial compression for example, induces shear, interfacial splitting and delamination failure as the crack propagation ingresses into the composite system. This feature becomes more prominent at higher strain rates. This hypothesis suggests that out-of-plane stresses become more dominant at increasing strain rates. As a result the systems failure modes are dominated by the fibre buckling, matrix interaction and interfacial (fibre-matrix) bonding strengths. Under compression at increasing strain rates the fibre failure under compression is dominated by non-linear strain rate sensitivity medium. This hypothesis would explain the strain rate sensitivity recorded in the compression specimens under increasing loading conditions, as well as the failure modes noted from the visual and microscopic analysis of the post impact damaged specimen.

7.5 SHEAR BEHAVIOUR OF FRP

7.5.1 MECHANICAL BEHAVIOUR

Lindholm suggested that an epoxy is strain rate sensitive under increasing strain rates of loading [19]. Therefore any increase in the strain rate of loading that the single lap shear specimen is subjected to is expected to result in increases in the ultimate stress recorded. Two features highlight the matrix dominated failure in the shear specimens, one being the magnitude of the ultimate stresses recorded and the second being examination of the micrographs. The ultimate stress recorded for CFRP and GFRP range between 40 MPa and 130 MPa for quasi-static and dynamic loadings, respectively. These values are typical of matrix shear failure of FRPs [45]. The microscopic analysis of the shear failure surface shows no evidence of other mechanisms of failure. This observed lack of other failure modes in the micrograph is apparent in all the micrographs for the full range of specimens (CFRP and GFRP) under varying loading conditions.

Knowing these details, the failure mechanism can be narrowed down to shear failure of the matrix and fibre-matrix interface. Therefore from past researchers who suggest that epoxy matrix is strain rate sensitive at increasing strain rates, the initial assumption of strain rate sensitivity under the specific loading conditions investigated becomes valid [19]. The investigation carried out gives the relationship between ultimate stress and strain rate without investigating the material science of the epoxy matrix under varying loading conditions. The shear failure initiates at the loaded end of the specimen and continues to propagate through the single lap specimen within the same plane. At higher strain rates the matrix becomes more ductile. The energy required to induce ultimate shear failure under dynamic shear loading conditions is larger than required to produce ultimate shear failure from the quasi-static shear loaded specimen. This results in higher ultimate stress failures at higher strain rates for both CFRP and GFRP. Delamination causes reductions in interlaminar shear strength [18]. As a result the notion that the single lap shear specimen failure is dominated by the matrix failure is strengthened.

7.5.2 DEVELOPMENT OF CONSTITUTIVE EQUATION

Previous experience in epoxy has shown non-linear strain rate behaviour. Based on this information the ultimate stress data was expected to increase within increasing strain rate, from quasi-static to dynamic strain rates. The non-linear constitutive equation is based on an empirical approach. Due to the nature of the rate dependence of the single lap shear results the constitutive equation is in the form of a second order polynomial equation with the constant variable that are equivalent to the quasi-static ultimate stress value. The constants D and q are determined from the straight-line graph. The $q_{shear\_cfrp}, D_{shear\_cfrp}, q_{shear\_gfrp}, D_{shear\_gfrp}$ have values 0.7 ± 0.1 and 688 ± 42, 0.5 and 622, respectively. The following equation applies to the CFRP system (AIK-EHKF-420-UD24K-40) under single lap shear loading

$$\dot{\varepsilon} = 688 \pm 42\left(\frac{\sigma_0'}{\sigma_0} - 1\right)^{0.7} \tag{7.3}$$

The glass fibre system (Material type: EPO UD EST 250/600 FT 102 35% Glass) under single lap shear loading follows the equation

$$\dot{\varepsilon} = 622\left(\frac{\sigma_0'}{\sigma_0} - 1\right)^{0.5} \tag{7.4}.$$

Equations (7.3) and (7.4) can be used with a 95 % confidence limit when determining the ultimate stress values under varying loading conditions of specimens made from the specific CFRP and GFRP specimens, respectively. The rate dependence of the specific CFRP and GFRP materials are described for increasing strain rates using equations (7.3) and (7.4), respectively. The two constants D and q for the two materials approximately equal. However, the q_{shear_cfrp} and D_{shear_cfrp} constants for the CFRP has more scatter therefore lower and upper bounds are given. The possible reason for the upper and lower bound is the inconsistency in the material lay-up and indeed the dimensions of the single lap shear specimen, which leads to failure outside the expected failure zone (chapter 5). The average values of the D and q constants for the two material systems, viz. CFRP and GFRP are equal; $q_{shear\_gfrp} \equiv q_{shear\_cfrp} \equiv 0.7$ and $D_{shear\_gfrp} \equiv D_{shear\_cfrp} \equiv 622 \equiv 688 \pm 42$. The proposed reason for this observation again leads to

the conclusion that the single lap specimens tested have a constant failure mode, viz. shear failure of the matrix.

7.5.3 NUMERICAL BEHAVIOUR

The numerical analysis of the single lap shear specimen is essentially based on a compression type load, the specimen design induces the shear failure. The numerical prediction results give ultimate stress values that are equal to the experimental results. Numerical contour plots of the single lap shear specimen show that ultimate failure occurs within the same zone as the experimental specimens. The single lap specimens are designed to fail along a specific failure plane due to initiation at the stress concentration in the specific plane. The numerical analysis succeeds in predicting failure within the same plane as the experimental specimens. The numerical prediction improves with the inclusion of the strain rate constitutive equations. This is not surprising since the rate dependence results in an increase in ultimate stress of 50 MPa to 120 MPa, with increases in strain rate from 10^{-3} s^{-1} at quasi-static to 900 s^{-1} at dynamic strain rates of loading, respectively.

7.5.4 SUMMARY OF SHEAR BEHAVIOUR

The single lap shear specimen is designed to determine the interlaminar shear strength of FRP [51,53,54]. The shear strength is described as the ability of a composite to resist delamination damage [45]. It is not clear from the results reported in this thesis however if pure delamination failure is achieved through this specimen design. Delamination in general would result from failure at the fibre-matrix interface. The experimental results at quasi-static strain rates especially give values that imply a matrix dominated failure, therefore approximately 40 MPa. At high strain rates the interlaminar shear strength according to the experimental results increase to 120 MPa. It is therefore not conclusive that this increasing strength is solely based on the strengthening of the matrix due to increasing strain rate. A portion of this strengthening could be due to the inducing of actual delamination at increasing strain rates.

7.6 TENSILE BEHAVIOUR OF FRP

7.6.1 MECHANICAL BEHAVIOUR

Previous experience in the field of high strain rate experimental work on CFRP and GFRP has suggested a rate dependent behaviour for GFRP [40]. CFRP is said to be brittle and therefore exhibits no rate dependency at increasing loading rates [10]. The experimental work and subsequent microscopic analysis attempts to elucidate the mechanism that lead to the increasing ultimate stress recorded in GFRP under dynamic loading conditions. Under tensile loading conditions the maximum stress values recorded will be a direct result of the fibre failure. This failure mechanism is known to have the highest energy associated with respect to failure in a laminate FRP [18].

The initial proposal, in terms of microscopic analysis, is to examine the failure surface of the fibres in a bid to establish differences in the fibre at quasi-static and dynamic strain rates. Secondly, to establish a difference in the failure surface of the brittle carbon fibres and "quasi-brittle" glass fibre. SEM analysis revealed cleavage planes for quasi-static and dynamic strain rates for both CFRP and GFRP. The existence of cleavage planes is synonymous with brittle failure. Indeed save for the experimental scatter in the results no rate dependency is recorded in the CFRP. No change in the carbon fibre failure surface is expected nor is any change observed in the SEM micrographs. This observation eliminates the fibre failure modes as the source of the rate dependency, for both laminate systems, CFRP and GFRP.

At higher strain rates the epoxy matrix is purported to undergo adiabatic heating. This results in increases in temperature of as much as 100° C [63]. Further softening of the matrix and successive increases in potential sites for fibre pull-out are reported. This feature is observed in the micrographs presented for both CFRP and GFRP loaded at high strain rates. However, from examination of the ultimate tensile stress values no significant change in the CFRP ultimate stress values are recorded. Fibre pull-out, increases with increasing strain rate. This mechanism however, does not appear to affect the rate dependency of the CFRP laminate system.

The tensile specimen will fail by progressive failure. Therefore as the specimen is loaded the various failure mechanisms come into play. Matrix failure occurs at lower stresses. As the stress increases fibre-matrix debonding and more matrix cracking will result. Subsequently sites of fibre pull-out become more prominent. The load carrying capabilities are limited to the fibres at the final stages of loading, close to the ultimate stress value of the FRP material. The failure mechanism sequence has been presented by Li *et al.* [63]. It is proposed that at high strain rates the fibre pull-out becomes more of a concern than at low strain rates of loading. It is also purported that the strain rate sensitivity reported in the GFRP arises from the interaction between fibre pull-out and final fibre fracture.

The ultimate stress of E-glass fibre is reported at 1700 MPa. The ultimate stress of carbon fibre is reported at 3100 MPa. When placed in an epoxy matrix the ultimate stress of the resulting laminate ranges from 650-950 MPa, for GFRP and 850-1500 MPa for CFRP [97]. The rate dependency in the GFRP may result from the increase in fibre pull-out zones at higher loading rates. The magnitude of this failure mechanism, fibre failure, at low strain rates has been reported to exist between 600-800 MPa [41]. Therefore in the case of GFRP this results in a strengthening mechanism. The ultimate stress for fibre pull-out is similar to the ultimate stress of the glass fibre epoxy. This interaction affects the overall ultimate stress of the laminate. Any rate dependency with respect to fibre pull-out would impact on the overall strength of the GFRP laminate. In the case of CFRP the final fibre failure occurs at a higher stresses than the fibre pull-out. Any increases in strength due to increases in sites of fibre pull-out, would in this case not, affect the overall strength of the CFRP laminate.

7.6.2 DEVELOPMENT OF CONSTITUTIVE EQUATION

The CFRP is expected to behave in a linear manner. Microscopic analysis of the failure mechanism has shown no significant change in the fibre failure mode with increasing strain rate. The high strength of the carbon fibre laminates suggests that the rate dependency would arise from a change in the post fibre cleavage plane, which dominants the quasi-static microscopic

analysis. However, observation of the high strain rate micrographs shows no change in the fractured fibre surface, the cleavage planes are still visible. This suggests that the carbon fibres maintain their brittle nature at high strain rates.

An empirical approach is again proposed. The experimental data of ultimate stress against strain rate results in a linear relationship, for both CFRP and GFRP. The D and q constants are deduced for both systems.

The following equation applies to the CFRP system (AIK-EHKF-420-UD24K-40) under tensile loading conditions

$$\dot{\varepsilon} = 54279 \pm 19072\left(\frac{\sigma_0'}{\sigma_0} - 1\right)^1 \tag{7.5}$$

The glass fibre system (Material type: EPO UD EST 250/600 FT 102 35% Glass) under tensile loading follows the equation.

$$\dot{\varepsilon} = 9136\left(\frac{\sigma_0'}{\sigma_0} - 1\right)^1 \tag{7.6}$$

The q constant in both cases is 1. This shows that both graphs have a constant/linear gradient. The D constants are large, in the case of GFRP above 9000. The values suggest only a slight change in gradient. The CFRP has a value of greater than 25000. It is suggested that the value is synonymous with a zero deformation gradient, hence on strain rate strengthening was expected.

7.6.3 NUMERICAL BEHAVIOUR

The ideal tensile specimen is designed to fail at the induced stress concentration zone. Numerical analysis of the tensile specimens shows failure at the desirable stress concentration zone. The numerical model of tensile test on CFRP shows that the ultimate stress occurs at approximately 1270 MPa. The experimental data gives a lower and upper bound of 1260 MPa and 1330 MPa, at quasi-static strain rates. Due to the limited rate dependency of the CFRP specimen the numerical analysis with a built-in strain rate dependency does not give a significant variation in the tensile failure at increasing strain rates.

The GFRP which has a certain degree of rate dependency benefits from the inclusion of the strain rate constitutive equation especially at high strain rates of loading. The GFRP is seen to increase its mean ultimate stress value from 760 MPa at quasi-static strain rates, to 910 MPa at dynamic strain rates. The ultimate stress in the numerical tensile mesh occurs at the stress concentration zone. Beyond the ultimate stress values the stress-strain graph show a significant drop in stress with increasing strain. Thereafter the stress value may fluctuate. The maximum shear stress is also monitored. It is interesting to note that both the ultimate tensile and ultimate shear stress in the 12-direction occur at the same time. Both contour plots also reveal that the failure point is located in the stress concentration zone. As mentioned previously in chapter 6, this implies that the peak stress for both shear and tension occur simultaneously.

7.6.4 SUMMARY OF TENSILE BEHAVIOUR

In the case of tensile testing a definite discrepancy exist between the ultimate stress reported for GFRP and CFRP under dynamic impact loading conditions. The GFRP shows increasing ultimate stress values as the strain rate goes from quasi-static to dynamic. CFRP on the other hand is not affected by increasing strain rates. Microscopic investigations have ruled out the influence of the actual glass and carbon fibre strands. In both cases the fibres show cleavage plans which are related to brittle failure. This implies the existence of another mechanism in glass fibre that is strain rate sensitive. This research has suggested increasing fibre pull-out for the

GFRP with increasing strain rate. However no quantitative analysis has been presented to substantiate this hypothesis.

7.7 COMBINATION OF STRAIN RATE AND FAILURE CRITERIA EQUATIONS

The following section will exploit the strain rate and failure criteria equations. These equations are combined and presented as they are in the form used in the numerical model via the VUMAT. The equations are separated into matrix cracking, delamination and fibre failure, they include out-of-plane stresses are proposed by Hou [82].

Equations (7.1) to (7.6) are rearranged to accommodate the dynamic ultimate stress (ϑ). The D and q are constants derived empirically. The equations are thus written as

$$\vartheta_{comp\_cfrp} = \left(1+\left(1863/\dot{\varepsilon}\right)^{4/3}\right)Y_c \tag{7.7}$$

for compression of CFRP

$$\vartheta_{comp\_gfrp} = \left(1+\left(2716/\dot{\varepsilon}\right)^{1/0.7}\right)Y_c \tag{7.8}$$

for compression of GFRP

$$\vartheta_{shear\_cfrp} = \left(1+\left(688/\dot{\varepsilon}\right)^{1/0.7}\right)S_{12} \tag{7.9}$$

for shear of CFRP

$$\vartheta_{shear\_gfrp} = \left(1+\left(622/\dot{\varepsilon}\right)^{0.5}\right)S_{12} \tag{7.10}$$

for shear of GFRP

$$\vartheta_{tension\_cfrp} = \left(1+\left(54279/\dot{\varepsilon}\right)\right)X_T \tag{7.11}$$

for tension of CFRP

$$\vartheta_{tension\_gfrp} = \left(1+\left(9139/\dot{\varepsilon}\right)\right)X_T \tag{7.12}$$

for tension of GFRP.

The specific strain rates are determined by the deformation gradient of the element in the numerical analysis. The following substitution of the strain rate equations presented previously in chapter 3, for example equation 3.6:

$$\left(\frac{\sigma_x}{X_T}\right)^2 + \left(\frac{\sigma_{xy}+\sigma_{xz}}{S_c}\right)^2 = e_f^2 \tag{7.13}$$

would account for strain rate in the fibre direction for the particular GFRP by substituting equation (7.10) and, (7.12), becoming

$$\left(\frac{\sigma_x}{\left(1+\left(9136/\dot{\varepsilon}\right)\right)X_T}\right)^2 + \left(\frac{\sigma_{xy}}{\left(1+\left(621.6/\dot{\varepsilon}\right)^{0.5}\right)S_{12}}\right)^2 = e_f^2 \tag{7.14}$$

this simplifies to

$$\left(\frac{\sigma_x}{\vartheta_{tension\_gfrp}}\right)^2 + \left(\frac{\sigma_{xy}+\sigma_{xz}}{\vartheta_{shear\_gfrp}}\right)^2 = e_f^2 \tag{7.15}$$

Equation (7.15) accounts for the rate sensitivity of the particular GFRP system. The same procedure is done for the remaining damage criteria equations. The numerical analysis is now fully automated to account for the rate dependant effect of both CFRP and GFRP systems under

compression, shear and tensile loads. The "new" equations account for matrix, delamination/shear and fibre failure at varying strain rates. The equations for matrix crushing is:

$$e_c^2 = \frac{1}{4}\left(\frac{-\sigma_y}{\vartheta_{shear\_gfrp}}\right)^2 + \frac{Y_C^2\sigma_y}{4\vartheta_{shear\_gfrp}^2\vartheta_{tension\_gfrp}} - \frac{\sigma_y}{\vartheta_{tension\_gfrp}} + \left(\frac{\sigma_{xy}}{\vartheta_{shear\_gfrp}}\right)^2 \geq 1 \tag{7.16}$$

for matrix failure

$$e_M^2 = \left(\frac{\sigma_y}{\vartheta_{comp\_gfrp}}\right)^2 + \left(\frac{\sigma_{xy}+\sigma_{yz}}{\vartheta_{shear\_gfrp}}\right)^2 \tag{7.17}$$

and for delamination growth

$$e_D^2 = D_a\left[\left(\frac{\bar{\sigma}_{33}}{\vartheta_{comp\_gfrp}}\right)^2 + \left(\frac{\bar{\sigma}_{13}}{\vartheta_{shear\_gfrp}}\right)^2 + \left(\frac{\bar{\sigma}_{23}}{\vartheta_{shear\_gfrp}}\right)^2\right] \tag{7.18}$$

The relevant substitutions are applied to the remaining equations to CFRP accordingly.

7.8 PLATE IMPACT BEHAVIOUR OF FRP

7.8.1 INTRODUCTION

The Chang-Chang criterion that has been widely used as a failure criteria for modelling progressive failure in laminates, combines elementary failure stresses in a system of quadratic equations covering the possibilities of failure resulting from fibre fracture, matrix cracking or delamination. Previous research has shown that experimental results have been used to compare the validity of various stress based failure criteria [76,103]. It has been shown that, while it is possible to explain experimental results, it is not always possible to provide accurate predictions of the extent of damage. Although the force and deflection history usually predicted by various numerical codes on composite beams and plates is in good agreement with experimental observations. The actual amounts of damage together with the observed mode of failure are not easily modelled [76]. It was thought that the method of solution of the finite element equations

involved time iteration which delays the process thus making it unsuitable for rapid damage growth. Secondly, the Chang-Chang criterion is based on bulk stresses, therefore any stress singularities at the edges of delaminations, fibre ends and matrix cracks may lead to doubt in the validity of the model. Thirdly, the contribution of strain rate effects on the validity of the prediction especially at high strain rates has not been evaluated; most impact models use quasi-static material data.

The main focus of the thesis was to investigate the effect of dynamic strain rate on CFRP and GFRP. The plate impact model is used to investigate to what extent the numerical prediction is improved for high/dynamic impact events. The generic approach, viz. uniaxial compression, shear and tension test provide data on the quasi-static and dynamic properties of CFRP and GFRP composites. This data is used in the empirical approach which involves modelling of GFRP laminate plates. In order to analyse the interaction between different plate thickness, 3 mm and 6 mm GFRP plates are tested and modelled to ensure that the interaction is valid for laminates of varying layers.

7.8.2 PLATE IMPACT WITH DAMAGE

Earlier research has shown improvements in the predictive capability of numerical models on quasi-static or low velocity impact models of laminate materials. Davies and Zhang used FE77 for modelling impact damage on CFRP at low velocity impacts, quasi-static strain rates [76]. A force-time history showed improvements of 45 % in the prediction capabilities of the numerical model when comparing the linear, undamaged FE77 model to the non-linear FE77 model [18]. The non-linear FE77 model compared well with the experimental force time history. The non-linear FE77 model predicted a maximum force of 780 N compared to the experimental results which gives maximum forces of 740 N. The Chang-Chang criteria were used as the damage criteria [18].

Quasi-static numerical predictions including Chang-Chang criteria for damage, implemented via the VUMAT in this work, are comparable to experimental results. Impact model results for a 6

mm thick laminate plate is compared with and without damage. The comparative study is aimed at investigating the effects of including a damage criteria to a laminate composite impacted at quasi-static strain rates. The study reveals improvements in the force time history of the laminate plate model. The linear model gives maximum forces of 4500 N. The experimental force time history graph give peak forces of 2950 N, resulting in a discrepancy of 54.2 %. Inclusion of the damage model results in peak forces of 2550 N, this gives improved prediction of 13.6 %. The enhancement due to the inclusion of damage is imperative for improved prediction of numerical modelling of laminate plates.

At quasi-static strain rates various failure mechanisms result in the absorption of energy in the laminate plates. The shear failure of a CFRP plate, for example, results in a change of stiffness of the laminate [38]. The load time histories will show a drop in the load with respect to time. This dip in load will correspond to the point at which shear failure occurs [38]. Similar features are reported in the results presented in this thesis. However, other reductions in force with respect to time are purported to occur due to delamination, fibre-matrix interfacial failure and debonding [38]. The Chang-Chang criteria as implemented in the numerical analysis reduce the relevant modulus as progressive damage takes place. The inclusion of Chang-Chang criteria, in the numerical model, results in an increased peak force. This is expected, as the reduction in stiffness/modulus will result in a reduced energy absorption and subsequent reduction in the peak force. The source of the improved numerical prediction with damage is therefore revealed.

At high strain rates the issue of rate dependency becomes important. From the experimental results presented in this work on compression, shear and tension, at higher strain rates a degree of strengthening is evident. Other authors have also reported on the strengthening of FRPs with increasing strain rate [18,41,42]. The inclusion of damage has shown improvements in the numerical model prediction capabilities. This premise is developed further for high strain rate modelling. Due to increases in ultimate stress values of CFRP and GFRP in general, from the experimental tests carried out at quasi-static to dynamic strain rates, any numerical model must in some form, therefore, include the strain rate sensitivity as a result of the increase in strain rate.

The strain rate sensitive constitutive equations derived empirically are implemented into the numerical model with damage. From the experimental work increases in strain rate have a negligible effect on the tensile strength of CFRP. For this reason it is suggested that GFRP properties are used for the numerical model validation. GFRP is strain rate sensitive for the three uniaxial tests conducted, viz. compression, shear and tension. Therefore a larger discrepancy is expected when comparing the quasi-static and dynamic plate impact results, to the experimental results for a GFRP plate impacted at 12 ms^{-1}.

The numerical prediction without the strain rate sensitive constitutive equation results in a 20 % variation in the numerical prediction as compared to the experimental reaction force. The inclusion of the various strain rate constitutive equations reduces the numerical prediction discrepancy as compared to the experimental value to 8 %. This is expected, the inclusion of the strain rate constitutive equations for GFRP increases the ultimate stress values accordingly. From the experimental results on compression, shear and tension increases are reported in ultimate stress. A single lap shear specimen of GFRP, for example, is reported to have a rise in ultimate stress of 300 MPa under increasing strain rates of 10^{-3} s^{-1} to 1200 s^{-1}.

The energy absorption mechanism of FRP is reported to be the strain energy to failure of the FRP system. This is equivalent to the area under the stress-strain graph. Any increases in ultimate stress will subsequently result in an increase in the energy absorbed by the FRP. The strain rate results under dynamic conditions have shown significant increases in the ultimate stress value. Therefore at increasing strain rates the energy absorption capabilities of the FRP plates is expected to increase. The numerical plate that includes the strain rate sensitive constitutive equations absorbs more energy and thus has a higher peak force, as compared to the numerical model without strain rate sensitivity.

Further investigations compare the tensile stress of the same element of the numerical prediction with strain rate against the tensile stress of a numerical prediction of the equivalent element without strain rate. The stress time relationship with strain rate reveals a higher maximum stress of 1180 MPa as compared to the same plate model without strain rate. Examination of the shear

stress of another element in the numerical plate models shows a higher shear stress for the numerical model that includes the strain rate sensitive constitutive equation. The deduction from these reported results cements the hypothesis further. Without strain rate included lower ultimate stresses are recorded. With strain rate included the rate dependent effect results in increased ultimate stresses. This is tantamount to increased energy absorption when related to the plate impact and consequently an improved numerical prediction of dynamic loads. The interaction of the various modes of failure at dynamic strain rates for GFRP will result in a combined increase in ultimate stress values. The numerical plate model accounts for this interaction of the failure mechanism. The need for a strain rate sensitive equation to supplement the damage model is therefore suggested for numerical modelling of plate impact damage at dynamic strain rates.

CHAPTER 8

CONCLUSIONS AND RECOMMENDATIONS FOR FUTURE WORK

One objective of this research was to observe and quantify the behaviour of FRP under varying loading conditions. High strain rate testing of FRP using the SHPB were performed with the intent of determining whether or not these materials performed differently to quasi-static conditions. Our studies have revealed that in general for different modes of failure, compression, shear and tension, the ultimate stress increases with increasing strain rate. In the case of compression loading, matrix and delamination failure appear to play crucial roles at increasing strain rates. Shear failure is dominated by matrix cracking and failure of the fibre-matrix interface for both FRP systems. This shear failure mode is seen to yield a significant increase in ultimate stress in shear as compared to compression and tension. The shear failure mode is more sensitive to strain rate when compared to compression and tension. This was inferred from the lower D values determined experimentally. The failure for both GFRP and CFRP systems were dominated by fibre breakage. Although the tensile strength was relatively insensitive to strain rate, it was found that the glass fibre system was more sensitive to strain rate in tension.

Experimental data derived from experimental test at different strain rates were used in the Cowper-Symonds relation to derive the q and D constants. Qualitative analysis through examination of the modes of failure for quasi-static to dynamic loading, coupled with quantitative analysis of the q and D constants developed from the material characterization results give a good foundation for understanding the behaviour of FRP under varying loading conditions.

Brittle materials are not expected to have any degree of strain rate sensitivity. Both CFRP and GFRP are considered to be brittle composites. However, "quasi-viscoelasticity" describes this family of materials better, under dynamic loading rates. This study has shown a change in the various modes of failure with increasing strain rates. Future work in the area of mode of failure

characterization versus changes in strain rate from quasi-static to dynamic would, it is believed, elaborate further on the reason for this change in ultimate stress recorded in the results given in chapter 5. Due to the brittle nature of FRPs, together with the inherent manufacturing flaws, a statistical margin of error is proposed to account for this inhomogeneity. Therefore, more work is required to ensure a wider database is developed for ultimate stress versus strain rate. This will result in better confidence in the suggested trends. Finally, the strain to failure behaviour versus strain rate has been neglected in this research. This is an important study. However, due to the brittle nature of failure of CFRP and GFRP, the sensitivity of the strain recording devices must be high. This will naturally lead to investigations of the elastic modulus relation with strain rate.

The experimental findings are compared to a parallel project using theoretical/numerical techniques to model the behaviour of the specimens. The connection between the projects is illustrated in Figure 8.1. Of course the good correlation in experimental and modelling results is not unexpected, since the model is programmed to fail according to the inputted experimental data, at least with regards to the simply loaded specimens, for compression, shear and tension. The plate impact model serves as a "diagnostic tool" (see Figure 8.1) to check for the accuracy of the numerical model. The plate impact model does not use any information from the experimental plate impact test, so in essence the concept of fitting of the experimental data does not arise in this case. To date, only one group of researchers is known to have published high strain rate modelling of a composite plate including damage caused by out-of-plane stresses. However they used quasi-static material property data [82]. If the disparity between the quasi-static material property data and dynamic material property data is significant (>15% of the overall ultimate stress), then it is inappropriate to use the quasi-static data universally, i.e. in quasi-static as well as dynamic scenarios. The field of FRP is "ridden with uncertainty" due to the anisotropic nature of the materials. This coupled with the flaws that may arise from manufacturing of the finished component is a recipe for an extremely complicated system macroscopically. On a more scientific level too, the sequence of composite modes of failures are numerous with each failure mode accounting for a certain degree of energy absorption in the system. Increases in the strain rate, from quasi-static to dynamic, are tantamount to reducing the time of response. It has been shown from the various visual and microscopic analysis that the specimen failure is notably

different except for shear failure of the matrix. Therefore for improved numerical modelling accuracy it is clear that the strain rate needs to be considered.

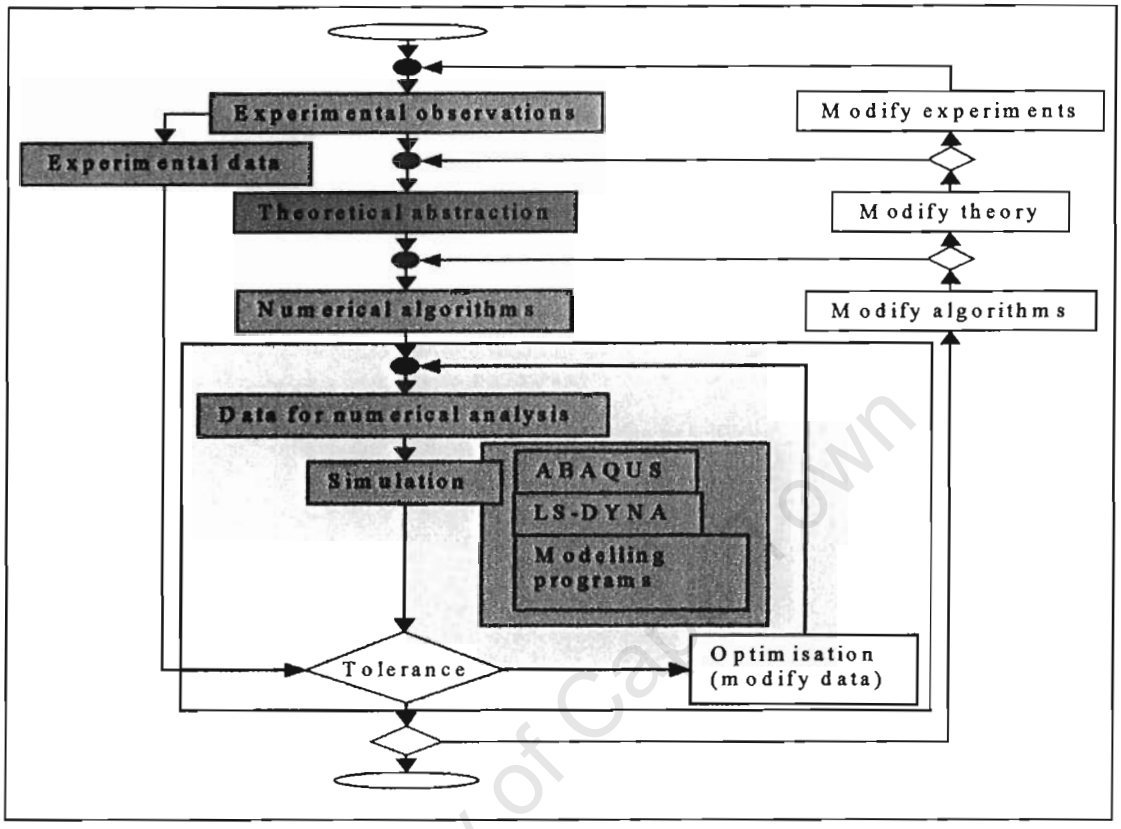

Figure 8.1: Integrated experimental and numerical approach to predictive modelling.

This thesis has also attempted to introduce preliminary modelling results of CFRP and GFRP materials at high strain rates. This model includes strain rate constants developed from the experimental work at varying loading rates. This information is built into a numerical model that includes damage. The model that was developed is the first published model that includes techniques for approximating the ultimate stress and forces with built-in strain rate constitutive equations that automatically account for the variation in ultimate stress at varying strain rates for particular GFRP and CFRP systems impacted under varying strain rates, ranging from quasi-static to dynamic. For the first time a model that uses separate q and D constants, that qualitatively describes the different levels of strain rate sensitivity in compression, shear and tension for CFRP and GFRP as well as built-in damage through the Chang-Chang criteria,

implement using a VUMAT has been published. This model has enhanced the predictive capabilities of a plate impact model of GFRP from 21 % to 8% of the experimental value.

Future work towards developing the model should firstly include other failure criteria mentioned in the Table 2.1 (chapter 2) versus strain rate. This will give a useful comparison with the Chang-Chang model used in this thesis. Further work in modelling must include a detailed post damage analysis. Presently the model only accounts for initial damage. The field of delamination damage in FRP is more complex when compared to other failure modes. As a result, a great deal of work is being undertaken to develop numerical models that simulate the onset and propagation of delamination failure. This possesses an area of research on its own. Experimental work undertaken in this research has suggested increasing sites of delamination with increasing strain rate. Given this background the relationship with delamination and strain rate needs more attention. A model that predicts the potential sites for delamination damage together with the approximate sizes of delamination at varying strain rates would be invaluable. Also, a rational methodology for incorporating a strain based failure criterion into the structural model is needed to supplement the stress based criteria.

REFERENCES

[1] World of Composites, Quarterly Publications of the SPI Reinforced Plastics/Composites Institute, Winter 2000.

2 Lin S.S. and Hogg P., "Assessing Industrial Capabilities for Carbon Fibre Production", SAMPE Journal, Vol. 54, No. 4, 2001.

3 Haddock R.N., "Status and Viability of Composite Materials in Structures of High Performance Aircraft", Grumman Aircraft Systems Division, a Presentation to the National Research Council, Aeronautics and Space Engineering Board, Naval Postgraduate School Monterey, 1990.

4 Aerospace Engineering, SAE International, January 2003.

5 European Aeronautic Defence and Space Company EADS N.V. Le Carré · Beechavenue pp. 130-132 1119 PR Schiphol Rijk, The Netherlands.

6 Okoli O.I. and Smith G.F., "High Strain Rate Characterization of a Glass/Epoxy Composite", Journal of Composites Technology and Research, Vol. 22, p.3, 2000.

7 Sierakowski R.L. and Chaturvedi S.K., "Dynamic Loading and Characterization of Fibre Reinforced Composites" Copyright John Wiley and Sons, Inc., 1997.

8 Lindholm U.S., "Review of Dynamic Testing Techniques and Material Behaviour", Proceedings of the Conference on Mechanical Properties of Materials at High Rates of Strain, Institute of Physics London and Bristol, Conference series number 21., p. 3, 1974.

9 Reinhart T.J., "Engineering Materials Handbook", ASM International handbook Committee, 1987.

10 Kawata K., Hondo A., Hashimoto S., Takeda N. and Chung H.L., "Dynamic Behaviour Analysis of Composite Materials", Composite Materials, Eds. Kawata K. and Akasaka T., Proceeding Japan-U.S. Conference, Tokyo, 1981.

11 Harding J. and Welsh L.M., "A Tensile Testing Technique for Fibre-Reinforced Composites at Impact Rates of Strain", Journal of Material Science Vol. 18, p. 1810, 1983.

12 Marom G., Fischer S., Tuler F.R. and Wagner H.D., "Hybrid Effects in Composites: Conditions for Positive or Negative Effects versus Rule-of-Mixtures Behaviour", Journal of Material Science, Vol. 13, p. 1419, 1978.

13 Phillips M.G., "Fracture and Fatigue of Hybrid Composites", in Fibre Composite Hybrid Materials, Ed: Hancox N.L., Applied Science Publishers Barking, Essex, 1981.

14 Adams D.F., ASTM STP 617, p.407, 1977.

15 Sierakowski R.L., Nevill G.E., Ross C.A. and Jones E.R., "Dynamic Compressive Strength and Failure of Steel Reinforced Epoxy Composites", Journal of Composite Materials Vol. 5, 1971.

16 Harding J. and Li Y.L., "Determination of Interlaminar Shear Strength for Glass/epoxy and Carbon/epoxy at Impact Rates of Strain", Composite Science and Technology, Vol. 45, p.161, 1992.

17 Chen Wai-Fah and Saleeb A.F., "Constitutive Equations for Engineering Materials", Volume I: Elasticity and Modelling, Wiley and Sons, 1982.

18 Rawlings R.D. and Matthews F.L., "Composite Materials: Engineering and Science", Chapman and Hall, 1995.

19 Lindholm U.S., "Some Experiments with The Split Hopkinson Bar", Journal of Mechanics and Physics of Solids, Vol.12, p.317, 1964.

20 Schultheisz C.R. and Waas A.M., "Compression Failure of Composites, Part I: Testing and Micromechanical Theories", Progress in Aerospace Science, Vol. 32, p.1, 1996.

21 Whitney J., "Structural Analysis of Laminated Anisotropic Plates", Technomic, Lancaster, PA, USA, 1989.

22 ASTM Standard D3410-87, "Standard Test Method for Compressive Properties of Unidirectional of Cross-Ply Fibre Resin Composites", Annual Book of ASTM Standards, Vol. 15 No. 3, p.189, 1991.

23 Berg J.S. and Adams D.F., "An Evaluation of Composites Material Compression Test Methods", Journal of Composite Technology and Research, Vol.11, No. 2, pp.41, 1989.

24 Dutta P.K., "Low Temperature Compressive Strength of Glass-Fibre Reinforced Polymer Composites", Proceedings of the 11th Conference on Offshore Mechanics and Arctic Engineering, June 1992.

25 Sierakowski R.L., "Strain Rate Effects in Composites", Applied Mechanical Review, ASME, Vol. 50, No.11, Part 1, 1997.

26 Griffiths L.J. and Nevill G.E., "A Study of the Dynamic Behaviour of a Carbon-fibre Composite Using the Split Hopkinson Pressure Bar", Journal of Physics D: Applied Physics, Vol. 7, p. 2329, 1974.

27 Kumar P., Garg A. and Agarwal B.D., "Dynamic Compressive Behaviour of Unidirectional GFRP for Various Fibre Orientations". Material Letters, Vol. 4, No.2, p. 111, 1986.

28 Daniel I.M. and LaBedz R.H., "Method of Compression Testing of Composite Materials at High Strain Rates", Compression Testing of Homogeneous Materials and Composites, ASTM STP 808, Eds. Chait R. and Papirno R., American Society for Testing and Materials, Philadelphia, p. 364, 1983.

29 El-Habak A.M.A., "Mechanical Behaviour of Woven Glass Fibre Reinforced Composites under Impact Compression Load", Composites, Vol. 22, No. 2, p. 129, 1991.

30 Harding J., "Effect of Strain Rate and Specimen Geometry on the Compressive Strength of Woven Glass-Reinforced Epoxy Laminates", Composites, Vol. 24, No. 4, p. 323, 1993.

31 El-Habak A.M.A., "Compressive Resistance of Unidirectional GFRP under High Rate of Loading" Journal of Composites Technology & Research, JCTRER, Vol. 15, No. 4, Winter, p. 311, 1993.

32 Tay T.E., Ang H.G. and Shim V.P.W. "An Empirical Strain Rate-dependent Constitutive Relationship for Glass-fibre Reinforced Epoxy and Pure Epoxy", Composite structures, Vol. 33, p. 201, 1995.

33 Takeda N. and Wan L., "Impact Compression Damage Evolution in Unidirectional Glass Fibre Reinforced Polymer Composites", AD-Vol. 48, High Strain Rate Effects on Polymer, Metal and Ceramic Matrix Composites and other Advanced Materials ASME 1995, p. 109 , 1995.

34 Hsiao. H.M. and1 Daniel I.M., "Strain Rate Behaviour of Composite Materials", Composites, Part B, 29B, p. 521, 1998.

35 Weeks C.A. and Sun C.T., "Modelling Non-linear Rate-dependent Behaviour in Fibre-Reinforced Composites", Composites Science and Technology, Vol. 58, p. 603, 1998.
36 Woldesenbet E. and Vinson J.R., "Specimen Geometry Effects on High-strain-rate Testing of Graphite/Epoxy Composites", AIAA Journal, Vol. 37, No.9, p.1103, 1999.
37 Gary G. and Zhao H., "Dynamic Testing of Fibre Polymer Matrix Composites Plates Under In-plane Compression", Composites Part A: Applied Science and Manufacturing, Vol. 31, p. 835, 2000.
38 Vinson J. and Woldesenbet E., "Fibre Orientation Effects on High Strain Rate Properties of Graphite/Epoxy Composites", Journal of Composite materials, Vol. 35, p. 509, 2001.
39 Ninan L., Tsai J. and Sun C.T., "Use of Split Hopkinson Pressure Bar for Testing Off-axis Composites", International Journal of Impact Engineering Vol. 25, p. 291, 2001.
40 Hosur M. V., Alexander J. and Vaidya U.K., "High Strain Rate Compression of Carbon/Epoxy Laminate Composites", Composite Structures 52, Vol. 52, p. 405, 2001.
41 Li Z. and Lambros J., "Determination of the Dynamic Response of Brittle Composites by the Use of the Split Hopkinson Pressure Bar", Composite Science and Technology Vol. 59, p. 1097, 1999.
42 Lankford J., "Compressive Damage and Failure at High Loading Rates in Graphite Fibre-Reinforced Polymeric Matrix Composites", Ceramic Transaction, Vol. 19, p.553, 1991.
43 Daniel I.M., Hamilton W.G. and LaBedz R.H., "Strain Rate Characterization of Unidirectional Graphite/Epoxy Composite", Composite Material: Testing and Design (Sixth Conference), ASTM STP 787, p.393, 1982.
44 Harding J. and Ruiz C., "The Mechanical Behaviour of Composite Materials under Impact Loading", Key Engineering Materials, Trans Tech Publications, Vols. 32, p.1, 1996.
45 Hallett S.R., Ruiz C. and Harding J., "The Effect of Strain Rate on the Interlaminar Shear Strength of Carbon/Epoxy Cross-ply Laminate: Comparison Between Experiment and Numerical Prediction", Composite Science and Technology, Vol. 59, pp. 749, 1999.
46 Iosipescu N., "New Accurate Procedure for Single Shear Testing of Metals", Journal of Materials, Vol. 2, No. 3, pp.537, 1967.

47 ASTM D 5379M-93, "Standard Test Method for Shear Properties of Composite Materials by the V-notched Beam Method".

48 wwweng.uwyo.edu/mechanical/Research/ cmrg/whatshappening.htm

49 Xing Y.M., Poon C.Y. and Ruiz C., "A Whole Field Strain Analysis of the Iosipescu Specimen and Evaluation of Experimental Errors", Composite Science and Technology, Vol. 47, p.251, 1993.

50 Morton J., Ho H., Tsai M.Y. and Farley G.L., "An Evaluation of the Iosipescu Specimen for Composite Materials Shear Property Measure Measurement", Journal of Composite Materials, Vol. 26, No. 5, p. 708, 1992.

51 Dong L. and Harding J., "A Single-Lap Shear Specimen for Determining the Effect of Strain Rate on the Interlaminar Shear Strength of Carbon Fibre-Reinforced Laminates", Composites, Vol. 25, No. 2, p. 129, 1994.

52 Harding J. and Dong L., "Effects of Strain Rate on the Interlaminar Shear Strength of Carbon-Fibre-Reinforced Laminates", Composites Science and Technology, Vol. 51, p. 347, 1994.

53 Bouette B., Cazeneuve C. and Oytana C. "Shear in Carbon/Epoxy Laminates at Various Strain Rates." In Fuller J., Gruninger G., Schulte K., Bunsell A.R., Massiah A., editors. Proc. ECCM-4, Developments in the Science and Technology of Composite Materials London and New York: Elsevier Applied Science, p. 517, 1990.

54 Bouette B., Cazeneuve C. and Oytana C. "Effect of Strain Rate on the Interlaminar Shear Specimen Shear Strength of Carbon Fibre Reinforced Laminates" Composites Science and Technology, (45) p. 313, 1992.

55 Werner S.M. and Dharan C.K.H., "The Dynamic Response of Graphite Fibre-Epoxy at High Shear Strain Rates", Journal of Composite Materials, Vol. 20, p.365, 1986.

56 Leber H. and Lifshitz J.M., "Interlaminar Shear Behaviour of Plain-Weave GRP at Static and High Rates of Strain", Composite Science and Technology, Vol. 56, p.391, 1996.

57 Lifshitz J.M. and Leber H., "Response of Fibre-Reinforced Polymer to High Strain Rate Loading in Interlaminar Tension and Combined Tension/Shear", Composite Science and Technology, Vol. 586, p.987, 1998.

58 Chiem C.Y. and Liu Z.G., "The Relationship between Tensile Strength and Shear Strength in Composite Materials Subjected to High Strain Rates", Journal of Engineering Materials and Technology, Vol. 110, p.191, 1988.

59 "ASTM Methods for Long-Fibre Composites", ASTM Committee on Standards, Philadelphia, Pa. 19103, 1982.

60 Gilat A. and Goldberg R.K. and Roberts G.D., "Experimental Study of Strain-Rate-Dependent Behaviour of Carbon/Epoxy Composites", Composite Science and Technology, Vol. 62, p.1469, 2002.

61 Pannkoke K., Hogen R. and Wulf A., "Mechanical Response of an Unidirectional Carbon Fibre Reinforced Plastic to Quasi-static and Dynamic Loads", Proceedings ICCE-1, Eds. David Hui, New Orleans, p.895f, 1994.

62 Yuanming X. and Xing W., "Constitutive Equation for Unidirectional Composites Under Tensile Impact", Composite Science and Technology, Vol. 56, p.155, 1996.

63 Li Z. and Lambros J., "Dynamic Thermo-mechanical Behaviour of Fibre Reinforced Composites", Composites Part A, Vol. 31, p. 537, 2000.

64 Walter M.E. and Ravichandran G., "An Experimental Investigation of Damage Evolution in a Ceramic Matrix Composite", Journal of Engineering Materials Technology, Vol.117, p. 101, 1995.

65 Staab G.H. and Gilat A., "High Strain Rate Response of Angle-Ply Glass/Epoxy Laminate", Journal of Composite Materials, Vol. 29, p. 1308, 1995.

66 Chiem C.Y. and Liu Z.G., "A New Technique for Tensile Testing of Composite Materials at High Strain Rates", Experimental Techniques, March 1988.

67 Saka K. and Harding J., "Behaviour of Fibre-reinforced Composites under Dynamic Tension", Final Report on Grant No. AFOSR-85-0042, September 1985, Oxford University Engineering Laboratory Report, OUEL 1654185.

68 Daniel I.M., Hamilton W.G. and Labedz R.H., "Strain Rate Characterization of Unidirectional Graphite Epoxy Composites", Composite Materials: Testing and Design, ASTM STP, 787:398, 1982.

69 Tsai S.W., "Composite Design", 4th Edition, Think Composites, Dayton Ohio, 1988.

70 Chen A.S. and Matthews F.L., "A Review of Multiaxial/Biaxial Loading Tests for Composite Materials", Composites, Vol. 24, p.395, 1993.

71 Daniel I.M. and Ishai O., "Engineering Mechanics of Composite Materials", Oxford University Press, Oxford, UK, 1994.

72 Kaw A.K., "Mechanics of Composite Materials', CRC Press LLC, 1997.

73 Soden P.D., Hinton M.J. and Kaddour A.S., "A Comparison of the Predictive Capabilities of Current Failure Theories for Composite Laminates", Composite Science and Technology, Vol. 58, p.1225, 1998.

74 Abrate S., "Impact on Laminated Composite Materials", Applied Mechanics Review, Vol. 44, p.155, 1991.

75 Cantwell W., J. and Morton J., "The Impact Resistance of Composite Materials – A Review", Composites, Vol. 22a, No. 5, pp.347-362, September 1991.

76 Davies G.A.O. and Zhang X., "Impact Damage Prediction in Carbon Composite Structures", International Journal of Impact Engineering, Vol. 16, No. 1, p. 149, 1995.

77 Jih C.J. and Sun C.T., "Prediction of Delamination in Composite Laminates Subjected to Low Velocity Impact", Journal of Composite Materials, Vol. 27, p. 684, 1993.

78 Tan T.M. and Sun C.T., "Use of Static Indentation Laws in the Impact Analysis of Laminated Composite Plates", Journal of Applied Mechanics, Vol. 52, p.6, 1985.

79 Choi H.Y. and Chang F.K., "A Model for Predicting Damage in Graphite/Epoxy Laminated Composites Resulting from Low-Velocity Point Impact", Journal of Composite Materials, Vol. 26, No. 14, p. 2134, 1992

80 Collombet F., Lalbin X. and Lataillade L.J., "Impact Behaviour of Laminated Composites: Physical Basis for Finite Element Analysis", Composite Science and Technology, Vol. 58, p. 463, 1998.

81 Li C.F., Hu N., Yin Y.J., Sekine H. and Fukunaga H., "Low-Velocity Impact-Induced Damage of Continuous Fibre-Reinforced Composite Laminates. Part I. An FEM Numerical Model", Composites: Part A, Vol. 33, p. 1055, 2002.

82 Hou J.P., Petrinic N., Ruiz C. and Hallet S.R., "Prediction of Impact Damage in Composite Plates", Composite Science and Technology, Vol. 60, p. 273, 2000.

83 Jen K.C. and Mao K., "Modelling Progressive Failure in Laminated Composites", ABAQUS Users' Conference Proceedings, Newport Rhode Island, p.223, 1992.

84 Aslan Z., Karakuzu R. and Okutan B., "Response of Laminated Composite Plates under Low-Velocity Impact Loading", Composite Structures, Vol. 59, p.119, 2003.

85 Chen J.K., Allahdadi A.A. and Carney T.C., "High-Velocity Impact of Graphite/Epoxy Composite Laminates", Composite Science and Technology, Vol. 57, p.1369, 1997.

86 Majeed O., Worswick M.J., Straznicky P.V. and Poon C., "Numerical Modelling of Transverse Impact on Composite Coupons", Canadian Aeronautics and Space Journal, Vol. 40, Issue 3, p.99, Sept. 1994.

87 Kuhl E. and Ramm E., "Simulation of Strain Localization with Gradient Enhanced Damage models", Computational Materials Science, 16, p.176-185, 1999.

88 Okoli O.I. and Latif A.A., 'Failure in Composite Laminates: Overview of An Attempt at Prediction", Composites: Part A, Vol. 33, p.315, 2002.

89 Harding J. and Ruiz C., "The Mechanical Behaviour of Composite Materials under Impact Loading", Key Engineering Materials, Trans Tech Publications, Vols., p.403, 1998.

90 Gray G.T., "Classical Split Hopkinson Pressure Bar Technique", ASM, Vol.8-Mechanical Testing, 1999.

91 Harding J., "Validation of the ELAN Software for Analysing the Tensile SHPB Test", UTC Report 122, 1998.

92 Hibbitt, Karlsson and Sorensen Inc., "ABAQUS Theory Manual Version 6.3.1", 2002.

93 Norman J., "Structural Impact", Cambridge University Press, 1989.

94 Hashin Z. and Rotem A., "A Fatigue Failure Criterion for Fibre Reinforced Materials", Journal of Composite Materials, Vol. 7, p. 448, 1973.

95 Yamada S.E. and Sun C.T., "Analysis of Laminate Strength and Its Distribution", Journal of Composite Materials, Vol. 12, p.275, 1978.

96 Chang F.K. and Chang K.Y., "A Progressive Damage Model for Laminated Composite Containing Stress Concentrations", Journal of Composite Materials, Vol. 21, p.834, 1987.

97 Chang F.K., Choi H.Y. and Jeng S.T., "Study on Impact Damage in Laminated Composites", Mechanics of Materials, Vol.10, No.1-2, p.83-95, 1990.

98 Valisiev V.V. and Morozov E.V., "Mechanics and Analysis of Composite Materials", Elsevier Science Ltd., 1st Edition, 2001.

99 Burnett D.S., "Finite Element Analysis, From Concepts to Applications", Addison-Wesley Publishing Company, Amsterdam 1987.

100 Matthews F.L., Davies G.A.O., Hitchings D. and Soutis C., "Finite Element Modelling of Composite Materials and Structures", Woodhead Publishing Limited, 2000.

101 Balden V., "Finite Element Analysis – MEC 564z Course Notes, Centre for Research in Computational & Applied Mathematics (CERECAM)", University of Cape Town, 1999.

102 Cook R.D., Malkus D.S. and Plesha M.E., "Concepts and Applications of Finite Element Analysis", Wiley , 3rd Edition, 1989.

103 Petrinic N., Wang L. and Elliott B., "An Approach to Predictive Modelling of Failure in Metals Subjected to Impact Loading", VII International Conference on Computational Plasticity, COMPLAS VII, Oñate E. & Owen D.R.J., (Eds), CIMNE, Barcelona, 2003

104 Petrinic N., "High Strain Rate Properties of GLARE®", Internal Report SMG 051, September 2002.

105 Devore J.L., "Probability and Statistics for Engineering and the Sciences, 5th ed., Pacific Grove, California. Duxbury/Thomson Learning, c2000.

106 Getting started with ABAQUS/Explicit section 3-1.

107 Zienkiewicz, O.C. and Taylor R.L., "The Finite Element Method", 5th Edition, Oxford, Boston: Butterworth-Heinemann, 2000.

108 Hibbitt, Karlsson and Sorensen, "ABAQUS Keywords Manual", Section 18., pp.20-1, ©Hibbitt, Karlsson and Sorensen Inc., 2000.

109 Hibbitt, Karlsson and Sorensen, "ABAQUS Explicit User Manual", Volume II, ©Hibbitt, Karlsson and Sorensen Inc., 2000.

110 Hibbitt, Karlsson and Sorensen, "ABAQUS Standard User's Manual", Volume II, Section 14.1.1, ©Hibbitt, Karlsson and Sorensen Inc., 2000.

111 Zienkiewicz O.C. and Taylor R.L., "The Finite Element Method", Fourth Edition, Volume 2, McGraw-Hill Book Company, Solid and Fluid Mechanics Dynamics and Non-Linearity, 1991.

112 Hibbitt, Karlsson and Sorensen, "ABAQUS Verification User Manual", ©Hibbitt, Karlsson and Sorensen Inc., 2000.

113 Welsh L.M. and Harding J., "Journal Proceedings DYMAT 85, International Conference on Mechanical and Physical Behaviour of Materials under Dynamic Loading", Journal de Physique, Colloque C5, pp. 405-414, 1985.

APPENDIX I

Compression specimen preparation

Initial 48 layers CFRP/GFRP plate

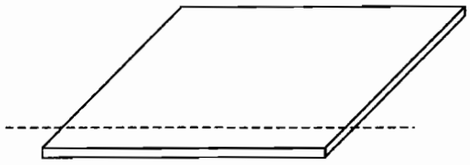

Plate sectioned parallel to dotted lines

Each section of the plate is then cut out and machined in to cylindrical section of diameter (*d*)

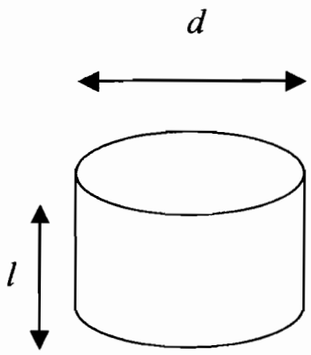

Finally the specimens are cut in to equal lengths of length (*l*)

$l = 9$ mm

$d = 8$ mm

Fig. 1: Schematic of compression samples.

APPENDIX II

Single lap shear specimen preparation

Initial 48 layers CFRP/GFRP plate

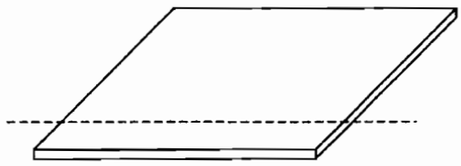

Plate sectioned parallel to dotted lines

Each section is cut into cuboids of width 15mm and height 10mm

Finally the cuboids are machined into Z-shaped specimens as shown in the schematic below

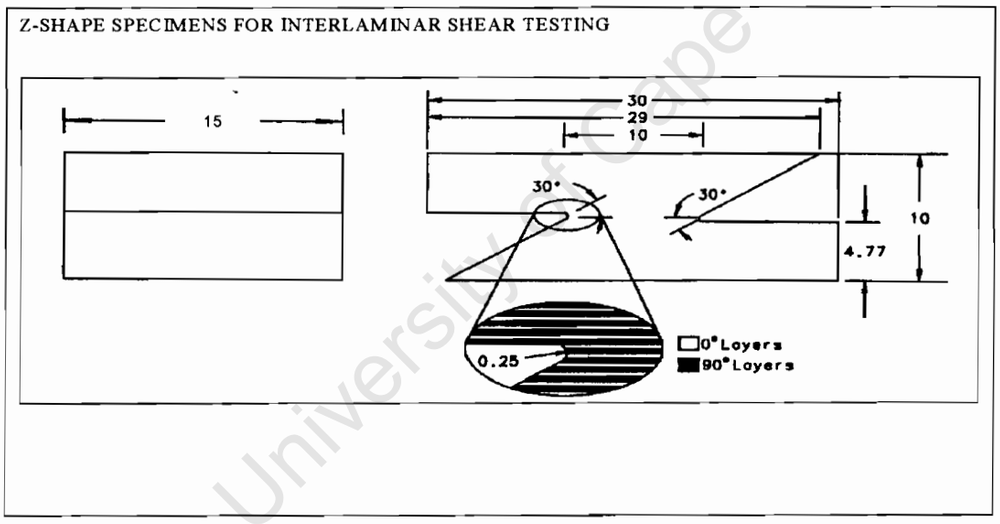

Fig. 1: Schematic of single lap shear samples (not this is not to scale and all the dimensions represent mm).

APPENDIX III

Tensile specimen preparation

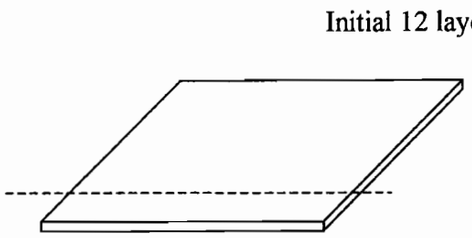

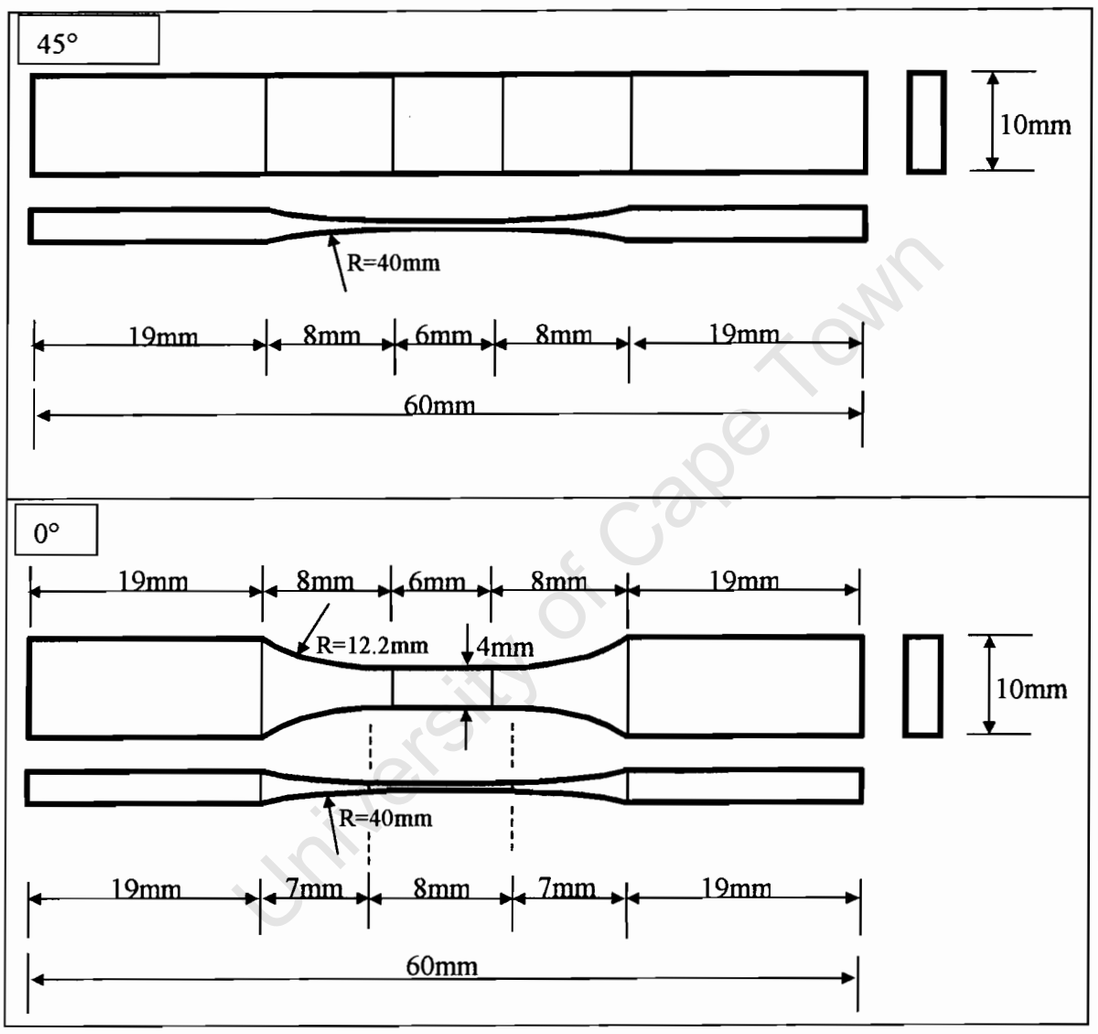

Fig. 1: Schematic of FRP tensile specimens showing dimensions for 0 and 45°.

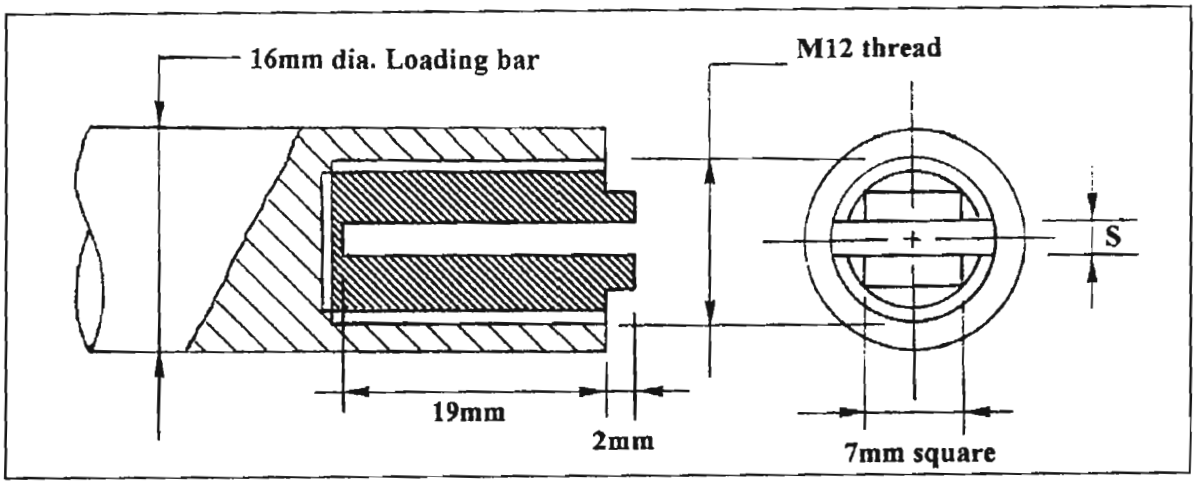

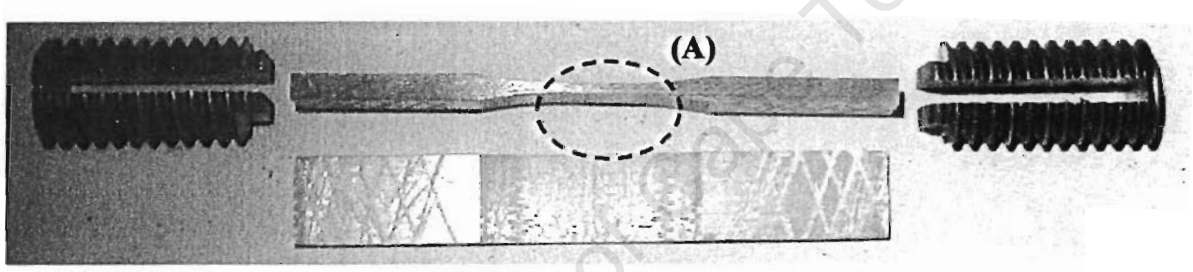

Fig. 1: Schematic of tensile samples showing the positioning of the metallic tab used to ensure failure occurs within the specimens and not prematurely at the grips. The careful machining of the specimen's mid section is shown (A), this induces stress concentration zone to again ensure failure within the specimen.

APPENDIX IV

Graphs for processing material characterisation results from the SHPB tests

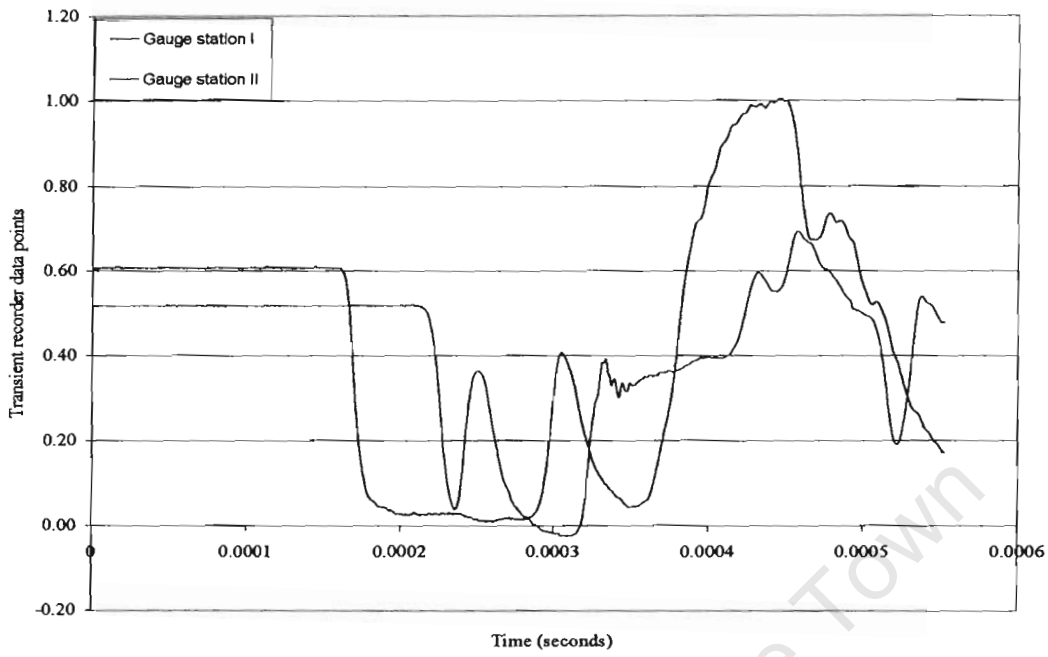

Fig. 1: Raw data for gauge stations I and II.

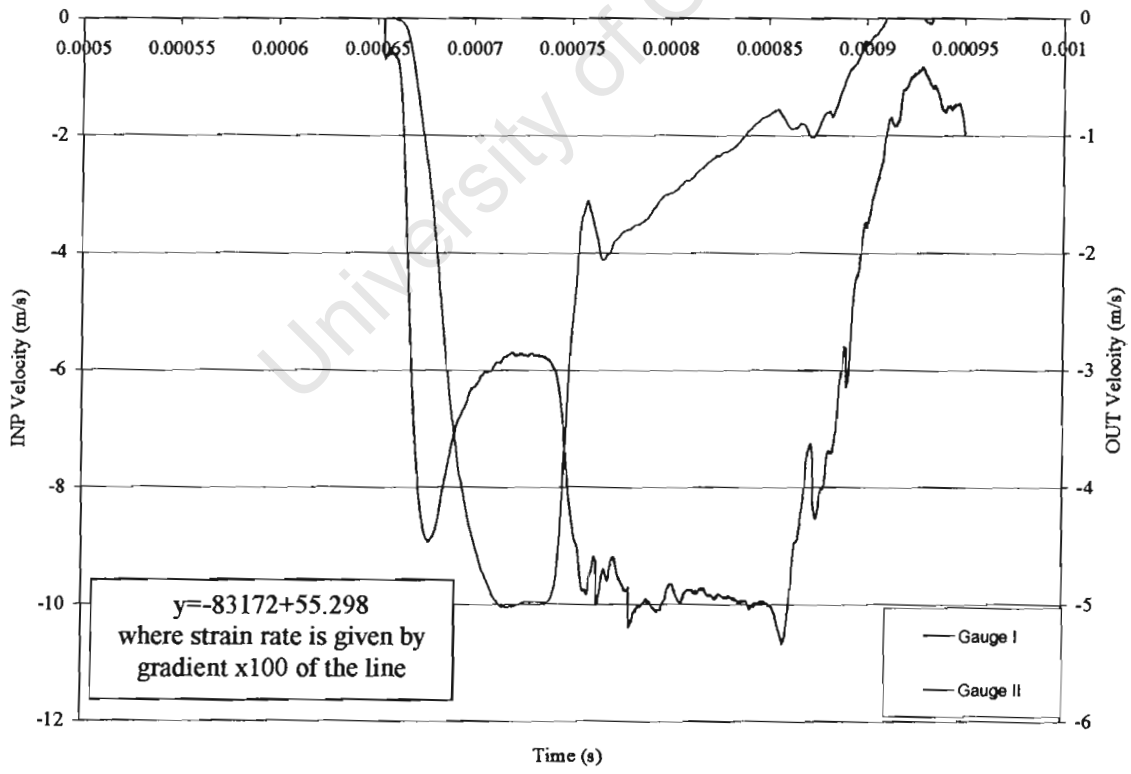

Fig. 2: INP/OUT Velocity-Time curves for gauge stations G_I and G_{II}.

The rapid reduction in the input bar velocity across the ends of the specimen is reversed, corresponding to a compressive strain rate. The corresponding specimen strain is determined by integrating between the two curves in Fig. 2, to give the displacement, and then to divide by the nominal gauge length, in this case taken as 8.85mm. Integration using Simpson's rule for successive time intervals of 0.2μs results in the graph, Fig. 3.

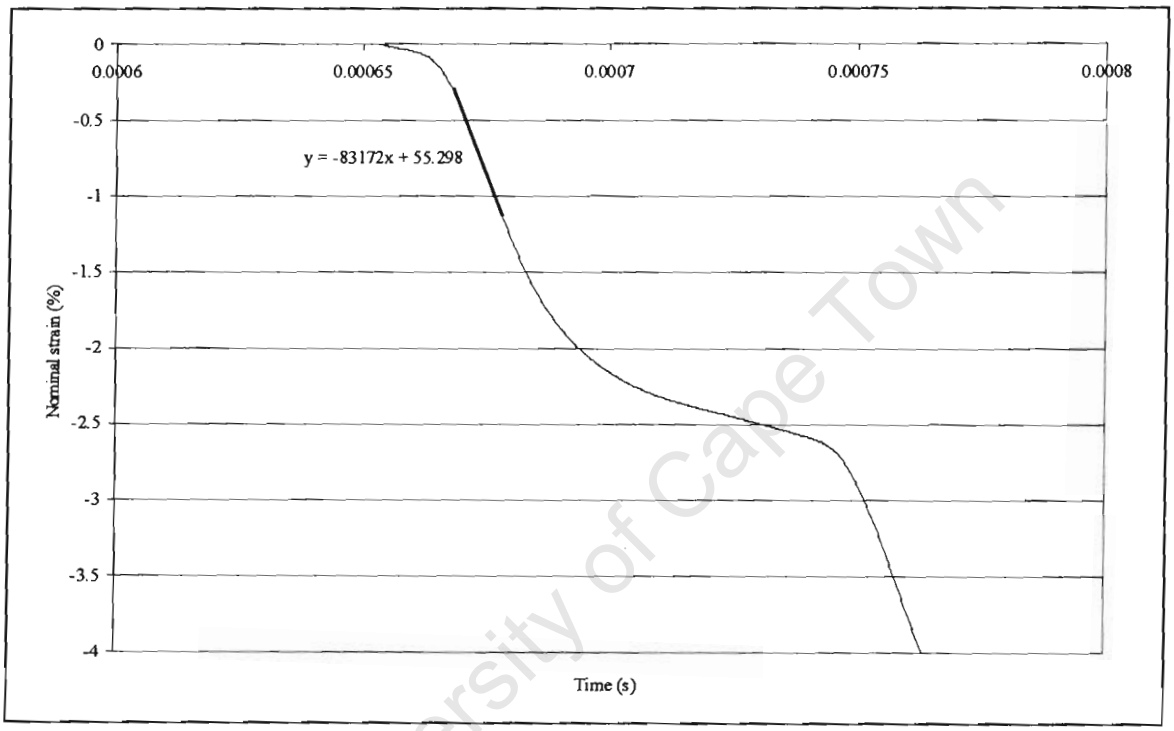

Fig. 3: Percentage Strain-Time curve.

Similarly the strain rate at any instant in the test may be derived directly from the difference between the input and output bar velocities at any given time, divided by the specimen nominal gauge length, Fig. 4.

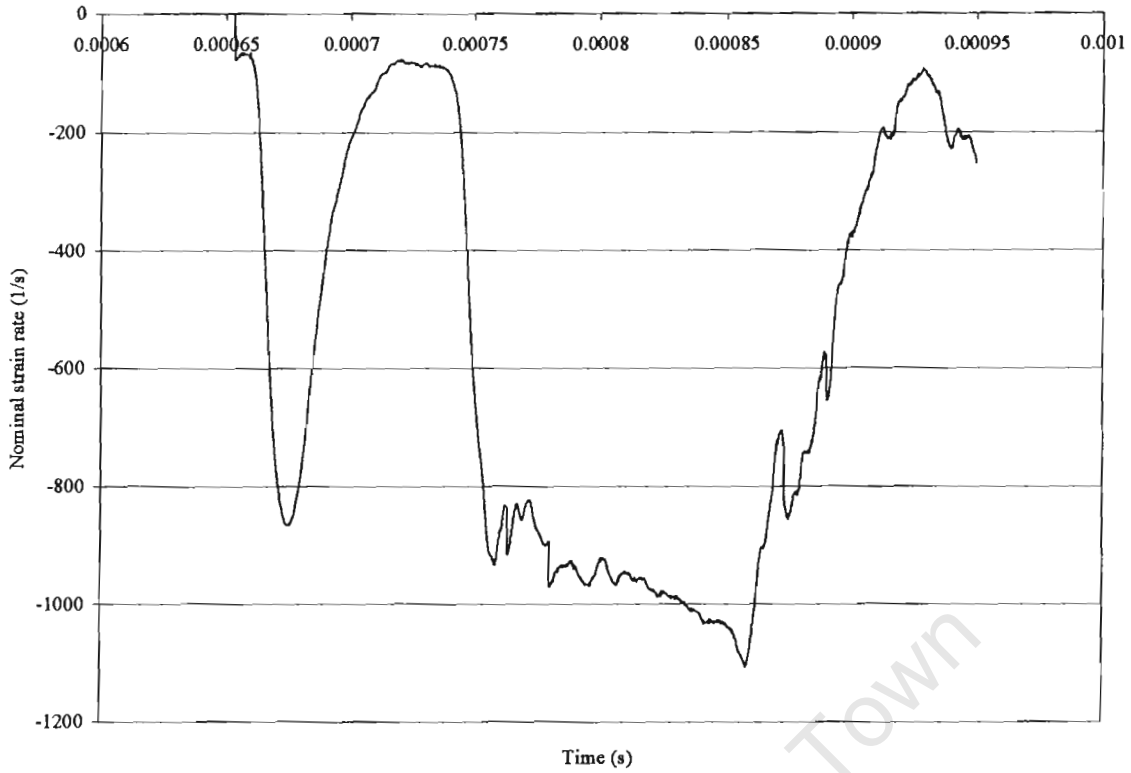

Fig. 4: Percentage Strain Rate-Time curve.

It is important to note that if the specimen has reached quasi-static equilibrium the input and out bar stresses, after correction for wave reflections, should be equal. In practice however, this is extremely difficult to obtain an accurate measure of the input bar stresses when the specimen transmits only a small proportion of the input loading wave, as is the case with brittle materials like CFRP and GFRP. Therefore, to it is proposed that the final stress-strain curve is based on the transmitted stress signal, G_{III} signal multiplied by the ratio of areas between the output bar and the specimen test section, in this case a ratio of (area of bars=$\pi r^2 = \pi(0.0075)^2$)/(area of specimen = $\pi r^2 = \pi(0.004)^2$) $\approx$ 3.5. Thus the stress in the specimen is obtained by multiplying the stress in the bars by this factor, Fig. 5.

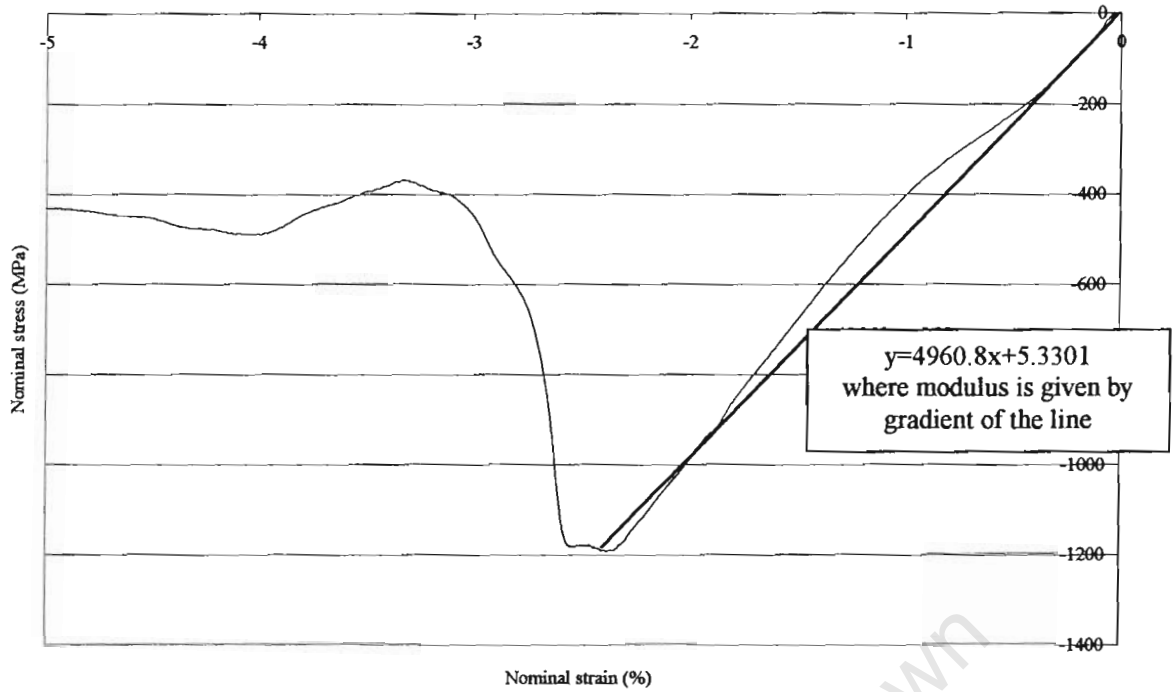

Fig. 5: Nominal (specimen) stress-Nominal strain curve

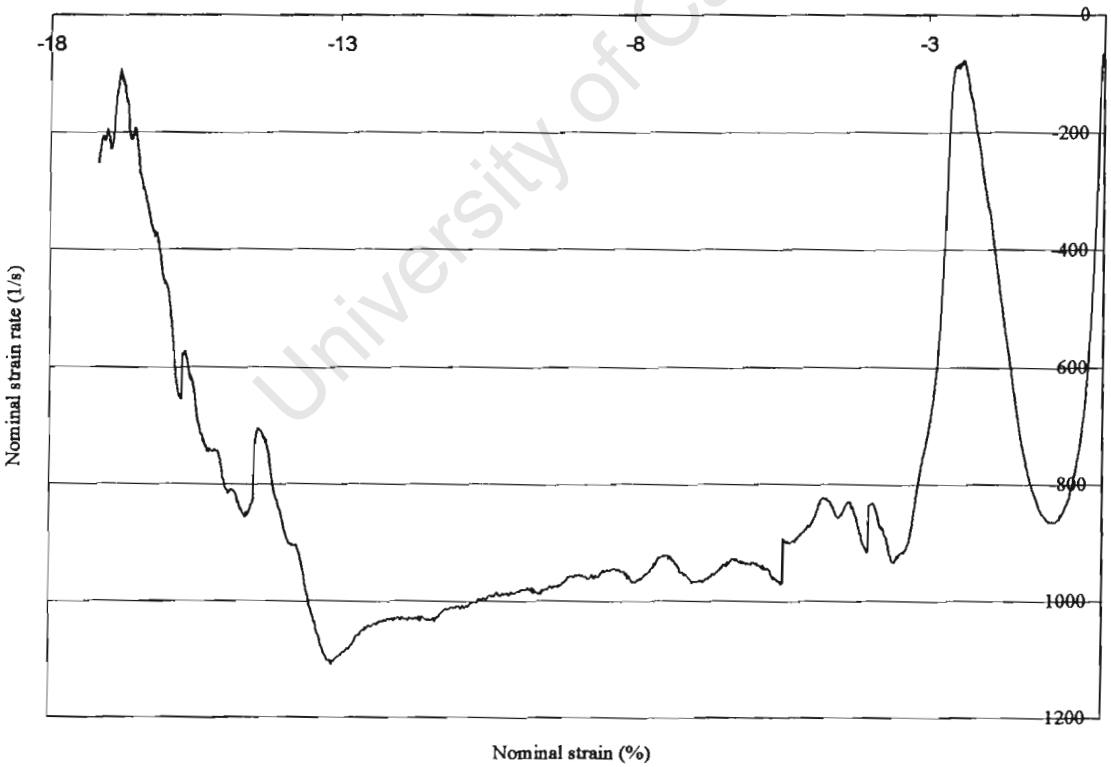

Fig. 6: Strain rate-Nominal strain curve

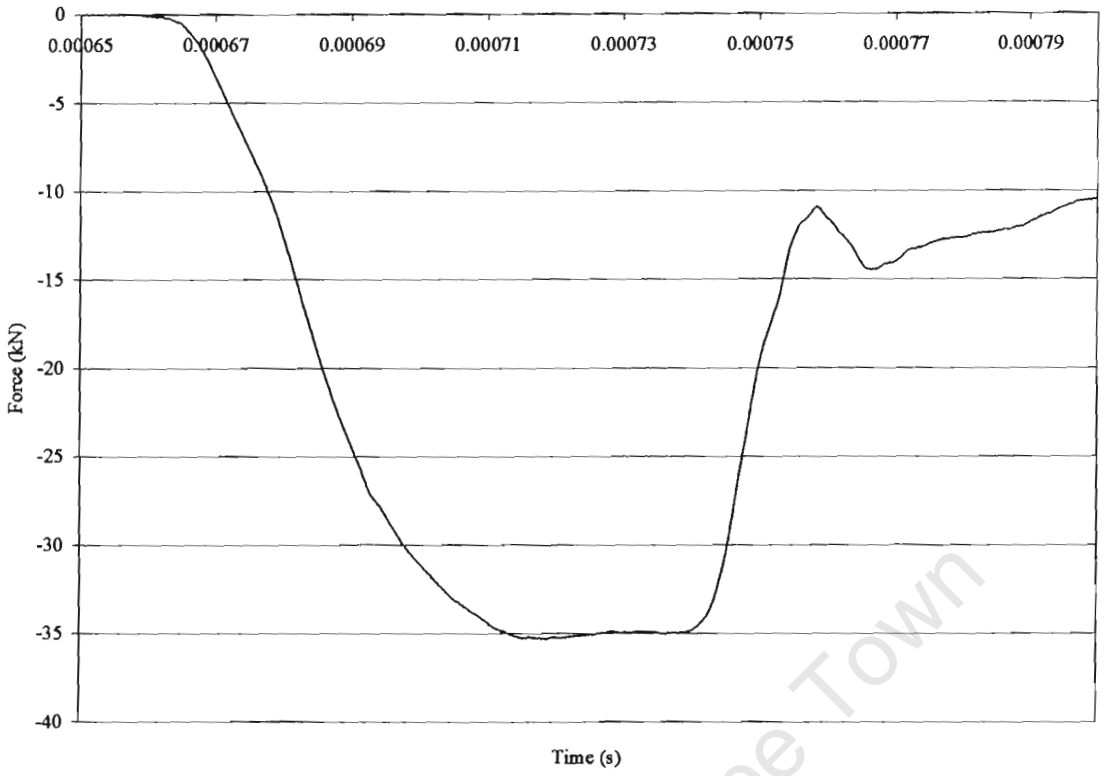

Fig. 7: Force-Time curve

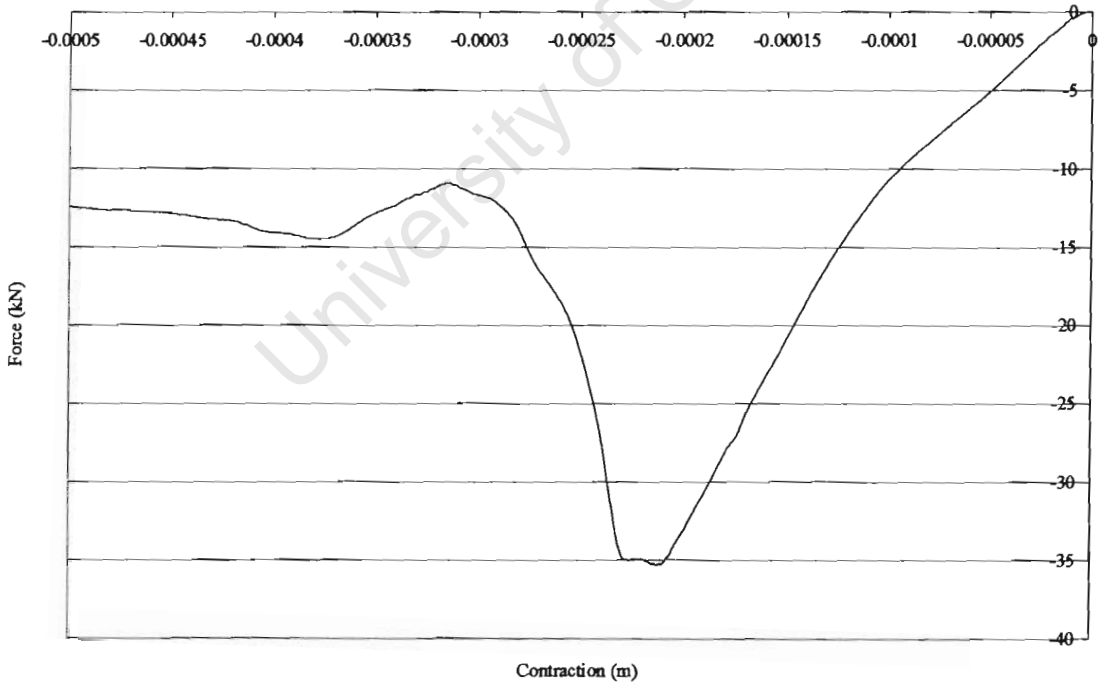

Fig 8: Force-Contraction curve

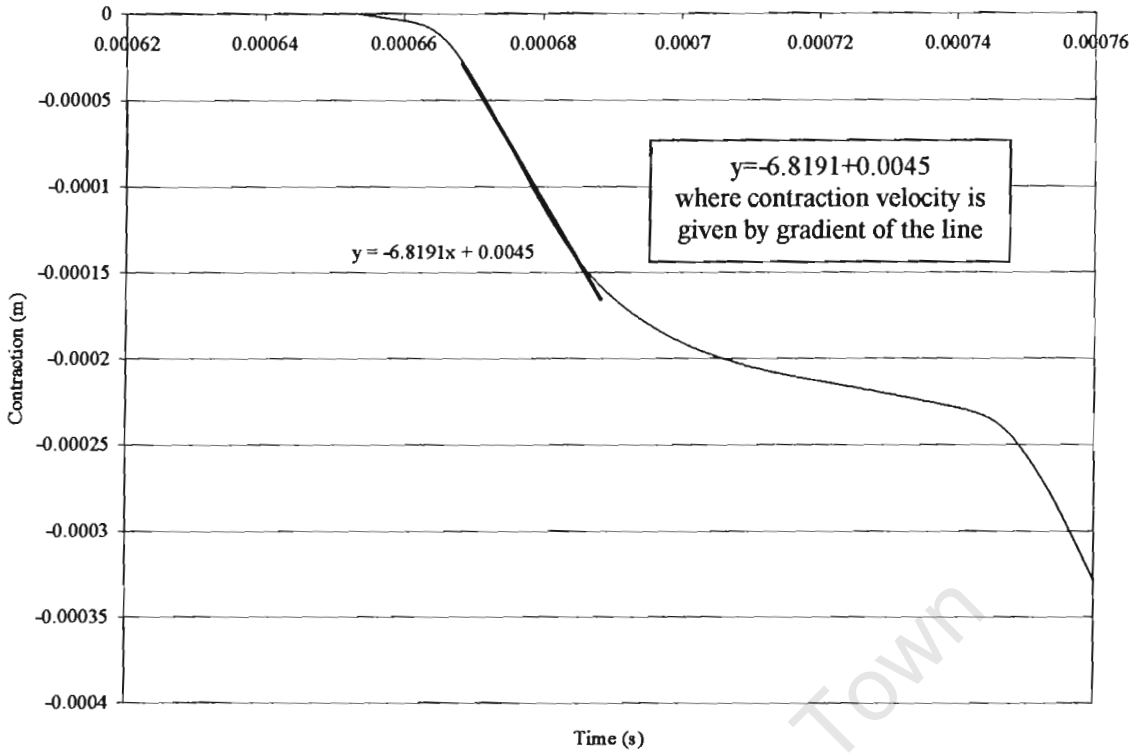

Fig. 9: Contraction-Time curve

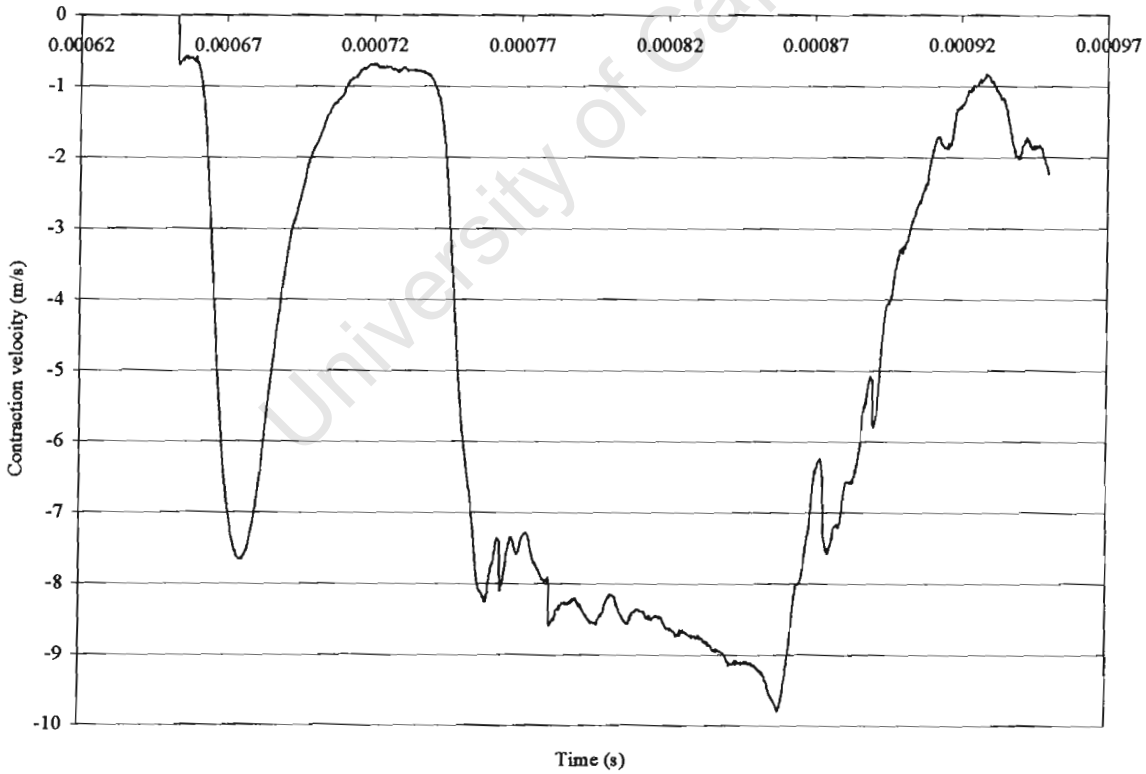

Fig. 10: Contraction Velocity-Time curve

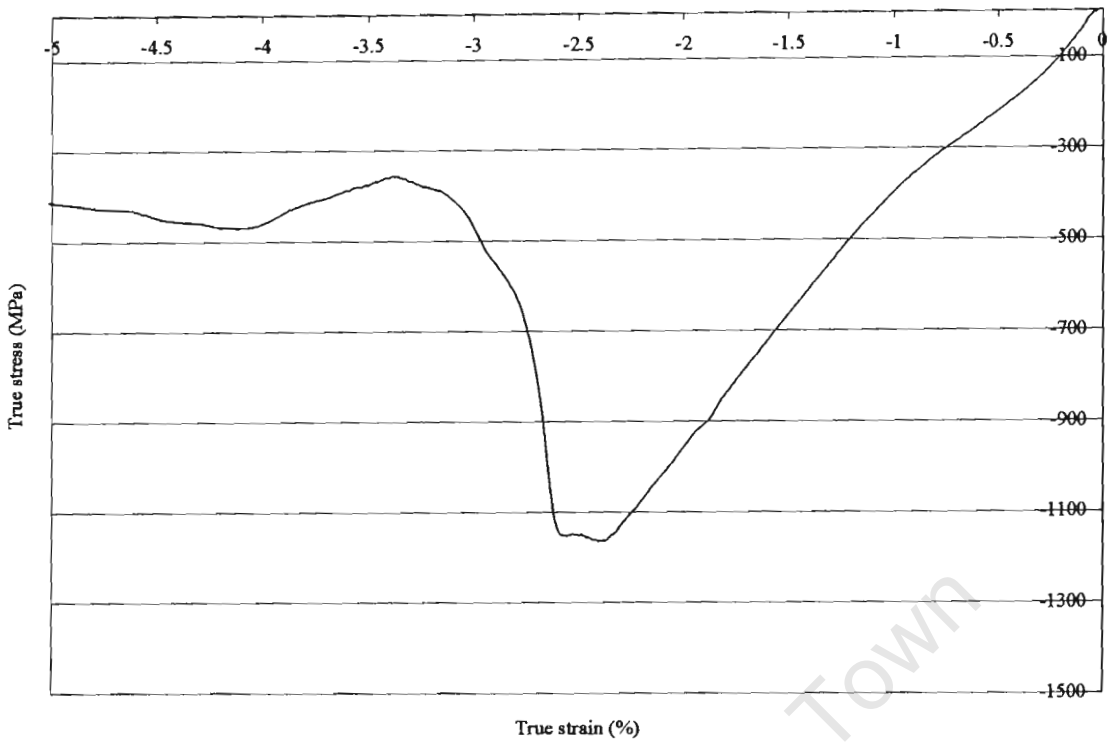

Fig. 11: True Stress-True Strain curve.

The engineering stress-strain curve does not give a true indication of the deformation characteristics of a laminate composite because it is based entirely on the original dimensions of the specimen, and these dimensions change continuously during the test. Also, brittle composite materials that are compressed become unstable and cracks propagate down during the course of the test. Because the cross-sectional area of the specimen is decreasing rapidly at this stage in the test, the load required continuing deformation falls off. The average stress based on original area like wise decreases, and this produces the fall-off in the stress-strain curve beyond the point of maximum load.

The true stress is expressed in terms of engineering stress by

$$\sigma_{True} = \frac{P}{A}\left(1+\frac{\varepsilon}{100}\right) \tag{1}$$

The derivation of Equation (1) assumes both constancy of volume and a homogenous distribution of strain along the gauge length of the compression specimen. The true strain may be determined from the engineering or conventional strain by

$$\varepsilon_{True} = \ln(1+\varepsilon) \tag{2}$$

APPENDIX V

Low and high strain rate compression results for CFRP and GFRP

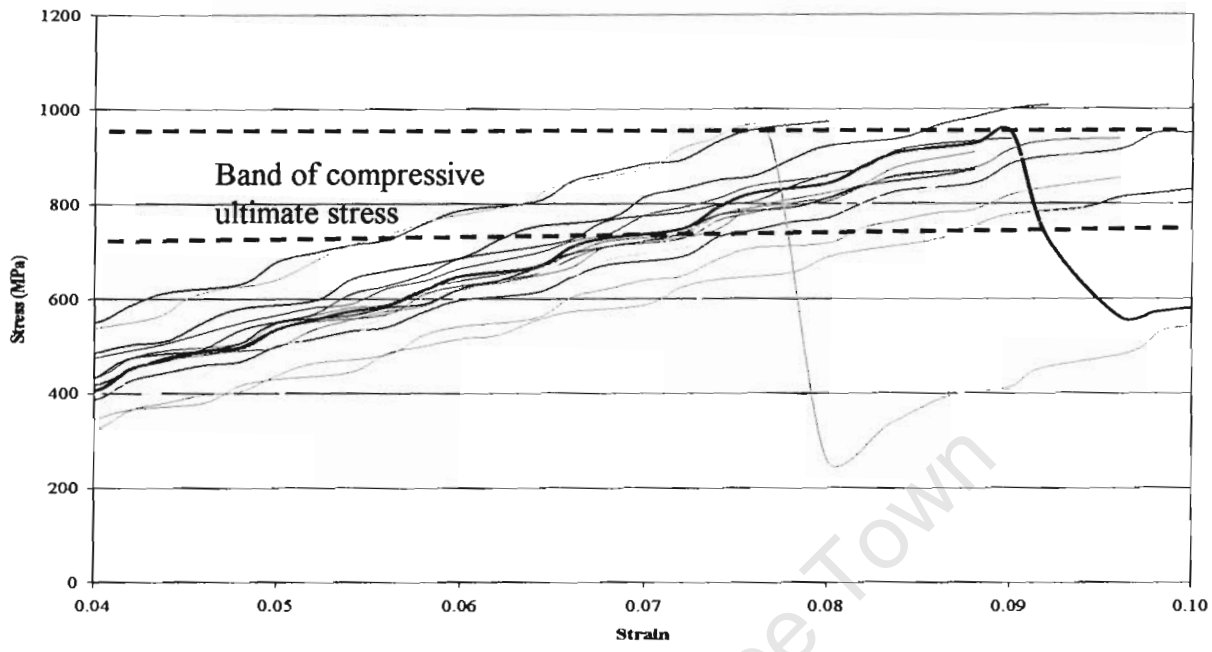

Figure1: Stress vs. strain graph showing the compressive strengths of 20 CFRP specimens under quasi-static loading.

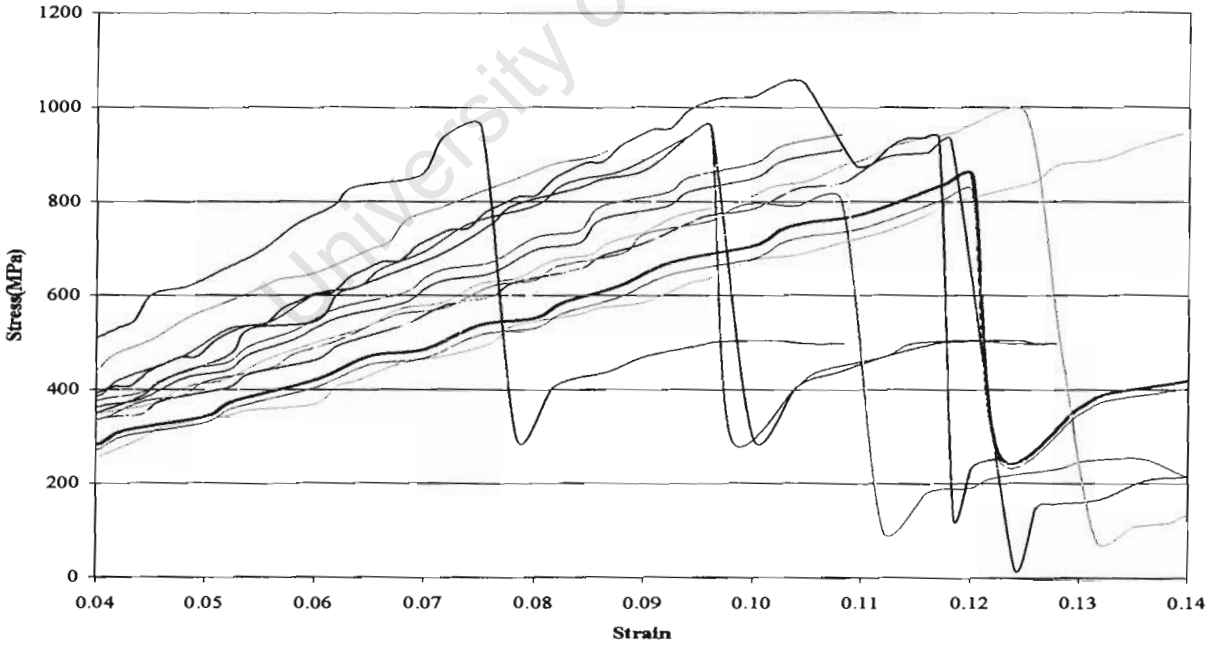

Figure 2: Stress vs. strain graph showing the compressive strengths of GFRP specimens under quasi-static loading.

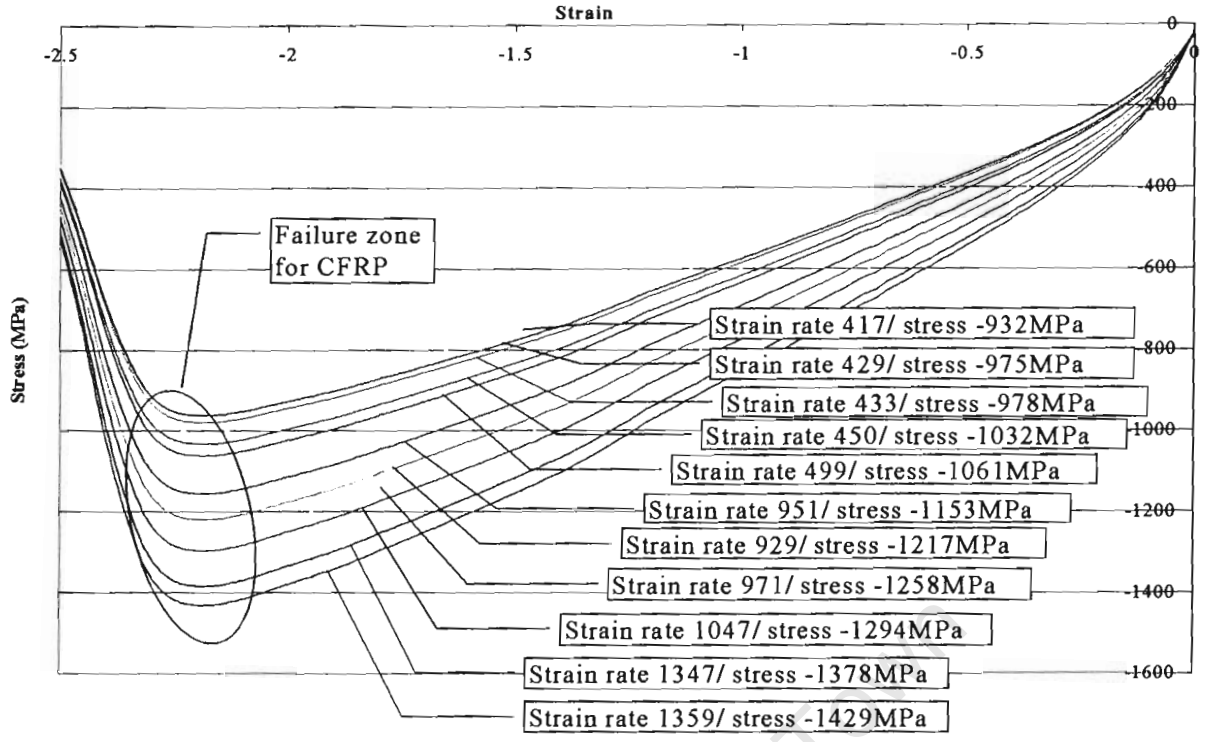

Figure 3: Stress vs. strain graph showing the compressive strengths of CFRP specimens under varying dynamic loading conditions.

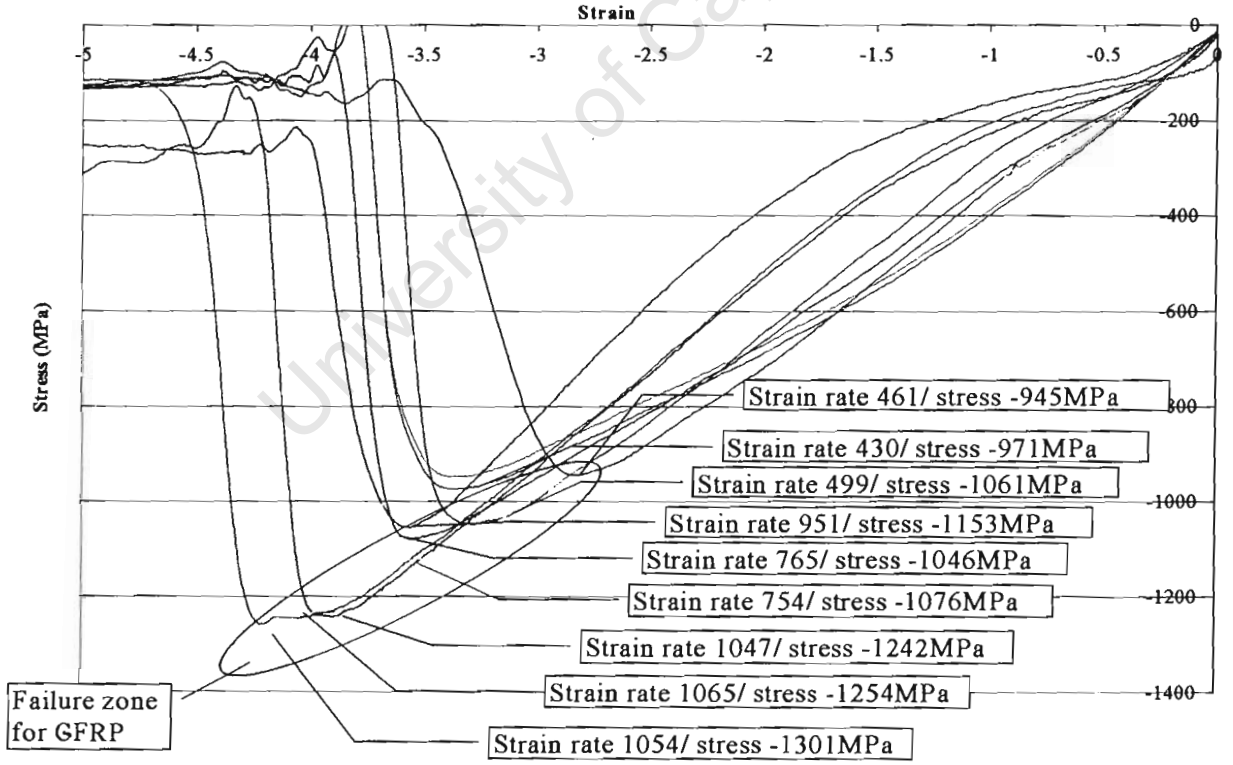

Figure 4: Stress vs. strain graph showing the compressive strengths of GFRP specimens under varying dynamic loading conditions.

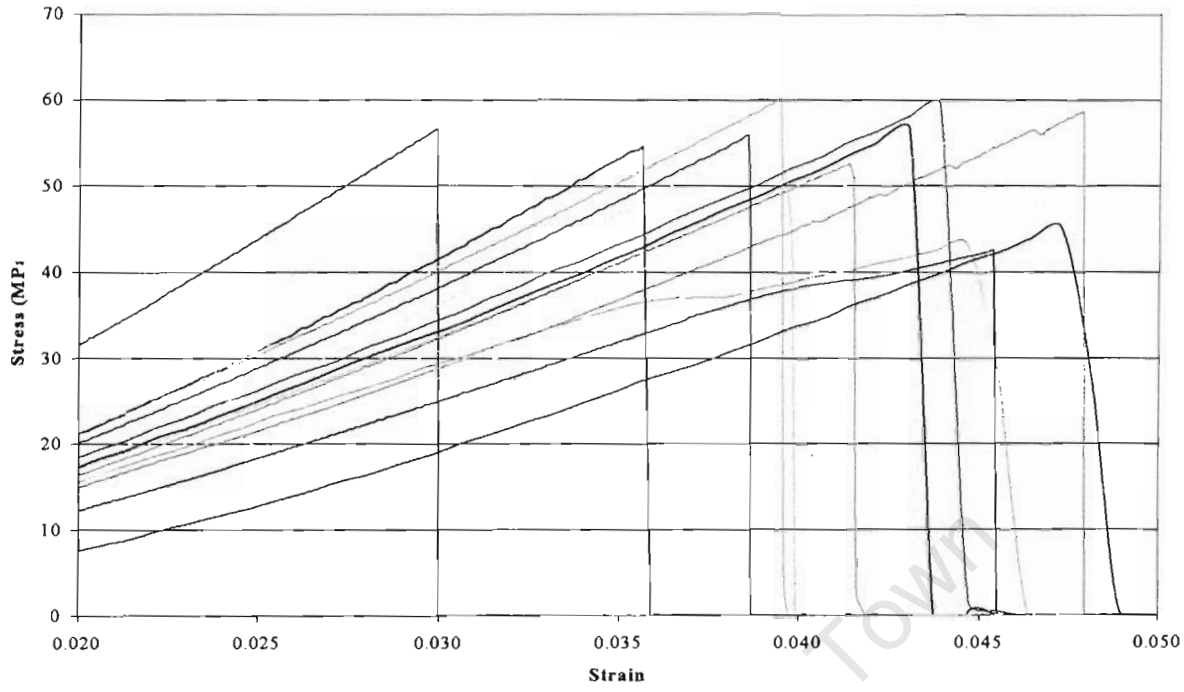

Figure 5: Stress vs. strain graph showing the shear strengths of CFRP specimens under quasi-static loading.

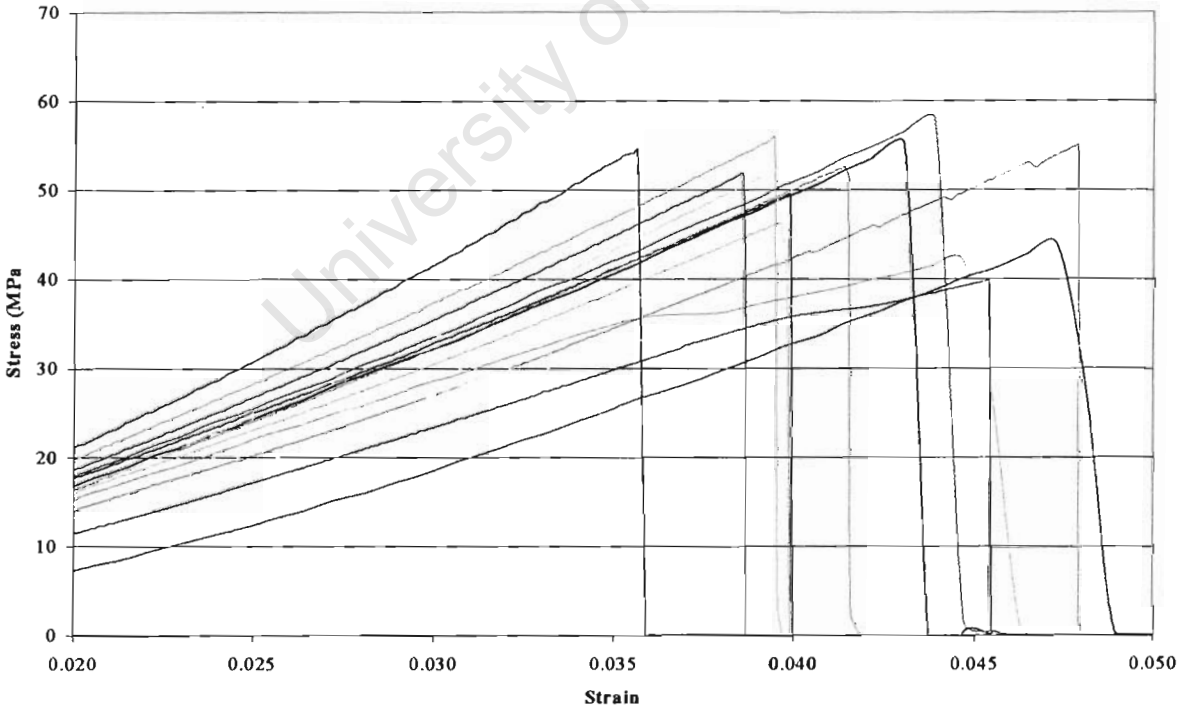

Figure 6: Stress vs. strain graph showing the shear strengths of GFRP specimens under quasi-static loading.

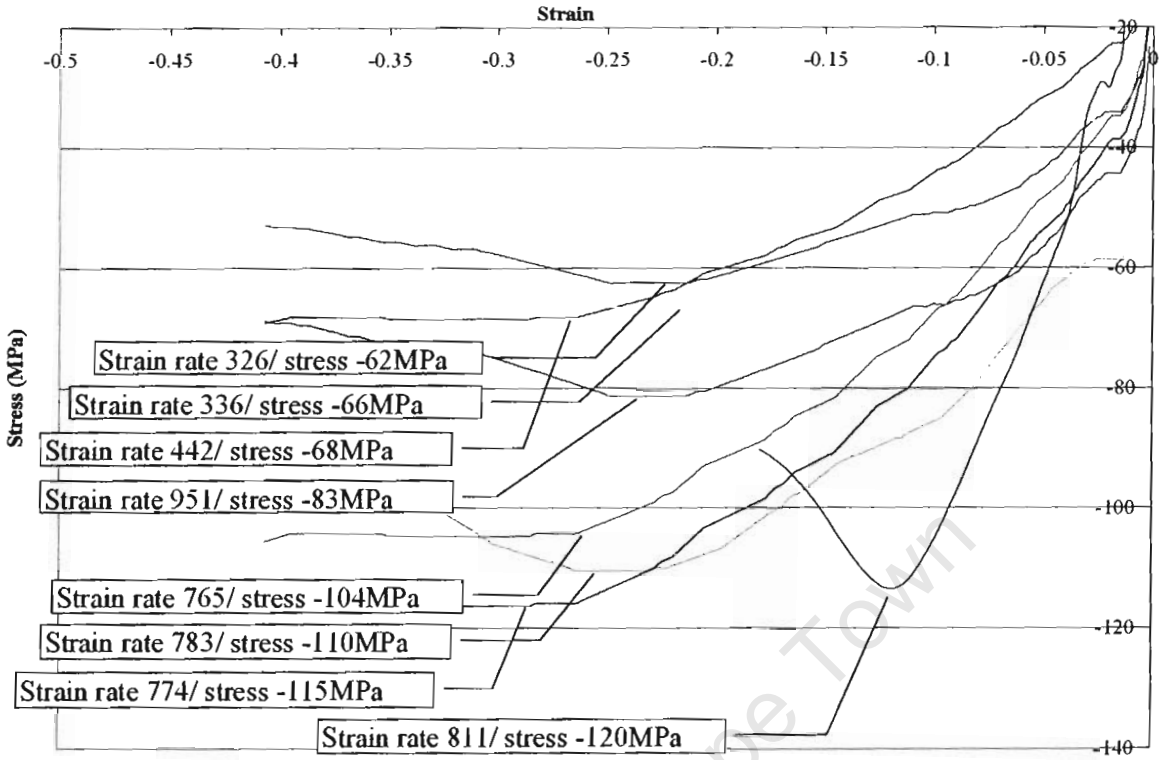

Figure 7: Stress vs. strain graph showing the shear strengths of CFRP specimens under dynamic loading.

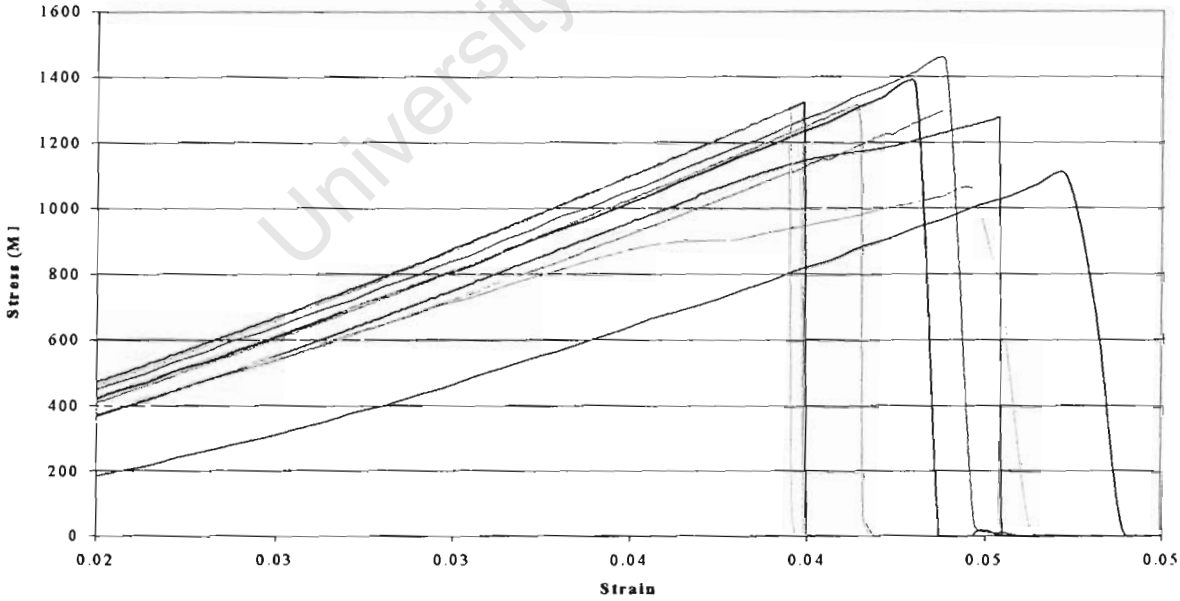

Figure 8: Stress-strain graphs for CFRP specimens under quasi-static tensile loading

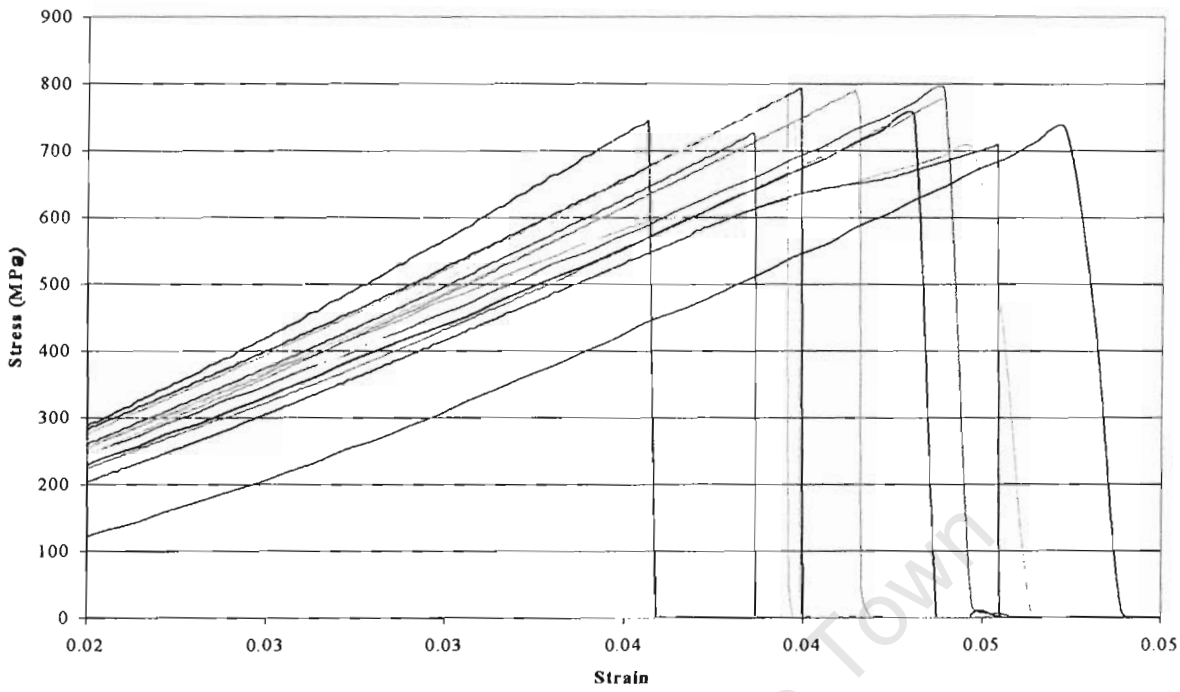

Figure 9: Stress vs. strain graph showing the tensile strengths of GFRP specimens under quasi-static loading.

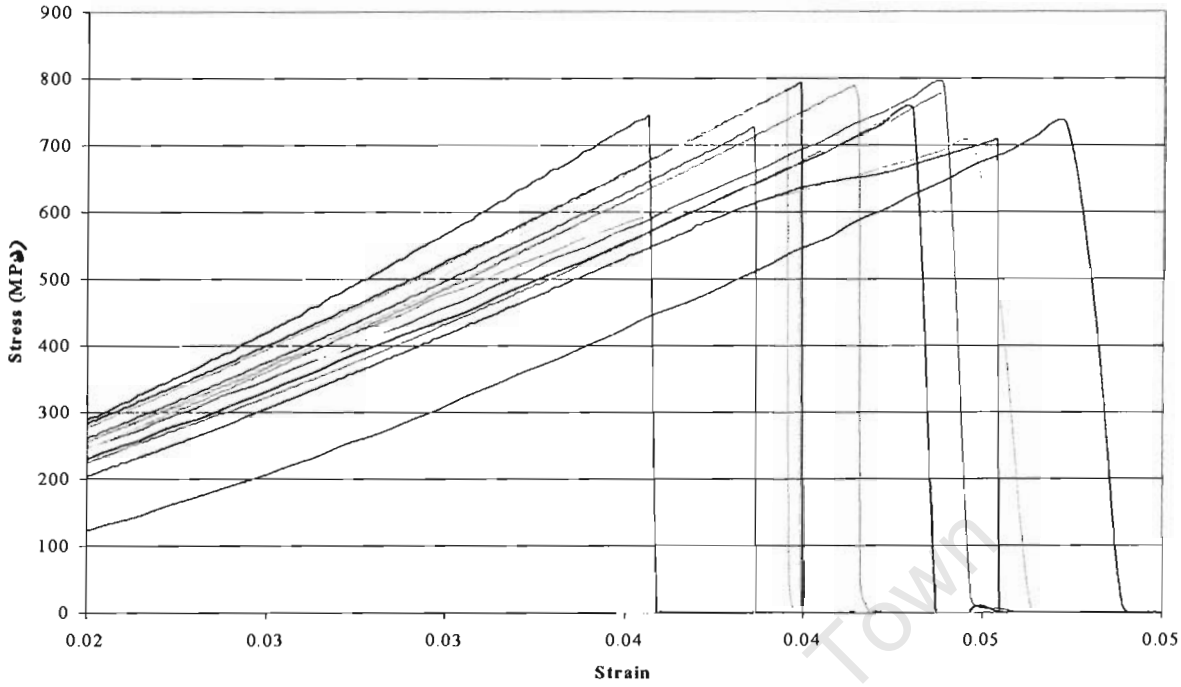

Figure 9: Stress vs. strain graph showing the tensile strengths of GFRP specimens under quasi-static loading.

Table 1: Compression strength values for CFRP specimens tested at an average of 30 different strain rates.

Specimen no.	Failure strength	Specimen no.	Failure strength	Specimen no.	Failure strength
test001	1023	test006	1087	test011	1003
test002	1045	test007	1056	test012	997
test003	1008	test008	1072	test013	1017
test004	1040	test009	1100	test014	1012
test005	1012	test010	1041	test015	1023
average strain rate	450.6	average strain rate	445	average strain rate	476.2
standard deviation	16.47	standard deviation	23.57	standard deviation	10.48
sqrt n	2.24	sqrt n	2.24	sqrt n	2.24
95% CI(lower)	1011.16	95% CI(lower)	1050.54	95% CI(lower)	1001.22
95% CI(upper)	1040.04	95% CI(upper)	1091.86	95% CI(upper)	1019.58
average strength	1025.6	average strength	1071.2	average strength	1010.4

Specimen no.	Failure strength	Specimen no.	Failure strength	Specimen no.	Failure strength
test016	978	test021	992	test026	1006
test017	993	test022	1009	test027	1024
test018	954	test023	1001	test028	980
test019	1012	test024	976	test029	994
test020	969	test025	963	test030	1009
average strain rate	482.6	average strain rate	433	average strain rate	479.8
standard deviation	22.29	standard deviation	18.67	standard deviation	16.55
sqrt n	2.24	sqrt n	2.24	sqrt n	2.24
95% CI(lower)	961.66	95% CI(lower)	971.83	95% CI(lower)	988.10
95% CI(upper)	1000.74	95% CI(upper)	1004.57	95% CI(upper)	1017.10
average strength	981.2	average strength	988.2	average strength	1002.6

Specimen no.	Failure strength	Specimen no.	Failure strength	Specimen no.	Failure strength
test031	1036	test036	1078	test041	973
test032	1021	test037	1064	test042	945
test033	1001	test038	1032	test043	979
test034	998	test039	1013	test044	961
test035	1011	test040	1048	test045	950
average strain rate	458	average strain rate	491.4	average strain rate	471.4
standard deviation	15.53	standard deviation	25.65	standard deviation	14.52
sqrt n	2.24	sqrt n	2.24	sqrt n	2.24
95% CI(lower)	999.78	95% CI(lower)	1024.52	95% CI(lower)	948.87
95% CI(upper)	1027.02	95% CI(upper)	1069.48	95% CI(upper)	974.33
average strength	1013.4	average strength	1047	average strength	961.6

Specimen no.	Failure strength	Specimen no.	Failure strength	Specimen no.	Failure strength
test046	921	test051	1133	test056	1196
test047	971	test052	1129	test057	1163
test048	960	test053	1109	test058	1150
test049	931	test054	1199	test059	1178
test050	954	test055	1099	test060	1183
average strain rate	427.6	average strain rate	830	average strain rate	958
standard deviation	20.77	standard deviation	39.05	standard deviation	17.87
sqrt n	2.24	sqrt n	2.24	sqrt n	2.24
95% CI(lower)	929.20	95% CI(lower)	1099.57	95% CI(lower)	1158.33
95% CI(upper)	965.60	95% CI(upper)	1168.03	95% CI(upper)	1189.67
average strength	947.4	average strength	1133.8	average strength	1174

Specimen no.	Failure strength	Specimen no.	Failure strength	Specimen no.	Failure strength
test061	1197	test066	1264	test071	1180
test062	1088	test067	1190	test072	1247
test063	1161	test068	1109	test073	1266
test064	1203	test069	1240	test074	1209
test065	1111	test070	1199	test075	1193
average strain rate	951.6	average strain rate	929.8	average strain rate	971
standard deviation	51.20	standard deviation	59.32	standard deviation	36.37
sqrt n	2.24	sqrt n	2.24	sqrt n	2.24
95% CI(lower)	1107.12	95% CI(lower)	1148.40	95% CI(lower)	1187.12
95% CI(upper)	1196.88	95% CI(upper)	1252.40	95% CI(upper)	1250.88
average strength	1152	average strength	1200.4	average strength	1219

Specimen no.	Failure strength	Specimen no.	Failure strength	Specimen no.	Failure strength
test076	1280	test081	1261	test086	1191
test077	1294	test082	1284	test087	1203
test078	1263	test083	1230	test088	1184
test079	1254	test084	1212	test089	1178
test080	1271	test085	1245	test090	1160
average strain rate	1017.8	average strain rate	1029.4	average strain rate	868.2
standard deviation	15.44	standard deviation	27.75	standard deviation	15.96
sqrt n	2.24	sqrt n	2.24	sqrt n	2.24
95% CI(lower)	1258.87	95% CI(lower)	1222.07	95% CI(lower)	1169.21
95% CI(upper)	1285.93	95% CI(upper)	1270.73	95% CI(upper)	1197.19
average strength	1272.4	average strength	1246.4	average strength	1183.2

Specimen no.	Failure strength	Specimen no.	Failure strength	Specimen no.	Failure strength
test091	1238	test096	1216	test101	1159
test092	1247	test097	1203	test102	1192
test093	1254	test098	1229	test103	1131
test094	1211	test099	1231	test104	1109
test095	1224	test100	1212	test105	1118
average strain rate	883	average strain rate	888.2	average strain rate	853
standard deviation	17.40	standard deviation	11.78	standard deviation	33.82
sqrt n	2.24	sqrt n	2.24	sqrt n	2.24
95% CI(lower)	1219.55	95% CI(lower)	1207.88	95% CI(lower)	1112.16
95% CI(upper)	1250.05	95% CI(upper)	1228.52	95% CI(upper)	1171.44
average strength	1234.8	average strength	1218.2	average strength	1141.8

Specimen no.	Failure strength	Specimen no.	Failure strength	Specimen no.	Failure strength
test106	1208	test111	1221	test116	1293
test107	1233	test112	1205	test117	1274
test108	1242	test113	1263	test118	1256
test109	1259	test114	1241	test119	1288
test110	1219	test115	1213	test120	1266
average strain rate	937.2	average strain rate	994.4	average strain rate	1024
standard deviation	19.84	standard deviation	23.43	standard deviation	15.29
sqrt n	2.24	sqrt n	2.24	sqrt n	2.24
95% CI(lower)	1214.81	95% CI(lower)	1208.07	95% CI(lower)	1262.00
95% CI(upper)	1249.59	95% CI(upper)	1249.13	95% CI(upper)	1288.80
average strength	1232.2	average strength	1228.6	average strength	1275.4

Specimen no.	Failure strength	Specimen no.	Failure strength	Specimen no.	Failure strength
test121	1280	test126	1339	test131	1506
test122	1261	test127	1384	test132	1478
test123	1253	test128	1350	test133	1466
test124	1290	test129	1341	test134	1451
test125	1253	test130	1370	test135	1494
average strain rate	1045.6	average strain rate	1347	average strain rate	1359.2
standard deviation	16.77	standard deviation	19.54	standard deviation	21.84
sqrt n	2.24	sqrt n	2.24	sqrt n	2.24
95% CI(lower)	1252.70	95% CI(lower)	1339.67	95% CI(lower)	1459.86
95% CI(upper)	1282.10	95% CI(upper)	1373.93	95% CI(upper)	1498.14
average strength	1267.4	average strength	1356.8	average strength	1479.00

Specimen no.	Failure strength	Specimen no.	Failure strength	Specimen no.	Failure strength
test136	1379	test141	1391	test146	1299
test137	1394	test142	1450	test147	1376
test138	1313	test143	1412	test148	1347
test139	1370	test144	1429	test149	1385
test140	1303	test145	1432	test150	1309
average strain rate	1209.4	average strain rate	1231.8	average strain rate	1261.8
standard deviation	41.05	standard deviation	22.31	standard deviation	38.60
sqrt n	2.24	sqrt n	2.24	sqrt n	2.24
95% CI(lower)	1315.82	95% CI(lower)	1403.25	95% CI(lower)	1309.36
95% CI(upper)	1387.78	95% CI(upper)	1442.35	95% CI(upper)	1377.04

Table 2: Compression strength values for GFRP specimens tested at an average of 30 different strain rates.

Specimen no.	Failure strength	Specimen no.	Failure strength	Specimen no.	Failure strength
test001	1060	test006	1084	test011	993
test002	1011	test007	1069	test012	1008
test003	1098	test008	1054	test013	1018
test004	1029	test009	1077	test014	971
test005	1052	test010	1099	test015	974
average strain rate	741	average strain rate	754	average strain rate	716.4
standard deviation	33.05	standard deviation	16.77	standard deviation	20.58
sqrt n	2.24	sqrt n	2.24	sqrt n	2.24
95% CI(lower)	1021.03	95% CI(lower)	1061.90	95% CI(lower)	974.76
95% CI(upper)	1078.97	95% CI(upper)	1091.30	95% CI(upper)	1010.84
average strength	1050	average strength	1076.6	average strength	992.8

Specimen no.	Failure strength	Specimen no.	Failure strength	Specimen no.	Failure strength
test016	1021	test021	1146	test026	991
test017	1039	test022	1126	test027	1015
test018	1056	test023	1101	test028	968
test019	1047	test024	989	test029	959
test020	1011	test025	1139	test030	973
average strain rate	741.4	average strain rate	771.8	average strain rate	747
standard deviation	18.53	standard deviation	64.49	standard deviation	22.21
sqrt n	2.24	sqrt n	2.24	sqrt n	2.24
95% CI(lower)	1018.56	95% CI(lower)	1043.67	95% CI(lower)	961.73
95% CI(upper)	1051.04	95% CI(upper)	1156.73	95% CI(upper)	1000.67
average strength	1034.8	average strength	1100.2	average strength	981.2

Specimen no.	Failure strength	Specimen no.	Failure strength	Specimen no.	Failure strength
test031	1019	test036	1096	test041	1041
test032	1039	test037	1109	test042	1023
test033	1046	test038	1065	test043	1001
test034	1010	test039	1103	test044	1066
test035	1003	test040	1077	test045	1045
average strain rate	746.4	average strain rate	705.6	average strain rate	725.8
standard deviation	18.50	standard deviation	18.44	standard deviation	24.48
sqrt n	2.24	sqrt n	2.24	sqrt n	2.24
95% CI(lower)	1007.18	95% CI(lower)	1073.84	95% CI(lower)	1013.74
95% CI(upper)	1039.62	95% CI(upper)	1106.16	95% CI(upper)	1056.66
average strength	1023.4	average strength	1090	average strength	1035.2

Specimen no.	Failure strength	Specimen no.	Failure strength	Specimen no.	Failure strength
test046	1077	test051	1166	test056	1261
test047	1064	test052	1132	test057	1289
test048	1013	test053	1120	test058	1297
test049	1043	test054	1179	test059	1219
test050	1034	test055	1119	test060	1237
average strain rate	765.4	average strain rate	1003	average strain rate	1043.8
standard deviation	25.13	standard deviation	27.62	standard deviation	33.24
sqrt n	2.24	sqrt n	2.24	sqrt n	2.24
95% CI(lower)	1024.17	95% CI(lower)	1118.99	95% CI(lower)	1231.47
95% CI(upper)	1068.23	95% CI(upper)	1167.41	95% CI(upper)	1289.73
average strength	1046.2	average strength	1143.2	average strength	1260.6

Specimen no.	Failure strength	Specimen no.	Failure strength	Specimen no.	Failure strength
test061	1119	test066	1287	test071	1194
test062	1135	test067	1213	test072	1182
test063	1101	test068	1269	test073	1259
test064	1189	test069	1231	test074	1249
test065	1150	test070	1209	test075	1231
average strain rate	995	average strain rate	1123.6	average strain rate	1043.8
standard deviation	33.47	standard deviation	34.66	standard deviation	33.76
sqrt n	2.24	sqrt n	2.24	sqrt n	2.24
95% CI(lower)	1109.46	95% CI(lower)	1211.42	95% CI(lower)	1193.41
95% CI(upper)	1168.14	95% CI(upper)	1272.18	95% CI(upper)	1252.59
average strength	1138.8	average strength	1241.8	average strength	1223

Specimen no.	Failure strength	Specimen no.	Failure strength	Specimen no.	Failure strength
test076	1229	test081	1251	test086	1294
test077	1309	test082	1296	test087	1278
test078	1266	test083	1242	test088	1299
test079	1247	test084	1233	test089	1231
test080	1222	test085	1282	test090	1259
average strain rate	1065.8	average strain rate	1086.4	average strain rate	1044.8
standard deviation	34.88	standard deviation	26.98	standard deviation	27.83
sqrt n	2.24	sqrt n	2.24	sqrt n	2.24
95% CI(lower)	1224.03	95% CI(lower)	1237.15	95% CI(lower)	1247.80
95% CI(upper)	1285.17	95% CI(upper)	1284.45	95% CI(upper)	1296.60
average strength	1254.6	average strength	1260.8	average strength	1272.2

Specimen no.	Failure strength	Specimen no.	Failure strength	Specimen no.	Failure strength
test091	1290	test096	1309	test101	969
test092	1239	test097	1291	test102	945
test093	1209	test098	1284	test103	931
test094	1249	test099	1323	test104	985
test095	1223	test100	1301	test105	994
average strain rate	1133.4	average strain rate	1054.8	average strain rate	450.8
standard deviation	30.87	standard deviation	15.29	standard deviation	26.52
sqrt n	2.24	sqrt n	2.24	sqrt n	2.24
95% CI(lower)	1214.94	95% CI(lower)	1288.20	95% CI(lower)	941.56
95% CI(upper)	1269.06	95% CI(upper)	1315.00	95% CI(upper)	988.04
average strength	1242	average strength	1301.6	average strength	964.8

Specimen no.	Failure strength	Specimen no.	Failure strength	Specimen no.	Failure strength
test106	967	test111	997	test116	1014
test107	981	test112	946	test117	1066
test108	928	test113	992	test118	1034
test109	941	test114	966	test119	1003
test110	963	test115	958	test120	1015
average strain rate	473	average strain rate	430.4	average strain rate	451.6
standard deviation	21.24	standard deviation	21.98	standard deviation	24.79
sqrt n	2.24	sqrt n	2.24	sqrt n	2.24
95% CI(lower)	937.39	95% CI(lower)	952.53	95% CI(lower)	1004.67
95% CI(upper)	974.61	95% CI(upper)	991.07	95% CI(upper)	1048.13
average strength	956	average strength	971.8	average strength	1026.4

Specimen no.	Failure strength	Specimen no.	Failure strength	Specimen no.	Failure strength
test121	950	test126	993	test131	1009
test122	963	test127	1006	test132	1014
test123	972	test128	976	test133	989
test124	931	test129	942	test134	1001
test125	911	test130	1007	test135	1006
average strain rate	461.4	average strain rate	454	average strain rate	457.8
standard deviation	24.64	standard deviation	27.01	standard deviation	9.52
sqrt n	2.24	sqrt n	2.24	sqrt n	2.24
95% CI(lower)	923.80	95% CI(lower)	961.12	95% CI(lower)	995.45
95% CI(upper)	967.00	95% CI(upper)	1008.48	95% CI(upper)	1012.15
average strength	945.4	average strength	984.8	average strength	1003.80

Specimen no.	Failure strength	Specimen no.	Failure strength	Specimen no.	Failure strength
test136	1054	test141	1066	test146	1032
test137	1023	test142	1051	test147	1047
test138	1069	test143	1048	test148	1041
test139	1013	test144	1077	test149	1039
test140	1041	test145	1083	test150	1056
average strain rate	470.2	average strain rate	467.8	average strain rate	460.2
standard deviation	22.67	standard deviation	15.44	standard deviation	9.03
sqrt n	2.24	sqrt n	2.24	sqrt n	2.24
95% CI(lower)	1020.13	95% CI(lower)	1051.46	95% CI(lower)	1035.09
95% CI(upper)	1059.87	95% CI(upper)	1078.54	95% CI(upper)	1050.91
average strength	1040	average strength	1065	average strength	1043

APPENDIX VI

High strain rate shear results for CFRP and GFRP

Table 1: Shear strength values for CFRP specimens tested at an average of 30 different strain rates.

Specimen no.	Failure strength	Specimen no.	Failure strength	Specimen no.	Failure strength
test001	65	test006	73	test011	60
test002	69	test007	83	test012	54
test003	67	test008	60	test013	83
test004	59	test009	69	test014	77
test005	72	test010	71	test015	61
average strain rate	336.4	average strain rate	367.2	average strain rate	348.4
standard deviation	4.88	standard deviation	8.26	standard deviation	12.35
sqrt n	2.24	sqrt n	2.24	sqrt n	2.24
95% CI(lower)	62.12	95% CI(lower)	63.96	95% CI(lower)	56.18
95% CI(upper)	70.68	95% CI(upper)	78.44	95% CI(upper)	77.82
average strength	66.4	average strength	71.2	average strength	67

Specimen no.	Failure strength	Specimen no.	Failure strength	Specimen no.	Failure strength
test016	67	test021	80	test026	72
test017	53	test022	74	test027	76
test018	81	test023	70	test028	88
test019	76	test024	64	test029	64
test020	63	test025	66	test030	59
average strain rate	373	average strain rate	332.4	average strain rate	452.8
standard deviation	11.00	standard deviation	6.42	standard deviation	11.23
sqrt n	2.24	sqrt n	2.24	sqrt n	2.24
95% CI(lower)	58.36	95% CI(lower)	65.17	95% CI(lower)	61.95
95% CI(upper)	77.64	95% CI(upper)	76.43	95% CI(upper)	81.65
average strength	68	average strength	70.8	average strength	71.8

Specimen no.	Failure strength	Specimen no.	Failure strength	Specimen no.	Failure strength
test031	87	test036	65	test041	55
test032	65	test037	54	test042	63
test033	75	test038	67	test043	69
test034	58	test039	59	test044	71
test035	61	test040	63	test045	91
average strain rate	442.4	average strain rate	377.2	average strain rate	455.4
standard deviation	11.84	standard deviation	5.18	standard deviation	13.39
sqrt n	2.24	sqrt n	2.24	sqrt n	2.24
95% CI(lower)	58.82	95% CI(lower)	57.06	95% CI(lower)	58.07
95% CI(upper)	79.58	95% CI(upper)	66.14	95% CI(upper)	81.53
average strength	69.2	average strength	61.6	average strength	69.8

Specimen no.	Failure strength	Specimen no.	Failure strength	Specimen no.	Failure strength
test046	83	test051	90	test056	77
test047	93	test052	80	test057	68
test048	64	test053	64	test058	59
test049	54	test054	73	test059	64
test050	51	test055	76	test060	89
average strain rate	446	average strain rate	375	average strain rate	412.6
standard deviation	18.34	standard deviation	9.53	standard deviation	11.84
sqrt n	2.24	sqrt n	2.24	sqrt n	2.24
95% CI(lower)	52.92	95% CI(lower)	68.25	95% CI(lower)	61.02
95% CI(upper)	85.08	95% CI(upper)	84.95	95% CI(upper)	81.78
average strength	69	average strength	76.6	average strength	71.4

Specimen no.	Failure strength	Specimen no.	Failure strength	Specimen no.	Failure strength
test061	78	test066	70	test071	89
test062	65	test067	73	test072	69
test063	91	test068	62	test073	74
test064	85	test069	59	test074	81
test065	71	test070	79	test075	66
average strain rate	373.8	average strain rate	412.6	average strain rate	372.2
standard deviation	10.44	standard deviation	8.14	standard deviation	9.31
sqrt n	2.24	sqrt n	2.24	sqrt n	2.24
95% CI(lower)	68.85	95% CI(lower)	61.46	95% CI(lower)	67.64
95% CI(upper)	87.15	95% CI(upper)	75.74	95% CI(upper)	83.96
average strength	78	average strength	68.6	average strength	75.8

Specimen no.	Failure strength	Specimen no.	Failure strength	Specimen no.	Failure strength
test076	118	test081	120	test086	109
test077	126	test082	116	test087	114
test078	130	test083	145	test088	102
test079	111	test084	130	test089	106
test080	108	test085	109	test090	112
average strain rate	774.2	average strain rate	809.4	average strain rate	783.2
standard deviation	9.42	standard deviation	13.98	standard deviation	4.77
sqrt n	2.24	sqrt n	2.24	sqrt n	2.24
95% CI(lower)	110.34	95% CI(lower)	111.74	95% CI(lower)	104.41
95% CI(upper)	126.86	95% CI(upper)	136.26	95% CI(upper)	112.79
average strength	118.6	average strength	124	average strength	108.6

Specimen no.	Failure strength	Specimen no.	Failure strength	Specimen no.	Failure strength
test091	120	test096	106	test101	115
test092	129	test097	101	test102	110
test093	118	test098	111	test103	108
test094	132	test099	118	test104	126
test095	114	test100	116	test105	117
average strain rate	877.4	average strain rate	918.8	average strain rate	775.2
standard deviation	7.60	standard deviation	7.02	standard deviation	7.05
sqrt n	2.24	sqrt n	2.24	sqrt n	2.24
95% CI(lower)	115.94	95% CI(lower)	104.25	95% CI(lower)	109.02
95% CI(upper)	129.26	95% CI(upper)	116.55	95% CI(upper)	121.38
average strength	122.6	average strength	110.4	average strength	115.2

Specimen no.	Failure strength	Specimen no.	Failure strength	Specimen no.	Failure strength
test106	120	test111	102	test116	113
test107	116	test112	117	test117	119
test108	112	test113	105	test118	124
test109	132	test114	111	test119	108
test110	115	test115	114	test120	115
average strain rate	784.6	average strain rate	774.4	average strain rate	875.4
standard deviation	7.81	standard deviation	6.22	standard deviation	6.06
sqrt n	2.24	sqrt n	2.24	sqrt n	2.24
95% CI(lower)	112.15	95% CI(lower)	104.35	95% CI(lower)	110.49
95% CI(upper)	125.85	95% CI(upper)	115.25	95% CI(upper)	121.11
average strength	119	average strength	109.8	average strength	115.8

Specimen no.	Failure strength	Specimen no.	Failure strength	Specimen no.	Failure strength
test121	106	test126	118	test131	123
test122	109	test127	114	test132	131
test123	113	test128	126	test133	114
test124	101	test129	109	test134	126
test125	120	test130	115	test135	130
average strain rate	896.6	average strain rate	780.6	average strain rate	811.6
standard deviation	7.19	standard deviation	6.27	standard deviation	6.83
sqrt n	2.24	sqrt n	2.24	sqrt n	2.24
95% CI(lower)	103.50	95% CI(lower)	110.91	95% CI(lower)	118.81
95% CI(upper)	116.10	95% CI(upper)	121.89	95% CI(upper)	130.79
average strength	109.8	average strength	116.4	average strength	124.80

Specimen no.	Failure strength	Specimen no.	Failure strength	Specimen no.	Failure strength
test136	109	test141	70	test146	65
test137	113	test142	79	test147	59
test138	119	test143	84	test148	67
test139	104	test144	69	test149	52
test140	116	test145	63	test150	69
average strain rate	790	average strain rate	500.2	average strain rate	497.4
standard deviation	5.89	standard deviation	8.40	standard deviation	6.91
sqrt n	2.24	sqrt n	2.24	sqrt n	2.24
95% CI(lower)	107.04	95% CI(lower)	65.64	95% CI(lower)	56.34
95% CI(upper)	117.36	95% CI(upper)	80.36	95% CI(upper)	68.46
average strength	112.2	average strength	73	average strength	62.4

Table 2: Shear strength values for GFRP specimens tested at an average of 30 different strain rates.

Specimen no.	Failure strength	Specimen no.	Failure strength	Specimen no.	Failure strength
test001	66	test006	66	test011	56
test002	60	test007	59	test012	55
test003	57	test008	51	test013	51
test004	63	test009	57	test014	59
test005	70	test010	63	test015	59
average strain rate	342.6	average strain rate	364.4	average strain rate	338
standard deviation	5.07	standard deviation	5.76	standard deviation	3.32
sqrt n	2.24	sqrt n	2.24	sqrt n	2.24
95% CI(lower)	58.76	95% CI(lower)	54.15	95% CI(lower)	53.09
95% CI(upper)	67.64	95% CI(upper)	64.25	95% CI(upper)	58.91
average strength	63.2	average strength	59.2	average strength	56

Specimen no.	Failure strength	Specimen no.	Failure strength	Specimen no.	Failure strength
test016	50	test021	53	test026	52
test017	51	test022	59	test027	58
test018	59	test023	56	test028	66
test019	58	test024	67	test029	63
test020	62	test025	63	test030	61
average strain rate	370.8	average strain rate	331.2	average strain rate	345.6
standard deviation	5.24	standard deviation	5.55	standard deviation	5.34
sqrt n	2.24	sqrt n	2.24	sqrt n	2.24
95% CI(lower)	51.40	95% CI(lower)	54.74	95% CI(lower)	55.32
95% CI(upper)	60.60	95% CI(upper)	64.46	95% CI(upper)	64.68
average strength	56	average strength	59.6	average strength	60

Specimen no.	Failure strength	Specimen no.	Failure strength	Specimen no.	Failure strength
test031	50	test036	51	test041	59
test032	59	test037	57	test042	47
test033	46	test038	56	test043	51
test034	53	test039	47	test044	56
test035	55	test040	43	test045	48
average strain rate	370.6	average strain rate	326.6	average strain rate	358.4
standard deviation	4.93	standard deviation	5.93	standard deviation	5.17
sqrt n	2.24	sqrt n	2.24	sqrt n	2.24
95% CI(lower)	48.28	95% CI(lower)	45.60	95% CI(lower)	47.67
95% CI(upper)	56.92	95% CI(upper)	56.00	95% CI(upper)	56.73
average strength	52.6	average strength	50.8	average strength	52.2

Specimen no.	Failure strength	Specimen no.	Failure strength	Specimen no.	Failure strength
test046	58	test051	106	test056	110
test047	55	test052	99	test057	118
test048	61	test053	115	test058	104
test049	57	test054	110	test059	109
test050	54	test055	102	test060	116
average strain rate	323.4	average strain rate	728.2	average strain rate	745.4
standard deviation	2.74	standard deviation	6.35	standard deviation	5.64
sqrt n	2.24	sqrt n	2.24	sqrt n	2.24
95% CI(lower)	54.60	95% CI(lower)	100.84	95% CI(lower)	106.46
95% CI(upper)	59.40	95% CI(upper)	111.96	95% CI(upper)	116.34
average strength	57	average strength	106.4	average strength	111.4

Specimen no.	Failure strength	Specimen no.	Failure strength	Specimen no.	Failure strength
test061	99	test066	109	test071	106
test062	103	test067	116	test072	97
test063	116	test068	110	test073	86
test064	86	test069	103	test074	101
test065	93	test070	106	test075	79
average strain rate	711.4	average strain rate	791.4	average strain rate	826.6
standard deviation	11.28	standard deviation	4.87	standard deviation	11.08
sqrt n	2.24	sqrt n	2.24	sqrt n	2.24
95% CI(lower)	89.51	95% CI(lower)	104.53	95% CI(lower)	84.09
95% CI(upper)	109.29	95% CI(upper)	113.07	95% CI(upper)	103.51
average strength	99.4	average strength	108.8	average strength	93.8

Specimen no.	Failure strength	Specimen no.	Failure strength	Specimen no.	Failure strength
test076	106	test081	107	test086	97
test077	103	test082	115	test087	91
test078	114	test083	113	test088	89
test079	97	test084	101	test089	105
test080	110	test085	99	test090	103
average strain rate	703.2	average strain rate	713.4	average strain rate	683.6
standard deviation	6.52	standard deviation	7.07	standard deviation	7.07
sqrt n	2.24	sqrt n	2.24	sqrt n	2.24
95% CI(lower)	100.29	95% CI(lower)	100.80	95% CI(lower)	90.80
95% CI(upper)	111.71	95% CI(upper)	113.20	95% CI(upper)	103.20
average strength	106	average strength	107	average strength	97

Specimen no.	Failure strength	Specimen no.	Failure strength	Specimen no.	Failure strength
test091	109	test096	96	test101	104
test092	102	test097	99	test102	109
test093	118	test098	89	test103	98
test094	123	test099	103	test104	112
test095	113	test100	102	test105	94
average strain rate	778.4	average strain rate	813.4	average strain rate	713
standard deviation	8.09	standard deviation	5.63	standard deviation	7.47
sqrt n	2.24	sqrt n	2.24	sqrt n	2.24
95% CI(lower)	105.91	95% CI(lower)	92.86	95% CI(lower)	96.85
95% CI(upper)	120.09	95% CI(upper)	102.74	95% CI(upper)	109.95
average strength	113	average strength	97.8	average strength	103.4

Specimen no.	Failure strength	Specimen no.	Failure strength	Specimen no.	Failure strength
test106	109	test111	97	test116	53
test107	123	test112	84	test117	47
test108	117	test113	106	test118	59
test109	97	test114	110	test119	51
test110	102	test115	93	test120	49
average strain rate	725.8	average strain rate	708	average strain rate	448.8
standard deviation	10.62	standard deviation	10.37	standard deviation	4.60
sqrt n	2.24	sqrt n	2.24	sqrt n	2.24
95% CI(lower)	100.29	95% CI(lower)	88.91	95% CI(lower)	47.76
95% CI(upper)	118.91	95% CI(upper)	107.09	95% CI(upper)	55.84
average strength	109.6	average strength	98	average strength	51.8

Specimen no.	Failure strength	Specimen no.	Failure strength	Specimen no.	Failure strength
test121	58	test126	51	test131	51
test122	47	test127	44	test132	46
test123	63	test128	56	test133	53
test124	55	test129	39	test134	59
test125	51	test130	42	test135	46
average strain rate	446.4	average strain rate	413.6	average strain rate	451.6
standard deviation	6.18	standard deviation	6.95	standard deviation	5.43
sqrt n	2.24	sqrt n	2.24	sqrt n	2.24
95% CI(lower)	49.38	95% CI(lower)	40.31	95% CI(lower)	46.24
95% CI(upper)	60.22	95% CI(upper)	52.49	95% CI(upper)	55.76
average strength	54.8	average strength	46.4	average strength	51.00

Specimen no.	Failure strength	Specimen no.	Failure strength	Specimen no.	Failure strength
test136	59	test141	56	test146	51
test137	56	test142	52	test147	59
test138	63	test143	58	test148	54
test139	68	test144	51	test149	53
test140	63	test145	53	test150	51
average strain rate	402.6	average strain rate	394.4	average strain rate	411
standard deviation	4.55	standard deviation	2.92	standard deviation	3.29
sqrt n	2.24	sqrt n	2.24	sqrt n	2.24
95% CI(lower)	57.81	95% CI(lower)	51.44	95% CI(lower)	50.72
95% CI(upper)	65.79	95% CI(upper)	56.56	95% CI(upper)	56.48
average strength	61.8	average strength	54	average strength	53.6

APPENDIX VII

High strain rate tensile results for CFRP and GFRP

Table 1: Tensile strength values for CFRP specimens tested at an average 30 different strain rates.

Specimen no.	Failure strength	Specimen no.	Failure strength	Specimen no.	Failure strength
test001	1325	test006	1233	test011	1226
test002	1256	test007	1326	test012	1245
test003	1312	test008	1357	test013	1256
test004	1289	test009	1297	test014	1251
test005	1344	test010	1286	test015	1238
average strain rate	612	average strain rate	619	average strain rate	580
standard deviation	34.01	standard deviation	46.42	standard deviation	11.73
sqrt n	2.24	sqrt n	2.24	sqrt n	2.24
95% CI(lower)	1275.39	95% CI(lower)	1259.11	95% CI(lower)	1232.91
95% CI(upper)	1335.01	95% CI(upper)	1340.49	95% CI(upper)	1253.49
average strength	1305.2	average strength	1299.8	average strength	1243.2

Specimen no.	Failure strength	Specimen no.	Failure strength	Specimen no.	Failure strength
test016	1329	test021	1367	test026	1386
test017	1228	test022	1374	test027	1362
test018	1346	test023	1348	test028	1329
test019	1338	test024	1362	test029	1338
test020	1333	test025	1349	test030	1356
average strain rate	627.8	average strain rate	539.4	average strain rate	1132.8
standard deviation	48.94	standard deviation	11.34	standard deviation	22.21
sqrt n	2.24	sqrt n	2.24	sqrt n	2.24
95% CI(lower)	1271.91	95% CI(lower)	1350.06	95% CI(lower)	1334.73
95% CI(upper)	1357.69	95% CI(upper)	1369.94	95% CI(upper)	1373.67
average strength	1314.8	average strength	1360	average strength	1354.2

Specimen no.	Failure strength	Specimen no.	Failure strength	Specimen no.	Failure strength
test031	1329	test036	1299	test041	1326
test032	1304	test037	1283	test042	1361
test033	1321	test038	1259	test043	1314
test034	1339	test039	1264	test044	1324
test035	1345	test040	1273	test045	1318
average strain rate	1147.6	average strain rate	1246.4	average strain rate	1222
standard deviation	16.09	standard deviation	15.96	standard deviation	18.73
sqrt n	2.24	sqrt n	2.24	sqrt n	2.24
95% CI(lower)	1313.50	95% CI(lower)	1261.61	95% CI(lower)	1312.18
95% CI(upper)	1341.70	95% CI(upper)	1289.59	95% CI(upper)	1345.02
average strength	1327.6	average strength	1275.6	average strength	1328.6

Specimen no.	Failure strength	Specimen no.	Failure strength	Specimen no.	Failure strength
test046	1339	test051	1368	test056	1315
test047	1346	test052	1380	test057	1329
test048	1328	test053	1367	test058	1346
test049	1341	test054	1359	test059	1328
test050	1326	test055	1372	test060	1334
average strain rate	1295.4	average strain rate	1602.4	average strain rate	1629.8
standard deviation	8.63	standard deviation	7.66	standard deviation	11.19
sqrt n	2.24	sqrt n	2.24	sqrt n	2.24
95% CI(lower)	1328.43	95% CI(lower)	1362.48	95% CI(lower)	1320.59
95% CI(upper)	1343.57	95% CI(upper)	1375.92	95% CI(upper)	1340.21
average strength	1336	average strength	1369.2	average strength	1330.4

Specimen no.	Failure strength	Specimen no.	Failure strength	Specimen no.	Failure strength
test061	1294	test066	1319	test071	1251
test062	1285	test067	1324	test072	1244
test063	1301	test068	1329	test073	1236
test064	1299	test069	1304	test074	1240
test065	1280	test070	1309	test075	1262
average strain rate	1558	average strain rate	1728.2	average strain rate	1761.2
standard deviation	9.04	standard deviation	10.37	standard deviation	10.24
sqrt n	2.24	sqrt n	2.24	sqrt n	2.24
95% CI(lower)	1283.88	95% CI(lower)	1307.91	95% CI(lower)	1237.63
95% CI(upper)	1299.72	95% CI(upper)	1326.09	95% CI(upper)	1255.57
average strength	1291.8	average strength	1317	average strength	1246.6

Specimen no.	Failure strength	Specimen no.	Failure strength	Specimen no.	Failure strength
test076	1320	test081	1361	test086	1329
test077	1364	test082	1342	test087	1332
test078	1318	test083	1366	test088	1341
test079	1348	test084	1349	test089	1320
test080	1362	test085	1322	test090	1348
average strain rate	1616.8	average strain rate	1734.4	average strain rate	1696.6
standard deviation	22.24	standard deviation	17.36	standard deviation	10.84
sqrt n	2.24	sqrt n	2.24	sqrt n	2.24
95% CI(lower)	1322.90	95% CI(lower)	1332.78	95% CI(lower)	1324.50
95% CI(upper)	1361.90	95% CI(upper)	1363.22	95% CI(upper)	1343.50
average strength	1342.4	average strength	1348	average strength	1334

Specimen no.	Failure strength	Specimen no.	Failure strength	Specimen no.	Failure strength
test091	1324	test096	1344	test101	1281
test092	1366	test097	1377	test102	1275
test093	1350	test098	1384	test103	1306
test094	1347	test099	1362	test104	1292
test095	1341	test100	1351	test105	1273
average strain rate	1594.2	average strain rate	1742.6	average strain rate	1150.6
standard deviation	15.21	standard deviation	16.89	standard deviation	13.69
sqrt n	2.24	sqrt n	2.24	sqrt n	2.24
95% CI(lower)	1332.27	95% CI(lower)	1348.79	95% CI(lower)	1273.40
95% CI(upper)	1358.93	95% CI(upper)	1378.41	95% CI(upper)	1297.40
average strength	1345.6	average strength	1363.6	average strength	1285.4

Specimen no.	Failure strength	Specimen no.	Failure strength	Specimen no.	Failure strength
test106	1203	test111	1301	test116	1316
test107	1209	test112	1286	test117	1294
test108	1187	test113	1293	test118	1304
test109	1219	test114	1272	test119	1311
test110	1211	test115	1284	test120	1323
average strain rate	1048.8	average strain rate	1008.2	average strain rate	1015
standard deviation	11.97	standard deviation	10.80	standard deviation	11.15
sqrt n	2.24	sqrt n	2.24	sqrt n	2.24
95% CI(lower)	1195.31	95% CI(lower)	1277.73	95% CI(lower)	1299.83
95% CI(upper)	1216.29	95% CI(upper)	1296.67	95% CI(upper)	1319.37
average strength	1205.8	average strength	1287.2	average strength	1309.6

Specimen no.	Failure strength	Specimen no.	Failure strength	Specimen no.	Failure strength
test121	1395	test126	1243	test131	1233
test122	1372	test127	1234	test132	1247
test123	1382	test128	1257	test133	1255
test124	1370	test129	1241	test134	1263
test125	1357	test130	1239	test135	1281
average strain rate	989.2	average strain rate	710.2	average strain rate	602
standard deviation	14.20	standard deviation	8.61	standard deviation	17.92
sqrt n	2.24	sqrt n	2.24	sqrt n	2.24
95% CI(lower)	1362.75	95% CI(lower)	1235.25	95% CI(lower)	1240.09
95% CI(upper)	1387.65	95% CI(upper)	1250.35	95% CI(upper)	1271.51
average strength	1375.2	average strength	1242.8	average strength	1255.80

Specimen no.	Failure strength	Specimen no.	Failure strength	Specimen no.	Failure strength
test136	1359	test141	1200	test146	1400
test137	1342	test142	1214	test147	1392
test138	1340	test143	1206	test148	1368
test139	1337	test144	1213	test149	1374
test140	1351	test145	1219	test150	1358
average strain rate	663.4	average strain rate	565.2	average strain rate	525
standard deviation	9.04	standard deviation	7.44	standard deviation	17.29
sqrt n	2.24	sqrt n	2.24	sqrt n	2.24
95% CI(lower)	1337.88	95% CI(lower)	1203.88	95% CI(lower)	1363.25
95% CI(upper)	1353.72	95% CI(upper)	1216.92	95% CI(upper)	1393.55
average strength	1345.8	average strength	1210.4	average strength	1378.4

Table 2: Tensile strength values for GFRP specimens tested at an average 30 different strain rates.

Specimen no.	Failure strength	Specimen no.	Failure strength	Specimen no.	Failure strength
test001	843	test006	864	test011	889
test002	858	test007	861	test012	878
test003	836	test008	857	test013	871
test004	847	test009	852	test014	882
test005	833	test010	861	test015	876
average strain rate	1262.8	average strain rate	1267.4	average strain rate	1207
standard deviation	9.86	standard deviation	4.64	standard deviation	6.76
sqrt n	2.24	sqrt n	2.24	sqrt n	2.24
95% CI(lower)	834.75	95% CI(lower)	854.94	95% CI(lower)	873.27
95% CI(upper)	852.05	95% CI(upper)	863.06	95% CI(upper)	885.13
average strength	843.4	average strength	859	average strength	879.2

Specimen no.	Failure strength	Specimen no.	Failure strength	Specimen no.	Failure strength
test016	852	test021	869	test026	932
test017	859	test022	872	test027	924
test018	847	test023	881	test028	936
test019	837	test024	861	test029	922
test020	839	test025	867	test030	929
average strain rate	1273.2	average strain rate	1232	average strain rate	1734.4
standard deviation	9.12	standard deviation	7.35	standard deviation	5.73
sqrt n	2.24	sqrt n	2.24	sqrt n	2.24
95% CI(lower)	838.80	95% CI(lower)	863.56	95% CI(lower)	923.58
95% CI(upper)	854.80	95% CI(upper)	876.44	95% CI(upper)	933.62
average strength	846.8	average strength	870	average strength	928.6

Specimen no.	Failure strength	Specimen no.	Failure strength	Specimen no.	Failure strength
test031	905	test036	897	test041	945
test032	908	test037	856	test042	941
test033	911	test038	891	test043	934
test034	894	test039	904	test044	930
test035	891	test040	907	test045	938
average strain rate	1670.4	average strain rate	1624.8	average strain rate	1644.8
standard deviation	8.81	standard deviation	20.53	standard deviation	5.86
sqrt n	2.24	sqrt n	2.24	sqrt n	2.24
95% CI(lower)	894.07	95% CI(lower)	873.00	95% CI(lower)	932.47
95% CI(upper)	909.53	95% CI(upper)	909.00	95% CI(upper)	942.73
average strength	901.8	average strength	891	average strength	937.6

Specimen no.	Failure strength	Specimen no.	Failure strength	Specimen no.	Failure strength
test046	909	test051	889	test056	917
test047	898	test052	871	test057	906
test048	917	test053	893	test058	893
test049	913	test054	877	test059	885
test050	905	test055	874	test060	899
average strain rate	1782.2	average strain rate	1076.2	average strain rate	1192.6
standard deviation	7.33	standard deviation	9.65	standard deviation	12.25
sqrt n	2.24	sqrt n	2.24	sqrt n	2.24
95% CI(lower)	901.97	95% CI(lower)	872.34	95% CI(lower)	889.26
95% CI(upper)	914.83	95% CI(upper)	889.26	95% CI(upper)	910.74
average strength	908.4	average strength	880.8	average strength	900

Specimen no.	Failure strength	Specimen no.	Failure strength	Specimen no.	Failure strength
test061	879	test066	871	test071	865
test062	874	test067	865	test072	890
test063	871	test068	890	test073	871
test064	869	test069	877	test074	859
test065	883	test070	896	test075	863
average strain rate	1030.4	average strain rate	988.4	average strain rate	1377.4
standard deviation	5.76	standard deviation	12.95	standard deviation	12.20
sqrt n	2.24	sqrt n	2.24	sqrt n	2.24
95% CI(lower)	870.15	95% CI(lower)	868.45	95% CI(lower)	858.91
95% CI(upper)	880.25	95% CI(upper)	891.15	95% CI(upper)	880.29
average strength	875.2	average strength	879.8	average strength	869.6

Specimen no.	strain rate	Specimen no.	strain rate	Specimen no.	strain rate
test076	1020	test081	1042	test086	870
test077	1003	test082	1029	test087	893
test078	1033	test083	1011	test088	890
test079	1012	test084	1046	test089	865
test080	1021	test085	1019	test090	823
average strain rate	1017.8	average strain rate	1029.4	average strain rate	868.2

Specimen no.	strain rate	Specimen no.	strain rate	Specimen no.	strain rate
test091	897	test096	910	test101	850
test092	900	test097	901	test102	869
test093	873	test098	860	test103	841
test094	865	test099	877	test104	832
test095	880	test100	893	test105	873
average strain rate	883	average strain rate	888.2	average strain rate	853

Specimen no.	strain rate	Specimen no.	strain rate	Specimen no.	strain rate
test106	923	test111	1003	test116	1026
test107	950	test112	1009	test117	1003
test108	963	test113	987	test118	1047
test109	914	test114	992	test119	1014
test110	936	test115	981	test120	1030
average strain rate	937.2	average strain rate	994.4	average strain rate	1024

Specimen no.	strain rate	Specimen no.	strain rate	Specimen no.	strain rate
test121	1052	test126	1384	test131	1391
test122	1041	test127	1321	test132	1367
test123	1029	test128	1339	test133	1352
test124	1068	test129	1372	test134	1346
test125	1038	test130	1319	test135	1340
average strain rate	1045.6	average strain rate	1347	average strain rate	1359.2
	1047.5				

Specimen no.	strain rate	Specimen no.	strain rate	Specimen no.	strain rate
test136	1201	test141	1229	test146	1289
test137	1194	test142	1238	test147	1287
test138	1232	test143	1208	test148	1256
test139	1211	test144	1265	test149	1222
test140	1209	test145	1219	test150	1255
average strain rate	1209.4	average strain rate	1231.8	average strain rate	1261.8

APPENDIX VIII

Time Integration Procedure

Basic equations of non-linear structural mechanics

The Hamilton principle

$$\int_{t=t_1}^{t=t_2} L dt \quad \Rightarrow \quad \text{Min.} \tag{1}$$

leads after spatial FE discretization to the following semi discrete form of the equations of motion

$$\begin{aligned} &\mathbf{M}\ddot{q} + \mathbf{C}\dot{\mathbf{q}} + \mathbf{f}_{\text{int}} = \mathbf{f}_{ext} \\ &\dot{\mathbf{q}}(t = t_0) = \dot{\mathbf{q}}_0 \\ &\mathbf{q}(t = t_0) = \mathbf{q}_0 \end{aligned} \tag{2}$$

where L is the Lagrangian function, $q(t), \dot{q}(t), \ddot{q}(t)$ are the vectors of generalized displacements, velocities and accelerations, M and C are the mass and damping matrices respectively, f_{int} is the vector of the internal resisting forces and f_{ext} is the vector of the external applied forces. The internal forces include the shares of material and geometric non-linearity. Therefore the internal force vector has to be updated at each time step as well as each iteration step during the time integration of the equations of motion. At the current position the internal forces may be evaluated from

$$f_{int} = \int_V D^T \sigma(t, \varepsilon, \dot{\varepsilon}, h) dV \tag{3}$$

where D is the incremental strain-displacement matrix, σ is the vector of Cauchy stresses, which may depend on the time t, strain ε, strain rate $\dot{\varepsilon}$ and internal parameters h. If linearity is assumed with respect to the displacements, the internal forces can be written in the form

$$f_{int} = Kq(t) \tag{4}$$

where $\boldsymbol{K}$ is the stiffness matrix of the system. The equations hold for the time t. To get a new equilibrium state at $t + \Delta t$ we use an updated Lagrangian formulation with second Piola-Kirchhoff stresses and Green-Lagrangian strains. Different types of constitutive relations can be used. In ANSALT we use e.g. an additive combination model for the simulation of rock materials.

$$\dot{\varepsilon} = \dot{\varepsilon}^{el} + \dot{\varepsilon}^{th} + \dot{\varepsilon}^{cr} + \dot{\varepsilon}^{vp} \tag{5}$$

This formulation consists of an elastic and a thermal part, creep deformations and a fracture describing model, where the fracture behaviour is represented by a viscoplastic model with an extended Drucker/Prager criterion using an associated flow rule.

Explicit time integration

Contrary to implicit schemes the generation and factorisation of system matrices, which are very memory and time consuming, may be avoided by explicit schemes (lumped mass and damping matrices). Working with system vectors (instead of system matrices), which may be added up by the finite element contributions, for the computation of the state variables $\boldsymbol{q}$ and $\dot{\boldsymbol{q}}$, it is possible to increase the number of degrees of freedom and thus large engineering problems can be treated. That is also a reason why in spite of the shortcomings, explicit algorithms are often preferred to the analysis of very complex structures (Underwood, Park 1982). From a software development point of view the application of the explicit time integration schemes provides the opportunity to create an uniform software concept both for the solution of static and dynamic problems. To this end a static problem has to be transformed into a dynamic one by adding an artificial acceleration and an artificial damping. This method is known as dynamic relaxation (Wood 1971 and Papadrakadis 1981, for a parallel version see Topping et al. 1994). If static problems are solved by dynamic relaxation both the mass and the damping matrices lose their physical background and become fictitious quantities that control the iteration process. The central difference method to approximate $\boldsymbol{q}$ and $\dot{\boldsymbol{q}}$ has proved to be a very effective procedure to integrate the initial value problem (1).

$$\dot{\boldsymbol{q}}^{t} = \frac{1}{\Delta t}(\boldsymbol{q}^{t+\frac{1}{2}\Delta t} - \boldsymbol{q}^{t-\frac{1}{2}\Delta t})$$
$$\ddot{\boldsymbol{q}}^{t} = \frac{1}{\Delta t}(\dot{\boldsymbol{q}}^{t+\frac{1}{2}\Delta t} - \dot{\boldsymbol{q}}^{t-\frac{1}{2}\Delta t}) \tag{6}$$

The stability consideration of the central difference scheme gives a limitation of the time step length of

$$\Delta t_{krit} \leq 2/\omega_{max} \tag{7}$$

where ω_{max} is the highest frequency of the FE model. If we insert the Eqs. (6) in Eq. (1), accept $\boldsymbol{C} = c\boldsymbol{M}$ with a lumped mass matrix M, the explicit solution scheme of Eq. (1) may be written as

$$\dot{q}_i^{\,t+\frac{1}{2}\Delta t} = \frac{2 - c^t \Delta t}{2 + c^t \Delta t}\dot{q}_i^{\,t-\frac{1}{2}\Delta t} + \frac{2\Delta t}{m_{ii}(2 + c\,\Delta t)}\left(f_{ext_i}^t - f_{int_i}^t\right)$$
$$q_i^{t+\Delta t} = q_i^t + \Delta t\,\dot{q}_i^{\,t+\frac{1}{2}\Delta t} \tag{8}$$

In Eq. (8) $f_{int\,i}^t$ is the internal force related to the degree of freedom i, which is calculated by using Eq. (3), and $f_{ext\,i}^t$ is the given external force at the degree of freedom i. If we solve a static problem the stability criterion of the central difference method Eq. (7) is used to estimate the diagonal element m_{ii} of the lumped mass matrix. The largest eigenvalue of a matrix $\boldsymbol{A}$ is always smaller than any matrix norm (e.g. maximum sum of the absolute elements of a matrix row, also known as Gerschgorin´s theorem). From this follows the estimation (note that in our case $\boldsymbol{A} = \boldsymbol{M}^{-1}\,\boldsymbol{K}$):

$$\omega_i^2 \leq \frac{1}{m_{ii}}\sum_{j=1}^{n}\left|k_{ij}\right| \tag{9}$$

Substitution of Eq. (7) in Eq. (9) gives an estimation of m_{ii}:

$$m_{ii} \geq \frac{1}{4}\Delta t^2 \sum_{j=1}^{n}\left|k_{ij}\right| \tag{10}$$

The damping coefficient c included in (8) may be calculated from the condition of an aperiodic oscillation, i.e.

$$\vartheta = 1 = \frac{c}{2\omega_0} \tag{11}$$

where ϑ, c, ω_0 are the decrement of the damping, the damping coefficient and the smallest eigenfrequency, respectively. The smallest eigenfrequency ω_0 is approximated by the Rayleigh's quotient of the FE system, i.e.

$$\omega_0^2 \leq \frac{\boldsymbol{q}^{t^T} \boldsymbol{K} \boldsymbol{q}^t}{\boldsymbol{q}^{t^T} \boldsymbol{M} \boldsymbol{q}^t} \tag{12}$$

The substitution of Eq. (12) in Eq. (13) gives the damping factor as

$$c^t = 2\sqrt{\frac{\mathbf{q}^{t^T} \mathbf{K} \mathbf{q}^t}{\mathbf{q}^{t^T} \mathbf{M} \mathbf{q}^t}} \tag{13}$$

It should be noted, that the quadratic forms in Eqs. (12) and (13) are simply calculated at the element level by adding up the shares of each element.

Advantage of the explicit time integration method

The explicit method is especially well-suited to solving high-speed dynamic events that require many small increments to obtain a high-resolution solution. If the duration of the event is short, the solution can be obtained efficiently. Contact conditions and other extremely discontinuous events are readily formulate in the explicit method and can be enforced on a node-by-node basis without iteration. The nodal accelerations can be adjusted to balance the external and internal forces during contact. The most striking feature of the explicit method is the lack of a global tangent stiffness matrix., which is required with implicit methods. Since the state of the model is advanced explicitly, iterations and tolerances are note required.

REFERENCES:

1. Papadrakakis,M.: A method for automated evaluation of the dynamic relaxation parameters. Computer Methods in Applied Mechanics and Engineering, 1981, Vol. 25, pp. 35-48
2. Wood,W.L.: Note on dynamic relaxation. Int. J. for Num. Meth. in Eng., 1971,Vol. 3, pp. 145-147
3. Topping,B.H.V., Khan,A.I.: Parallel computation schemes for dynamic relaxation. Engineering Computations, Vol. 11, 1994, pp. 513-548
4. Underwood,P.G.,Park, K.C.: A stand-alone explicit time integration package for structural dynamic analysis, Int. J. for Num. Meth. in Engineering,1982, Vol. 18, pp. 609-622

APPENDIX IX

ABAQUS Scripting Interface

This script performs a parametric study for updating the mesh geometry as well as changing the impacting velocity of loading.

```
Before executing this script you must fetch the appropriate
files: abaqus fetch job=compressionCFRP
       abaqus fetch job=compressionCFRPUtils.py
"""

import part
import mesh
from mesh import C3D8R,EXPLICIT
import job
from compressionCFRP import getResults, createXYPlot

# Create a list of angle parameters and a list of
# element type parameters.

density = [0.1, 0.2, 0.3, 0.4, 0.5,0.6]
elemTypeCodes = [C3D8R]

# Open the model database.
openMdb('compressionCFRP.cae')

model = mdb.models['Model-1']
part = model.parts['Plate']
feature = part.features['Continuumplanar-1']
assembly = model.rootAssembly
```

```
instance = assembly.instances['Plate-1']
job = mdb.jobs['CompressionCFRP']

allFaces = instance.faces
regions =(allFaces[0], allFaces[1], allFaces[2], allFaces[3])
assembly.setMeshControls(regions=regions, technique=STRUCTURED)
face1 = allFaces.findAt((0.,0.,0.), )
face2 = allFaces.findAt((0.,1.,0.), )
face3 = allFaces.findAt((1.,1.,0.), )
face4 = allFaces.findAt((1.,0.,0.), )
allVertices = instance.vertices
v1 = allVertices.findAt((0.,0.,0.), )
v2 = allVertices.findAt((0.,.5,0.), )
v3 = allVertices.findAt((0.,1.,0.), )
v4 = allVertices.findAt((.5,1.,0.), )
v5 = allVertices.findAt((1.,1.,0.), )
v6 = allVertices.findAt((1.,.5,0.), )
v7 = allVertices.findAt((1.,0.,0.), )
v8 = allVertices.findAt((.5,0.,0.), )
v9 = allVertices.findAt((.5,.5,0.), )

# Create a copy of the feature sketch to modify.

tmpSketch = model.Sketch('tmp', feature.sketch)
v, d = tmpSketch.vertices, tmpSketch.dimensions

# Create some dictionaries to hold results. Seed the
# dictionaries with the theoretical results.

dispData, maxMomentData, minMomentData = {}, {}, {}
dispData['Theoretical'] = ((90, -.001478), (80, -.001409),
   (60, -0.000932), (40, -0.000349), (30, -0.000148))
```

```
maxMomentData['Theoretical'] = ((90, 0.0479), (80, 0.0486),
   (60, 0.0425), (40, 0.0281), (30, 0.0191))
minMomentData['Theoretical'] = ((90, 0.0479), (80, 0.0448),
   (60, 0.0333), (40, 0.0180), (30, 0.0108))

# Loop over the parameters to perform the parameter study.

for elemCode in elemTypeCodes:

   # Convert the element type codes to strings.

   elemName = repr(elemCode)
   dispData[elemName], maxMomentData[elemName], \
      minMomentData[elemName] = [], [], []

   # Set the element type.

   elemType = mesh.ElemType(elemCode=elemCode, elemLibrary=EXPLICIT)
   assembly.setElementType(regions=(instance.faces,),
      elemTypes=(elemType,))

   for angle in angles:

      # Change the mesh density of the geometry and regenerate the mesh.

      tmpSketch.changeDimension(dimension=d[9],  value=density,
         vertexList=(v[2], ))
      tmpSketch.changeDimension(dimension=d[10], value=density,
         vertexList=(v[4], ))
      feature.setValues(sketch=tmpSketch)
      part.regenerate()
      assembly.regenerate()
```

```
        assembly.setLogicalCorners(region=face1, corners=(v1,v2,v9,v8))
        assembly.setLogicalCorners(region=face2, corners=(v2,v3,v4,v9))
        assembly.setLogicalCorners(region=face3, corners=(v9,v4,v5,v6))
        assembly.setLogicalCorners(region=face4, corners=(v8,v9,v6,v7))
        assembly.generateMesh(regions=(instance,))

        # Run the job, then process the results.

        job.submit()
        job.waitForCompletion()
        print 'Completed job for %s at %s degrees' % (elemName,
            angle)
        disp, maxMoment, minMoment = getResults()
        dispData[elemName].append((angle, disp))
        maxMomentData[elemName].append((angle, maxMoment))
        minMomentData[elemName].append((angle, minMoment))

# Plot the results.

createXYPlot((10,10), 'Skew 1', 'Displacement, 4x4 Mesh',
    dispData)
createXYPlot((160,10), 'Skew 2', 'Max Moment, 4x4 Mesh',
    maxMomentData)
createXYPlot((310,10), 'Skew 3', 'Min Moment, 4x4 Mesh',
    minMomentData)
```

The script imports two functions from compressionCFRPUtils.. The functions do the following:

·Retrieve the displacement and calculate the maximum stress at the center of the plate.

·Display curves of theoretical and computed results in a new viewport.

"""

CompressionCFRPUtils.py

```
"""

from abaqus import *
import visualization

#~~~~~~~~~~~~~~~~~~~~~~~~~~~~~~~~~~~~~~~~~~~~~~~~~~~~~~~~~~~~~~~~~~~~~~~~~~~~~~~
def getResults():

    """
    Retrieve the displacement and calculate the minimum
    and maximum stress at the center of compression specimen.
    """

    from visualization import ELEMENT_NODAL

    # Open the output database.

    odb = visualization.openOdb('compressionCFRP.odb')
    centerNSet = odb.rootAssembly.nodeSets['CENTER']
    frame = odb.steps['Step-1'].frames[-1]

    # Retrieve Z-displacement at the center of the plate.

    dispField = frame.fieldOutputs['U']
    dispSubField = dispField.getSubset(region=centerNSet)
    disp = dispSubField.values[0].data[2]

    # Average the contribution from each element to the stress,
    # then calculate the minimum and maximum stress at
    # the center of the plate using relevant VUMAT values

    momentField = frame.fieldOutputs['SM']
```

```
    momentSubField = momentField.getSubset(region=centerNSet,
        position=ELEMENT_NODAL)
    m1, m2, m3 = 0, 0, 0
    for value in momentSubField.values:
        m1 = m1 + value.data[0]
        m2 = m2 + value.data[1]
        m3 = m3 + value.data[2]
    numElements = len(momentSubField.values)
    m1 = m1 / numElements
    m2 = m2 / numElements
    m3 = m3 / numElements
    momentA = 0.5 * (abs(m1) + abs(m2))
    momentB = sqrt(0.25 * (m1 - m2)**2 + m3**2)
    maxMoment = momentA + momentB
    minMoment = momentA - momentB

    odb.close()

    return disp, maxMoment, minMoment

#~~~~~~~~~~~~~~~~~~~~~~~~~~~~~~~~~~~~~~~~~~~~~~~~~~~~~~~~~~~~~~~~~~~~~~~~~~~~~~~
def createXYPlot(vpOrigin, vpName, plotName, data):

    """
    Display curves of theoretical and computed results in
    a new viewport.
    """

    from visualization import  USER_DEFINED

    vp = session.Viewport(name=vpName, origin=vpOrigin,
        width=150, height=100)
```

```
xyPlot = session.XYPlot(plotName)
for elemName, xyValues in data.items():
    xyData = visualization.XYData(elemName, xyValues)
    xyPlot.Curve(elemName, xyData)
xyPlot.setValues(curvesToPlot=data.keys(),
    xAxisTitle='Skew Angle', xAxisTitleSource=USER_DEFINED,
    yAxisTitle=plotName, yAxisTitleSource=USER_DEFINED)
vp.setValues(displayedObject=xyPlot)
```

APPENDIX X

Patch Test Procedure

Loading and analytical solution

STEP 1: PERTURBATION

Loading:

Displacement boundary conditions at all exterior nodes:

$$u_x = 10^{-3}(2x+y+z)/2,\ u_y = 10^{-3}(2x+y+z)/2,\ u_z = 10^{-3}(2x+y+z)/2.$$

Analytical solution:

$\sigma_{x(ABAQUS)} = 2000$ $\sigma_{x(VUMAT)} = 2000$

$\sigma_{y(ABAQUS)} = \sigma_{z(ABAQUS)} = 1200$ $\sigma_{y(VUMAT)} = \sigma_{z(VUMAT)} = 1200$

$\sigma_{xy} = 400$

$\sigma_{xy} = \sigma_{xz} = 300$

$\varepsilon_x = 10^{-3}$

$\varepsilon_y = \varepsilon_z = 10^{-3}$

$\gamma_{xy} = 10^{-3}$

$\gamma_{yz} = \gamma_{xz} = 10^{-3}$

STEP 2: NLGEOM

Loading:

Rigid body impact on a single element: 10000 (Rigid body motion is constrained.)

Analytical solution:

$\sigma_{x(ABAQUS)} = 10000$ $\sigma_{x(VUMAT)} = 10000$ $\sigma_y = \sigma_z = 7000$

$\sigma_{xy} = 0$ $\sigma_{xy} = \sigma_{xz} = 0$

$\varepsilon_x = 5.0 \times 10^{-3}$

$\varepsilon_y = \varepsilon_z = 2.0 \times 10^{-3}$

$\gamma_{xy} = 0$

$\gamma_{yz} = \gamma_{xz} = 0$

APPENDIX XI

VUMAT FORTRAN Code

```
C
C UPDATED 3D CONTINUUM VUMAT SUBROUTINE FOR ABAQUS/EXPLICIT
C VERSION 6.3.1 WITH MATERIAL DEGRADATION INCLUDED
C
C
C User subroutine VUMAT
      subroutine vumat (
C Read only -
     *     nblock, ndir, nshr, nstatev, nfieldv, nprops, lanneal,
     *     stepTime, totalTime, dt, cmname, coordMp, charLength,
     *     props, density, strainInc, relSpinInc,
     *     tempOld, stretchOld, defgradOld, fieldOld,
     *     stressOld, stateOld, enerInternOld, enerInelasOld,
     *     tempNew, stretchNew, defgradNew, fieldNew,
C Write only -
     *     stressNew, stateNew, enerInternNew, enerInelasNew )
C
      include 'vaba_param.inc'
C
      dimension coordMp(nblock,*), charLength(nblock), props(nprops),
     1     density(nblock), strainInc(nblock,ndir+nshr),
     2     relSpinInc(nblock,nshr), tempOld(nblock),
     3     stretchOld(nblock,ndir+nshr),
     4     defgradOld(nblock,ndir+nshr+nshr),
     5     fieldOld(nblock,nfieldv), stressOld(nblock,ndir+nshr),
     6     stateOld(nblock,nstatev), enerInternOld(nblock),
     7     enerInelasOld(nblock), tempNew(nblock),
     8     stretchNew(nblock,ndir+nshr),
     9     defgradNew(nblock,ndir+nshr+nshr),
```

```
     1    fieldNew(nblock,nfieldv),
     2    stressNew(nblock,ndir+nshr), stateNew(nblock,nstatev),
     3    enerInternNew(nblock), enerInelasNew(nblock)
C
      character*80 cmname
      dimension intv(2)
      parameter ( zero = 0.d0, one = 1.d0, two = 2.d0, three = 3.d0,
     *    third = one / three, half = 0.5d0, twothds = two / three,
     *    threehalfs = 1.5d0, pc95 = 0.95d0, factor = 5.0d0,
     *    sf12 = 5.8d9, alpha = 2.44d-2, sc = 105d6, s12 = 85d6,
     *    op5 = 1.5d0 )
      parameter ( tempFinal = 1.d2, timeFinal = 1.d-2 )
C
C
C=======================================================================
C
C    VUMAT WRITTEN BY ROBERT OCHOLA ON 15TH FEBRUARY 2003
C
C    EXPLICIT VERSION 6.3.1
C
C    Orthotropic elastic properties
C    Solid 3D element case C3D8R
C
C    Failure model: Compressive Fibre failure, Matrix cracking
C                   and Axial splitting
C
C    Degradation model: Directional stress and stiffness
C                       elimation
C
C=======================================================================
C
C Check to see if it is 3-D element if not give error only
```

```
C VUMAT only suitable for 3-D elements
C
C=======================================================================
==
C
    if ( ndir + nshr .ne.6) then
    write (6,*)'ERROR: USER SUBROUTINE ONLY SUITABLE FOR 3-D ELEMENTS'
    endif
C
C=======================================================================
C         Stress_new(*,1) = stress component 11
C         Stress_new(*,2) = stress component 22
C         Stress_new(*,3) = stress component 33
C         Stress_new(*,4) = stress component 12
C         Stress_new(*,5) = stress component 23
C         Stress_new(*,6) = stress component 13
C
C
C ***NB BUG IN ABAQUS, THE SHEAR STRESS COMPONENTS ARE MUDDLED UP
C   FOR THE C3D8R ELEMENTS. THE ACTUAL ORDER IS 12, 23, 13 AND NOT
C   AS STATED IN THE MANUAL
C
C=======================================================================
C         6 State dependent variables are defined (*DEPVAR)
C
C         State_new(*,1) = is the failure flag  (any direction)
C         State_new(*,2) = is the time of failure
C         State_new(*,3) = presently unused
C         State_new(*,4) = is 11 failure flag (fibre failure)
C         State_new(*,5) = is 22 failure flag (axial splitting)
C         State_new(*,6) = is the failure flag (Delamination not used for now)
C
```

```
C=======================================================================
C
C       INPUT MATERIAL PROPERTIES DATA FROM THE ABAQUS INPUT DECK
C       THE NUMBER OF CONSTANTS IS DEFINED IN THE INPUT DECK
C       14 MATERIALS PROPERTIES DEFINED:
C
C       YOUNG'S MODULUS (3 VALUES)
C       POISSON'S RATIO (3 VALUES)
C       SHEAR MODULUS (3 VALUES)
C       ULTIMATE STRESSES IN COMPRESSION, TENSION AND SHEAR FROM
C       EXPERIMENTAL WORK
C
C=======================================================================
C
      e1     = props(1)
      e2     = props(2)
      e3     = props(3)
      xnu12  = props(4)
      xnu13  = props(5)
      xnu23  = props(6)
      g12    = props(7)
      g13    = props(8)
      g23    = props(9)
      ult11c = props(10)
      ult11t = props(11)
      ult22c = props(12)
      ult22t = props(13)
      ult33c = props(14)
      ult33t = props(15)
      ult12q = props(16)
      ult13q = props(17)
      ult23q = props(18)
```

```
      Dcomp  = props(19)
      qcomp  = props(20)
      Dshr   = props(21)
      qshr   = props(22)
      Dten   = props(23)
      qten   = props(24)
      vel    = props(25)
      length = props(26)
C
C=======================================================================
C
C       Derive strain rate from deformation gradient
C
C       Note vel = velocity of initial impact
C
C=======================================================================
C
      stnrat = vel / length
C
C
      write(6,*)'strain rate',stnrat
C
C=======================================================================
C
C       Derive other Poisson's ratios from the above
C=======================================================================
C
      xnu21  = xnu12 * e2/e1
      xnu31  = xnu13 * e3/e1
      xnu32  = xnu23 * e3/e2
C
C
```

```
C=======================================================================
C
C  Define the constants in the D matrix
C
C  note that Abaqus provides engineering shear strain
C  constants for shear are twice those usually quoted in a
C  D matrix
C  Epsilon_ij = 0.5* Gamma_ij
C
C=======================================================================
C
C
      dconst = one /
     1      (one - xnu12*xnu21-xnu23*xnu32-xnu13*xnu31
     2         - 2*xnu21*xnu32*xnu13)
C
C
      d1111  = dconst * e1 * (one - xnu23*xnu32)
      d1122  = dconst * e1 * (xnu21 + xnu31*xnu23)
      d1133  = dconst * e1 * (xnu31 + xnu21*xnu32)
C
C
      d2211  = d1122
      d2222  = dconst * e2 * (one - xnu13*xnu31)
      d2233  = dconst * e2 * (xnu32 + xnu12*xnu32)
C
C
      d3311  = d1133
      d3322  = d2233
      d3333  = dconst * e3 * (one - xnu12*xnu21)
C
C     NB bug in Abaqus reverses S13, S23
```

```
C
C
      d4444 = g12
      d5555 = g23
      d6666 = g13
C
C
C=======================================================================
C The following loop will only be carried out during the datacheck
C In datacheck, dt, step_time and total time are all one
C The loop initializes status of material points and ensures that
C material calculations are not skipped during the datacheck
C
C=======================================================================
C
      if (( dt .eq. one ).and.(totalTime.eq.one)) then
C
C
        do 50 k = 1, nblock
        stateOld(k,1) = one
        stateOld(k,2) = zero
        stateOld(k,3) = zero
        stateOld(k,4) = one
        stateOld(k,5) = one
        stateOld(k,6) = one
   50   continue
C
      end if
*
*
C=======================================================================
C Carry out material calculations for each block of data size of
```

```
C nblock is defined by ABAQUS
C these calculations are part of vectorised routines
C
C=======================================================================
C
C
C
      do 100 k = 1, nblock
C
C
C=======================================================================
C Evaluate new state of stress and check for each type of failure
C
C=======================================================================
C
      stateNew(k,1) = stateOld(k,1)
      stateNew(k,2) = stateOld(k,2)
      stateNew(k,3) = stateOld(k,3)
      stateNew(k,4) = stateOld(k,4)
      stateNew(k,5) = stateOld(k,5)
      stateNew(k,6) = stateOld(k,6)
C
C=======================================================================
C Update the stress (add incremental stress to existing stress)
C
C=======================================================================
C
*
* sig1
*
*
      sig1 = stressOld(k,1) +
     *     d1111 * strainInc(k,1) + d1122
```

```
     *        * strainInc(k,2) + d1133 * strainInc(k,3)
*
*
* sig2
*
*
          sig2 = stressOld(k,2) +
     *       d1122 * strainInc(k,1) + d2222
     *         * strainInc(k,2) + d2233 * strainInc(k,3)
*
*
* sig3
*
          sig3 = stressOld(k,3) +
     *       d1133 * strainInc(k,1) + d2233
     *         * strainInc(k,2) + d3333 * strainInc(k,3)
*
*
* sig4
*
          sig4 = stressOld(k,4) + d4444 * strainInc(k,4)
*
*
* sig5
*
          sig5 = stressOld(k,5) + d5555 * strainInc(k,5)
*
*
* sig6
*
          sig6 = stressOld(k,6) + d6666 * strainInc(k,6)
C
```

```
C=======================================================================
==
C If element has not already failed set time to current time
C
C=======================================================================
C
      if (stateNew(k,1).eq.one)stateNew(k,2) = totalTime
C
C=======================================================================
C Set ultimate failure values according to stress being in
C compression or tension
C
C=======================================================================
C
      if (sig1.ge.zero)then
      ult11 = ult11t*(((stnrat/Dten)**(1/qten)) + one )
      else
      ult11 = ult11c*(((stnrat/Dcomp)**(1/qcomp)) + one)
      end if
C
C
      if (sig2.ge.zero)then
      ult22 = ult22t*(((stnrat/Dten)**(1/qten)) + one )
      else
      ult22 = ult22c*(((stnrat/Dcomp)**(1/qcomp)) + one)
      end if
C
      if (sig3.ge.zero)then
      ult33 = ult33t*(((stnrat/Dten)**(1/qten)) + one )
      else
      ult33 = ult33c*(((stnrat/Dcomp)**(1/qcomp)) + one)
      end if
```

```
C
      ult12 = ult12q*(((stnrat/Dshr)**(1/qshr)) + one)
C     ult13 = ult13q*(((stnrat/Dshr)**(1/qshr)) + one )
C     ult23 = ult23q*(((stnrat/Dshr)**(1/qshr)) + one )
C
      c1 = ((2*(sig4**2))/ult12) + (3*(sig4**4))
      c2 = ((2*(sc**2))/ult12)  + ((3*alpha)*(sc**4))
C
C
C=====================================================================
C Check for element failure in each direction
C set stress to zero and failure flags if appropriate
C
C DO NOT PERFORM STRESS DEGRADATION DURING DATA CHECK
C
C NB Square roots unnecessary so not included
C
C=====================================================================
C
      if ((dt.eq.one).and.(totalTime.eq.one))then
C
C
      write(6,*)'datacheck phase',dt
C
C
      else
C
C
      f1 = ((sig1/ult11)**two) + (c1/c2)
C
C
        end if
```

```
C
C
      if (f1.ge.one)then
      stateNew(k,1)  = stateOld(k,1) - one
      stateNew(k,4)  = stateold(k,4) - one
      stressNew(k,1) = zero
      stressNew(k,4) = zero
      stressNew(k,6) = zero
C
C
      else
C
*
         stressNew(k,1) = sig1
         stressNew(k,4) = sig4
         stressNew(k,6) = sig6
*
C
         end if
C
C
     if (stateNew(k,4).eq.zero)then
         e1    = zero
         xnu12 = zero
         xnu13 = zero
         g12   = zero
         g13   = zero
        end if
C
C
     if ((dt.eq.one).and.(totalTime.eq.one))then
C
```

```
C
      write(6,*)'datacheck phase',dt
C
C
      else
C
      f2 = ((sig2/ult22)**two)+ (c1/c2)
C
        end if
C
      if (f2.ge.one)then
      stateNew(k,1)  = stateOld(k,1) - one
      stateNew(k,5)  = stateOld(k,5) - one
      stressNew(k,2) = zero
      stressNew(k,4) = zero
      stressNew(k,5) = zero
C
      else
C
C
        stressNew(k,2) = sig2
        stressNew(k,4) = sig4
        stressNew(k,5) = sig5
C
        end if
C
C
      if (stateNew(k,5).eq.zero)then
        e2    = zero
        xnu21 = zero
        xnu23 = zero
        g12   = zero
```

```
          g23   = zero
          end if
C
      if ((dt.eq.one).and.(totalTime.eq.one))then
C
C
      write(6,*)'datacheck phase',totalTime
C
C
      else
C
      f3 = ((sig3/ult33)**two) + (c1/c2)
C
          end if
C
C
      if (f3.ge.one)then
      stateNew(k,1)  = stateOld(k,1) - one
      stateNew(k,6)  = stateOld(k,6) - one
      stressNew(k,3) = zero
      stressNew(k,5) = zero
      stressNew(k,6) = zero
C
      else
C
C
          stressNew(k,3) = sig3
          stressNew(k,5) = sig5
          stressNew(k,6) = sig6
C
          end if
C
```

```
C
      if (stateNew(k,6).eq.zero)then
          e3    = zero
          xnu32 = zero
          xnu31 = zero
          g32   = zero
          g13   = zero
         end if
C
C
* Update the specific internal energy
* has something to do with time step
*
         stressPower = half * (
     1       (stressOld(k,1) + stressNew(k,1) ) * strainInc(k,1)
     2   +    (stressOld(k,2) + stressNew(k,2) ) * strainInc(k,2)
     3   +    (stressOld(k,3) + stressNew(k,3) ) * strainInc(k,3)
     4   +two*(stressOld(k,4) + stressNew(k,4) ) * strainInc(k,4)
     5   +two*(stressOld(k,5) + stressNew(k,5) ) * strainInc(k,5)
     6   +two*(stressOld(k,6) + stressNew(k,6) ) * strainInc(k,6))
*
         enerInternNew(k) = enerInternOld(k) + stressPower/density(k)
*
*
*    Update the dissipated inelastic specific energy -
         smean = third *
     *       ( stressNew(k,1) + stressNew(k,2) + stressNew(k,3) )
         equivStress = sqrt ( op5 * (
     *       ( stressNew(k,1) - smean )**2 +
     *       ( stressNew(k,2) - smean )**2 +
     *       ( stressNew(k,3) - smean )**2 +
     *       ( two * stressNew(k,4)**2 )   +
```

```
     *       ( two * stressNew(k,5)**2 )   +
     *         two * stressNew(k,6)**2 ) )
           plasticWorkInc = equivStress * deqps
           enerInelasNew(k) = enerInelasOld(k)
     *       + plasticWorkInc / density(k)
C
C=======================================================================
==
C Initialise inelastic energy to zero (elastic behaviour)
C note that this has to be done, even though the manuals indicates
C it is optional
C
C=======================================================================
C
      enerInelasNew(k) = zero
C
C=======================================================================
C end of material calculation loop
C
C=======================================================================
C
  100  continue
C
C
C=======================================================================
C The following loop will only be carried out during the datacheck
C In datacheck, dt, step_time and total_time are all one
C The loop sets the initial values of the SDV"s before teh main
C analysis begins
C
C=======================================================================
C
```

```
      if((dt.eq.one).and.(totalTime.eq.one))then
C
      do 150 k = 1, nblock
C
      stateNew(i,1) = one
      stateNew(i,2) = zero
      stateNew(i,3) = zero
      stateNew(i,4) = one
      stateNew(i,5) = one
      stateNew(i,6) = one
C
C
 150  continue
     end if
C
C=============================================================
C end of subroutine, return to Abaqus code
C
C=============================================================
C
C
*
     return
     end
```

APPENDIX XII

Plate Impact Test Results

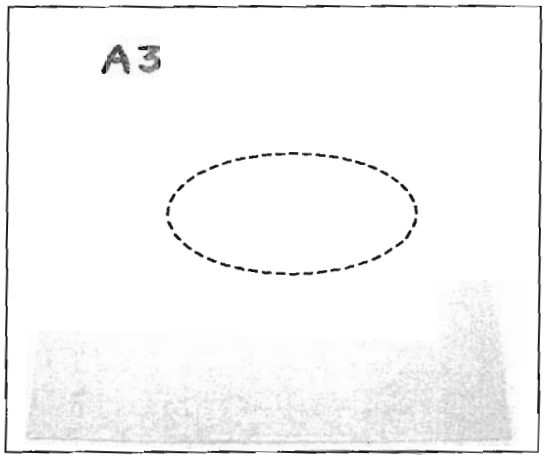

Figure 1: Plate Impact test on GFRP specimen at quasi-static strain rates showing regions with multiple delaminations.

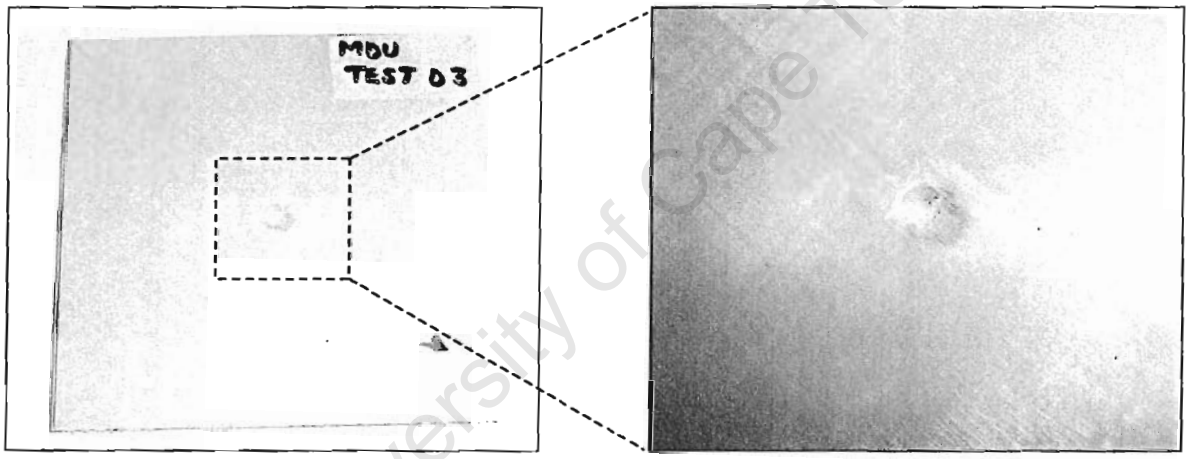

Figure 2: Plate Impact test on GFRP specimen at dynamic strain rates showing region that has been perforated.

APPENDIX XIII

Determination of Stability in Numerical Model

An unrealistic growth in the kinetic energy may indicate that the analysis has become unstable. The energies are useful indications of the solution stability, the history of the total strain (ALLIE) and external work (ALLWK), as well as the artificial strain energy (ALLAE) and kinetic energy (ALLKE) are shown in Fig. 1. The ALLIE and ALLWK increase with a constant gradient for 2 μs therefore during the elastic linear regime. On initial failure the ALLIE and ALLWK curves deviate, Fig. 1. The ALLKE undergoes a gradual then steep rise, followed by a fall in energy as the point of failure is achieved. The recorded kinetic energy is deemed realistic. Finally the "artificial" strain energy undergoes an initially linear rise followed by an exponential rise in energy. The energy analysis shows a stable realistic model due to practical rise in energy recorded. These curves hold for all numerical models run in this thesis.

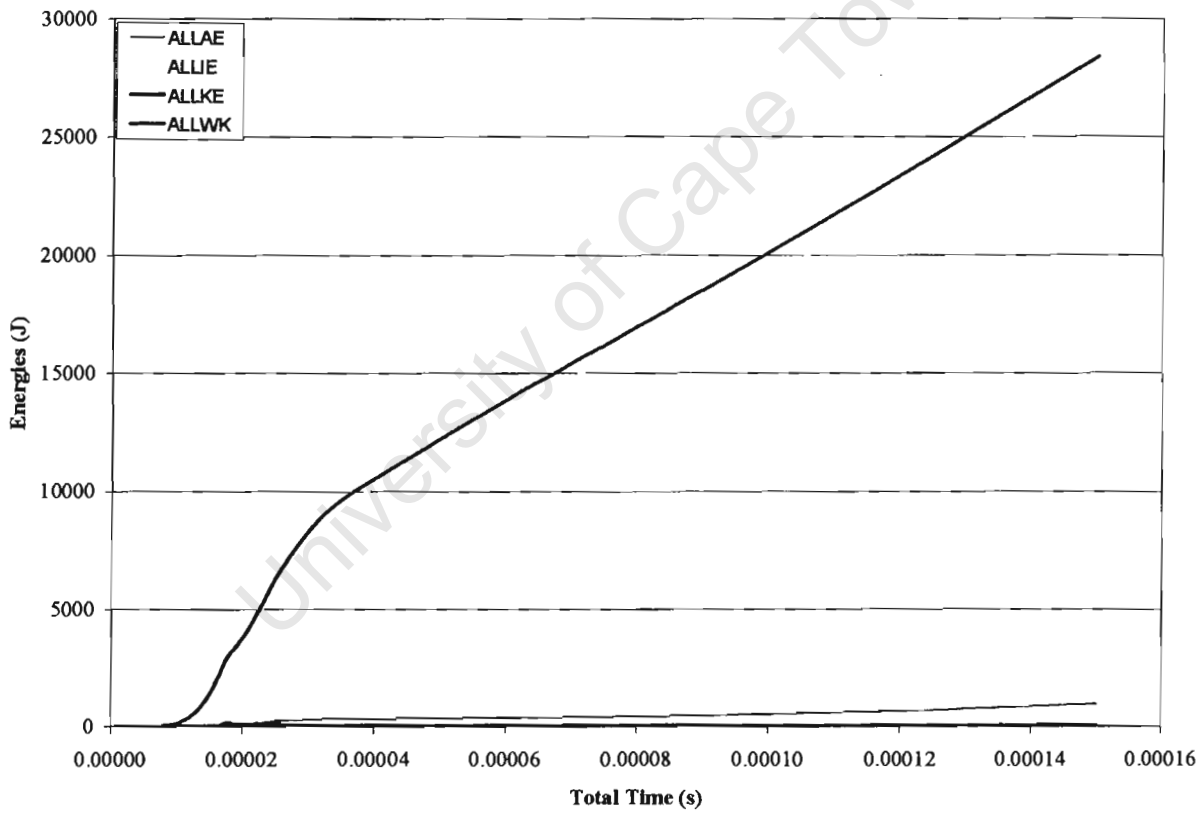

Figure 1: Plots of energies, strain and external work from the selected results showing the degree of stability in the system.

VITA

Robert Ochola was born on the 5th of May 1974 in Addis Ababa Ethiopia. He attended high school in Kenya completing his IGCSE studies at St. Austin's Academy, Nairobi in 1990. Robert went on to do his A' levels in the UK at a school in know as Bedford Modern School in Bedford, England.

In 1992 Robert enrolled at Imperial College London for a Bachelors degree in Materials Science and Engineering. On completing this BEng program he immediately went on to pursue an MSc at the Center for Composite Materials again based at Imperial College London.

Robert then proceeded back to Kenya to work for four years. He started his doctoral degree at the University of Cape Town's Mechanical Engineering department, South Africa, under the guidance of Dr. Kashif Marcus and Prof. Gerald Nurick in October 2000.